Kolditz · Shao · Görke · Wang · Bauer
(Editors)

Terrestrial Environmental Sciences

Thermo-Hydro-Mechanical Chemical Processes in Fractured Porous Media: Modelling and Benchmarking

Benchmarking Initiatives

25th November 2015

Springer

Terrestrial Environmental Sciences

Series Editors

Olaf Kolditz
Hua Shao
Uwe-Jens Görke
Wenqing Wang
Sebastian Bauer

Guest Editors

Jens T Birkhölzer
Steve Yabusaki

Managing Editors

Barbara Kolditz
Leslie Jakobs

Contents

Preface

This is the third volume of the THMC benchmark book series dealing with benchmarks and examples of thermo-hydro-mechanical-chemical processes in fractured-porous media:

1. `http://www.springer.com/de/book/9783642271762`
2. `http://www.springer.com/de/book/9783319118932`

Recently, the benchmark books became items of the new book series in "Terrestrial Environmental Sciences" `http://www.springer.com/series/13468`.

The book is subtitled with "Benchmarking Initiative" as we give a short outline about those activities in past and ongoing of benchmarking initiatives such as DECOVALEX, SeS-Bench (Steefel et al., 2014), MoMaS etc. These initiative provide a substantial contribution to the idea of benchmarking codes and improving numerical modeling of coupled processes in porous and fractured media. Other related benchmarking activities in hydrology and carbon capture storage (CCS) are e.g. HM-INTERCOMP Maxwell et al. (2014) and CO2BENCH Kolditz et al. (2012a).

The book structure follows the "classic" scheme, first single processes and then coupled processes with increasing complexity. The list of symbols and an index you will fined at the end of the book. With this book we also want to award the work of merit of distinguished scientists in the field "Modelling and Benchmarking of THMC Processes". The contributing scientists and institutions are acknowledged in the introduction. As Appendices we present new features of GINA, the OGS preprocessing tool for geotechnical applications as well as an overview of the new ogs^6 version coming soon.

With this version we also provide the input files for self-exercising. This can be found at the OGS community page `http://docs.opengeosys.org/books` (Figure next page) where you can also find the material of the first published OGS Tutorials on "Computational Hydrology I" (Sachse et al., 2015).

- `http://www.springer.com/de/book/9783319133348`

and '"Introduction to Geothermal Processes". Enjoy reading and exercising.

Leipzig, Dresden, Hannover, Chemnitz, Kiel,   *Olaf Kolditz*
November 2015   *Hua Shao*
                                                                   Wenqing Wang
                                                                   Uwe-Jens Görke
                                                                   Sebastian Bauer

Contributors

We appreciate the contributions to the third benchmark book by:

- Ales Balvin (TUL, Technical University of Liberec, CZ)
- Lars Bilke (UFZ, Helmholtz Centre for Environmental Research, DE)
- Jens Birkhölzer (LBNL, Lawrence Berkeley National Laboratory, Energy Geosciences Division, USA)
- Norbert Böttcher (UFZ, Helmholtz Centre for Environmental Research, DE)
- Anke Bucher (HTWK, Leipzig University of Applied Sciences, DE)

- Jens-Olaf Delfs (CAU, Christian-Albrechts-Universität zu Kiel, DE)
- Thomas Fischer (UFZ, Helmholtz Centre for Environmental Research, DE)
- Payton W. Gardner (SANDIA, Sandia National Laboratories, USA)
- Benoit Garitte (NAGRA, National Cooperative for the Disposal of Radioactive Waste, CH)
- Uwe-Jens Görke (UFZ, Helmholtz Centre for Environmental Research, DE)
- Thomas Graf (Leibniz-Universität Hannover, DE)
- Wenkui He (UFZ, Helmholtz Centre for Environmental Research, TU Dresden, DE)
- Carolin Helbig (UFZ, Helmholtz Centre for Environmental Research, DE)
- Philipp Hein (HTWK, Leipzig University of Applied Sciences, DE)
- James W. Heiss (University of Delaware, USA)
- Milan Hokr (TUL, Technical University of Liberec, CZ)
- Yonghui Huang (UFZ, Helmholtz Centre for Environmental Research, TU Dresden, DE)
- Eunseon Jang (UFZ, Helmholtz Centre for Environmental Research, TU Dresden, DE)
- Thomas Kalbacher (UFZ, Helmholtz Centre for Environmental Research, TU Dresden, DE)
- Thomas Kempka (GFZ, Helmholtz Centre Potsdam, German Research Centre for Geosciences, DE)
- Olaf Kolditz (UFZ, Helmholtz Centre for Environmental Research, TU Dresden, DE)
- Georg Kosakowski (PSI, Laboratory for Waste Management (LES), Paul Scherrer Institut)
- Herbert Kunz (BGR, Federal Institute for Geosciences and Natural Resources, DE)
- Christoph Lehmann (UFZ, Helmholtz Centre for Environmental Research, TU Dresden, DE)
- Renchao Lu (UFZ, Helmholtz Centre for Environmental Research, TU Dresden, DE)
- Urs Mäder (Rock Water Interaction, Institute of Geological Sciences, University of Bern, CH)
- Fabien Magri (UFZ, Helmholtz Centre for Environmental Research, DE)
- Jobst Maßmann (BGR, Federal Institute for Geosciences and Natural Resources, DE)
- Xing-Yuan Miao (UFZ, Helmholtz Centre for Environmental Research, TU Dresden, DE)
- Thomas Nagel (UFZ, Helmholtz Centre for Environmental Research, DE / Trinity College Dublin, IE)
- Dmitri Naumov (HTWK, Leipzig University of Applied Sciences / UFZ, Helmholtz Centre for Environmental Research, DE)
- Son Nguyen (CNSC, Canadian Nuclear Safety Commission, CA)

- Erik Nixdorf (UFZ, Helmholtz Centre for Environmental Research, TU Dresden, DE)
- Jenna Poonoosamy (PSI, Laboratory for Waste Management (LES), Paul Scherrer Institut, CH)
- Karsten Rink (UFZ, Helmholtz Centre for Environmental Research, DE)
- Agnes Sachse (UFZ, Helmholtz Centre for Environmental Research, DE)
- Haibing Shao (UFZ, Helmholtz Centre for Environmental Research, DE / Technische Universität Bergakademie Freiberg)
- Hua Shao (BGR, Federal Institute for Geosciences and Natural Resources, DE)
- Elena Tillner (GFZ, Helmholtz Centre Potsdam, German Research Centre for Geosciences, DE)
- Luc R. Van Loon (PSI, Laboratory for Waste Management (LES), Paul Scherrer Institut, CH)
- Peter Vogel (BGR, Federal Institute for Geosciences and Natural Resources, DE)
- Marc Walther (TU Dresden / UFZ, Helmholtz Centre for Environmental Research, DE)
- Wenqing Wang (UFZ, Helmholtz Centre for Environmental Research, DE)
- Xuerui Wang (BGR, Federal Institute for Geosciences and Natural Resources, TU Dresden, DE)
- Norihiro Watanabe (UFZ, Helmholtz Centre for Environmental Research, DE)
- Steve Yabusaki (PNNL, Pacific Northwest National Laboratory, US)
- Haiyang Yi (CUMTB, China University of Mining and Technology, CN)
- Tianyuan Zheng (UFZ, Helmholtz Centre for Environmental Research, TU Dresden, DE)
- Hongwei Zhou (CUMTB, China University of Mining and Technology, CN)
- Gesa Ziefle (BGR, Federal Institute for Geosciences and Natural Resources, DE)
- Günter Zimmermann (GFZ, Helmholtz Centre Potsdam, German Research Centre for Geosciences, DE)

Happy Birthday - Dear Wenqing

We would like to take this opportunity - your 50-ties birthday - to appraise your tremendous contributions to the scientific community dealing with THMC (thermo-hydro-mechanical-chemical) processes in porous media. Wenqing started his scientific education at the Department of Mathematics and Mechanics of Lanzhou University, China (1983-1987). Lanzhou is the capital and largest city of Gansu Province in Northwest China (`https://en.wikipedia.org/wiki/Lanzhou`). A beautiful place, we recently started cooperation activities with the Cold and Arid Regions Environmental and Engineering Research Institute of the Chinese Academy of Sciences CAEERI (`http://english.careeri.cas.cn/`) concerning the water resources of the Heihe River Basin. Then Wenqing moved to Xi'an and obtained his ME from the Department of Engineering Mechanics of Xi'an Jiaotong University (1987-1990). Then he did a big step becoming a PhD student of an international exchange program and joined the Faculty of Engineering Mechanics, Shinshu University (Nagano, Japan) (1995-1996). He finished his PhD study at the Department of Engineering Mechanics, Tongji University in Shanghai in 1997 and continued working as lecturer there until 1999. He returned to Japan and worked from 1999-2000 as a research associate at the Department of Mechanical Engineering and Intelligent Systems, University of Electro-Communications in Tokyo. Again Wenqing decided to make another big move (to Germany) and became a Post-Doc with the Numerical Analysis Group, Department of Mathematics, University of Tübingen (Prof. Hiptmayr). This was a nice coincidence as Wenqings and my ways crossed each other when I started as a Professor for Geohydrology/Hydroinformatics at Tübingen University exactly at the same time. It took one meeting (at least for me) to recognize that Wenqing is the right person for launching the OpenGeoSys idea, he is a brilliant mathematician, dedicated to numerical and computational methods and most of all he is the personal loyalty to the open source initiative. Meanwhile he supported so many young scientists in

their academic career never asking "what is my personal benefit out of this" - this is just extraordinary. Wenqing is one of the finest persons I have ever met and which I consider a tremendous personal gift to me. I was very lucky that Wenqing followed the OGS route to UFZ Leipzig into the Eastern part of Germany. He became a staff scientist with the Helmholtz Centre for Environmental Research UFZ (tenured in 2008). Wenqing did very important scientific contributions to numerical modeling of THM processes in porous media (his most cited works see below). He received several awards during his career as a young scientist, Kwang-Hua Award for PhD student, Tongji University, Scholarship of International Student Exchange Program between China and Japan. In 2014 Wenqing received the "OpenGeoSys Award" for his outstanding contributions to the scientific community in open source developments - he is a real a pioneer in this regard.

Dear Wenqing: We wish you all the best for you personally and your family in the future and - of course - we count on you in the future of ogs^6++ developments ...

Wenqings publication list (links to papers and citations):

- Research ID: www.researcherid.com/rid/B-9702-2008
- ResearchGate: www.researchgate.net/profile/Wenqing_Wang2

Chapter 1
Benchmarking Initiatives

Benchmarking has been recognized as an efficient tool for model validation as well as scientific collaboration. Several workshop series have been established to foster the benchmarking idea: setting up test cases with increasing complexity for method development and code comparison. In addition to representing model complexity, one of the key efforts is to develop codes that are suitable for modern HPC platforms such as PetaFlop supercomputers. It has been realized that those challenges are beyond single team capabilities. Some of these ongoing initiatives are, for example, Sim-SEQ (Mukhopadhyay et al., 2012, 2015), CO2BENCH (for CO2 storage) (Kolditz et al., 2012a), DECOVALEX (1.1), SeS-Bench (1.2) (Steefel et al., 2014) and MoMaS (1.3) (Ackerer, 2010).

1.1 DECOVALEX

by Jens Birkhölzer

DECOVALEX is a multinational model comparison project for advancing the understanding and mathematical modeling of coupled thermo-hydro-mechanical (THM) and thermo-hydro-chemical (THC) processes in geologic and engineered systems associated with geologic disposal of radioactive waste. DECOVALEX is an acronym for "Development of Coupled Models and their Validation against Experiments" Starting in 1992, the project has made important progress and played a key role in the development and validation of advanced numerical models. In-depth knowledge has been gained of the complex THM and THC behavior of different host rock formations and buffer/backfill materials, and significant advances have been made in numerical simulation methods for their quantitative analysis. Over the years, DECOVALEX has involved research teams from a large number of radioactive-waste-management organizations and regulatory authorities, from countries such as

Canada, Czech Republic, China, Finland, France, Germany, Japan, Republic of Korea, Spain, Sweden, Switzerland, United Kingdom, and the United States. A good overview is provided at `www.decovalex.org`.

1.1.1 DECOVALEX Framework

DECOVALEX activities are typically conducted in separate four-year modeling phases. Each phase features a small number (typically three to six) of modeling tasks of importance to radioactive waste disposal. Modeling tasks can either be Test Cases (TC) or Benchmark Tests (BMT). TCs are laboratory and field experiments that have been conducted by one of the project partners and are then collectively studied and modeled by DECOVALEX participants. BMTs involve less complex modeling problems, often targeted at comparing specific solution methods or developing new constitutive relationships. Participating research teams work collaboratively on selected modeling cases, followed by comparison of model results between different models and between models and measurements. While code verification and benchmarking efforts have been undertaken elsewhere to test simulation codes, the model comparison conducted within the DECOVALEX framework is different, because (a) the modeling tasks are often actual laboratory and field experiments, and (b) DECOVALEX engages model comparison in a broad and comprehensive sense, including the modelers' choice of interpretation of experimental data, boundary conditions, rock and fluid properties, etc., in addition to their choice of simulators. Over the years, a number of large-scale, multiyear field experiments have been studied within the project (e.g., the Kamaishi THM Experiment in Japan, the FEBEX heater test at Grimsel Test Site in Switzerland, and the Yucca Mountain Drift-Scale Heater Test).

1.1.2 Current DECOVALEX Activities

DECOVALEX-2015 is the current and 6th project phase and runs from 2012 through 2015. Modeling teams from ten international partner organizations participate in the comparative evaluation of five modeling tasks involving complex field and/or laboratory experiments in Switzerland, France, Japan, and Czech Republic:

- SEALEX Experiment: HM Simulation of a long-term test of the hydraulic (sealing) performance of a swelling bentonite core (5 m long) in a mini tunnel (60 cm diameter) at the Tournemire Underground Research Laboratory (URL) in France,

- HE-E Heater Test: THM Simulation of bentonite/rock interaction to evaluate sealing and clay barrier performance, in a micro-tunnel at the Mont Terri URL in Switzerland,
- EBS Experiment: Simulation of the THMC behavior of the EBS under heating conditions in both the early resaturation and post-closure stages of the repository, in a vertical emplacement hole at the Horonobe URL in Japan (see Figure 1.1.1),
- Bedrichov Tunnel Experiment: Model interpretation of inflow patterns and tracer transport behavior in a fractured granite formation in the Czech Republic.

Together, these tasks address a wide range of relevant issues related to engineered and natural system behavior in argillaceous and crystalline host rocks. A new DECOVALEX phase will start in April 2016 and run until December 2019, referred to as DECOVALEX-2019.
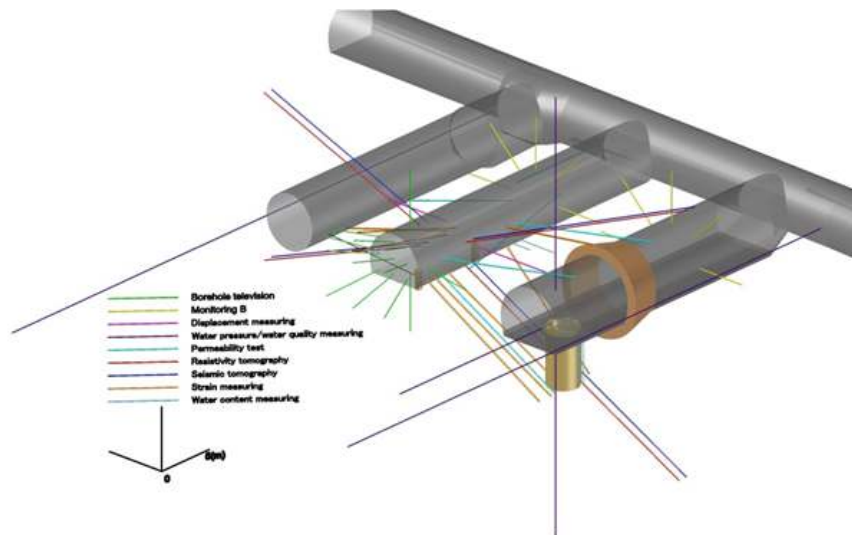
Fig. 1.1.1: EBS Experiment at Horonobe URL: Design of monitoring boreholes for sensor installation (from DECOVALEX web site, `www.decovalex.org`)

1.1.3 DECOVALEX Success Story

The +20-year "young" DECOVALEX project has played, and continues to play, a key role in the development of the coupled THM, THC, and recently

THMC, models of geosystems and their applications to deep geological disposal of radioactive waste and spent nuclear fuel. New and sophisticated coupled simulation tools have been developed to study the near- and far-field behaviors of potential nuclear waste repositories under various scenarios, including understanding geosphere responses to glaciation and permafrost. A model comparison framework has been developed that fosters intensive interactions among research teams of different disciplines and modeling approaches, and that features successful application to both complex in situ experiments and benchmark test problems. Many doctoral theses were completed in the course of this project and related model results and comparisons have been published in Special Issues in different journals, several other journal contributions, book chapters, and progress reports. The results of these efforts have been of major benefit to the advancement of knowledge on waste disposal in general, and to funding organizations of the DECOVALEX project in particular. The research teams have been able to share data and results from very expensive long-term and large-scale field tests, generate new ideas and concepts, raise technical issues in joint publications, and perform critical reviews of each other's work. The insight obtained in such integrated, cooperative efforts would have been impossible if the teams had worked independently.

Special Issues:

- Special Issue on DECOVALEX 2011 - Part 1, Journal of Rock Mechanics and Geotechnical Engineering (Volume 5, Issue 1, Pages 1-84, 2013),
- Special Issue on DECOVALEX 2011 Part 2, Journal of Rock Mechanics and Geotechnical Engineering (Volume 5, Issue 2, Pages 85-155, 2013),
- The DECOVALEX-THMC PROJECT (Safety assessment of nuclear waste repositories), Journal of Environmental Geology (Volume 57, Number 6, Pages 1217-1456, 2009),
- Special Issue on Research Results from the DECOVALEX III & Benchpar projects, International Journal of Rock Mechanics and Mining Sciences (Volume 42, Number 5-6, Pages 591-870, 2005),
- Special Issue in Elsevier Geo-Engineering Book Series: Coupled Thermo-Hydro-Mechanical-Chemical Processes in Geo-Systems - Fundamentals, Modelling, Experiments and Applications (Volume 2, Pages 3-832, 2004).
- DECOVALEX-II Special Issue, International Journal of Rock Mechanics and Mining Sciences (Volume 38, Number 1, Pages 1-162, 2001).
- Special Issue in Elsevier Book Series Developments in Geotechnical Engineering: Coupled Thermo-Hydro-Mechanical Processes of Fractured Media: Mathematical and Experimental Studies (Volume 79, Pages 1-575, 1996).

• The results of the ongoing DECOVALEX phase will be published in a Thematic Issue of Environmental Earth Sciences (EES) in 2016, forthcoming.

1.2 Subsurface Environmental Simulation Benchmarking (SeS-Bench)

by Steve Yabusaki

The Subsurface Environmental Simulation Benchmarking (SeS-Bench) working group was initiated to develop, publish, and make publicly available well-described benchmark problems that could be used to demonstrate simulator conformance with norms established by the subsurface science and engineering community. The working group held its first organizational meeting in Berkeley, California, USA in 2011 with follow-up workshops at the National Central University in Taipei, Taiwan; the Helmholtz Centre for Environmental Research in Leipzig, Germany; and in Cadarache, France, coorganized by the Commisariat à l'Energie Atomique (CEA), ANDRA, BRGM and MINES ParisTech (Fig. 1.2.1). The activities of the SeS-Bench working group have led to the development and publication of a special issue of the journal, Computational Geosciences[1], "Reactive Transport Benchmarks for Subsurface Environmental Simulation" in 2015.

Fig. 1.2.1: SeS-Bench Meeting 2014 in Cadarache (Photo by Olaf Kolditz)

SeS-Bench supports the development of environmentally-relevant benchmark problem sets that provide rigorous tests for process model conceptualiz-

---

[1] Computational Geosciences, Volume 19 (2015) No. 3, ISSN 1420 0597, Springer.

ation, numerical implementation, process coupling, and accuracy. The scope of the benchmarking targets simulation capabilities based on the continuum (non-pore-scale) modeling approach for porous media. Each benchmark contribution consists of a principal comprehensive problem and supporting component problems. This is intended to isolate key attributes of the benchmark problem for higher scrutiny before addressing the full complement of interacting processes, properties, and conditions. To ensure the accuracy and validity of a published benchmark, SeS-Bench requires each benchmark to have a minimum of three different code bases to obtain the same or nearly the same results. Workshops are used as a forum to propose benchmark problem sets, recruit participants (and simulators) for proposed benchmarks, and report on findings and progress.

The initial SeS-Bench focus on multicomponent reactive transport modeling reflects the expanding range of mechanisms and increasing complexity needed to address issues relevant to climate change, nuclear waste management, contaminant remediation, and pollution prevention. The published reactive transport modeling benchmarks, while addressing comprehensive and detailed biogeochemical reaction networks, generally have relatively simple flow fields and transport specifications. The intent is for these benchmarks to be accessible to a wide range of interests and skill levels. All the benchmark problem sets contain specifications that can be run using modest standard computing resources. Furthermore, the simpler component benchmarks included in each problem set require less expertise and time to address. The belief is that these benchmark problem sets can also be instructional, providing a progression from conceptualization to the specification of actual reaction networks. Even for experienced modelers, these benchmarks can provide an entree into new reaction processes and provide templates that can be adapted for other scenarios. The hope is that this benchmarking effort will aid the training of a new generation of modelers who will continue to expand the role of reactive transport modeling in subsurface environmental simulation.

The 14 contributed articles in the Computational Geosciences special issue are from teams of participants in the SeS-Bench working group. A high level and non-exhaustive overview of the mathematical and numerical bases of modern reactive simulators is provided in the first paper. The benchmark problems are organized by topic: 1) microbially-mediated reactions, 2) isotopes, 3) multi-component diffusion, 4) uranium fate and transport, 5) metal mobility in mining affected systems, and 6) geologic waste repository material interactions.

Microbially-Mediated Reactions. Microbially-mediated Cr reduction in a one-dimensional column experiment was investigated with standard Monod (or Michaelis-Menten) rate formulations using sediment and chemical conditions from a contaminated site at the Hanford Nuclear Reservation in Washington State, USA. The remarkable agreement between the codes on this benchmark likely reflects in part the focus on kinetic as opposed to

thermodynamic formulations, which proved to be the biggest source of discrepancies in many of the benchmarks.

Isotopes. A benchmark problem was developed for the simulation of kinetic Cr isotope fractionation in 1D and 2D domains. The benchmark was based on a field study where Cr(VI) reduction and accompanying Cr isotope fractionation occurs abiotically through reaction with dissolved Fe(II). The benchmark demonstrates that excellent agreement can be obtained between codes, despite differences in the approaches to implement isotope fractionation.

Multi-component Diffusion. The number of reactive transport simulators that include electrochemical migration and consider the chemical potential gradient as a driving force of diffusion has been growing in recent years. Two multi-component diffusion benchmarks used the Nernst-Planck equation rather than the simpler Fick's Law to account for electrochemical migration. The first benchmark problem set was specifically designed to highlight strong electric coupling effects. A second benchmark addressed multi-species diffusion through compacted bentonite and included an explicit treatment of electrostatic effects associated with charged clay surfaces.

Uranium Fate and Transport. Uranium mobility is notoriously sensitive to pH, Eh, alkalinity, major ions, surface sites, etc. The three benchmarks that considered uranium fate and transport represent some of the successes in using coupled process modeling to develop a systematic understanding of uranium behavior in naturally complex subsurface materials. The first benchmark was based on a field experiment conducted at the Rifle site in western Colorado, USA in which acetate was injected into uranium-contaminated groundwater to drive microbially-mediated reduction and immobilization of uranium. A second benchmark focused on the important role of Fe-hydroxides in re-oxidizing biogenically reduced uranium. A third benchmark focused on multi-rate models to simulate uranium leaching and migration.

Metal Mobility in Mining Affected Areas. Two benchmarks considered metal mobility in the context of mining activities. The first used reactive transport modeling to simulate the generation of acidity as a result of sulfide oxidation and its subsequent effect on metal mobility above and below the water table. A second benchmark focused on metal accumulation and mobility in lake sediments downstream of mining operations. The modeling assumed a 1-D geometry that extends from the lake-sediment interface to depth and includes component problems with and without sediment burial.

Geologic Waste Repository Material Interactions. Three benchmarks focused on topics related to the storage of nuclear waste in geological repositories. The first addressed reactive transport associated with large concentration gradients across a cement-clay interface, as might be expected in the engineered barrier system for a waste repository. The challenge in this problem resulted from the high geochemical contrast between the cement and clay, which drove diffusive mixing across the interface and nonlinear mineral dissolution and precipitation. A second benchmark relevant to nuclear

waste repositories considered the effects of porosity, permeability and tortuosity evolution. The porosity reduction was the result of reactions (principally gypsum precipitation), which decreased the permeability to the point where flow was effectively stopped. The last benchmark focused on simulations of reactive transport and solute mobility resulting from cracks developed in concrete. The problem set addressed the effect of discrete fractures on the decalcification of cement structures.

1.3 MoMaS

MoMaS stands for Modeling, Mathematics and numerical Simulations and is related to nuclear waste management problems (Fig. 1.3.1). MoMaS proposes numerical benchmarks to help evaluate computer codes. MoMaS was initiated by a federation of French research groups involving CERMICS - Ecole Nationale des Ponts et Chaussees, Laboratoire Jacques-Louis Lions, UPMC Paris among others. Parkhurst and Wissmeier (2015) recently used MoMaS for testing a reaction module for transport simulators based on the geochemical model PHREEQC. MoMaS was extensively utilized for verifying a global reduction scheme for reactive transport modeling (RTM) (Amir and Kern, 2010; Carrayrou et al., 2010b; de Dieuleveult and Erhel, 2010; Hoffmann et al., 2010, 2012). Several RTM codes participated the MoMaS initiatives, e.g. HYTEC (Lagneau and van der Lee, 2010), MIN3P (Mayer and MacQuarrie, 2010), SPECY (Carrayrou, 2010) and recently OpenGeoSys (Huang et al., 2015a). Carrayrou et al. (2010a) compared different numerical methods for simulating strongly nonlinear and heterogeneous reactive transport problems. A special issue in Computers and Geosciences was dedicated the results of the MoMaS benchmarking initiative (Ackerer, 2010).
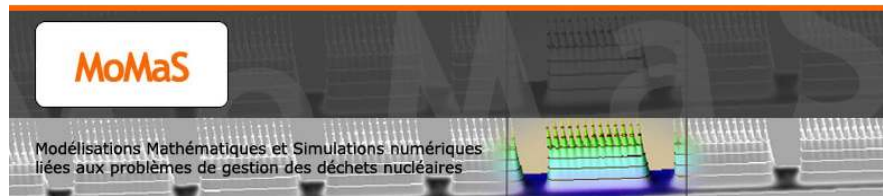
Fig. 1.3.1: The official MoMaS website and further information can be found at `https://www.ljll.math.upmc.fr/cances/gdrmomas/benchmarks-en.html`

1.3.1 Finished benchmarks

MoMaS has a number of finished benchmarking exercises:

- Anisotropic and Heterogeneous Diffusion: A benchmark on numerical methods for heterogeneous and anisotropic diffusion in a 2D domain,
- Geochemistry: A benchmark on numerical aspects of coupling between transport and chemistry in porous media,
- Heterogeneous and anisotropic diffusion: A benchmark on numerical methods for heterogeneous and anisotropic diffusion,
- Couplex-Gas: A benchmark addressing the main problems to simulate two phases (liquid, gas) two components (water, H2) flows in porous media. This benchmark was defined by Andra, with a collaboration from MoMaS `http://math.univ-lyon1.fr/homes-www/bourgeat/MoMaS/cas_test`.
- Hydro-mechanical behavior of an excavation: A benchmark on geoscientific studies of the Excavation Damaged and Disturbed Zones in sedimentary rocks.
- Couplex: Several benchmarks are a set of realistic test cases aimed at simulating the transport of nuclides around a nuclear waste repository (Bourgeat et al., 2009).

1.3.2 Currently running benchmarks

MoMaS has two ongoing benchmarking exercises:

- Two phase flows: Several numerical test cases, with a simplified physics, so as to concentrate on a single numerical difficulty in each case (Marchand and Knabner, 2014a)
- 3D diffusion: A benchmark addressing a three-dimensional anisotropic diffusion problem, which is discretized on general, possibly non-conforming meshes `http://www.i2m.univ-amu.fr/latp_numerique/?q=node/4`.

In this benchmark book new results are presented in Chapter 6 considering two-phase two-component transport processes with phase transition phenomenon related to the MoMaS Couplex benchmarks.

Part II Single Processes

Chapter 2
Thermal Processes

2.1 Transient heat conduction in a transversal isotropic porous medium

by Son Nguyen, Hua Shao, Benoit Garitte

The thermal field in the heating experiment in a bedded clay rock is the key driver for the hydraulic and mechanical response. It is therefore important to verify that the codes being used, COMSOL multiphysics and OGS can correctly calculate the temperature field. Due to low permeability of the clay rock, thermal conduction is the dominant process for the heat transfer. An analytical solution for a constant point heat source in an infinite transversely isotropic medium is used as a benchmark (Garitte et al., 2012).

2.1.1 Theory

Heat transfer including conduction, convection and radiation is the passage of thermal energy from a hot to a cold body. Transfer of thermal energy occurs, when a body and its surroundings have not yet reached thermal equilibrium yet. Conduction takes place when there is a temperature gradient in a solid. Consider a boundary value problem for heat conduction in a continuously non-homogeneous anisotropic medium, which is governed by the following equation:

$$\rho c_p \frac{\partial T}{\partial t} + \operatorname{div}(\boldsymbol{\lambda} \operatorname{grad} T) = q \qquad (2.1.1)$$

where $T(x_i, t)$ is the temperature field, $q(x_i, t)$ is the heat sources. $\boldsymbol{\lambda}(x_i, t)$ is the thermal conductivity tensor and is defined to quantify the ease with which a particular medium conducts, $\rho(x_i)$ is the mass density and $c_p(x_i)$

the specific heat. The index i (=1, 2, and 3) instead of Cartesian coordinate system (x, y, z). The global boundary Γ consists of two parts $\Gamma = \Gamma_T + \Gamma_q$ (Γ_T Dirichlet and Γ_q Cauchy conditions).

2.1.2 Problem definition

A cubic geometry with an edge length of 20 m x 20 m x 20 m is selected to present an infinite transversely isotropic medium. A constant heat source is applied in the middle of the cube. Due to the symmetrical geometry, only 1/8 of the cube is used for the simulation. The finite element model for this problem is shown in Figure 2.1.1. The source is located at point (0, 0, 0). The initial temperature in the medium is 21.5°C.
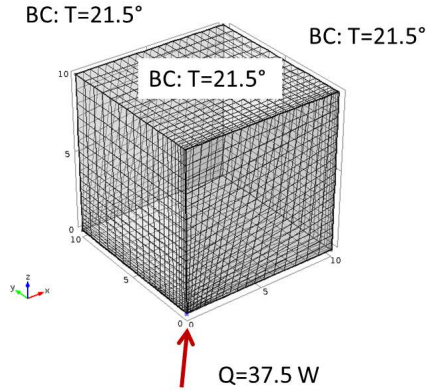
Fig. 2.1.1: Finite element mesh for the COMSOL-simulation.

The outer boundaries are set at a distance of 10 m from the source where T is fixed at 21.5°C. The finite element results are compared to the analytical solution at four points: two at horizontal distances of 0.5 and 2 m from the source, and two at vertical distances of 0.5 and 2 m. In this verification problem, the following parameters are considered (Table 2.1.1). The total simulation time is 10000 days with variable time steps.

2.1.3 Analytical solution

In case of constant parameters (Tab. 2.1.1), and taking into account of transversal isotropic medium, the thermal conductivity tensor $\boldsymbol{\lambda}(x_i)$ may follow:

Table 2.1.1: Used parameters

	Quantity	Value/Unit
ρ	Density of the solid	$2.45\,\mathrm{t\,m^3}$
c_p	Heat capacity	$1000\,\mathrm{J\,kg^{-1}\,K^{-1}}$
$\lambda\|$	Thermal conductivity in horizontal direction $(r = x, y)$	$2.1\,\mathrm{W\,m^{-1}\,K^{-1}}$
$\lambda\perp$	Thermal conductivity in vertical direction (z)	$1\,\mathrm{W\,m^{-1}\,K^{-1}}$

$$\kappa_{xy} = \kappa_{xz} = \kappa_{yz} = \kappa_{zx} = \kappa_{zy} = \kappa_{yx} = 0 \qquad (2.1.2)$$

$$\kappa_{xx} = \kappa_{yy} = \kappa_{\perp}$$

$$\kappa_{zz} = \kappa_{\|}$$

The analytical solution proposed by Booker and Savvidou (1985b) for a point heat source in an infinite isotropic medium of the heat conduction equation in the porous medium (Carslaw and Jaeger, 1959) can be transformed to take anisotropy into account (Garitte et al., 2012):

$$\Delta T = \frac{q}{4\pi\lambda_0 R_0}\,\mathrm{erfc}\frac{R_0}{s\sqrt{\lambda_0 t/\rho c_p}} \qquad (2.1.3)$$

where ΔT is the temperature increment induced by the applied power q (in W), λ_0 is the equivalent thermal conductivity (in W/m/K):

$$\lambda_0 = \sqrt[3]{\lambda_{\|}\lambda_{\|}\lambda_{\perp}} \qquad (2.1.4)$$

and erfc() stands for the complementary error function. The solution is calculated in a Cartesian reference system where x- and y-axes are defined within the bedding plane and z perpendicular to the bedding. The transformed radius R_0 is a function of the isotropy-like distances ξ, η, ζ in x, y and z direction, respectively:

$$R_0 = \sqrt{\xi^2 + \eta^2 + \zeta^2} \qquad (2.1.5)$$

where ξ, η, ζ are related to the real distances x, y and z through:

$$x = \frac{\sqrt{\lambda_{\|}}}{\sqrt{\lambda_0}}\xi \qquad (2.1.6)$$

$$y = \frac{\sqrt{\lambda_{\|}}}{\sqrt{\lambda_0}}\eta$$

$$z = \frac{\sqrt{\lambda_{\perp}}}{\sqrt{\lambda_0}}\zeta$$

2.1.4 Results

The results of the analytical equation (2.1.3) for the temperature evolution at the selected points are compared to those of the numerical simulations by COMSOL and OGS (Fig. 2.1.2). The analytical solution is based on an infinite geometry assumption, therefore the boundary effects become more pronounced at later times in the numerical simulations. The relative error between the modelled temperature and the result from analytical solution is about 4%. A big model (40 m x 40 m x 40 m) with a relative coarse mesh improves the boundary effect (Fig. 2.1.3). Mesh effect plays also an important role. A much finer mesh for the OGS simulator seems to be needed in order to get comparable results.
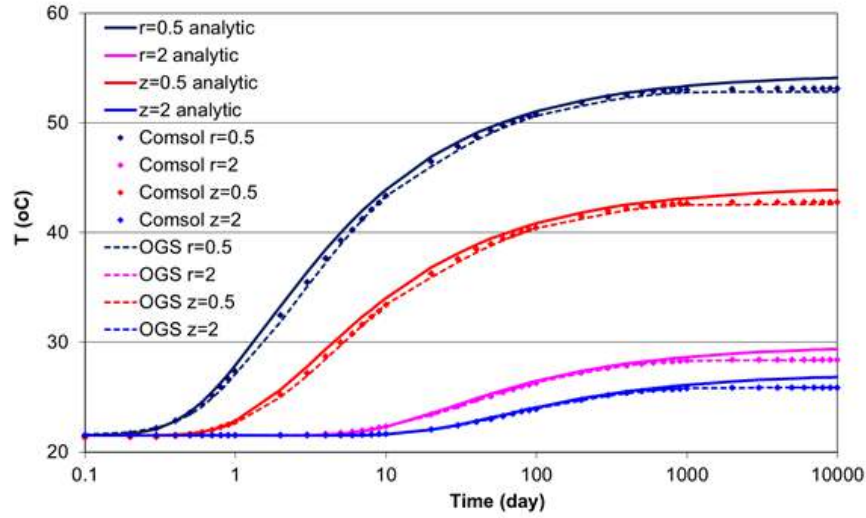
Fig. 2.1.2: Comparison of finite element and analytical results.

Fig. 2.1.4 shows the temperature distribution in domain at 10000 days. Obviously, heat transfers much faster in the horizontal than in the vertical direction because of transversal isotropic thermal conductivity.
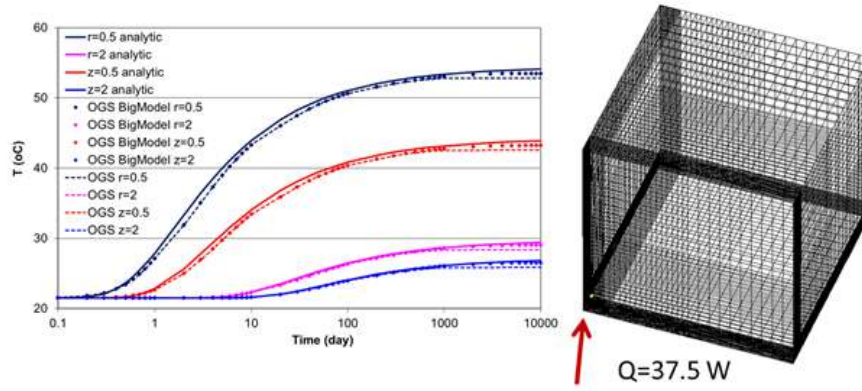
Fig. 2.1.3: OGS results from the big model.
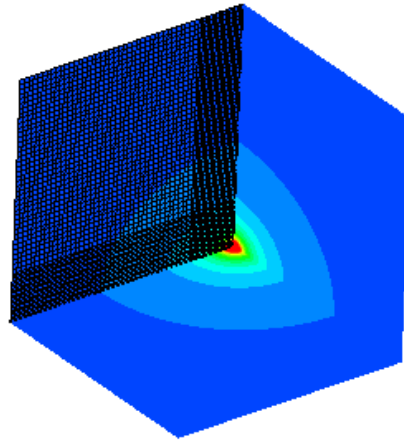
Fig. 2.1.4: Temperature distribution at 10000 days calculated by code OGS.

2.2 Freezing-Thawing

Tianyuan Zheng, Thomas Nagel and Haibing Shao

In this chapter, we are going to show how to simulate the heat transport process with freezing and thawing features. To handle such phase change behaviour, both kinetic and equilibrium approaches have been implemented into to the numerical model. The extended feature is verified by comparing the numerical results against analytical solutions.

2.2.1 Mathematical Model

Heat Conduction

Conventionally, when only considering heat conduction, the governing equation of the heat transport process reads,

$$\rho \frac{\partial h(T)}{\partial t} - \nabla \cdot (\boldsymbol{\lambda} \nabla T) = 0 \qquad (2.2.1)$$

where $h(T)$ denotes the specific enthalpy [J/kg], ρ is the density [kg/m^3] of the porous media, T refers to the temperature [K], and $\boldsymbol{\lambda}$ is the thermal conductivity [W m^{-1} K^{-1}]. By applying the chain rule to the time derivative term, one gets

$$\rho \frac{\partial h}{\partial T} \frac{\partial T}{\partial t} - \nabla \cdot (\boldsymbol{\lambda} \nabla T) = 0 \qquad (2.2.2)$$

The term $\frac{\partial h}{\partial T}$ represents the derivative of enthalpy with respect to temperature, which is equivalent to the specific heat capacity c_p [J kg^{-1} K^{-1}]. Eq. (2.2.2) can be rewritten as

$$\rho c_{\mathrm{p}} \frac{\partial T}{\partial t} - \nabla \cdot (\boldsymbol{\lambda} \nabla T) = 0 \qquad (2.2.3)$$

2.2.2 Freezing and Thawing Processes

Kinetic Approach

Based on the governing equation (2.2.3), thawing and freezing processes can be taken into account by quantifying the change of the apparent fluid density over time. When the temperature drops below the freezing point, part of the water in the pore space is transformed into ice, leading to a drop in

the apparent water density. In order to model this physical process, we first introduce the mass balance equation.

$$\dot{\rho}_\alpha + \nabla \cdot (\rho_\alpha \boldsymbol{v}_\alpha) = \hat{\rho}_\alpha \qquad (2.2.4)$$

Where $\dot{\rho}_\alpha$ represents the partial time derivative of the partial density of phase α, $\boldsymbol{v}_\alpha$ represents the velocity of phase α, and $\hat{\rho}_\alpha$ is the density production of phase α, which is caused by the phase change process. Since all phases are considered immobile in this model $\boldsymbol{v}_\alpha = 0$, thus for the ice phase Eq. (2.2.4) can be simplified as

$$\dot{\rho}_I = \hat{\rho}_I \qquad (2.2.5)$$

For a simple freezing model, $\hat{\rho}_I$ is assumed to be linearly dependent on the temperature difference from the freezing point temperature T_m to the current temperature T, with k referring to a non-negative rate coefficient [kg m^{-3} s^{-1} K^{-1}].

$$\hat{\rho}_I = k(T_m - T), \quad k \geq 0 \qquad (2.2.6)$$

Here we define the ice volume fraction ϕ_I as the volume of ice over the total volume of REV, and it is constrained by the porosity ϕ, i.e. $\phi_I \in [0, \phi]$. Eq. (2.2.6) then becomes

$$\hat{\rho}_I = k(T_m - T) = \frac{\partial \phi_I \rho_{IR}}{\partial t} \qquad (2.2.7)$$

Where ρ_{IR} refers to the real density of ice. Then we can add the phase change term into Eq. (2.2.3).

$$\rho c_p \frac{\partial T}{\partial t} - L_I \hat{\rho}_I - \nabla \cdot (\boldsymbol{\lambda} \nabla T) = 0, \qquad (2.2.8)$$

where L_I denotes the latent heat [J kg^{-1}] and the term $L_I \hat{\rho}_I$ regulates the amount of energy released or absorbed through the phase change process. When freezing and thawing occur, $\boldsymbol{\lambda}$ and ρc_p are no longer constants, but rather functions of the ice volume fraction ϕ_I.

$$\boldsymbol{\lambda} = \boldsymbol{\lambda}_S(1 - \phi) + \boldsymbol{\lambda}_I(\phi_I) + \boldsymbol{\lambda}_W(\phi - \phi_I) \qquad (2.2.9)$$

$$\rho c_p = \rho_{SR} c_{pS}(1 - \phi) + \rho_{IR} c_{pI}(\phi_I) + \rho_{WR} c_{pW}(\phi - \phi_I) \qquad (2.2.10)$$

Equilibrium Approach

In the equilibrium approach, one follows the same governing equations as in the kinetic approach (Eq.(2.2.1) to (2.2.8)). The difference lies in the calculation of the ice phase density production $\hat{\rho}_I$. Here, the phase change process

is assumed to be very fast, and will reach equilibrium within a typical time step. Instead of calculating the phase production rate, the ice volume fraction is directly related to temperature, and is updated with a certain function before every time step. Assuming the partial density of ice is a function of temperature T, we have

$$\rho_I = \rho_{eq}(T) \tag{2.2.11}$$

$\rho_{eq}(T)$ defines the relationship between partial density of ice and temperature, which can be regulated by either a sigmoid function

$$\rho_I = \phi \rho_{IR} \frac{1}{1 + e^{-wt}} \tag{2.2.12}$$

or an exponential function which is also steadily differentiable (Mottaghy and Rath, 2006).

$$\rho_I = \begin{cases} \phi \rho_I & \text{if} \quad T < T_s \\ \phi \rho_{IR}(1 - e^{-(\frac{T - T_m}{w})^2}) & \text{if} \quad T < T_m \\ 0 & \text{if} \quad T > T_m \end{cases} \tag{2.2.13}$$

Where T_m represents the melting temperature and T_s represents the temperature at which all water has frozen into ice. When freezing is taken into account, the specific enthalpy h is regarded as a function of T and ρ_I, one gets

$$\rho \frac{\partial h(T, \rho_I)}{\partial t} = \rho \left(\frac{\partial h}{\partial T} \bigg|_{\rho_I} \frac{\partial T}{\partial t} + \frac{\partial h}{\partial \rho_I} \bigg|_T \frac{\partial \rho_I}{\partial t} \right). \tag{2.2.14}$$

By applying the chain rule on Eq. (2.2.14) and using Eq. (2.2.11), we get

$$\frac{\partial \rho_I}{\partial t} = \frac{\partial \rho_{eq}(T)}{\partial T} \frac{\partial T}{\partial t} \tag{2.2.15}$$

After integrating the above expressions into Eq. (2.2.8), we have

$$\left(\rho c_p - \frac{\partial \rho_{eq}}{\partial T} L_I \right) \frac{\partial T}{\partial t} - \nabla \cdot (\boldsymbol{\lambda} \nabla T) = 0 \tag{2.2.16}$$

Eq. (2.2.16) serves as the governing equation of the heat transport process with freezing and thawing features in the equilibrium approach.

2.2.3 Benchmark Validation and Discussion

Mottaghy and Rath (2006) proposed a benchmark case, with a 1 meter long water column connected to a freezing wall. Over time, the water in the vicinity of the wall slowly freezes. The propogation of the freezing front is calculated by the Neumann analytical solution (Carslaw and Jaeger, 1959)

(see Appendix). In our numerical model, the Finite Difference Method was implemented for the time discretization. For the spatial discretization, we have adopted the Galerkin Finite Element Method, with 1000 line elements, each 1 cm long. Picard and Newton methods were introduced to resolve the nonlinearity. Since the analytical solution was developed for a pure phase change scenario, i.e. only water and ice, we set the porosity to be 1 in the numerical model. The initial temperature was given as $0\,°\text{C}$ throughout the domain. For the boundary condition, the left hand side of the column x = 0 was constrained to a temperature value T=-3 $°\text{C}$ throughout the simulation. All other parameters used in the model are listed in Table 2.2.1.
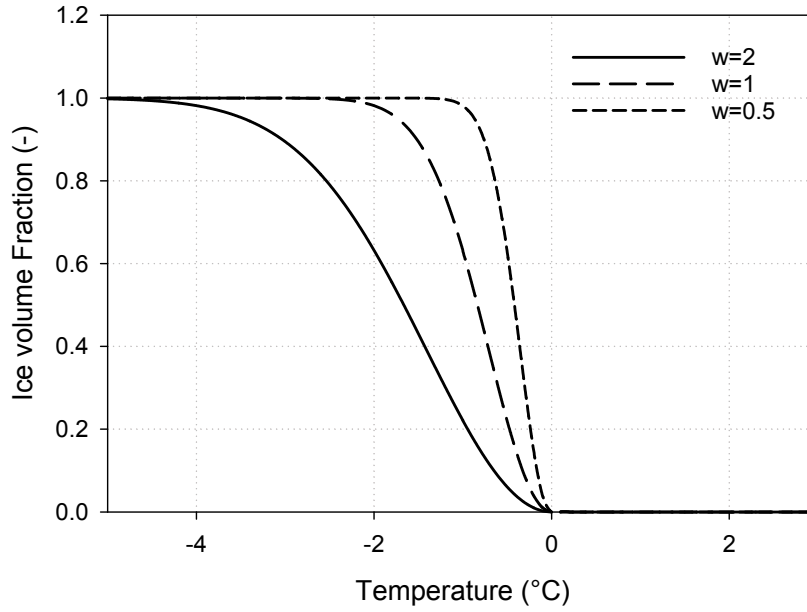
Fig. 2.2.1: Ice volume fraction versus temperature for exponential functions

Fig. 2.2.2 shows the evolution of temperature profile during the freezing process. The location of the phase change front $X(t)$ is compared with the analytical solution in Fig. 2.2.3. The red symbols are the numerical results and the blue line is the Neumann analytical solution (see Appendix for the details). Here, the exponential function was applied to calculate the partial density of ice in Eq. (2.2.13), with $\rho_{\text{IR}} = 920$ kg m^{-3}, $w = 2$ and $T_{\text{s}} = -4°\text{C}$. As shown in Fig 2.2.3, the numerical results correspond well to the analytical solution.

Table 2.2.1: Parameters used in the benchmark case, following Mottaghy and Rath (2006)

Parameters	Values	Units
Grid size	0.001	m
Initial Temperature	0	°C
Boundary Temperature	-3	°C
Porosity	1	-
Water heat capacity	4179	J kg^{-1} K^{-1}
Water thermal conductivity	0.613	W m^{-1} K^{-1}
Water density	920	kg m^{-3}
Ice heat capacity	2052	J kg^{-1} K^{-1}
Ice thermal conductivity	2.14	W m^{-1} K^{-1}
Ice density	920	kg m^{-3}
Time step size	864	sec
Total simulation time	100	day
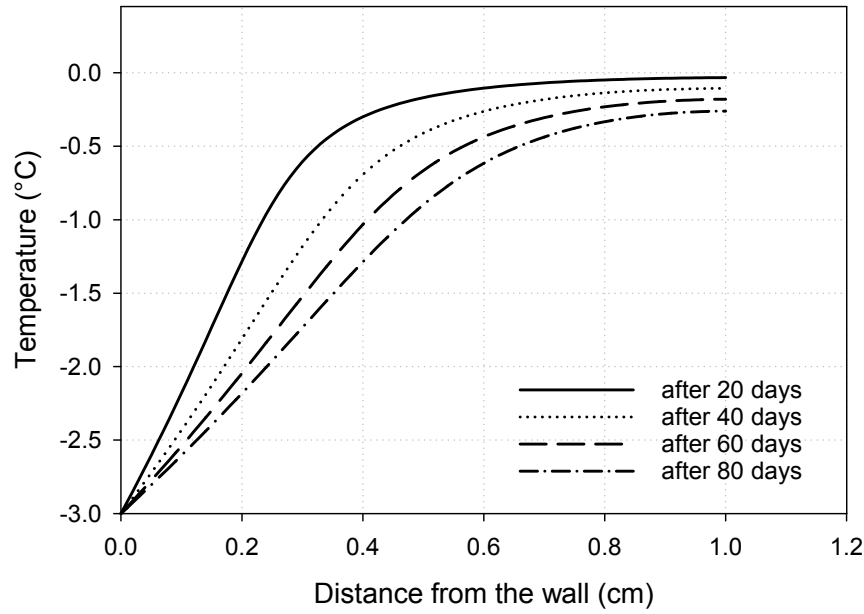
Fig. 2.2.2: The temperature field during the freezing process
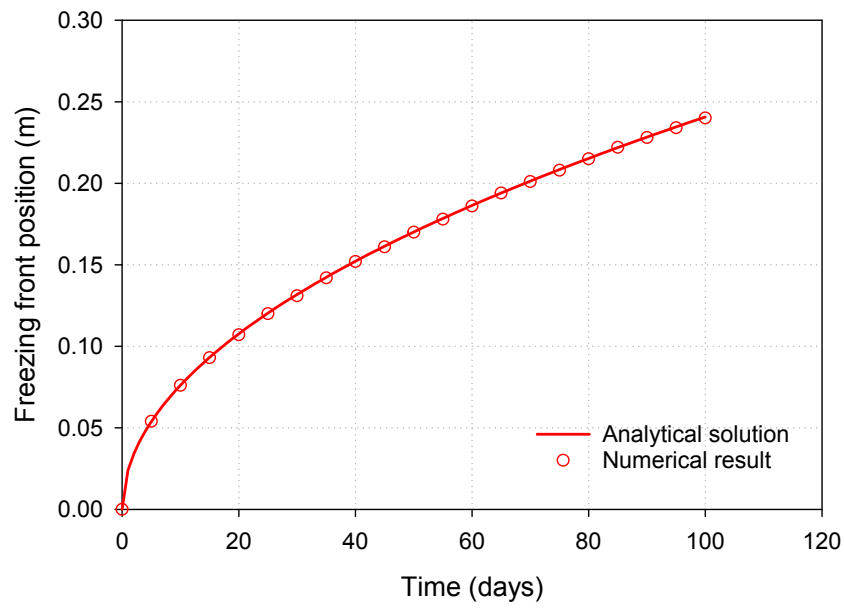
Fig. 2.2.3: Propagation of the freezing front X over time. The analytical solution by Neumann is depicted by the blue line, and the numerical results are shown in red symbols.

Appendix

A classical solution for a semi-infinite medium with constant temperature to conductive heat transfer problems with solidification phase change was given by Neumann (1860) and has been expanded by Carslaw and Jaeger (1959). It is called the Neumann solution and specifies the location $X(t)$ of the phase front as a function of time.

$$X(t) = 2\gamma\sqrt{\alpha_\mathrm{I} t} \tag{2.2.17}$$

$\alpha_\mathrm{I,W}$ indicates the thermal diffusivity of ice and water respectively. The parameter γ must be determined from the following equation that related to the boundary condition of the associated differential equation (with the thermal conductivities $\lambda_\mathrm{I,W}$ of both materials)

$$\frac{\exp\left[\left(\alpha_\mathrm{I} - \alpha_\mathrm{W}\right)\gamma^2\right]\mathrm{erfc}\left(\gamma\sqrt{\alpha_\mathrm{I}/\alpha_\mathrm{W}}\right)}{\mathrm{erf}\left(\gamma\right)} - \frac{\left(T_\mathrm{m} - T_\mathrm{s}\right)\lambda_\mathrm{W}\sqrt{\alpha_\mathrm{I}}}{\left(T_\mathrm{s} - T_0\right)\lambda_\mathrm{I}\sqrt{\alpha_\mathrm{W}}} = 0 \tag{2.2.18}$$

The latent heat for the phase change is considered by adding into the thermal diffusivity of the water.

$$\alpha_\mathrm{W} = \frac{\lambda w}{\rho_\mathrm{W} c_\mathrm{W} - \rho_\mathrm{I} L_\mathrm{I}\frac{\mathrm{d}\phi_\mathrm{I}}{\mathrm{d}T}} \tag{2.2.19}$$

In the numerical model we choose $w = 2$ (Fig 2.2.1) for the exponential function and the corresponding $\triangle T$ is 4 (see Table 2.2.2). Then $\gamma = 0.039$ should be chosen for the analytical solution.

Table 2.2.2: The parameter γ for the different widths of freezing range (Mottaghy and Rath, 2006)

γ	$\triangle T(^\circ C)$
0.039	4
0.041	3
0.043	2

2.3 Shallow geothermal systems - Borehole Heat Exchanger

Philipp Hein and Haibing Shao

To use the shallow geothermal resources, borehole heat exchangers are often coupled with heat pumps to provide heating or cooling in the buildings. The OpenGeoSys software has recently been extended to simulate the evolution of temperature profile within and around the BHEs. Here in this section, two benchmark cases are presented. One compares the simulated soil temperature curve to analytical line source models . The other one validates the numerical model against monitoring data from an in-door sandbox experiment.

2.3.1 Borehole heat exchangers - Comparison to line source models

Model setup

In this benchmark, the evolution of soil temperature was simulated by the numerical model OpenGeoSys. The results were compared against the analytical **infinite line source** (ILS) model (c.f. Stauffer et al. (2014)). As by the ILS model, the temperature difference to the undisturbed initial temperature T_0 at a radial distance r_b is given by

$$T - T_0 = \frac{q_b}{4\pi\lambda} E_1\left(\frac{r_b^2}{4\alpha t}\right) \tag{2.3.1}$$

with heat flow rate q_b per length of BHE, thermal diffusivity $\alpha = \frac{\lambda}{\rho c_p}$ and the exponential integral function E_1.

In the numerical model, the temperature evolution inside and around a BHE was simulated with a constant power $Q = q_b \cdot L_{BHE}$ imposed as a boundary condition. Both numerical and analytical models have been established with the same geometry, initial conditions, and material parameters etc. They are listed in Tab. 2.3.1. It is known that the analytical line source model will produce inaccurate results of soil temperature in the immediate vicinity of the BHE, still it should converge with the numerical model at a certain distance. The results are presented in the next section.

Table 2.3.1: Parameters used in the line source model comparison

Parameter	Value	Unit
q_b	-5.68	$W\ m^{-1}$
L_{BHE}	46	m
Q	-261.68	W
λ_{soil}	1.34	$W\ m^{-1}\ K^{-1}$
$(\rho c_p)_{soil}$	2×10^6	$J\ m^{-3}\ K^{-1}$
BHE Type	$1U$	
D_{BHE}	15	cm
d_{pipe}	3.98	cm
b_{pipe}	0.36	cm
w	6.3	cm
λ_{pipe}	0.39	$W\ m^{-1}\ K^{-1}$
λ_{grout}	0.73	$W\ m^{-1}\ K^{-1}$
$(\rho c_p)_{grout}$	3.8×10^6	$J\ m^{-3}\ K^{-1}$
$\lambda_{refrigerant}$	0.477	$W\ m^{-1}\ K^{-1}$
$(\rho c_p)_{refrigerant}$	$3.838 \cdot 10^6$	$J\ m^{-3}\ K^{-1}$
$\mu_{refrigerant}$	$3.04 \cdot 10^{-3}$	$kg\ m^{-1}\ s^{-1}$
$Q_{refrigerant}$	15.087	$m^3\ d^{-1}$

Results

Soil temperatures were observed at two locations, one at a distance of $r_1 = 6.0\ m$ and another at $r_2 = 1.6\ m$ (c.f. Fig. 2.3.1). Good agreement has been reached between the analytical line source model solution and the numerical results. The comparison of temperature profiles can be found in Fig. 2.3.2 and Fig. 2.3.3.
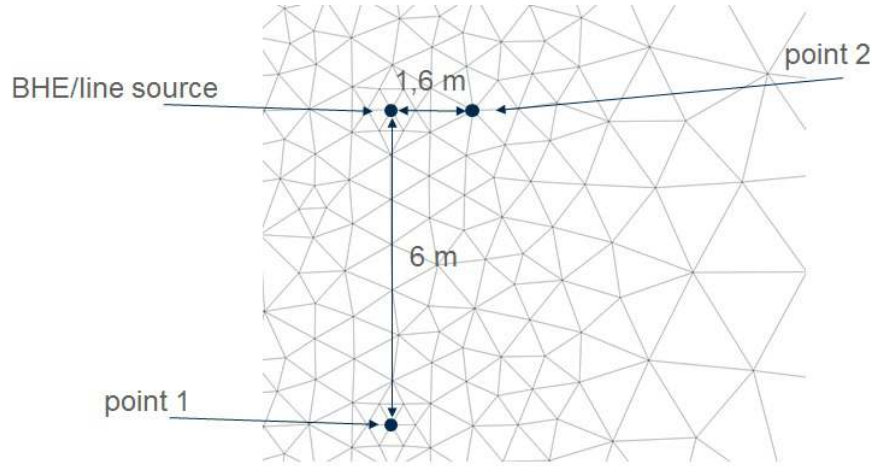
Fig. 2.3.1: Observation points in line source model
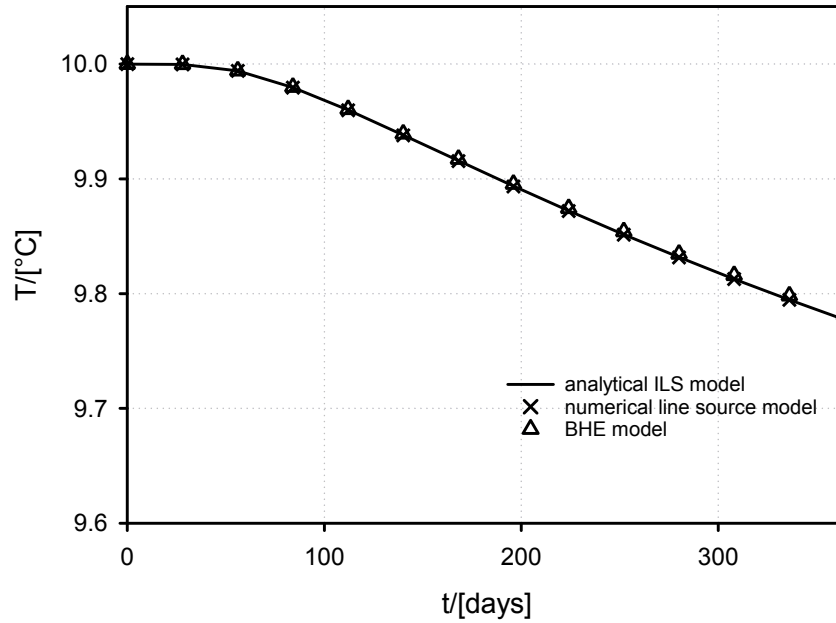
Fig. 2.3.2: Comparison of soil temperature profile at 6.0 m distance

2.3.2 Borehole heat exchangers - Sandbox benchmark

In this benchmark, the Borehole Heat Exchanger (BHE) feature in the Open-GeoSys software is validated against experimental results obtained by Beier et al. (2011). In their experiment, a Thermal Response Test (TRT) was performed under controlled conditions on a single U-tube borehole heat exchanger placed inside a sand box. Inlet and outlet fluid temperatures were monitored together with temperatures at the borehole wall and at different locations in the sand box.

Model Setup

The model was built according to the experimental configurations. The BHE is represented by line elements which are embedded in a 3D prism mesh representing the sandbox (Fig. 2.3.4). The length of the box is 18 m with
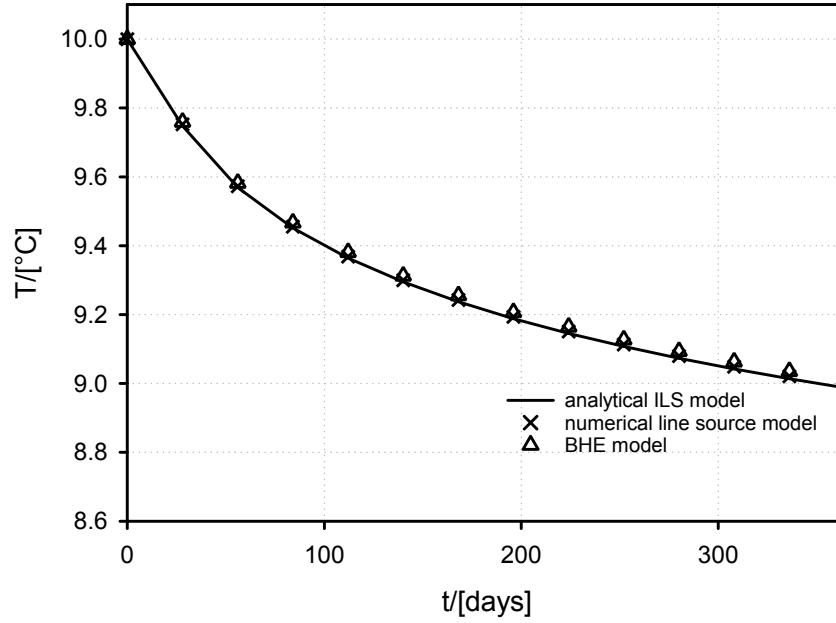
Fig. 2.3.3: Comparison of soil temperature profile at 1.6 m distance

a square cross section of 1.8 m per side. Detailed parameters for the model configuration can be found in Tab. 2.3.2.

In Beier's experiment, there was an aluminium pipe acting as the borehole wall. It cannot be represented by the BHE model itself, therefore the borehole diameter was taken as the aluminium pipe's outer diameter of 0.13 m in the numerical model. The grout's thermal conductivity was increased from originally 0.73 W m^{-1} K^{-1} to 0.806 W m^{-1} K^{-1}, in order to include the aluminium pipe's thermal conductivity and its geometry. The BHE is filled with water. Thermal properties and viscosity of water are taken at an average temperature of approx. 36 °C.

Initial and Boundary Conditions

Initial conditions for fluid inlet/outlet temperatures and wall temperature were directly taken from the measurements at $t = 0$. For the initial soil temperature, the mean value of all sensors placed in the sand was taken. As initial grout temperatures, arithmetic mean between wall and fluid inlet/outlet temperature was taken. Detailed initial temperatures can be found in Tab. 2.3.3.
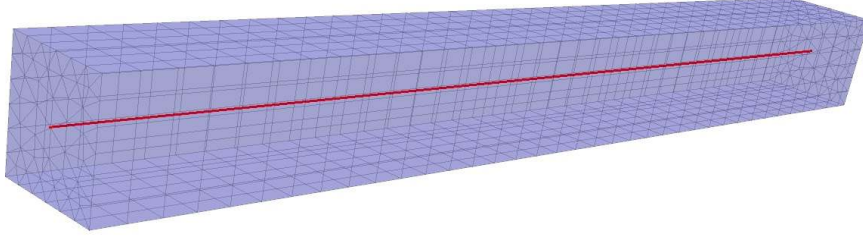
Fig. 2.3.4: Sandbox model

Table 2.3.2: Benchmark parameters according to the sandbox experiment of Beier et al. (2011)

Parameter	Value	Unit
λ_{soil}	2.78	$Wm^{-1}K^{-1}$
$(\rho c_p)_{soil}$	3.2×10^6	$Jm^{-3}K^{-1}$
D_{BHE}	13	cm
d_{pipe}	2.733	cm
b_{pipe}	0.3035	cm
w	5.3	cm
λ_{pipe}	0.39	$Wm^{-1}K^{-1}$
λ_{grout}	0.806	$Wm^{-1}K^{-1}$
$(\rho c_p)_{grout}$	3.8×10^6	$Jm^{-3}K^{-1}$

For the boundary conditions, they are given on the BHE as time series of measured inlet fluid temperature and flow rate as demonstrated in Fig. 2.3.5.

Table 2.3.3: Initial conditions of sandbox model

Parameter	Value	Unit
T_{in}	22.21	°C
T_{out}	21.98	°C
T_{grout1}	22.08	°C
T_{grout2}	21.97	°C
T_{soil}	22.10	°C
T_{wall}	21.95	°C

Results

The outlet temperature (Fig. 2.3.6) as well as the borehole wall temperature and soil temperatures at 24 cm and 44 cm distance to the wall (Fig. 2.3.7) were compared to the experimental results. We can observe a good match between experimental and simulation results. The largest relative error is about 2.5%
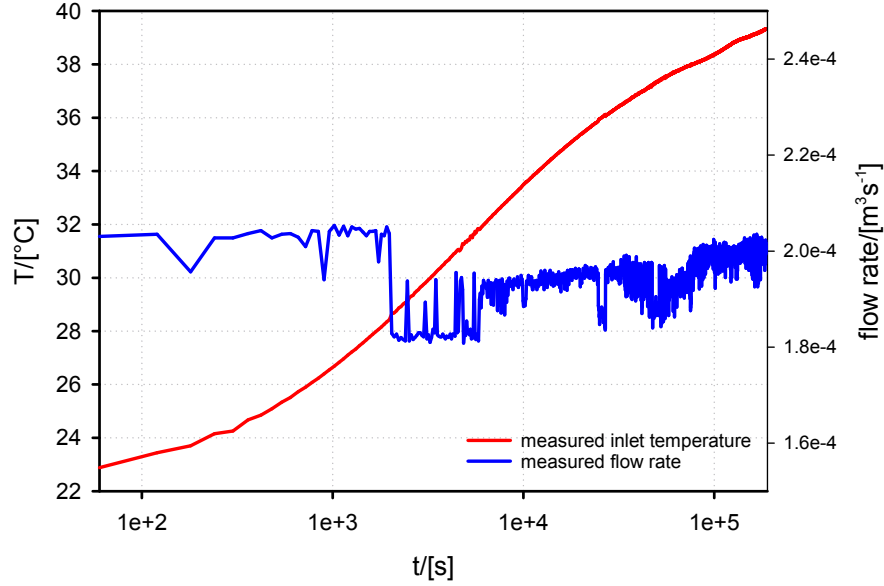
Fig. 2.3.5: Time series of inlet temperature and flow rate

on the wall temperature. Considering the error of measuring temperatures, flow rate and thermal conductivity values are in the same range, we consider the numerical model to be fully validated.

Requirement on the Mesh

As mentioned in Diersch et al. (2011), when the BHE is represented by 1D elements, the amount of heat flux between the BHE and the surrounding soil is heavily dependent on the size of mesh elements in the vicinity of the BHE node. Diersch et al. proposed a procedure to determine the optimal nodal distance, depending on the number of nodes surrounding the BHE center node as well as the borehole diameter. The optimal distance Δ can be obtained

$$\Delta = ar_b, \ a = e^{\frac{2\pi}{\vartheta}}, \vartheta = n \ tan\frac{\pi}{n} \tag{2.3.2}$$

with r_b the borehole radius and n the number of surrounding nodes. Δ is increasing with n. When designing the mesh, the above equation needs to be considered to ensure the correct heat flux over the borehole wall, since it will control all inlet, outlet and grout temperatures on the BHE nodes. Deviation from Eq. 2.3.2 will lead to inaccurate solutions. In the model at hand, we
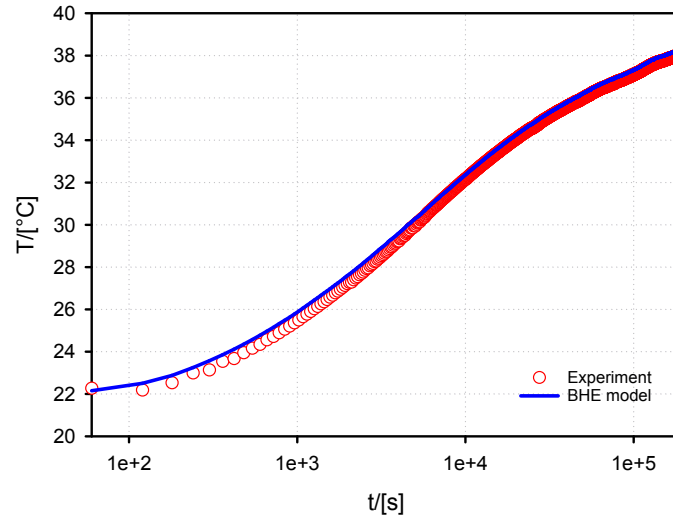
Fig. 2.3.6: Comparison of simulated and measured outlet temperature profile in the sandbox experiment
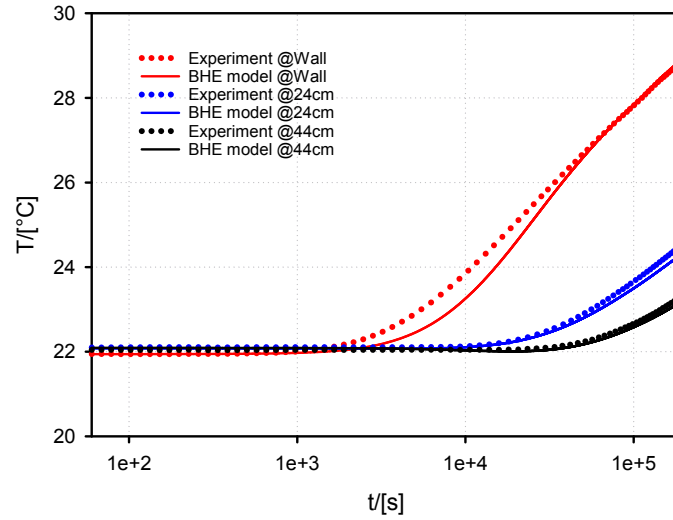
Fig. 2.3.7: Comparison of modelled and measured wall and soil temperatures

have $n = 6$ nodes surrounding the BHE center node with a borehole radius of $r_b = 0.065\ m$. With Eq. 2.3.2 the nodal distance evaluates to $\Delta = 0.398\ m$.

Chapter 3
Flow Processes

3.1 Flow in fracture/matrix system

By Milan Hokr, Hua Shao, Payton, W. Gardner, Herbert Kunz, Ales Balvin

Flow velocity is a key parameter for the mass transport in fractured rock, which can be generally described by the groundwater flow equation (3.1.1). Lots of benchmark examples in different dimension have been performed for the plausibility of the code (Kolditz et al., 2015), but a coupled fracture and matrix system, numerically using an integrated 2D and 3D finite element mesh, was not considered. In such an integrated system, 2D finite elements may be used to simulate fracture and fracture network and 3D ones to rock matrix to increase the computational efficiency.

3.1.1 Theory

The transient saturated groundwater flow is described by:

$$S_0 \frac{\partial h}{\partial t} - \operatorname{div} \cdot (K \operatorname{grad} h) = Q \qquad (3.1.1)$$

where $h(x,t)$ is the piezometric head, S_0 the specific storativity, q the fluid sink/source, and $\kappa_f(x,t)$ is the hydraulic conductivity tensor. The global boundary Γ consists of two parts $\Gamma = \Gamma_T + \Gamma_q$ (Γ_T Dirichlet's and Γ_q Cauchy's conditions). The average fluid velocity vector can be calculated using the generalised Darcy's law:

$$\mathbf{q} = K \operatorname{grad} h \qquad (3.1.2)$$

Analytical solutions for the partial differential equation (3.1.1) are only available for some simplified cases, e.l. steady state flow, radial pumping flow.

A generalised solution for a fracture/matrix system is only possible with the help of numerical method.

3.1.2 Problem definition

Based on a practical application, the Bedrichov tunnel case (CZ), four conceptual models have been developed within the international project DECOVALEX-2015 (Hokr, 2014). From that three cases (Fig. 3.1.1) have been simplified for the benchmark exercise.
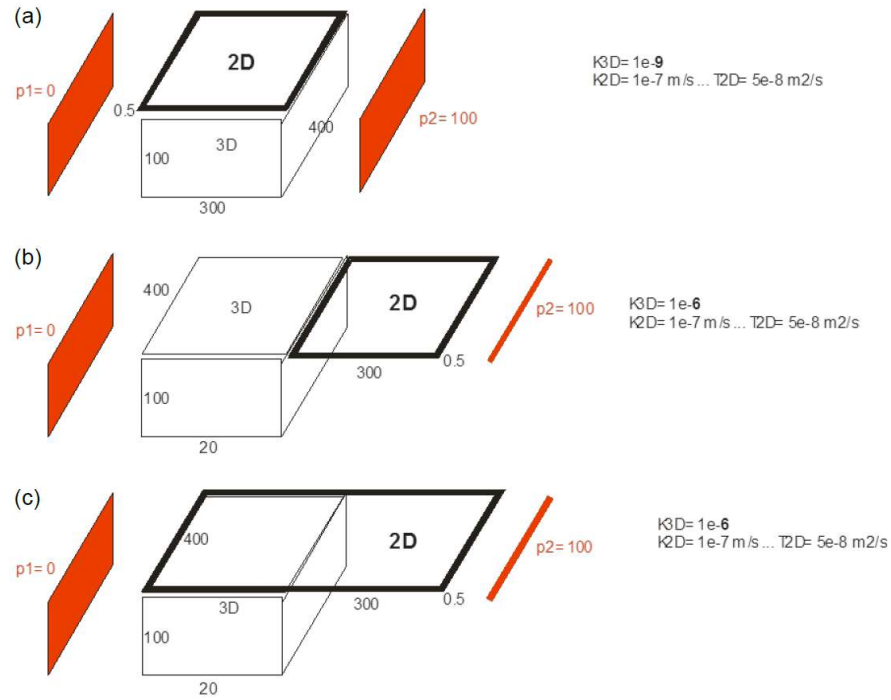
Fig. 3.1.1: Simplified benchmark cases

Geometry of all three cases is comparable with she Bedrichov site. The dimension of the matrix block in the case (a) is 300 m $\times$ 400 m $\times$ 100 m (L$\times$B$\times$H) and in the cases (b) and (c) 20 m $\times$ 400 m $\times$ 100 m. The fracture has an aperture of 0.5 m and a hydraulic conductivity of 1E-7 m/s. The transmissivity of the fracture can be calculated to 5e-8 m^2/s. The hydraulic conductivity of the rock mass is 1e-9 w/s in the first case (Fig. 3.1.1(a)) and

1e-6 m/s in the other two cases (Fig. 3.1.1(b) and (c)). The initial hydraulic head was set to 0. On the left side of the model the pressure was kept to 0.

Table 3.1.1: Used parameters

Symbol	Quantity	Value
a	Fracture aperture	0.5 m
$f_{fracture}$	Transmissivity	5e-8 $m^2 \cdot s^{-1}$
$k_{fracture}$	Fracture hydraulic conductivity	1e-7 $m \cdot s^{-1}$
K_{matrix}	Rock mass hydraulic conductivity	1e-9 $m \cdot s^{-1}$

3.1.3 Analytical solution

There is no generalised analytical solution available for the groundwater flow (1) in a fracture/matrix system (Fig. 3.1.1). A comparison between codes is therefore necessary for a simplified case.

The first problem is constructed so that each dimension can be evaluated separately by an analytical solution (1D problem equivalent). Taking account of the case 1 (Fig. 3.1.1(a)), the flux through fracture zone and matrix zone can be calculated correspondingly according to the velocity:

$$Q_{fracture} = T\frac{p_2 - p_1}{L}B = 5 \times 10^{-8}\frac{100 - 0}{300}400 = 6.67 \times 10^{-6} m^3/s$$

$$Q_{matrix} = T\frac{p_2 - p_1}{L}B\,H = 1 \times 10^{-9}\frac{100 - 0}{300}400 \times 100 = 1.33 \times 10^{-5} m^3/s$$

The total inflow/outflow in the system can be calculated as $Q2 = Q_{fracture} + Q_{matrix} =$ 2e-5 m³/s. The calculated flow rate from both fracture and rock mass agree well with the analytical results (Table 3.1.2) in case of pressure is known. It is meaningful to check both types of boundary conditions for each case, e.g. given pressure to get flow and given flow to get pressure. Therefore, instead of pressure (p2), Cauchy's condition (Q2) can be used as boundary condition, in particular the uniform flux is prescribed 2e-5m³/s per 40200m² area which is 4.97512e-10 m/s on both the fracture boundary (200 m²) and tie matrix boundary (40000 m²). As result the hydraulic head in the fracture (90.7 m) is lower than the maximal pressure in the matrix (109.2 o) because of high hydraulic conductivity of fracture (Fig. 3.1.3).

For the numerical method, the flow velocity is calculated within the element. The nodal output for velocity is a mean value from all neighbor elements (Fig. 3.1.2) and is therefore not suitable for the flux calculation especially in case of fracture/matrix system due to high difference on the hydraulic conductivities.

$$v_1 = (v_f^i + v_m^j)/2$$

$$v_2 = (v_f^i + v_m^j)/2$$

$$v_3 = (v_f^i + v_m^j)/2$$

$$v_4 = (v_f^i + v_m^j)/2$$
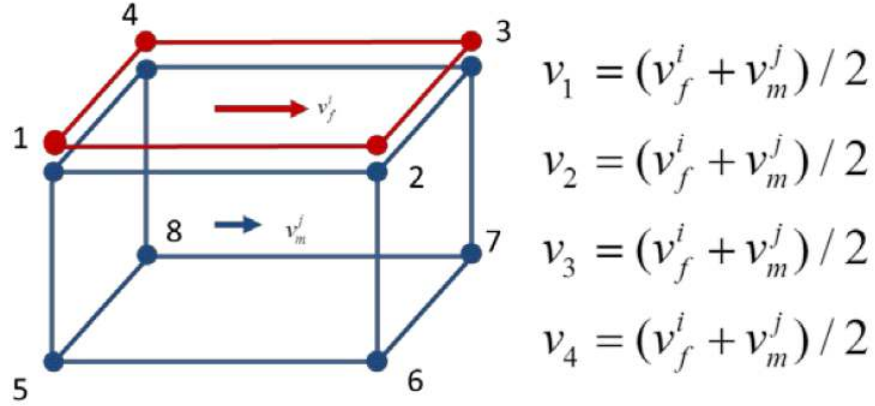
Fig. 3.1.2: Calculation of velocity of interface elements in a fracture/matrix system
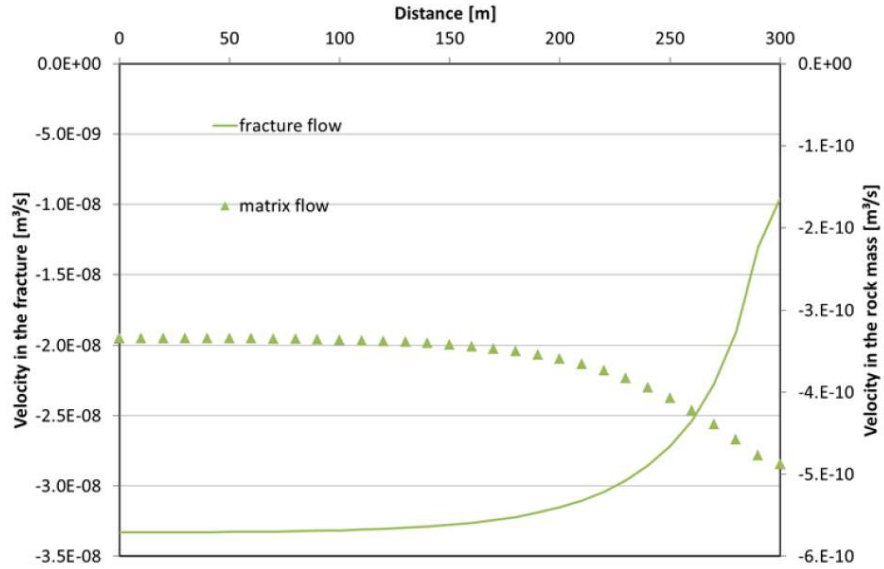
Fig. 3.1.3: Profile of velocity alone fracture and matrix given by code OGS

Table 3.1.2: Results from case (a)

	P2 = 100 m Q – fracture (m^3/s) (node/element)	Q – matrix (a^3/s)	Q2 = 2e-5 m^3/s P2 – fracture (m)	P2 – matrix (m) (maximal)
Analytical	6.67e-6	1.33e-5		
Flow123D	6.6667e-6	1.3333e-5	89.86	107.7
OGS	3.37e-6 / 6.67e-6	1.33e-5	90.7	109.2

A spatial distribution of the velocity values in a 3D view (code Flow123D) (Fig. 3.1.4) are in correspondence with the graph (Fig. 3.1.3).

velocity_x component

3e-009   1.81e-008   3.33e-008
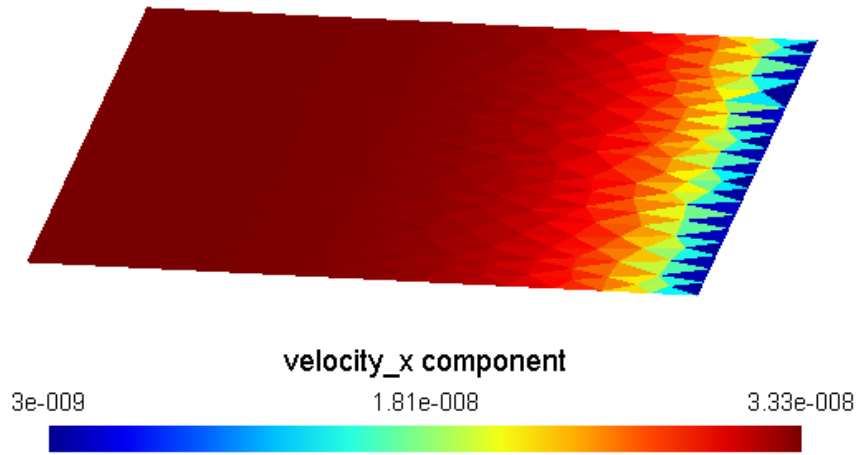
Fig. 3.1.4: Distribution of velocity Vx given by code Flow123

Table 3.1.3: Results from case (b) and (c)

	Case (b) P2 = 100 m Q – outflow (m^3/s)	Case (b) Q2 = 6.67s-5 m^3/e P2 – pressure (m)	Case (c) P2 = 100 m Q – inflow (m^3/s)	Case (c) Q2 = 6.67e-5 m^3/s P2 – pressure (m)
Flow123D	6.65312e-06	100.20364	6.62004e-06 (c) 6.64631e-05 (f)	100.70816 (c) 100.30633 (f
OGS	6.67e-6	100.03	6.66e-6	100.03

Flow123D results are in two variants for coarser (8m) and finer mesh (2m) at the 2D/3D contact edge. Practically, the case (b) is not exactly following the definition, as the mixed-hybrid formulation does not allow the 2D/3D communication through an edge (only through a side), so there is a 1 m wide overlap of the 2D domain above the 3D domain. The mesh here corresponds to the finer variant of the case (c).

It is worthwhile to have a benchmark exercise based on the application orientated cases. In most cases there are no analytical solutions available. Results comparison from different codes is therefore important to guarantee the quality in the development, implementation, and application of a code.

3.2 Water table experiment

by Wenkui He

3.2.1 Description

This benchmark problem described here is based on the laboratory experiment of Vauclin et al. (1979), in which water infiltration in variably saturated sandy soil was conducted. The dimensions of the soil slab are 3 m long, 2 m high and 5 cm thick. The initial water table was 0.65 m above the bottom. A constant flux of 0.148 m/h was imposed over a region on the soil surface, which has a width of 0.5 m. There was no lateral flow on the left hand side of the domain. The pressure head of the right hand side of the domain was fixed by connecting with a constant head reservoir. The water table elevations on different positions of the domain were measured during the experiment which lasted 8 h.

3.2.2 Model setup

The soil parameters applied for the two-dimensional model are given in Table 3.2.1, which are based on Vauclin et al. (1979) and Clement et al. (1994). The initial and boundary conditions are shown in Fig. 3.2.1. The entire model domain consists of 1200 uniform rectangular elements with a length of 0.10 m and a width of 0.05 m. A fixed time step size of 60 s is applied for the simulation.

Table 3.2.1: Soil properties

Symbol	Parameter	Value	Unit
ϕ	Porosity	0.30	-
k_s	Saturated hydraulic conductivity	8.40	md^{-1}
S_r	Residual water saturation	0.01	-
S_{max}	Maximum water saturation	1.0	-
α	Van Genuchten parameter	3.3	$1/m$
n	Van Genuchten parameter	4.1	-
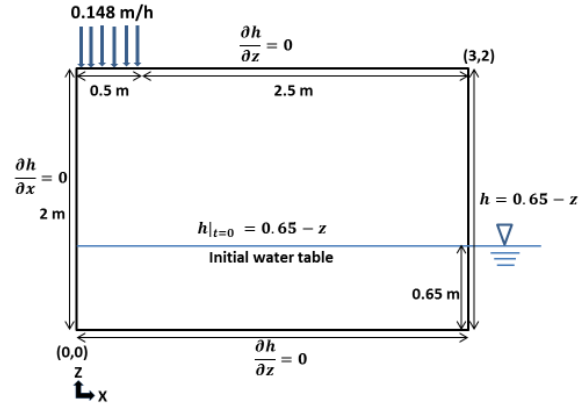
Fig. 3.2.1: Initial and boundary condition of the model (from He et al. (2015b)).$h(x, z, t)$ is pressure head at coordinates x and z at time t.
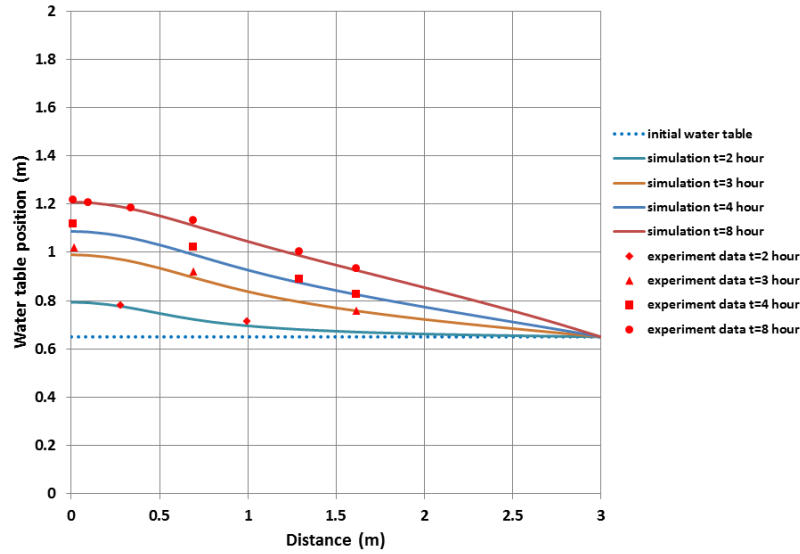
Fig. 3.2.2: A comparison of the water table positions simulated by using OGS with the experimental data (Vauclin et al. (1979)).

3.2.3 Results

The simulated water table positions at different times are illustrated in Fig. 3.2.2 together with the experimental data of Vauclin et al. (1979). The simulated results can match to the experiment data generally quite well.

Chapter 4
Deformation processes

by Norbert Böttcher, Jobst Maßmann, Peter Vogel and Thomas Nagel

4.1 Linear elasticity - Shear and torsion

Peter Vogel and Jobst Maßmann

This section presents a set of closed form solutions of 3D problems on shear and torsion. The associated simulation exercises have been checked by OGS; they may serve as verification tests. We focus on the closed form solutions; for the underlying theory of linear elasticity see Gurtin (1972), for more advanced 3D examples see Lurje (1963).

4.1.1 Due to specified surface loads an elastic square deforms into a lozenge

The domain is a rectangular plate discretized by $8 \times 8 \times 4$ equally sized hexahedral elements. Given size $2D = 2$ m and thickness $2H = 0.2$ m the vertices of the top face have the x-y-z-coordinates $(D, 0, H)$, $(0, D, H)$, $(-D, 0, H)$, and $(0, -D, H)$, respectively; the bottom face is located on the $z = -H$ level. The plate is represented by an elastic material. Young's modulus $E = 500$ MPa and Poisson's ratio $\nu = 0.2$ have been assigned, gravity is neglected via zero material density. Fixities have been prescribed in the interior of the domain with zero x-displacement along the plane $x = 0$, zero y-displacement along the plane $y = 0$, and zero z-displacement along the plane $z = 0$. Specified loads $P(x, y, z)$ prevail along the entire surface of the domain. With the aid of the stress $\sigma_0 = -100$ MPa these loads read along the lateral face $x > 0$, $y > 0$

$$P(x, D - x, z) = \sigma_0 \begin{pmatrix} 0 \\ 1 \\ 0 \end{pmatrix}, \qquad (4.1.1)$$

along the lateral face $x < 0$, $y > 0$

$$P(x, D + x, z) = \sigma_0 \begin{pmatrix} 0 \\ 1 \\ 0 \end{pmatrix}, \qquad (4.1.2)$$

along the lateral face $x < 0$, $y < 0$

$$P(x, -D - x, z) = -\sigma_0 \begin{pmatrix} 0 \\ 1 \\ 0 \end{pmatrix}, \qquad (4.1.3)$$

along the lateral face $x > 0$, $y < 0$

$$P(x, -D + x, z) = -\sigma_0 \begin{pmatrix} 0 \\ 1 \\ 0 \end{pmatrix}, \qquad (4.1.4)$$

and along the top face $z = H$ and the bottom face $z = -H$

$$P(x, y, H) = \begin{pmatrix} 0 \\ 0 \\ 0 \end{pmatrix}, \quad P(x, y, -H) = \begin{pmatrix} 0 \\ 0 \\ 0 \end{pmatrix}. \qquad (4.1.5)$$

The simulation comprises one timestep to evaluate the stresses, the strains, and the displacement vector (u_x, u_y, u_z)(Fig. 4.1.1).

The stress tensor

$$\boldsymbol{\sigma} = \begin{pmatrix} \sigma_{11} & \sigma_{12} & \sigma_{13} \\ \sigma_{12} & \sigma_{22} & \sigma_{23} \\ \sigma_{13} & \sigma_{23} & \sigma_{33} \end{pmatrix} = \sqrt{2}\sigma_0 \begin{pmatrix} 0 & 0 & 0 \\ 0 & 1 & 0 \\ 0 & 0 & 0 \end{pmatrix} \qquad (4.1.6)$$

satisfies the equation of mechanical equilibrium

$$\nabla \cdot \boldsymbol{\sigma} = 0 \qquad (4.1.7)$$

as well as the specified surface loads because along the lateral face $x > 0$, $y > 0$

$$\boldsymbol{\sigma}\sqrt{1/2} \begin{pmatrix} 1 \\ 1 \\ 0 \end{pmatrix} = \sqrt{1/2} \begin{pmatrix} \sigma_{11} + \sigma_{12} \\ \sigma_{12} + \sigma_{22} \\ \sigma_{13} + \sigma_{23} \end{pmatrix} = \sigma_0 \begin{pmatrix} 0 \\ 1 \\ 0 \end{pmatrix}, \qquad (4.1.8)$$

along the lateral face $x < 0$, $y > 0$
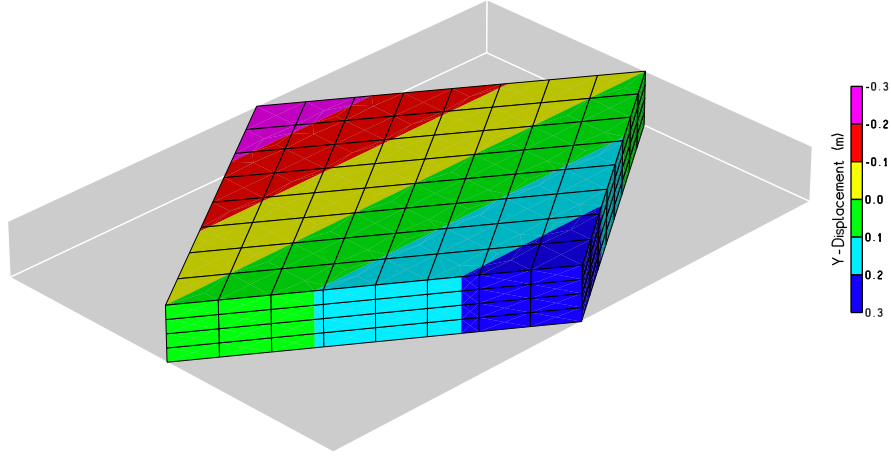
Fig. 4.1.1: Deformed mesh, y-displacements

$$\boldsymbol{\sigma}\sqrt{1/2}\begin{pmatrix} -1 \\ 1 \\ 0 \end{pmatrix} = \sqrt{1/2}\begin{pmatrix} -\sigma_{11}+\sigma_{12} \\ -\sigma_{12}+\sigma_{22} \\ -\sigma_{13}+\sigma_{23} \end{pmatrix} = \sigma_0\begin{pmatrix} 0 \\ 1 \\ 0 \end{pmatrix},$$ (4.1.9)

along the lateral face $x < 0$, $y < 0$

$$\boldsymbol{\sigma}\sqrt{1/2}\begin{pmatrix} -1 \\ -1 \\ 0 \end{pmatrix} = \sqrt{1/2}\begin{pmatrix} -\sigma_{11}-\sigma_{12} \\ -\sigma_{12}-\sigma_{22} \\ -\sigma_{13}-\sigma_{23} \end{pmatrix} = -\sigma_0\begin{pmatrix} 0 \\ 1 \\ 0 \end{pmatrix},$$ (4.1.10)

along the lateral face $x > 0$, $y < 0$

$$\boldsymbol{\sigma}\sqrt{1/2}\begin{pmatrix} 1 \\ -1 \\ 0 \end{pmatrix} = \sqrt{1/2}\begin{pmatrix} \sigma_{11}-\sigma_{12} \\ \sigma_{12}-\sigma_{22} \\ \sigma_{13}-\sigma_{23} \end{pmatrix} = -\sigma_0\begin{pmatrix} 0 \\ 1 \\ 0 \end{pmatrix},$$ (4.1.11)

along the top face $z = H$

$$\boldsymbol{\sigma}\begin{pmatrix} 0 \\ 0 \\ 1 \end{pmatrix} = \begin{pmatrix} \sigma_{13} \\ \sigma_{23} \\ \sigma_{33} \end{pmatrix} = \begin{pmatrix} 0 \\ 0 \\ 0 \end{pmatrix},$$ (4.1.12)

and along the bottom face $z = -H$

$$\boldsymbol{\sigma}\begin{pmatrix} 0 \\ 0 \\ -1 \end{pmatrix} = \begin{pmatrix} -\sigma_{13} \\ -\sigma_{23} \\ -\sigma_{33} \end{pmatrix} = \begin{pmatrix} 0 \\ 0 \\ 0 \end{pmatrix}.$$ (4.1.13)

Hooke's law reads for the strains

$$\epsilon_{11} = \frac{1}{E}\left[\sigma_{11} - \nu(\sigma_{22} + \sigma_{33})\right] = -\nu\sqrt{2}\frac{\sigma_0}{E},$$

$$\epsilon_{22} = \frac{1}{E}\left[\sigma_{22} - \nu(\sigma_{11} + \sigma_{33})\right] = \sqrt{2}\frac{\sigma_0}{E},$$

(4.1.14)

$$\epsilon_{33} = \frac{1}{E}\left[\sigma_{33} - \nu(\sigma_{11} + \sigma_{22})\right] = -\nu\sqrt{2}\frac{\sigma_0}{E},$$

$$\epsilon_{12} = \epsilon_{13} = \epsilon_{23} = 0.$$

Integrating the strains with respect to the fixities at the coordinate planes yields the displacement vector (u_x, u_y, u_z)

$$u_x(x) = -\nu\sqrt{2}\frac{\sigma_0}{E}x,$$

$$u_y(y) = \sqrt{2}\frac{\sigma_0}{E}y,$$

(4.1.15)

$$u_z(z) = -\nu\sqrt{2}\frac{\sigma_0}{E}z.$$

The deformed square takes the shape of a lozenge.

4.1.2 Due to specified surface loads an elastic plate undergoes simple shear

The domain is a rectangular plate located in the first octant with three faces on the coordinate planes. It is $H = 2$ m thick, has an extent of $L = 10$ m in x- and y-direction and is discretized by $8 \times 8 \times 2$ equally sized hexahedral elements. The plate is represented by an elastic material. Young's modulus $E = 12,500$ MPa and Poisson's ratio $\nu = 0.25$ have been assigned, gravity is neglected via zero material density. The face $x = 0$ is entirely fixed, specified loads $P(x, y, z)$ prevail along the remaining faces. With the aid of the stress $\sigma_0 = 500$ MPa these loads read along the face $x = L$

$$P(L, y, z) = \sigma_0 \begin{pmatrix} 0 \\ 0 \\ 1 \end{pmatrix},$$

(4.1.16)

along the faces $y = L$ and $y = 0$

$$P(x, L, z) = P(x, 0, z) = \begin{pmatrix} 0 \\ 0 \\ 0 \end{pmatrix},$$

(4.1.17)

and along the faces $z = H$ and $z = 0$

$$P(x, y, H) = \sigma_0 \begin{pmatrix} 1 \\ 0 \\ 0 \end{pmatrix}, \quad P(x, y, 0) = -\sigma_0 \begin{pmatrix} 1 \\ 0 \\ 0 \end{pmatrix}. \tag{4.1.18}$$

The simulation comprises one timestep to evaluate the stresses, the strains, and the displacement vector (u_x, u_y, u_z) (Fig. 4.1.2).
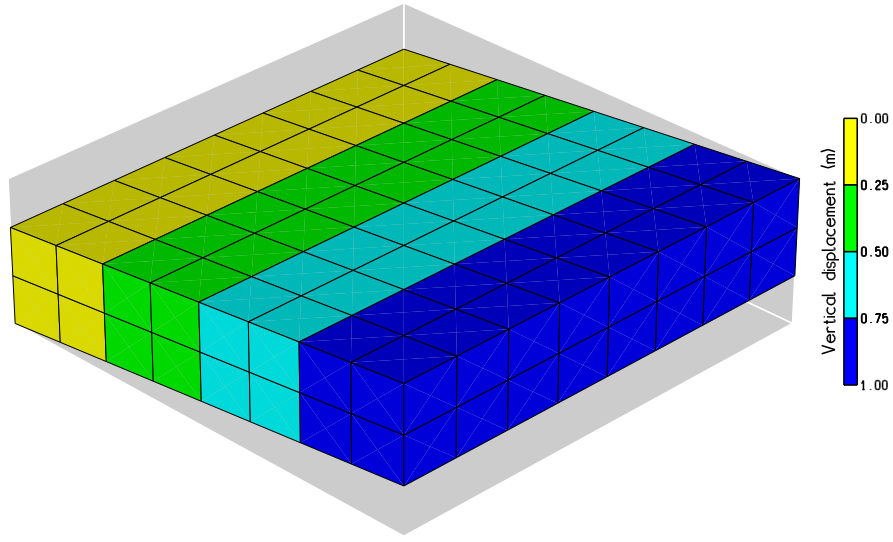
Fig. 4.1.2: Deformed mesh, vertical displacements

The stress tensor

$$\boldsymbol{\sigma} = \begin{pmatrix} \sigma_{11} & \sigma_{12} & \sigma_{13} \\ \sigma_{12} & \sigma_{22} & \sigma_{23} \\ \sigma_{13} & \sigma_{23} & \sigma_{33} \end{pmatrix} = \sigma_0 \begin{pmatrix} 0 & 0 & 1 \\ 0 & 0 & 0 \\ 1 & 0 & 0 \end{pmatrix} \tag{4.1.19}$$

satisfies the equation of mechanical equilibrium

$$\nabla \cdot \boldsymbol{\sigma} = 0 \tag{4.1.20}$$

as well as the specified surface loads because along the face $x = L$

$$\boldsymbol{\sigma} \begin{pmatrix} 1 \\ 0 \\ 0 \end{pmatrix} = \begin{pmatrix} \sigma_{11} \\ \sigma_{12} \\ \sigma_{13} \end{pmatrix} = \sigma_0 \begin{pmatrix} 0 \\ 0 \\ 1 \end{pmatrix}, \tag{4.1.21}$$

along the faces $y = L$ and $y = 0$

$$\sigma \begin{pmatrix} 0 \\ 1 \\ 0 \end{pmatrix} = -\sigma \begin{pmatrix} 0 \\ -1 \\ 0 \end{pmatrix} = \begin{pmatrix} \sigma_{12} \\ \sigma_{22} \\ \sigma_{23} \end{pmatrix} = \begin{pmatrix} 0 \\ 0 \\ 0 \end{pmatrix}, \qquad (4.1.22)$$

and along the faces $z = H$ and $z = 0$

$$\sigma \begin{pmatrix} 0 \\ 0 \\ 1 \end{pmatrix} = -\sigma \begin{pmatrix} 0 \\ 0 \\ -1 \end{pmatrix} = \begin{pmatrix} \sigma_{13} \\ \sigma_{23} \\ \sigma_{33} \end{pmatrix} = \sigma_0 \begin{pmatrix} 1 \\ 0 \\ 0 \end{pmatrix}. \qquad (4.1.23)$$

Hooke's law reads for the strains

$$\epsilon_{11} = \frac{1}{E} \left[\sigma_{11} - \nu(\sigma_{22} + \sigma_{33}) \right],$$

$$\epsilon_{22} = \frac{1}{E} \left[\sigma_{22} - \nu(\sigma_{11} + \sigma_{33}) \right],$$

$$\epsilon_{33} = \frac{1}{E} \left[\sigma_{33} - \nu(\sigma_{11} + \sigma_{22}) \right],$$

$$\epsilon_{12} = \frac{2(1+\nu)}{E} \sigma_{12}, \qquad\qquad (4.1.24)$$

$$\epsilon_{13} = \frac{2(1+\nu)}{E} \sigma_{13},$$

$$\epsilon_{23} = \frac{2(1+\nu)}{E} \sigma_{23},$$

which constitute a set of equations for the partial derivatives of the displacements. Employing the stresses above

$$\epsilon_{11} = \epsilon_{22} = \epsilon_{33} = \frac{\partial u_x}{\partial x} = \frac{\partial u_y}{\partial y} = \frac{\partial u_z}{\partial z} = 0,$$

$$\epsilon_{12} = \frac{\partial u_x}{\partial y} + \frac{\partial u_y}{\partial x} = 0,$$

$$\epsilon_{13} = \frac{\partial u_x}{\partial z} + \frac{\partial u_z}{\partial x} = \frac{2(1+\nu)}{E} \sigma_0, \qquad (4.1.25)$$

$$\epsilon_{23} = \frac{\partial u_y}{\partial z} + \frac{\partial u_z}{\partial y} = 0.$$

The displacements (u_x, u_y, u_z) will next be obtained from the strains.

$$\frac{\partial u_x}{\partial x} = \frac{\partial u_y}{\partial y} = \frac{\partial u_z}{\partial z} = 0 \qquad\qquad (4.1.26)$$

yield

$$
\begin{aligned}
u_x &= u_x(y, z), \\
u_y &= u_y(x, z), \\
u_z &= u_z(x, y),
\end{aligned}
\tag{4.1.27}
$$

thus reducing the number of independent variables. Because $u_x(y, z)$ does not depend on x and the face $x = 0$ is entirely fixed

$$
u_x(y, z) = 0.
\tag{4.1.28}
$$

Then

$$
\epsilon_{13} = \frac{\partial u_x}{\partial z} + \frac{\partial u_z}{\partial x} = \frac{\partial}{\partial x} u_z(x, y) = \frac{2(1 + \nu)}{E} \sigma_0,
\tag{4.1.29}
$$

and due to the fixities at the face $x = 0$

$$
u_z(x) = x \frac{2(1 + \nu)}{E} \sigma_0.
\tag{4.1.30}
$$

Because

$$
\begin{aligned}
\epsilon_{12} &= \frac{\partial u_y}{\partial x} + \frac{\partial u_x}{\partial y} = \frac{\partial u_y}{\partial x} = 0, \\
\epsilon_{23} &= \frac{\partial u_y}{\partial z} + \frac{\partial u_z}{\partial y} = \frac{\partial u_y}{\partial z} = 0,
\end{aligned}
\tag{4.1.31}
$$

the fixities at the face $x = 0$ yield

$$
u_y(x, z) = 0.
\tag{4.1.32}
$$

The displacement vector (u_x, u_y, u_z) becomes

$$
\begin{aligned}
u_x &= u_y = 0, \\
u_z(x) &= x \frac{2(1 + \nu)}{E} \sigma_0.
\end{aligned}
\tag{4.1.33}
$$

Due to the applied load the plate undergoes shear in the x-z-plane.

4.1.3 Due to specified surface loads an elastic plate undergoes shear in two planes

The domain is a rectangular plate located in the first octant with three faces on the coordinate planes. It is $H = 2$ m thick, has an extent of $L = 10$ m in x- and y-direction and is discretized by $8 \times 8 \times 2$ equally sized hexahedral elements. The plate is represented by an elastic material. Young's modulus

$E = 12,500$ MPa and Poisson's ratio $\nu = 0.25$ have been assigned, gravity is neglected via zero material density. The face $x = 0$ is entirely fixed, specified loads $P(x, y, z)$ prevail along the remaining faces. With the aid of the stress $\sigma_0 = 1000$ MPa these loads read along the face $x = L$

$$P(L, y, z) = \sigma_0 \begin{pmatrix} 0 \\ 1 \\ 1 \end{pmatrix}, \qquad (4.1.34)$$

along the faces $y = L$ and $y = 0$

$$P(x, L, z) = \sigma_0 \begin{pmatrix} 1 \\ 0 \\ 0 \end{pmatrix}, \quad P(x, 0, z) = -\sigma_0 \begin{pmatrix} 1 \\ 0 \\ 0 \end{pmatrix}, \qquad (4.1.35)$$

and along the faces $z = H$ and $z = 0$

$$P(x, y, H) = \sigma_0 \begin{pmatrix} 1 \\ 0 \\ 0 \end{pmatrix}, \quad P(x, y, 0) = -\sigma_0 \begin{pmatrix} 1 \\ 0 \\ 0 \end{pmatrix}. \qquad (4.1.36)$$

The simulation comprises one timestep to evaluate the stresses, the strains, and the displacement vector (u_x, u_y, u_z) (Fig. 4.1.3).
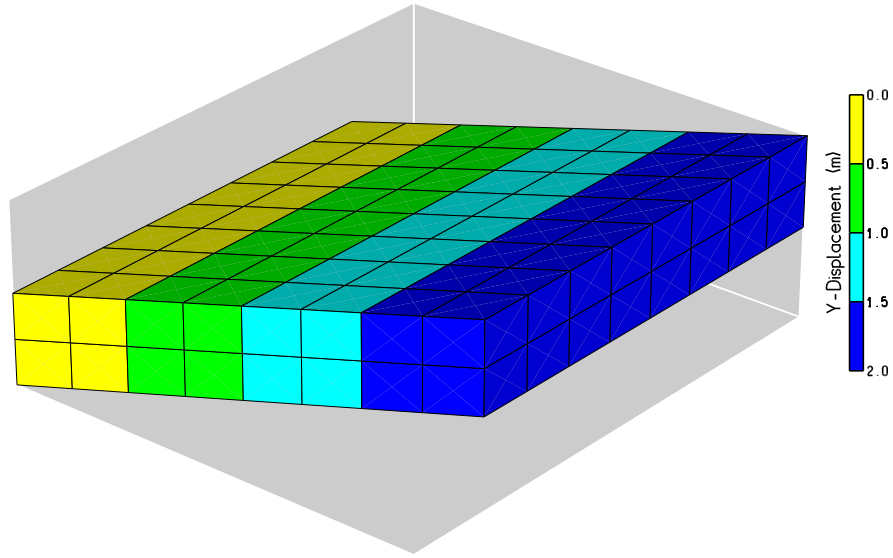
Fig. 4.1.3: Deformed mesh, y-displacements

The stress tensor

$$\boldsymbol{\sigma} = \begin{pmatrix} \sigma_{11} & \sigma_{12} & \sigma_{13} \\ \sigma_{12} & \sigma_{22} & \sigma_{23} \\ \sigma_{13} & \sigma_{23} & \sigma_{33} \end{pmatrix} = \sigma_0 \begin{pmatrix} 0 & 1 & 1 \\ 1 & 0 & 0 \\ 1 & 0 & 0 \end{pmatrix} \tag{4.1.37}$$

satisfies the equation of mechanical equilibrium

$$\nabla \cdot \boldsymbol{\sigma} = 0 \tag{4.1.38}$$

as well as the specified surface loads because along the face $x = L$

$$\boldsymbol{\sigma} \begin{pmatrix} 1 \\ 0 \\ 0 \end{pmatrix} = \begin{pmatrix} \sigma_{11} \\ \sigma_{12} \\ \sigma_{13} \end{pmatrix} = \sigma_0 \begin{pmatrix} 0 \\ 1 \\ 1 \end{pmatrix}, \tag{4.1.39}$$

along the faces $y = L$ and $y = 0$

$$\boldsymbol{\sigma} \begin{pmatrix} 0 \\ 1 \\ 0 \end{pmatrix} = -\boldsymbol{\sigma} \begin{pmatrix} 0 \\ -1 \\ 0 \end{pmatrix} = \begin{pmatrix} \sigma_{12} \\ \sigma_{22} \\ \sigma_{23} \end{pmatrix} = \sigma_0 \begin{pmatrix} 1 \\ 0 \\ 0 \end{pmatrix}, \tag{4.1.40}$$

and along the faces $z = H$ and $z = 0$

$$\boldsymbol{\sigma} \begin{pmatrix} 0 \\ 0 \\ 1 \end{pmatrix} = -\boldsymbol{\sigma} \begin{pmatrix} 0 \\ 0 \\ -1 \end{pmatrix} = \begin{pmatrix} \sigma_{13} \\ \sigma_{23} \\ \sigma_{33} \end{pmatrix} = \sigma_0 \begin{pmatrix} 1 \\ 0 \\ 0 \end{pmatrix}. \tag{4.1.41}$$

Hooke's law reads for the strains

$$\epsilon_{11} = \frac{1}{E} \left[\sigma_{11} - \nu(\sigma_{22} + \sigma_{33}) \right],$$

$$\epsilon_{22} = \frac{1}{E} \left[\sigma_{22} - \nu(\sigma_{11} + \sigma_{33}) \right],$$

$$\epsilon_{33} = \frac{1}{E} \left[\sigma_{33} - \nu(\sigma_{11} + \sigma_{22}) \right],$$

$$\epsilon_{12} = \frac{2(1+\nu)}{E} \sigma_{12}, \tag{4.1.42}$$

$$\epsilon_{13} = \frac{2(1+\nu)}{E} \sigma_{13},$$

$$\epsilon_{23} = \frac{2(1+\nu)}{E} \sigma_{23},$$

which constitute a set of equations for the partial derivatives of the displacements. Employing the stresses above

$$\epsilon_{11} = \epsilon_{22} = \epsilon_{33} = \frac{\partial u_x}{\partial x} = \frac{\partial u_y}{\partial y} = \frac{\partial u_z}{\partial z} = 0,$$

$$\epsilon_{12} = \frac{\partial u_x}{\partial y} + \frac{\partial u_y}{\partial x} = \frac{2(1+\nu)}{E}\sigma_0,$$

$$\epsilon_{13} = \frac{\partial u_x}{\partial z} + \frac{\partial u_z}{\partial x} = \frac{2(1+\nu)}{E}\sigma_0,$$ \hfill (4.1.43)

$$\epsilon_{23} = \frac{\partial u_y}{\partial z} + \frac{\partial u_z}{\partial y} = 0.$$

The displacements (u_x, u_y, u_z) will next be obtained from the strains.

$$\frac{\partial u_x}{\partial x} = \frac{\partial u_y}{\partial y} = \frac{\partial u_z}{\partial z} = 0 \hfill (4.1.44)$$

yield

$$u_x = u_x(y, z),$$
$$u_y = u_y(x, z), \hfill (4.1.45)$$
$$u_z = u_z(x, y),$$

thus reducing the number of independent variables. Because $u_x(y, z)$ does not depend on x and the face $x = 0$ is entirely fixed

$$u_x(y, z) = 0. \hfill (4.1.46)$$

Then

$$\epsilon_{12} = \frac{\partial u_x}{\partial y} + \frac{\partial u_y}{\partial x} = \frac{\partial}{\partial x} u_y(x, z) = \frac{2(1+\nu)}{E}\sigma_0, \hfill (4.1.47)$$

and due to the fixities at the face $x = 0$

$$u_y(x) = x \frac{2(1+\nu)}{E}\sigma_0. \hfill (4.1.48)$$

Because

$$\epsilon_{13} = \frac{\partial u_x}{\partial z} + \frac{\partial u_z}{\partial x} = \frac{\partial}{\partial x} u_z(x, y) = \frac{2(1+\nu)}{E}\sigma_0, \hfill (4.1.49)$$

the fixities at the face $x = 0$ yield

$$u_z(x) = x \frac{2(1+\nu)}{E}\sigma_0, \hfill (4.1.50)$$

and the above $u_y(x)$ and $u_z(x)$ also satisfy $\epsilon_{23} = 0$. The displacement vector (u_x, u_y, u_z) becomes

$$u_x = 0,$$

$$u_y(x) = x\frac{2(1+\nu)}{E}\sigma_0, \qquad\qquad (4.1.51)$$

$$u_z(x) = x\frac{2(1+\nu)}{E}\sigma_0.$$

Due to the applied load the plate undergoes shear in the x-y-plane and in the x-z-plane.

4.1.4 Due to specified surface loads a rectangular elastic beam undergoes torsion

Given length $2L = 10$ m and thickness $2H = 2$ m the domain represents the rectangular beam $[-L, L] \times [-H, H] \times [-H, H]$. It is discretized by $20 \times 4 \times 4$ equally sized hexahedral elements and represented by an elastic material. Young's modulus $E = 25,000$ MPa and Poisson's ratio $\nu = 0.25$ have been assigned, gravity is neglected via zero material density. Fixities have been prescribed in the interior of the domain with zero x-displacement along the plane $x = 0$, zero y-displacement along the z-axis, and zero z-displacement along the y-axis. Specified loads $P(x, y, z)$ prevail along the entire surface of the domain. With the aid of the stress $\sigma_0 = 1000$ MPa these loads read along the faces $x = L$ and $x = -L$

$$P(L, y, z) = \frac{\sigma_0}{H}\begin{pmatrix} 0 \\ z \\ -y \end{pmatrix}, \quad P(-L, y, z) = -\frac{\sigma_0}{H}\begin{pmatrix} 0 \\ z \\ -y \end{pmatrix}, \qquad (4.1.52)$$

along the faces $y = H$ and $y = -H$

$$P(x, H, z) = \frac{\sigma_0}{H}\begin{pmatrix} z \\ 0 \\ 0 \end{pmatrix}, \quad P(x, -H, z) = -\frac{\sigma_0}{H}\begin{pmatrix} z \\ 0 \\ 0 \end{pmatrix}, \qquad (4.1.53)$$

and along the faces $z = H$ and $z = -H$

$$P(x, y, H) = \frac{\sigma_0}{H}\begin{pmatrix} -y \\ 0 \\ 0 \end{pmatrix}, \quad P(x, y, -H) = -\frac{\sigma_0}{H}\begin{pmatrix} -y \\ 0 \\ 0 \end{pmatrix}. \qquad (4.1.54)$$

The simulation comprises one timestep to evaluate the stresses, the strains, and the displacement vector (u_x, u_y, u_z) (Fig. 4.1.4).

The stress tensor
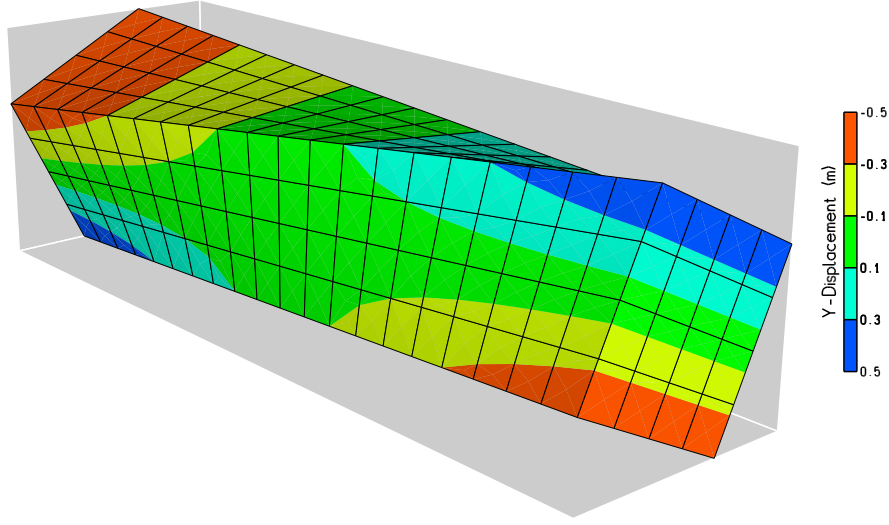
Fig. 4.1.4: Deformed mesh, y-displacements

$$\boldsymbol{\sigma} = \begin{pmatrix} \sigma_{11} & \sigma_{12} & \sigma_{13} \\ \sigma_{12} & \sigma_{22} & \sigma_{23} \\ \sigma_{13} & \sigma_{23} & \sigma_{33} \end{pmatrix} = \frac{\sigma_0}{H} \begin{pmatrix} 0 & z & -y \\ z & 0 & 0 \\ -y & 0 & 0 \end{pmatrix} \qquad (4.1.55)$$

satisfies the equation of mechanical equilibrium

$$\nabla \cdot \boldsymbol{\sigma} = 0 \qquad (4.1.56)$$

as well as the specified surface loads because along the faces $x = L$ and $x = -L$

$$\boldsymbol{\sigma} \begin{pmatrix} 1 \\ 0 \\ 0 \end{pmatrix} = -\boldsymbol{\sigma} \begin{pmatrix} -1 \\ 0 \\ 0 \end{pmatrix} = \begin{pmatrix} \sigma_{11} \\ \sigma_{12} \\ \sigma_{13} \end{pmatrix} = \frac{\sigma_0}{H} \begin{pmatrix} 0 \\ z \\ -y \end{pmatrix}, \qquad (4.1.57)$$

along the faces $y = H$ and $y = -H$

$$\boldsymbol{\sigma} \begin{pmatrix} 0 \\ 1 \\ 0 \end{pmatrix} = -\boldsymbol{\sigma} \begin{pmatrix} 0 \\ -1 \\ 0 \end{pmatrix} = \begin{pmatrix} \sigma_{12} \\ \sigma_{22} \\ \sigma_{23} \end{pmatrix} = \frac{\sigma_0}{H} \begin{pmatrix} z \\ 0 \\ 0 \end{pmatrix}, \qquad (4.1.58)$$

and along the faces $z = H$ and $z = -H$

$$\boldsymbol{\sigma} \begin{pmatrix} 0 \\ 0 \\ 1 \end{pmatrix} = -\boldsymbol{\sigma} \begin{pmatrix} 0 \\ 0 \\ -1 \end{pmatrix} = \begin{pmatrix} \sigma_{13} \\ \sigma_{23} \\ \sigma_{33} \end{pmatrix} = \frac{\sigma_0}{H} \begin{pmatrix} -y \\ 0 \\ 0 \end{pmatrix}. \tag{4.1.59}$$

Hooke's law reads for the strains

$$\epsilon_{11} = \frac{1}{E} \left[\sigma_{11} - \nu(\sigma_{22} + \sigma_{33}) \right],$$

$$\epsilon_{22} = \frac{1}{E} \left[\sigma_{22} - \nu(\sigma_{11} + \sigma_{33}) \right],$$

$$\epsilon_{33} = \frac{1}{E} \left[\sigma_{33} - \nu(\sigma_{11} + \sigma_{22}) \right],$$

$$\epsilon_{12} = \frac{2(1+\nu)}{E} \sigma_{12}, \tag{4.1.60}$$

$$\epsilon_{13} = \frac{2(1+\nu)}{E} \sigma_{13},$$

$$\epsilon_{23} = \frac{2(1+\nu)}{E} \sigma_{23},$$

which constitute a set of equations for the partial derivatives of the displacements. Employing the stresses above

$$\epsilon_{11} = \epsilon_{22} = \epsilon_{33} = \frac{\partial u_x}{\partial x} = \frac{\partial u_y}{\partial y} = \frac{\partial u_z}{\partial z} = 0,$$

$$\epsilon_{12} = \frac{\partial u_x}{\partial y} + \frac{\partial u_y}{\partial x} = \frac{2(1+\nu)}{E} \frac{\sigma_0}{H} z,$$

$$\epsilon_{13} = \frac{\partial u_x}{\partial z} + \frac{\partial u_z}{\partial x} = \frac{2(1+\nu)}{E} \frac{\sigma_0}{H} (-y), \tag{4.1.61}$$

$$\epsilon_{23} = \frac{\partial u_y}{\partial z} + \frac{\partial u_z}{\partial y} = 0.$$

The displacements (u_x, u_y, u_z) will next be obtained from the strains.

$$\frac{\partial u_x}{\partial x} = \frac{\partial u_y}{\partial y} = \frac{\partial u_z}{\partial z} = 0 \tag{4.1.62}$$

yield

$$u_x = u_x(y, z),$$
$$u_y = u_y(x, z), \tag{4.1.63}$$
$$u_z = u_z(x, y),$$

thus reducing the number of independent variables. Because $u_x(y, z)$ does not depend on x and u_x is zero along the plane $x = 0$

$$u_x(y, z) = 0. \tag{4.1.64}$$

Then

$$\epsilon_{12} = \frac{\partial u_x}{\partial y} + \frac{\partial u_y}{\partial x} = \frac{\partial}{\partial x} u_y(x, z) = \frac{2(1 + \nu)}{E} \frac{\sigma_0}{H} z,$$

$$\epsilon_{13} = \frac{\partial u_x}{\partial z} + \frac{\partial u_z}{\partial x} = \frac{\partial}{\partial x} u_z(x, y) = \frac{2(1 + \nu)}{E} \frac{\sigma_0}{H}(-y). \tag{4.1.65}$$

Due to the fixities along the z-axis and along the y-axis

$$u_y(x, z) = \frac{2(1 + \nu)}{E} \frac{\sigma_0}{H} xz,$$

$$u_z(x, y) = -\frac{2(1 + \nu)}{E} \frac{\sigma_0}{H} xy, \tag{4.1.66}$$

and the above $u_y(x, z)$ and $u_z(x, y)$ also satisfy $\epsilon_{23} = 0$. The displacement vector (u_x, u_y, u_z) becomes

$$u_x = 0,$$

$$u_y(x, z) = xz \frac{2(1 + \nu)}{E} \frac{\sigma_0}{H},$$

$$u_z(x, y) = -xy \frac{2(1 + \nu)}{E} \frac{\sigma_0}{H}. \tag{4.1.67}$$

4.1.5 Due to specified surface loads an elastic plate takes a hyperbolic shape

Given length $2L = 20$ m and thickness $2H = 1$ m the domain represents the rectangular plate $[-L, L] \times [-L, L] \times [-H, H]$. It is discretized by $20 \times 20 \times 2$ equally sized hexahedral elements and represented by an elastic material. Young's modulus $E = 25,000$ MPa and Poisson's ratio $\nu = 0.25$ have been assigned, gravity is neglected via zero material density. The plane $x = 0$ is entirely fixed, specified loads $P(x, y, z)$ prevail along the entire surface of the domain. With the aid of the stress $\sigma_0 = 500$ MPa these loads read along the faces $x = L$ and $x = -L$

$$P(L, y, z) = \frac{\sigma_0}{H} \begin{pmatrix} 0 \\ 0 \\ y \end{pmatrix}, \quad P(-L, y, z) = -\frac{\sigma_0}{H} \begin{pmatrix} 0 \\ 0 \\ y \end{pmatrix}, \tag{4.1.68}$$

along the faces $y = L$ and $y = -L$

$$P(x, L, z) = \frac{\sigma_0}{H} \begin{pmatrix} 0 \\ 0 \\ x \end{pmatrix}, \quad P(x, -L, z) = -\frac{\sigma_0}{H} \begin{pmatrix} 0 \\ 0 \\ x \end{pmatrix}, \quad (4.1.69)$$

and along the faces $z = H$ and $z = -H$

$$P(x, y, H) = \frac{\sigma_0}{H} \begin{pmatrix} y \\ x \\ 0 \end{pmatrix}, \quad P(x, y, -H) = -\frac{\sigma_0}{H} \begin{pmatrix} y \\ x \\ 0 \end{pmatrix}. \quad (4.1.70)$$

The simulation comprises one timestep to evaluate the stresses, the strains, and the displacement vector (u_x, u_y, u_z) (Fig. 4.1.5).
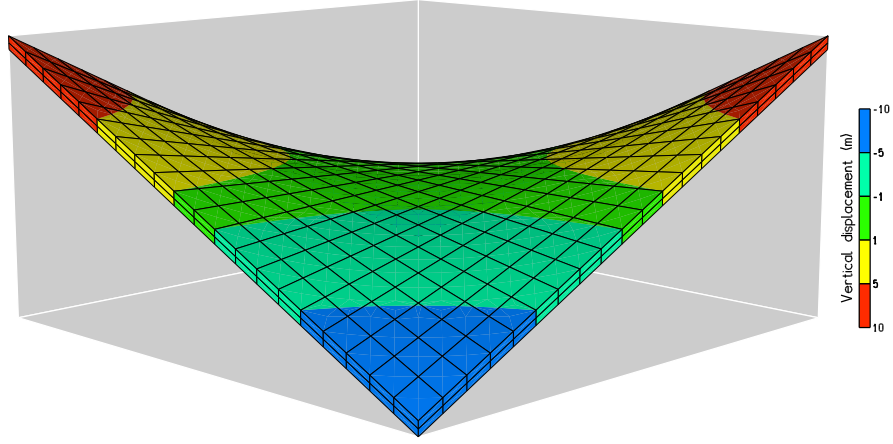
Fig. 4.1.5: Deformed mesh, vertical displacements

The stress tensor

$$\boldsymbol{\sigma} = \begin{pmatrix} \sigma_{11} & \sigma_{12} & \sigma_{13} \\ \sigma_{12} & \sigma_{22} & \sigma_{23} \\ \sigma_{13} & \sigma_{23} & \sigma_{33} \end{pmatrix} = \frac{\sigma_0}{H} \begin{pmatrix} 0 & 0 & y \\ 0 & 0 & x \\ y & x & 0 \end{pmatrix} \quad (4.1.71)$$

satisfies the equation of mechanical equilibrium

$$\nabla \cdot \boldsymbol{\sigma} = 0 \quad (4.1.72)$$

as well as the specified surface loads because along the faces $x = L$ and $x = -L$

$$\boldsymbol{\sigma}\begin{pmatrix} 1 \\ 0 \\ 0 \end{pmatrix} = -\boldsymbol{\sigma}\begin{pmatrix} -1 \\ 0 \\ 0 \end{pmatrix} = \begin{pmatrix} \sigma_{11} \\ \sigma_{12} \\ \sigma_{13} \end{pmatrix} = \frac{\sigma_0}{H}\begin{pmatrix} 0 \\ 0 \\ y \end{pmatrix}, \qquad (4.1.73)$$

along the faces $y = L$ and $y = -L$

$$\boldsymbol{\sigma}\begin{pmatrix} 0 \\ 1 \\ 0 \end{pmatrix} = -\boldsymbol{\sigma}\begin{pmatrix} 0 \\ -1 \\ 0 \end{pmatrix} = \begin{pmatrix} \sigma_{12} \\ \sigma_{22} \\ \sigma_{23} \end{pmatrix} = \frac{\sigma_0}{H}\begin{pmatrix} 0 \\ 0 \\ x \end{pmatrix}, \qquad (4.1.74)$$

and along the faces $z = H$ and $z = -H$

$$\boldsymbol{\sigma}\begin{pmatrix} 0 \\ 0 \\ 1 \end{pmatrix} = -\boldsymbol{\sigma}\begin{pmatrix} 0 \\ 0 \\ -1 \end{pmatrix} = \begin{pmatrix} \sigma_{13} \\ \sigma_{23} \\ \sigma_{33} \end{pmatrix} = \frac{\sigma_0}{H}\begin{pmatrix} y \\ x \\ 0 \end{pmatrix}. \qquad (4.1.75)$$

Hooke's law reads for the strains

$$\epsilon_{11} = \frac{1}{E}\left[\sigma_{11} - \nu(\sigma_{22} + \sigma_{33})\right],$$

$$\epsilon_{22} = \frac{1}{E}\left[\sigma_{22} - \nu(\sigma_{11} + \sigma_{33})\right],$$

$$\epsilon_{33} = \frac{1}{E}\left[\sigma_{33} - \nu(\sigma_{11} + \sigma_{22})\right],$$

$$\epsilon_{12} = \frac{2(1+\nu)}{E}\sigma_{12}, \qquad\qquad\qquad (4.1.76)$$

$$\epsilon_{13} = \frac{2(1+\nu)}{E}\sigma_{13},$$

$$\epsilon_{23} = \frac{2(1+\nu)}{E}\sigma_{23},$$

which constitute a set of equations for the partial derivatives of the displacements. Employing the stresses above

$$\epsilon_{11} = \epsilon_{22} = \epsilon_{33} = \frac{\partial u_x}{\partial x} = \frac{\partial u_y}{\partial y} = \frac{\partial u_z}{\partial z} = 0,$$

$$\epsilon_{12} = \frac{\partial u_x}{\partial y} + \frac{\partial u_y}{\partial x} = 0,$$

$$\epsilon_{13} = \frac{\partial u_x}{\partial z} + \frac{\partial u_z}{\partial x} = \frac{2(1+\nu)}{E}\frac{\sigma_0}{H}y, \qquad (4.1.77)$$

$$\epsilon_{23} = \frac{\partial u_y}{\partial z} + \frac{\partial u_z}{\partial y} = \frac{2(1+\nu)}{E}\frac{\sigma_0}{H}x.$$

The displacements (u_x, u_y, u_z) will next be obtained from the strains.

$$\frac{\partial u_x}{\partial x} = \frac{\partial u_y}{\partial y} = \frac{\partial u_z}{\partial z} = 0 \tag{4.1.78}$$

yield

$$\begin{aligned}
u_x &= u_x(y, z), \\
u_y &= u_y(x, z), \\
u_z &= u_z(x, y),
\end{aligned} \tag{4.1.79}$$

thus reducing the number of independent variables. Because $u_x(y, z)$ does not depend on x and u_x is zero along the plane $x = 0$

$$u_x(y, z) = 0. \tag{4.1.80}$$

Then

$$\epsilon_{12} = \frac{\partial u_x}{\partial y} + \frac{\partial u_y}{\partial x} = \frac{\partial}{\partial x} u_y(x, z) = 0. \tag{4.1.81}$$

Hence, $u_y(x, z)$ does not depend on x and u_y is zero along the plane $x = 0$. Therefore,

$$u_y(x, z) = 0. \tag{4.1.82}$$

Because

$$\epsilon_{13} = \frac{\partial u_x}{\partial z} + \frac{\partial u_z}{\partial x} = \frac{\partial}{\partial x} u_z(x, y) = \frac{2(1 + \nu)}{E} \frac{\sigma_0}{H} y, \tag{4.1.83}$$

and due to the fixities along the plane $x = 0$

$$u_z(x, y) = \frac{2(1 + \nu)}{E} \frac{\sigma_0}{H} xy. \tag{4.1.84}$$

The above $u_y(x, z)$ and $u_z(x, y)$ also satisfy

$$\frac{\partial u_y}{\partial z} + \frac{\partial u_z}{\partial y} = 0 + \frac{2(1 + \nu)}{E} \frac{\sigma_0}{H} x = \epsilon_{23}. \tag{4.1.85}$$

The displacement vector (u_x, u_y, u_z) becomes

$$\begin{aligned}
u_x &= u_y = 0, \\
u_z(x, y) &= xy \frac{2(1 + \nu)}{E} \frac{\sigma_0}{H}.
\end{aligned} \tag{4.1.86}$$

4.1.6 Two elastic plates are deformed in a stress field with three non-constant components of shear

Given length $L = 10$ m and thickness $2H = 1$ m the domain comprises two plates, $[-L, 0] \times [-L, 0] \times [-H, H]$ and $[0, L] \times [0, L] \times [-H, H]$, respectively. They are discretized by $8 \times 8 \times 4$ equally sized hexahedral elements each and represented by an elastic material. Young's modulus $E = 25,000$ MPa and Poisson's ratio $\nu = 0.25$ have been assigned, gravity is neglected via zero material density. The faces $x = 0$ are entirely fixed, specified loads $P(x, y, z)$ prevail along the surface of every plate. For the plate $[0, L] \times [0, L] \times [-H, H]$ and with the aid of the stress $\sigma_0 = 500$ MPa these loads read along the faces $x = L$ and $x = 0$

$$P(L, y, z) = \frac{\sigma_0}{H} \begin{pmatrix} 0 \\ z \\ y \end{pmatrix}, \quad P(0, y, z) = -\frac{\sigma_0}{H} \begin{pmatrix} 0 \\ z \\ y \end{pmatrix}, \tag{4.1.87}$$

along the faces $y = L$ and $y = 0$

$$P(x, L, z) = \frac{\sigma_0}{H} \begin{pmatrix} z \\ 0 \\ 2x \end{pmatrix}, \quad P(x, 0, z) = -\frac{\sigma_0}{H} \begin{pmatrix} z \\ 0 \\ 2x \end{pmatrix}, \tag{4.1.88}$$

and along the faces $z = H$ and $z = -H$

$$P(x, y, H) = \frac{\sigma_0}{H} \begin{pmatrix} y \\ 2x \\ 0 \end{pmatrix}, \quad P(x, y, -H) = -\frac{\sigma_0}{H} \begin{pmatrix} y \\ 2x \\ 0 \end{pmatrix}. \tag{4.1.89}$$

For the plate $[-L, 0] \times [-L, 0] \times [-H, H]$ we have along the faces $x = 0$ and $x = -L$

$$P(0, y, z) = \frac{\sigma_0}{H} \begin{pmatrix} 0 \\ z \\ y \end{pmatrix}, \quad P(-L, y, z) = -\frac{\sigma_0}{H} \begin{pmatrix} 0 \\ z \\ y \end{pmatrix}, \tag{4.1.90}$$

along the faces $y = 0$ and $y = -L$

$$P(x, 0, z) = \frac{\sigma_0}{H} \begin{pmatrix} z \\ 0 \\ 2x \end{pmatrix}, \quad P(x, -L, z) = -\frac{\sigma_0}{H} \begin{pmatrix} z \\ 0 \\ 2x \end{pmatrix}, \tag{4.1.91}$$

and along the faces $z = H$ and $z = -H$

$$P(x, y, H) = \frac{\sigma_0}{H} \begin{pmatrix} y \\ 2x \\ 0 \end{pmatrix}, \quad P(x, y, -H) = -\frac{\sigma_0}{H} \begin{pmatrix} y \\ 2x \\ 0 \end{pmatrix}. \tag{4.1.92}$$

The simulation comprises one timestep to evaluate the stresses, the strains, and the displacement vector (u_x, u_y, u_z) (Fig. 4.1.6).
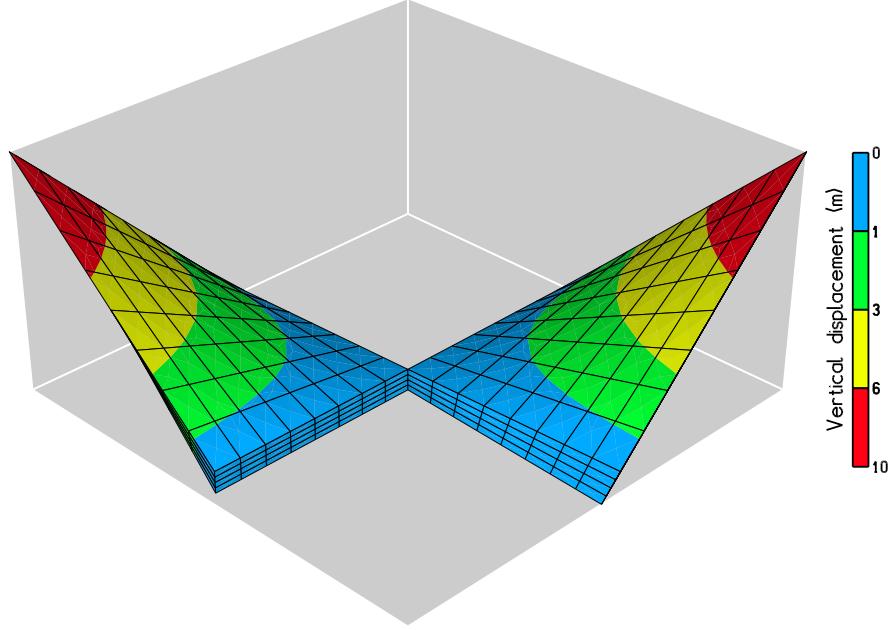
Fig. 4.1.6: Deformed mesh, vertical displacements

The stress tensor

$$\boldsymbol{\sigma} = \begin{pmatrix} \sigma_{11} & \sigma_{12} & \sigma_{13} \\ \sigma_{12} & \sigma_{22} & \sigma_{23} \\ \sigma_{13} & \sigma_{23} & \sigma_{33} \end{pmatrix} = \frac{\sigma_0}{H} \begin{pmatrix} 0 & z & y \\ z & 0 & 2x \\ y & 2x & 0 \end{pmatrix} \qquad (4.1.93)$$

satisfies the equation of mechanical equilibrium

$$\nabla \cdot \boldsymbol{\sigma} = 0 \qquad (4.1.94)$$

as well as the specified surface loads. For the plate $[0, L] \times [0, L] \times [-H, H]$ we have along the faces $x = L$ and $x = 0$

$$\boldsymbol{\sigma} \begin{pmatrix} 1 \\ 0 \\ 0 \end{pmatrix} = -\boldsymbol{\sigma} \begin{pmatrix} -1 \\ 0 \\ 0 \end{pmatrix} = \begin{pmatrix} \sigma_{11} \\ \sigma_{12} \\ \sigma_{13} \end{pmatrix} = \frac{\sigma_0}{H} \begin{pmatrix} 0 \\ z \\ y \end{pmatrix}, \qquad (4.1.95)$$

along the faces $y = L$ and $y = 0$

$$\boldsymbol{\sigma} \begin{pmatrix} 0 \\ 1 \\ 0 \end{pmatrix} = -\boldsymbol{\sigma} \begin{pmatrix} 0 \\ -1 \\ 0 \end{pmatrix} = \begin{pmatrix} \sigma_{12} \\ \sigma_{22} \\ \sigma_{23} \end{pmatrix} = \frac{\sigma_0}{H} \begin{pmatrix} z \\ 0 \\ 2x \end{pmatrix}, \qquad (4.1.96)$$

and along the faces $z = H$ and $z = -H$

$$\boldsymbol{\sigma} \begin{pmatrix} 0 \\ 0 \\ 1 \end{pmatrix} = -\boldsymbol{\sigma} \begin{pmatrix} 0 \\ 0 \\ -1 \end{pmatrix} = \begin{pmatrix} \sigma_{13} \\ \sigma_{23} \\ \sigma_{33} \end{pmatrix} = \frac{\sigma_0}{H} \begin{pmatrix} y \\ 2x \\ 0 \end{pmatrix}. \qquad (4.1.97)$$

For the plate $[-L, 0] \times [-L, 0] \times [-H, H]$ we have along the faces $x = 0$ and $x = -L$

$$\boldsymbol{\sigma} \begin{pmatrix} 1 \\ 0 \\ 0 \end{pmatrix} = -\boldsymbol{\sigma} \begin{pmatrix} -1 \\ 0 \\ 0 \end{pmatrix} = \begin{pmatrix} \sigma_{11} \\ \sigma_{12} \\ \sigma_{13} \end{pmatrix} = \frac{\sigma_0}{H} \begin{pmatrix} 0 \\ z \\ y \end{pmatrix}, \qquad (4.1.98)$$

along the faces $y = 0$ and $y = -L$

$$\boldsymbol{\sigma} \begin{pmatrix} 0 \\ 1 \\ 0 \end{pmatrix} = -\boldsymbol{\sigma} \begin{pmatrix} 0 \\ -1 \\ 0 \end{pmatrix} = \begin{pmatrix} \sigma_{12} \\ \sigma_{22} \\ \sigma_{23} \end{pmatrix} = \frac{\sigma_0}{H} \begin{pmatrix} z \\ 0 \\ 2x \end{pmatrix}, \qquad (4.1.99)$$

and along the faces $z = H$ and $z = -H$

$$\boldsymbol{\sigma} \begin{pmatrix} 0 \\ 0 \\ 1 \end{pmatrix} = -\boldsymbol{\sigma} \begin{pmatrix} 0 \\ 0 \\ -1 \end{pmatrix} = \begin{pmatrix} \sigma_{13} \\ \sigma_{23} \\ \sigma_{33} \end{pmatrix} = \frac{\sigma_0}{H} \begin{pmatrix} y \\ 2x \\ 0 \end{pmatrix}. \qquad (4.1.100)$$

Therefore, the stress tensor $\boldsymbol{\sigma}$ satisfies the specified surface loads. Hooke's law reads for the strains

$$\epsilon_{11} = \frac{1}{E} \left[\sigma_{11} - \nu(\sigma_{22} + \sigma_{33}) \right],$$

$$\epsilon_{22} = \frac{1}{E} \left[\sigma_{22} - \nu(\sigma_{11} + \sigma_{33}) \right],$$

$$\epsilon_{33} = \frac{1}{E} \left[\sigma_{33} - \nu(\sigma_{11} + \sigma_{22}) \right],$$

$$\epsilon_{12} = \frac{2(1+\nu)}{E} \sigma_{12}, \qquad\qquad (4.1.101)$$

$$\epsilon_{13} = \frac{2(1+\nu)}{E} \sigma_{13},$$

$$\epsilon_{23} = \frac{2(1+\nu)}{E} \sigma_{23},$$

which constitute a set of equations for the partial derivatives of the displacements. Employing the stresses above

$$\epsilon_{11} = \epsilon_{22} = \epsilon_{33} = \frac{\partial u_x}{\partial x} = \frac{\partial u_y}{\partial y} = \frac{\partial u_z}{\partial z} = 0,$$

$$\epsilon_{12} = \frac{\partial u_x}{\partial y} + \frac{\partial u_y}{\partial x} = \frac{2(1+\nu)}{E} \frac{\sigma_0}{H} z,$$

$$\epsilon_{13} = \frac{\partial u_x}{\partial z} + \frac{\partial u_z}{\partial x} = \frac{2(1+\nu)}{E} \frac{\sigma_0}{H} y,$$

$$\epsilon_{23} = \frac{\partial u_y}{\partial z} + \frac{\partial u_z}{\partial y} = \frac{2(1+\nu)}{E} \frac{\sigma_0}{H} 2x.$$

(4.1.102)

The displacements (u_x, u_y, u_z) will next be obtained from the strains.

$$\frac{\partial u_x}{\partial x} = \frac{\partial u_y}{\partial y} = \frac{\partial u_z}{\partial z} = 0 \tag{4.1.103}$$

yield

$$u_x = u_x(y, z),$$
$$u_y = u_y(x, z),$$
$$u_z = u_z(x, y),$$

(4.1.104)

thus reducing the number of independent variables. Because $u_x(y, z)$ does not depend on x and u_x is zero along the faces $x = 0$

$$u_x(y, z) = 0. \tag{4.1.105}$$

Then

$$\epsilon_{12} = \frac{\partial u_x}{\partial y} + \frac{\partial u_y}{\partial x} = \frac{\partial}{\partial x} u_y(x, z) = \frac{2(1+\nu)}{E} \frac{\sigma_0}{H} z,$$

$$\epsilon_{13} = \frac{\partial u_x}{\partial z} + \frac{\partial u_z}{\partial x} = \frac{\partial}{\partial x} u_z(x, y) = \frac{2(1+\nu)}{E} \frac{\sigma_0}{H} y.$$

(4.1.106)

Due to the fixities along the faces $x = 0$

$$u_y(x, z) = \frac{2(1+\nu)}{E} \frac{\sigma_0}{H} xz,$$

$$u_z(x, y) = \frac{2(1+\nu)}{E} \frac{\sigma_0}{H} xy,$$

(4.1.107)

and the above $u_y(x, z)$ and $u_z(x, y)$ also satisfy

$$\frac{\partial u_y}{\partial z} + \frac{\partial u_z}{\partial y} = \frac{2(1+\nu)}{E}\frac{\sigma_0}{H}x + \frac{2(1+\nu)}{E}\frac{\sigma_0}{H}x = \epsilon_{23}. \qquad (4.1.108)$$

The displacement vector (u_x, u_y, u_z) becomes

$$u_x = 0,$$
$$u_y(x,z) = xz\frac{2(1+\nu)}{E}\frac{\sigma_0}{H}, \qquad (4.1.109)$$
$$u_z(x,y) = xy\frac{2(1+\nu)}{E}\frac{\sigma_0}{H}.$$

4.2 Norton creep

Peter Vogel and Jobst Maßmann

This section presents a set of closed form solutions of shear problems on creeping plates. The associated simulation exercises have been checked by OGS; they may serve as verification tests. We focus on the closed form solutions; for the underlying theory see Jaeger and Cook (1971).

4.2.1 Due to instant surface loads a square of Norton material deforms into a lozenge

The domain is a rectangular plate discretized by $8 \times 8 \times 4$ equally sized hexahedral elements. Given size $2D = 2$ m and thickness $2H = 0.2$ m the vertices of the top face have the x-y-z-coordinates $(D, 0, H)$, $(0, D, H)$, $(-D, 0, H)$, and $(0, -D, H)$, respectively; the bottom face is located on the $z = -H$ level. The plate is represented by a Norton material. Young's modulus $E = 25,000$ MPa and Poisson's ratio $\nu = 0.25$ have been assigned, gravity is neglected via zero material density. Various additional parameters are involved in the rheological model; details are given below. Fixities have been prescribed in the interior of the domain with zero x-displacement along the plane $x = 0$, zero y-displacement along the plane $y = 0$, and zero z-displacement along the plane $z = 0$. Specified loads $P(x, y, z)$ prevail along the entire surface of the domain for times $t > 0$. With the aid of the stress $\sigma_0 = -20$ MPa these loads read along the lateral face $x > 0, y > 0$

$$P(x, D-x, z) = \sigma_0 \begin{pmatrix} 0 \\ 1 \\ 0 \end{pmatrix}, \qquad (4.2.1)$$

along the lateral face $x < 0$, $y > 0$

$$P(x, D + x, z) = \sigma_0 \begin{pmatrix} 0 \\ 1 \\ 0 \end{pmatrix}, \qquad (4.2.2)$$

along the lateral face $x < 0$, $y < 0$

$$P(x, -D - x, z) = -\sigma_0 \begin{pmatrix} 0 \\ 1 \\ 0 \end{pmatrix}, \qquad (4.2.3)$$

along the lateral face $x > 0$, $y < 0$

$$P(x, -D + x, z) = -\sigma_0 \begin{pmatrix} 0 \\ 1 \\ 0 \end{pmatrix}, \qquad (4.2.4)$$

and along the top face $z = H$ and the bottom face $z = -H$

$$P(x, y, H) = \begin{pmatrix} 0 \\ 0 \\ 0 \end{pmatrix}, \quad P(x, y, -H) = \begin{pmatrix} 0 \\ 0 \\ 0 \end{pmatrix}. \qquad (4.2.5)$$

Starting from an initial setup free of load the simulation evaluates stresses, strains, and displacements through time with output after 5 and 10 days.

Let $\boldsymbol{\sigma}$ denote the stress tensor, $\mathbf{I}$ the unit tensor,

$$\boldsymbol{\sigma}^D = \boldsymbol{\sigma} - \frac{\mathrm{tr}\boldsymbol{\sigma}}{3}\mathbf{I} \qquad (4.2.6)$$

the stress deviator, and

$$\sigma_{\mathrm{eff}} = \sqrt{\frac{3}{2} \sum_{i=1}^{3} \sum_{j=1}^{3} \sigma_{ij}^D \sigma_{ji}^D} \qquad (4.2.7)$$

the v. Mises or effective stress. The rheological model envolved yields the fundamental stress/strain relationships as a system of differential equations for the creep strains

$$\frac{\partial}{\partial t} \boldsymbol{\epsilon}^{cr} = \frac{3}{2} \frac{\boldsymbol{\sigma}^D}{\sigma_{\mathrm{eff}}} (N\sigma_{\mathrm{eff}}^n) \qquad (4.2.8)$$

and the total strains

$$\boldsymbol{\epsilon}^{tot} = \boldsymbol{\epsilon}^{el} + \boldsymbol{\epsilon}^{cr}, \qquad (4.2.9)$$

where $\boldsymbol{\epsilon}^{el}$ denotes the elastic strains via Hooke's law. Both equations have to be solved with respect to the imposed initial and boundary conditions. For the present examples the creep behaviour of the Norton material is specified

with the aid of the parameters

$$n = 5,$$
$$N = A \exp\left(-\frac{Q}{RT}\right),$$
(4.2.10)

where $R = 8.31441$ J/(mol·K) is the gas constant, T is the absolute temperature (we have $T = 273.15$ K by default), and experimental data obtained from rock salt yield

$$A = 0.18 \ 1/(\mathrm{d} \cdot \mathrm{MPa}^5),$$
$$Q = 54,000 \ \mathrm{J/mol}.$$
(4.2.11)

Note that day is required as unit of time and stresses have to be in MPa.

The stress tensor

$$\boldsymbol{\sigma} = \begin{pmatrix} \sigma_{11} & \sigma_{12} & \sigma_{13} \\ \sigma_{12} & \sigma_{22} & \sigma_{23} \\ \sigma_{13} & \sigma_{23} & \sigma_{33} \end{pmatrix} = \sqrt{2}\,\sigma_0 \begin{pmatrix} 0 & 0 & 0 \\ 0 & 1 & 0 \\ 0 & 0 & 0 \end{pmatrix}$$
(4.2.12)

satisfies the equation of mechanical equilibrium

$$\nabla \cdot \boldsymbol{\sigma} = 0$$
(4.2.13)

as well as the specified surface loads because along the lateral face $x > 0$, $y > 0$

$$\boldsymbol{\sigma}\sqrt{1/2}\begin{pmatrix} 1 \\ 1 \\ 0 \end{pmatrix} = \sqrt{1/2}\begin{pmatrix} \sigma_{11} + \sigma_{12} \\ \sigma_{12} + \sigma_{22} \\ \sigma_{13} + \sigma_{23} \end{pmatrix} = \sigma_0 \begin{pmatrix} 0 \\ 1 \\ 0 \end{pmatrix},$$
(4.2.14)

along the lateral face $x < 0$, $y > 0$

$$\boldsymbol{\sigma}\sqrt{1/2}\begin{pmatrix} -1 \\ 1 \\ 0 \end{pmatrix} = \sqrt{1/2}\begin{pmatrix} -\sigma_{11} + \sigma_{12} \\ -\sigma_{12} + \sigma_{22} \\ -\sigma_{13} + \sigma_{23} \end{pmatrix} = \sigma_0 \begin{pmatrix} 0 \\ 1 \\ 0 \end{pmatrix},$$
(4.2.15)

along the lateral face $x < 0$, $y < 0$

$$\boldsymbol{\sigma}\sqrt{1/2}\begin{pmatrix} -1 \\ -1 \\ 0 \end{pmatrix} = \sqrt{1/2}\begin{pmatrix} -\sigma_{11} - \sigma_{12} \\ -\sigma_{12} - \sigma_{22} \\ -\sigma_{13} - \sigma_{23} \end{pmatrix} = -\sigma_0 \begin{pmatrix} 0 \\ 1 \\ 0 \end{pmatrix},$$
(4.2.16)

along the lateral face $x > 0$, $y < 0$

$$\boldsymbol{\sigma}\sqrt{1/2}\begin{pmatrix} 1 \\ -1 \\ 0 \end{pmatrix} = \sqrt{1/2}\begin{pmatrix} \sigma_{11} - \sigma_{12} \\ \sigma_{12} - \sigma_{22} \\ \sigma_{13} - \sigma_{23} \end{pmatrix} = -\sigma_0 \begin{pmatrix} 0 \\ 1 \\ 0 \end{pmatrix},$$
(4.2.17)

along the top face $z = H$

$$\boldsymbol{\sigma} \begin{pmatrix} 0 \\ 0 \\ 1 \end{pmatrix} = \begin{pmatrix} \sigma_{13} \\ \sigma_{23} \\ \sigma_{33} \end{pmatrix} = \begin{pmatrix} 0 \\ 0 \\ 0 \end{pmatrix}, \tag{4.2.18}$$

and along the bottom face $z = -H$

$$\boldsymbol{\sigma} \begin{pmatrix} 0 \\ 0 \\ -1 \end{pmatrix} = \begin{pmatrix} -\sigma_{13} \\ -\sigma_{23} \\ -\sigma_{33} \end{pmatrix} = \begin{pmatrix} 0 \\ 0 \\ 0 \end{pmatrix}. \tag{4.2.19}$$

The stress tensor

$$\boldsymbol{\sigma} = \sqrt{2}\,\sigma_0 \begin{pmatrix} 0\,0\,0 \\ 0\,1\,0 \\ 0\,0\,0 \end{pmatrix} \tag{4.2.20}$$

yields the trace of $\boldsymbol{\sigma}$

$$\mathrm{tr}\boldsymbol{\sigma} = \sqrt{2}\,\sigma_0, \tag{4.2.21}$$

the stress deviator

$$\boldsymbol{\sigma}^D = \frac{\sqrt{2}}{3}\sigma_0 \begin{pmatrix} -1 & 0 & 0 \\ 0 & 2 & 0 \\ 0 & 0 & -1 \end{pmatrix}, \tag{4.2.22}$$

the v. Mises or effective stress

$$\sigma_{\mathrm{eff}} = \frac{\sqrt{2}}{3}|\sigma_0|\sqrt{3/2}\sqrt{1^2 + 2^2 + 1^2} = \sqrt{2}|\sigma_0|, \tag{4.2.23}$$

and the time derivative of the creep strains

$$\frac{\partial}{\partial t}\boldsymbol{\epsilon}^{cr} = \sqrt{2}^3 N\sigma_0^5 \begin{pmatrix} -1 & 0 & 0 \\ 0 & 2 & 0 \\ 0 & 0 & -1 \end{pmatrix}. \tag{4.2.24}$$

The entire domain is initially free of creep strains. Integrating with respect to time t the creep strains become

$$\boldsymbol{\epsilon}^{cr} = \sqrt{2}^3 N\sigma_0^5 \begin{pmatrix} -t & 0 & 0 \\ 0 & 2t & 0 \\ 0 & 0 & -t \end{pmatrix}. \tag{4.2.25}$$

The elastic strains are obtained from the stress $\boldsymbol{\sigma}$ via Hooke's law

$$\boldsymbol{\epsilon}^{el} = \sqrt{2}\frac{\sigma_0}{E} \begin{pmatrix} -\nu & 0 & 0 \\ 0 & 1 & 0 \\ 0 & 0 & -\nu \end{pmatrix}. \tag{4.2.26}$$

The total strains in terms of the displacements (u_x, u_y, u_z) read

$$\boldsymbol{\epsilon}^{tot} = \boldsymbol{\epsilon}^{el} + \boldsymbol{\epsilon}^{cr} = \begin{pmatrix} \partial u_x/\partial x & 0 & 0 \\ 0 & \partial u_y/\partial y & 0 \\ 0 & 0 & \partial u_z/\partial z \end{pmatrix}. \qquad (4.2.27)$$

The strains $\partial u_x/\partial x$, $\partial u_y/\partial y$, and $\partial u_z/\partial z$ are thus given by

$$\epsilon_{11}^{tot}(t) = \frac{\partial u_x}{\partial x} = -\sqrt{2}\frac{\nu\,\sigma_0}{E} - \sqrt{2}^3\,N\,\sigma_0^5\,t\,,$$

$$\epsilon_{22}^{tot}(t) = \frac{\partial u_y}{\partial y} = \sqrt{2}\frac{\sigma_0}{E} + 2\sqrt{2}^3\,N\,\sigma_0^5\,t\,, \qquad (4.2.28)$$

$$\epsilon_{33}^{tot}(t) = \frac{\partial u_z}{\partial z} = -\sqrt{2}\frac{\nu\,\sigma_0}{E} - \sqrt{2}^3\,N\,\sigma_0^5\,t\,.$$

Integrating the strains with respect to the fixities at the coordinate planes yields the displacement vector (u_x, u_y, u_z)

$$u_x(x,t) = x\left(-\sqrt{2}\frac{\nu\,\sigma_0}{E} - \sqrt{2}^3\,N\,\sigma_0^5\,t\right)\,,$$

$$u_y(y,t) = y\left(\sqrt{2}\frac{\sigma_0}{E} + 2\sqrt{2}^3\,N\,\sigma_0^5\,t\right)\,, \qquad (4.2.29)$$

$$u_z(z,t) = z\left(-\sqrt{2}\frac{\nu\,\sigma_0}{E} - \sqrt{2}^3\,N\,\sigma_0^5\,t\right)\,.$$

The deformed square takes the shape of a lozenge, the deformations increase with time.

4.2.2 Due to increasing surface loads a square of Norton material deforms into a lozenge

The setup of this exercise has been adopted from the previous example, however, the specified surface loads depend linearly on time. The domain is a rectangular plate discretized by $8 \times 8 \times 4$ equally sized hexahedral elements. Given size $2D = 2$ m and thickness $2H = 0.2$ m the vertices of the top face have the x-y-z-coordinates $(D, 0, H)$, $(0, D, H)$, $(-D, 0, H)$, and $(0, -D, H)$, respectively; the bottom face is located on the $z = -H$ level. The plate is represented by a Norton material. Young's modulus $E = 25,000$ MPa and Poisson's ratio $\nu = 0.25$ have been assigned, gravity is neglected via zero material density. The additional parameters involved in the rheological model are identical to those of the previous example. Fixities have been prescribed in the interior of the domain with zero x-displacement along the plane $x = 0$, zero y-displacement along the plane $y = 0$, and zero z-displacement along the plane $z = 0$. Specified loads $P(x, y, z, t)$ prevail along the entire surface of the domain for times $t > 0$. The stress $\sigma_0 \cdot t$ ($\sigma_0 = -80$ MPa/d) depends

linearly on time t; in terms of this stress the specified loads read along the lateral face $x > 0$, $y > 0$

$$P(x, D - x, z, t) = \sigma_0\, t \begin{pmatrix} 0 \\ 1 \\ 0 \end{pmatrix}, \tag{4.2.30}$$

along the lateral face $x < 0$, $y > 0$

$$P(x, D + x, z, t) = \sigma_0\, t \begin{pmatrix} 0 \\ 1 \\ 0 \end{pmatrix}, \tag{4.2.31}$$

along the lateral face $x < 0$, $y < 0$

$$P(x, -D - x, z, t) = -\sigma_0\, t \begin{pmatrix} 0 \\ 1 \\ 0 \end{pmatrix}, \tag{4.2.32}$$

along the lateral face $x > 0$, $y < 0$

$$P(x, -D + x, z, t) = -\sigma_0\, t \begin{pmatrix} 0 \\ 1 \\ 0 \end{pmatrix}, \tag{4.2.33}$$

and along the top face $z = H$ and the bottom face $z = -H$

$$P(x, y, H, t) = \begin{pmatrix} 0 \\ 0 \\ 0 \end{pmatrix}, \quad P(x, y, -H, t) = \begin{pmatrix} 0 \\ 0 \\ 0 \end{pmatrix}. \tag{4.2.34}$$

Starting from an initial setup free of load the simulation evaluates stresses, strains, and displacements through time with output after 0.7 and 1.0 days (Fig. 4.2.1).

The rheological model of the Norton material and its underlying theory have been sketched just before; we focus on the special features of the present example. The stress tensor

$$\boldsymbol{\sigma} = \begin{pmatrix} \sigma_{11} & \sigma_{12} & \sigma_{13} \\ \sigma_{12} & \sigma_{22} & \sigma_{23} \\ \sigma_{13} & \sigma_{23} & \sigma_{33} \end{pmatrix} = \sqrt{2}\,\sigma_0\, t \begin{pmatrix} 0 & 0 & 0 \\ 0 & 1 & 0 \\ 0 & 0 & 0 \end{pmatrix} \tag{4.2.35}$$

satisfies the equation of mechanical equilibrium

$$\nabla \cdot \boldsymbol{\sigma} = 0 \tag{4.2.36}$$

as well as the specified surface loads because along the lateral face $x > 0$, $y > 0$
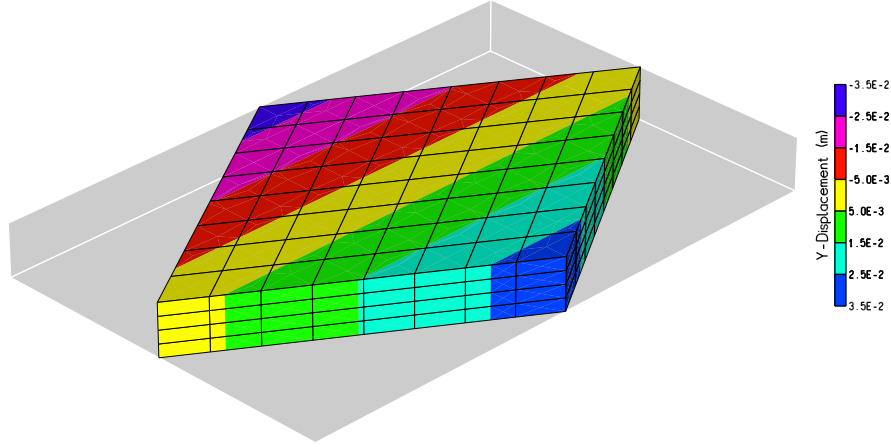
Fig. 4.2.1: Deformations scaled up, y-displacements after one day

$$\boldsymbol{\sigma}\sqrt{1/2}\begin{pmatrix}1\\1\\0\end{pmatrix}=\sqrt{1/2}\begin{pmatrix}\sigma_{11}+\sigma_{12}\\\sigma_{12}+\sigma_{22}\\\sigma_{13}+\sigma_{23}\end{pmatrix}=\sigma_0\,t\begin{pmatrix}0\\1\\0\end{pmatrix},\qquad(4.2.37)$$

along the lateral face $x<0$, $y>0$

$$\boldsymbol{\sigma}\sqrt{1/2}\begin{pmatrix}-1\\1\\0\end{pmatrix}=\sqrt{1/2}\begin{pmatrix}-\sigma_{11}+\sigma_{12}\\-\sigma_{12}+\sigma_{22}\\-\sigma_{13}+\sigma_{23}\end{pmatrix}=\sigma_0\,t\begin{pmatrix}0\\1\\0\end{pmatrix},\qquad(4.2.38)$$

along the lateral face $x<0$, $y<0$

$$\boldsymbol{\sigma}\sqrt{1/2}\begin{pmatrix}-1\\-1\\0\end{pmatrix}=\sqrt{1/2}\begin{pmatrix}-\sigma_{11}-\sigma_{12}\\-\sigma_{12}-\sigma_{22}\\-\sigma_{13}-\sigma_{23}\end{pmatrix}=-\sigma_0\,t\begin{pmatrix}0\\1\\0\end{pmatrix},\qquad(4.2.39)$$

along the lateral face $x>0$, $y<0$

$$\boldsymbol{\sigma}\sqrt{1/2}\begin{pmatrix}1\\-1\\0\end{pmatrix}=\sqrt{1/2}\begin{pmatrix}\sigma_{11}-\sigma_{12}\\\sigma_{12}-\sigma_{22}\\\sigma_{13}-\sigma_{23}\end{pmatrix}=-\sigma_0\,t\begin{pmatrix}0\\1\\0\end{pmatrix},\qquad(4.2.40)$$

along the top face $z=H$

$$\boldsymbol{\sigma}\begin{pmatrix}0\\0\\1\end{pmatrix}=\begin{pmatrix}\sigma_{13}\\\sigma_{23}\\\sigma_{33}\end{pmatrix}=\begin{pmatrix}0\\0\\0\end{pmatrix},\qquad(4.2.41)$$

and along the bottom face $z = -H$

$$\boldsymbol{\sigma} \begin{pmatrix} 0 \\ 0 \\ -1 \end{pmatrix} = \begin{pmatrix} -\sigma_{13} \\ -\sigma_{23} \\ -\sigma_{33} \end{pmatrix} = \begin{pmatrix} 0 \\ 0 \\ 0 \end{pmatrix}. \tag{4.2.42}$$

The stress tensor

$$\boldsymbol{\sigma} = \sqrt{2}\,\sigma_0\,t \begin{pmatrix} 0 & 0 & 0 \\ 0 & 1 & 0 \\ 0 & 0 & 0 \end{pmatrix} \tag{4.2.43}$$

yields the trace of $\boldsymbol{\sigma}$

$$\mathrm{tr}\boldsymbol{\sigma} = \sqrt{2}\,\sigma_0\,t, \tag{4.2.44}$$

the stress deviator

$$\boldsymbol{\sigma}^D = \frac{\sqrt{2}}{3}\sigma_0\,t \begin{pmatrix} -1 & 0 & 0 \\ 0 & 2 & 0 \\ 0 & 0 & -1 \end{pmatrix}, \tag{4.2.45}$$

the v. Mises or effective stress

$$\sigma_{\mathrm{eff}} = \sqrt{2}\,|\sigma_0|\,t, \tag{4.2.46}$$

and the time derivative of the creep strains

$$\frac{\partial}{\partial t}\boldsymbol{\epsilon}^{cr} = \sqrt{2}^3 N\sigma_0^5\,t^5 \begin{pmatrix} -1 & 0 & 0 \\ 0 & 2 & 0 \\ 0 & 0 & -1 \end{pmatrix}. \tag{4.2.47}$$

The entire domain is initially free of creep strains. Integrating with respect to time t the creep strains become

$$\boldsymbol{\epsilon}^{cr} = \frac{\sqrt{2}}{3} N\sigma_0^5\,t^6 \begin{pmatrix} -1 & 0 & 0 \\ 0 & 2 & 0 \\ 0 & 0 & -1 \end{pmatrix}. \tag{4.2.48}$$

The elastic strains are obtained from the stress $\boldsymbol{\sigma}$ via Hooke's law

$$\boldsymbol{\epsilon}^{el} = \sqrt{2}\frac{\sigma_0\,t}{E} \begin{pmatrix} -\nu & 0 & 0 \\ 0 & 1 & 0 \\ 0 & 0 & -\nu \end{pmatrix}. \tag{4.2.49}$$

The total strains in terms of the displacements (u_x, u_y, u_z) read

$$\boldsymbol{\epsilon}^{tot} = \boldsymbol{\epsilon}^{el} + \boldsymbol{\epsilon}^{cr} = \begin{pmatrix} \partial u_x/\partial x & 0 & 0 \\ 0 & \partial u_y/\partial y & 0 \\ 0 & 0 & \partial u_z/\partial z \end{pmatrix}. \tag{4.2.50}$$

The strains $\partial u_x/\partial x$, $\partial u_y/\partial y$, and $\partial u_z/\partial z$ are thus given by

$$\epsilon_{11}^{tot}(t) = \frac{\partial u_x}{\partial x} = -\sqrt{2}\frac{\nu\,\sigma_0}{E}t - \frac{\sqrt{2}}{3}\,N\,\sigma_0^5\,t^6,$$

$$\epsilon_{22}^{tot}(t) = \frac{\partial u_y}{\partial y} = \sqrt{2}\frac{\sigma_0}{E}t + 2\frac{\sqrt{2}}{3}\,N\,\sigma_0^5\,t^6, \qquad (4.2.51)$$

$$\epsilon_{33}^{tot}(t) = \frac{\partial u_z}{\partial z} = -\sqrt{2}\frac{\nu\,\sigma_0}{E}t - \frac{\sqrt{2}}{3}\,N\,\sigma_0^5\,t^6.$$

Integrating the strains with respect to the fixities at the coordinate planes yields the displacement vector (u_x, u_y, u_z)

$$u_x(x,t) = x\left(-\sqrt{2}\frac{\nu\,\sigma_0}{E}t - \frac{\sqrt{2}}{3}\,N\,\sigma_0^5\,t^6\right),$$

$$u_y(y,t) = y\left(\sqrt{2}\frac{\sigma_0}{E}t + 2\frac{\sqrt{2}}{3}\,N\,\sigma_0^5\,t^6\right), \qquad (4.2.52)$$

$$u_z(z,t) = z\left(-\sqrt{2}\frac{\nu\,\sigma_0}{E}t - \frac{\sqrt{2}}{3}\,N\,\sigma_0^5\,t^6\right).$$

The deformed square takes the shape of a lozenge, the deformations increase with time.

4.2.3 Due to instant surface loads a plate of Norton material undergoes simple shear

The domain is a rectangular plate located in the first octant with three faces on the coordinate planes. It is $H = 2$ m thick, has an extent of $L = 10$ m in x- and y-direction and is discretized by $8 \times 8 \times 2$ equally sized hexahedral elements. The plate is represented by a Norton material. Young's modulus $E = 25,000$ MPa and Poisson's ratio $\nu = 0.25$ have been assigned, gravity is neglected via zero material density. The additional parameters involved in the rheological model are identical to those of the previous examples. The face $x = 0$ is entirely fixed, specified loads $P(x, y, z)$ prevail along the remaining faces for times $t > 0$. With the aid of the stress $\sigma_0 = 50$ MPa these loads read along the face $x = L$

$$P(L, y, z) = \sigma_0 \begin{pmatrix} 0 \\ 0 \\ 1 \end{pmatrix}, \qquad (4.2.53)$$

along the faces $y = L$ and $y = 0$

$$P(x, L, z) = P(x, 0, z) = \begin{pmatrix} 0 \\ 0 \\ 0 \end{pmatrix}, \tag{4.2.54}$$

and along the faces $z = H$ and $z = 0$

$$P(x, y, H) = \sigma_0 \begin{pmatrix} 1 \\ 0 \\ 0 \end{pmatrix}, \quad P(x, y, 0) = -\sigma_0 \begin{pmatrix} 1 \\ 0 \\ 0 \end{pmatrix}. \tag{4.2.55}$$

Starting from an initial setup free of load the simulation evaluates stresses, strains, and displacements through time with output after 0.5 and 1.0 days.

The rheological model of the Norton material and its underlying theory have already been outlined before; we focus on the special features of the present example. The stress tensor

$$\boldsymbol{\sigma} = \begin{pmatrix} \sigma_{11} & \sigma_{12} & \sigma_{13} \\ \sigma_{12} & \sigma_{22} & \sigma_{23} \\ \sigma_{13} & \sigma_{23} & \sigma_{33} \end{pmatrix} = \sigma_0 \begin{pmatrix} 0 & 0 & 1 \\ 0 & 0 & 0 \\ 1 & 0 & 0 \end{pmatrix} \tag{4.2.56}$$

satisfies the equation of mechanical equilibrium

$$\nabla \cdot \boldsymbol{\sigma} = 0 \tag{4.2.57}$$

as well as the specified surface loads because along the face $x = L$

$$\boldsymbol{\sigma} \begin{pmatrix} 1 \\ 0 \\ 0 \end{pmatrix} = \begin{pmatrix} \sigma_{11} \\ \sigma_{12} \\ \sigma_{13} \end{pmatrix} = \sigma_0 \begin{pmatrix} 0 \\ 0 \\ 1 \end{pmatrix}, \tag{4.2.58}$$

along the faces $y = L$ and $y = 0$

$$\boldsymbol{\sigma} \begin{pmatrix} 0 \\ 1 \\ 0 \end{pmatrix} = -\boldsymbol{\sigma} \begin{pmatrix} 0 \\ -1 \\ 0 \end{pmatrix} = \begin{pmatrix} \sigma_{12} \\ \sigma_{22} \\ \sigma_{23} \end{pmatrix} = \begin{pmatrix} 0 \\ 0 \\ 0 \end{pmatrix}, \tag{4.2.59}$$

and along the faces $z = H$ and $z = 0$

$$\boldsymbol{\sigma} \begin{pmatrix} 0 \\ 0 \\ 1 \end{pmatrix} = -\boldsymbol{\sigma} \begin{pmatrix} 0 \\ 0 \\ -1 \end{pmatrix} = \begin{pmatrix} \sigma_{13} \\ \sigma_{23} \\ \sigma_{33} \end{pmatrix} = \sigma_0 \begin{pmatrix} 1 \\ 0 \\ 0 \end{pmatrix}. \tag{4.2.60}$$

The stress tensor

$$\boldsymbol{\sigma} = \sigma_0 \begin{pmatrix} 0 & 0 & 1 \\ 0 & 0 & 0 \\ 1 & 0 & 0 \end{pmatrix} \tag{4.2.61}$$

yields the trace of $\boldsymbol{\sigma}$

$$\mathrm{tr}\,\boldsymbol{\sigma} = 0, \tag{4.2.62}$$

the stress deviator

$$\boldsymbol{\sigma}^D = \sigma_0 \begin{pmatrix} 0\ 0\ 1 \\ 0\ 0\ 0 \\ 1\ 0\ 0 \end{pmatrix}, \tag{4.2.63}$$

the v. Mises or effective stress

$$\sigma_{\text{eff}} = \sqrt{3}\,\sigma_0, \tag{4.2.64}$$

and the time derivative of the creep strains

$$\frac{\partial}{\partial t}\boldsymbol{\epsilon}^{cr} = \frac{27}{2}N\sigma_0^5 \begin{pmatrix} 0\ 0\ 1 \\ 0\ 0\ 0 \\ 1\ 0\ 0 \end{pmatrix}. \tag{4.2.65}$$

The entire domain is initially free of creep strains. Integrating with respect to time t the creep strains become

$$\boldsymbol{\epsilon}^{cr} = \frac{27}{2}N\sigma_0^5\,t \begin{pmatrix} 0\ 0\ 1 \\ 0\ 0\ 0 \\ 1\ 0\ 0 \end{pmatrix}. \tag{4.2.66}$$

The elastic strains are obtained from the stress $\boldsymbol{\sigma}$ via Hooke's law

$$\boldsymbol{\epsilon}^{el} = 2(1+\nu)\frac{\sigma_0}{E} \begin{pmatrix} 0\ 0\ 1 \\ 0\ 0\ 0 \\ 1\ 0\ 0 \end{pmatrix}. \tag{4.2.67}$$

The total strains in terms of the displacements (u_x, u_y, u_z) read

$$\boldsymbol{\epsilon}^{tot} = \begin{pmatrix} \dfrac{\partial u_x}{\partial x} & \dfrac{\partial u_x}{\partial y}+\dfrac{\partial u_y}{\partial x} & \dfrac{\partial u_x}{\partial z}+\dfrac{\partial u_z}{\partial x} \\[2mm] \dfrac{\partial u_y}{\partial x}+\dfrac{\partial u_x}{\partial y} & \dfrac{\partial u_y}{\partial y} & \dfrac{\partial u_y}{\partial z}+\dfrac{\partial u_z}{\partial y} \\[2mm] \dfrac{\partial u_z}{\partial x}+\dfrac{\partial u_x}{\partial z} & \dfrac{\partial u_z}{\partial y}+\dfrac{\partial u_y}{\partial z} & \dfrac{\partial u_z}{\partial z} \end{pmatrix} \tag{4.2.68}$$

$$= \boldsymbol{\epsilon}^{el} + \boldsymbol{\epsilon}^{cr} = \left(2(1+\nu)\frac{\sigma_0}{E} + \frac{27}{2}N\sigma_0^5 t\right) \begin{pmatrix} 0\ 0\ 1 \\ 0\ 0\ 0 \\ 1\ 0\ 0 \end{pmatrix}.$$

The displacements (u_x, u_y, u_z) will next be obtained from the total strains.

$$\frac{\partial u_x}{\partial x} = \frac{\partial u_y}{\partial y} = \frac{\partial u_z}{\partial z} = 0 \tag{4.2.69}$$

yield

$$u_x = u_x(y, z, t) \,,$$
$$u_y = u_y(x, z, t) \,, \tag{4.2.70}$$
$$u_z = u_z(x, y, t) \,,$$

thus reducing the number of independent variables. Because $u_x(y, z, t)$ does not depend on x and the face $x = 0$ is entirely fixed

$$u_x(y, z, t) = 0 \,. \tag{4.2.71}$$

Then

$$\frac{\partial u_x}{\partial z} + \frac{\partial u_z}{\partial x} = \frac{\partial}{\partial x} u_z(x, y, t) = \frac{2(1 + \nu)}{E} \sigma_0 + \frac{27}{2} N \sigma_0^5 t \,, \tag{4.2.72}$$

and due to the fixities at the face $x = 0$

$$u_z(x, t) = x \left[2(1 + \nu) \frac{\sigma_0}{E} + \frac{27}{2} N \sigma_0^5 t \right] \,. \tag{4.2.73}$$

Because

$$\frac{\partial u_y}{\partial x} + \frac{\partial u_x}{\partial y} = \frac{\partial u_y}{\partial x} = 0,$$
$$\frac{\partial u_y}{\partial z} + \frac{\partial u_z}{\partial y} = \frac{\partial u_y}{\partial z} = 0, \tag{4.2.74}$$

the fixities at the face $x = 0$ yield

$$u_y(x, z, t) = 0. \tag{4.2.75}$$

The displacement vector (u_x, u_y, u_z) becomes

$$u_x = u_y = 0,$$
$$u_z(x, t) = x \left[2(1 + \nu) \frac{\sigma_0}{E} + \frac{27}{2} N \sigma_0^5 t \right] \,. \tag{4.2.76}$$

The plate undergoes shear in the x-z-plane, the deformations increase with time.

4.2.4 Due to increasing surface loads a plate of Norton material undergoes simple shear

The setup of this exercise has been adopted from the previous example, however, the specified surface loads depend linearly on time. The domain is a rectangular plate located in the first octant with three faces on the coordin-

ate planes. It is $H = 2\,\text{m}$ thick, has an extent of $L = 10\,\text{m}$ in x- and y-direction and is discretized by $8 \times 8 \times 2$ equally sized hexahedral elements. The plate is represented by a Norton material. Young's modulus $E = 25,000$ MPa and Poisson's ratio $\nu = 0.25$ have been assigned, gravity is neglected via zero material density. The additional parameters involved in the rheological model are identical to those of the previous examples. The face $x = 0$ is entirely fixed, specified loads $P(x, y, z, t)$ prevail along the remaining faces for times $t > 0$. The stress $\sigma_0 \cdot t$ ($\sigma_0 = 50$ MPa/d) depends linearly on time t; in terms of this stress the specified loads read along the face $x = L$

$$P(L, y, z, t) = \sigma_0 t \begin{pmatrix} 0 \\ 0 \\ 1 \end{pmatrix}, \tag{4.2.77}$$

along the faces $y = L$ and $y = 0$

$$P(x, L, z, t) = P(x, 0, z, t) = \begin{pmatrix} 0 \\ 0 \\ 0 \end{pmatrix}, \tag{4.2.78}$$

and along the faces $z = H$ and $z = 0$

$$P(x, y, H, t) = \sigma_0 t \begin{pmatrix} 1 \\ 0 \\ 0 \end{pmatrix}, \quad P(x, y, 0, t) = -\sigma_0 t \begin{pmatrix} 1 \\ 0 \\ 0 \end{pmatrix}. \tag{4.2.79}$$

Starting from an initial setup free of load the simulation evaluates stresses, strains, and displacements through time with output after 0.6 and 1.0 days (Fig. 4.2.2).

The rheological model of the Norton material and its underlying theory have already been outlined before; we focus on the special features of the present example. The stress tensor

$$\boldsymbol{\sigma} = \begin{pmatrix} \sigma_{11} & \sigma_{12} & \sigma_{13} \\ \sigma_{12} & \sigma_{22} & \sigma_{23} \\ \sigma_{13} & \sigma_{23} & \sigma_{33} \end{pmatrix} = \sigma_0 t \begin{pmatrix} 0 & 0 & 1 \\ 0 & 0 & 0 \\ 1 & 0 & 0 \end{pmatrix} \tag{4.2.80}$$

satisfies the equation of mechanical equilibrium

$$\nabla \cdot \boldsymbol{\sigma} = 0 \tag{4.2.81}$$

as well as the specified surface loads because along the face $x = L$

$$\boldsymbol{\sigma} \begin{pmatrix} 1 \\ 0 \\ 0 \end{pmatrix} = \begin{pmatrix} \sigma_{11} \\ \sigma_{12} \\ \sigma_{13} \end{pmatrix} = \sigma_0 t \begin{pmatrix} 0 \\ 0 \\ 1 \end{pmatrix}, \tag{4.2.82}$$
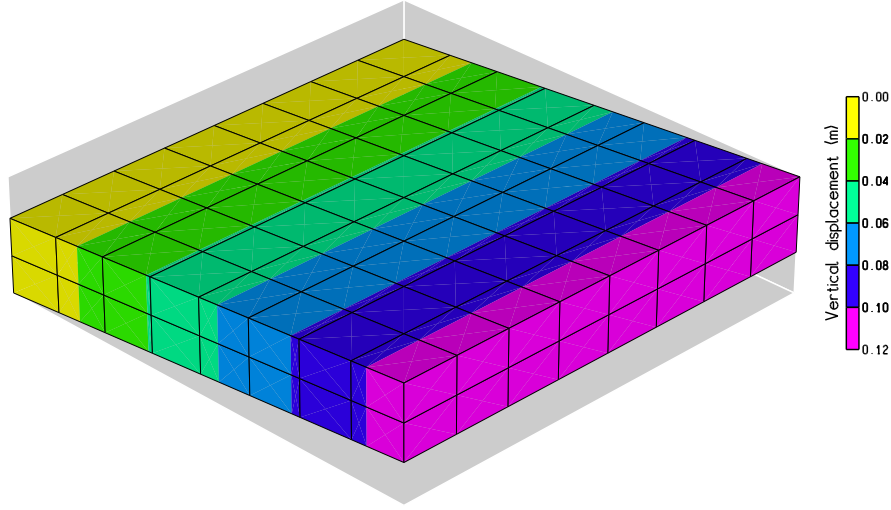
Fig. 4.2.2: Deformations scaled up, vertical displacements after one day

along the faces $y = L$ and $y = 0$

$$\boldsymbol{\sigma} \begin{pmatrix} 0 \\ 1 \\ 0 \end{pmatrix} = -\boldsymbol{\sigma} \begin{pmatrix} 0 \\ -1 \\ 0 \end{pmatrix} = \begin{pmatrix} \sigma_{12} \\ \sigma_{22} \\ \sigma_{23} \end{pmatrix} = \begin{pmatrix} 0 \\ 0 \\ 0 \end{pmatrix} , \qquad (4.2.83)$$

and along the faces $z = H$ and $z = 0$

$$\boldsymbol{\sigma} \begin{pmatrix} 0 \\ 0 \\ 1 \end{pmatrix} = -\boldsymbol{\sigma} \begin{pmatrix} 0 \\ 0 \\ -1 \end{pmatrix} = \begin{pmatrix} \sigma_{13} \\ \sigma_{23} \\ \sigma_{33} \end{pmatrix} = \sigma_0 t \begin{pmatrix} 1 \\ 0 \\ 0 \end{pmatrix} . \qquad (4.2.84)$$

The stress tensor

$$\boldsymbol{\sigma} = \sigma_0 t \begin{pmatrix} 0 & 0 & 1 \\ 0 & 0 & 0 \\ 1 & 0 & 0 \end{pmatrix} \qquad (4.2.85)$$

yields the trace of $\boldsymbol{\sigma}$

$$\mathrm{tr}\boldsymbol{\sigma} = 0 , \qquad (4.2.86)$$

the stress deviator

$$\boldsymbol{\sigma}^D = \sigma_0 t \begin{pmatrix} 0 & 0 & 1 \\ 0 & 0 & 0 \\ 1 & 0 & 0 \end{pmatrix} , \qquad (4.2.87)$$

the v. Mises or effective stress

$$\sigma_{\text{eff}} = \sqrt{3}\,\sigma_0 t\,, \tag{4.2.88}$$

and the time derivative of the creep strains

$$\frac{\partial}{\partial t}\boldsymbol{\epsilon}^{cr} = \frac{27}{2}N\sigma_0^5 t^5 \begin{pmatrix} 0 & 0 & 1 \\ 0 & 0 & 0 \\ 1 & 0 & 0 \end{pmatrix}. \tag{4.2.89}$$

The entire domain is initially free of creep strains. Integrating with respect to time t the creep strains become

$$\boldsymbol{\epsilon}^{cr} = \frac{9}{4}N\sigma_0^5 t^6 \begin{pmatrix} 0 & 0 & 1 \\ 0 & 0 & 0 \\ 1 & 0 & 0 \end{pmatrix}. \tag{4.2.90}$$

The elastic strains are obtained from the stress $\boldsymbol{\sigma}$ via Hooke's law

$$\boldsymbol{\epsilon}^{el} = 2(1+\nu)\frac{\sigma_0}{E}t \begin{pmatrix} 0 & 0 & 1 \\ 0 & 0 & 0 \\ 1 & 0 & 0 \end{pmatrix}. \tag{4.2.91}$$

The total strains in terms of the displacements (u_x, u_y, u_z) read

$$\boldsymbol{\epsilon}^{tot} = \begin{pmatrix} \dfrac{\partial u_x}{\partial x} & \dfrac{\partial u_x}{\partial y} + \dfrac{\partial u_y}{\partial x} & \dfrac{\partial u_x}{\partial z} + \dfrac{\partial u_z}{\partial x} \\[2.5ex] \dfrac{\partial u_y}{\partial x} + \dfrac{\partial u_x}{\partial y} & \dfrac{\partial u_y}{\partial y} & \dfrac{\partial u_y}{\partial z} + \dfrac{\partial u_z}{\partial y} \\[2.5ex] \dfrac{\partial u_z}{\partial x} + \dfrac{\partial u_x}{\partial z} & \dfrac{\partial u_z}{\partial y} + \dfrac{\partial u_y}{\partial z} & \dfrac{\partial u_z}{\partial z} \end{pmatrix} \tag{4.2.92}$$

$$= \boldsymbol{\epsilon}^{el} + \boldsymbol{\epsilon}^{cr} = \left(2(1+\nu)\frac{\sigma_0}{E}t + \frac{9}{4}N\sigma_0^5 t^6 \right) \begin{pmatrix} 0 & 0 & 1 \\ 0 & 0 & 0 \\ 1 & 0 & 0 \end{pmatrix}.$$

The displacements (u_x, u_y, u_z) will next be obtained from the total strains.

$$\frac{\partial u_x}{\partial x} = \frac{\partial u_y}{\partial y} = \frac{\partial u_z}{\partial z} = 0 \tag{4.2.93}$$

yield

$$\begin{aligned} u_x &= u_x(y, z, t)\,, \\ u_y &= u_y(x, z, t)\,, \\ u_z &= u_z(x, y, t)\,, \end{aligned} \tag{4.2.94}$$

thus reducing the number of independent variables. Because $u_x(y, z, t)$ does not depend on x and the face $x = 0$ is entirely fixed

$$u_x(y, z, t) = 0\,. \tag{4.2.95}$$

Then

$$\frac{\partial u_x}{\partial z} + \frac{\partial u_z}{\partial x} = \frac{\partial}{\partial x} u_z(x, y, t) = \frac{2(1+\nu)}{E}\sigma_0 t + \frac{9}{4}N\sigma_0^5 t^6\,, \tag{4.2.96}$$

and due to the fixities at the face $x = 0$

$$u_z(x, t) = x\left[2(1+\nu)\frac{\sigma_0}{E}t + \frac{9}{4}N\sigma_0^5 t^6\right]\,. \tag{4.2.97}$$

Because

$$\begin{aligned}
\frac{\partial u_y}{\partial x} + \frac{\partial u_x}{\partial y} &= \frac{\partial u_y}{\partial x} = 0\,, \\
\frac{\partial u_y}{\partial z} + \frac{\partial u_z}{\partial y} &= \frac{\partial u_y}{\partial z} = 0\,,
\end{aligned} \tag{4.2.98}$$

the fixities at the face $x = 0$ yield

$$u_y(x, z, t) = 0. \tag{4.2.99}$$

The displacement vector (u_x, u_y, u_z) becomes

$$\begin{aligned}
u_x &= u_y = 0, \\
u_z(x, t) &= x\left[2(1+\nu)\frac{\sigma_0}{E}t + \frac{9}{4}N\sigma_0^5 t^6\right]\,.
\end{aligned} \tag{4.2.100}$$

The plate undergoes shear in the x-z-plane, the deformations increase with time.

4.2.5 Due to instant surface loads a plate of Norton material undergoes shear in two planes

The domain is a rectangular plate located in the first octant with three faces on the coordinate planes. It is $H = 2$ m thick, has an extent of $L = 10$ m in x- and y-direction and is discretized by $8 \times 8 \times 2$ equally sized hexahedral elements. The plate is represented by a Norton material. Young's modulus $E = 25,000$ MPa and Poisson's ratio $\nu = 0.25$ have been assigned, gravity is neglected via zero material density. The additional parameters involved in the rheological model are identical to those of the previous examples. The face $x = 0$ is entirely fixed, specified loads $P(x, y, z)$ prevail along the remaining faces for times $t > 0$. With the aid of the stress $\sigma_0 = 40$ MPa these loads

read along the face $x = L$

$$P(L, y, z) = \sigma_0 \begin{pmatrix} 0 \\ 1 \\ 1 \end{pmatrix}, \qquad (4.2.101)$$

along the faces $y = L$ and $y = 0$

$$P(x, L, z) = \sigma_0 \begin{pmatrix} 1 \\ 0 \\ 0 \end{pmatrix}, \quad P(x, 0, z) = -\sigma_0 \begin{pmatrix} 1 \\ 0 \\ 0 \end{pmatrix}, \qquad (4.2.102)$$

and along the faces $z = H$ and $z = 0$

$$P(x, y, H) = \sigma_0 \begin{pmatrix} 1 \\ 0 \\ 0 \end{pmatrix}, \quad P(x, y, 0) = -\sigma_0 \begin{pmatrix} 1 \\ 0 \\ 0 \end{pmatrix}. \qquad (4.2.103)$$

Starting from an initial setup free of load the simulation evaluates stresses, strains, and displacements through time with output after 0.5 and 1.0 days.

The rheological model of the Norton material and its underlying theory have already been outlined before; we focus on the special features of the present example. The stress tensor

$$\boldsymbol{\sigma} = \begin{pmatrix} \sigma_{11} & \sigma_{12} & \sigma_{13} \\ \sigma_{12} & \sigma_{22} & \sigma_{23} \\ \sigma_{13} & \sigma_{23} & \sigma_{33} \end{pmatrix} = \sigma_0 \begin{pmatrix} 0 & 1 & 1 \\ 1 & 0 & 0 \\ 1 & 0 & 0 \end{pmatrix} \qquad (4.2.104)$$

satisfies the equation of mechanical equilibrium

$$\nabla \cdot \boldsymbol{\sigma} = 0 \qquad (4.2.105)$$

as well as the specified surface loads because along the face $x = L$

$$\boldsymbol{\sigma} \begin{pmatrix} 1 \\ 0 \\ 0 \end{pmatrix} = \begin{pmatrix} \sigma_{11} \\ \sigma_{12} \\ \sigma_{13} \end{pmatrix} = \sigma_0 \begin{pmatrix} 0 \\ 1 \\ 1 \end{pmatrix}, \qquad (4.2.106)$$

along the faces $y = L$ and $y = 0$

$$\boldsymbol{\sigma} \begin{pmatrix} 0 \\ 1 \\ 0 \end{pmatrix} = -\boldsymbol{\sigma} \begin{pmatrix} 0 \\ -1 \\ 0 \end{pmatrix} = \begin{pmatrix} \sigma_{12} \\ \sigma_{22} \\ \sigma_{23} \end{pmatrix} = \sigma_0 \begin{pmatrix} 1 \\ 0 \\ 0 \end{pmatrix}, \qquad (4.2.107)$$

and along the faces $z = H$ and $z = 0$

$$\boldsymbol{\sigma} \begin{pmatrix} 0 \\ 0 \\ 1 \end{pmatrix} = -\boldsymbol{\sigma} \begin{pmatrix} 0 \\ 0 \\ -1 \end{pmatrix} = \begin{pmatrix} \sigma_{13} \\ \sigma_{23} \\ \sigma_{33} \end{pmatrix} = \sigma_0 \begin{pmatrix} 1 \\ 0 \\ 0 \end{pmatrix}. \tag{4.2.108}$$

The stress tensor

$$\boldsymbol{\sigma} = \sigma_0 \begin{pmatrix} 0\;1\;1 \\ 1\;0\;0 \\ 1\;0\;0 \end{pmatrix} \tag{4.2.109}$$

yields the trace of $\boldsymbol{\sigma}$

$$\mathrm{tr}\boldsymbol{\sigma} = 0\,, \tag{4.2.110}$$

the stress deviator

$$\boldsymbol{\sigma}^D = \sigma_0 \begin{pmatrix} 0\;1\;1 \\ 1\;0\;0 \\ 1\;0\;0 \end{pmatrix}, \tag{4.2.111}$$

the v. Mises or effective stress

$$\sigma_{\mathrm{eff}} = \sqrt{6}\,\sigma_0, \tag{4.2.112}$$

and the time derivative of the creep strains

$$\frac{\partial}{\partial t}\boldsymbol{\epsilon}^{cr} = 54N\sigma_0^5 \begin{pmatrix} 0\;1\;1 \\ 1\;0\;0 \\ 1\;0\;0 \end{pmatrix}. \tag{4.2.113}$$

The entire domain is initially free of creep strains. Integrating with respect to time t the creep strains become

$$\boldsymbol{\epsilon}^{cr} = 54N\sigma_0^5\,t \begin{pmatrix} 0\;1\;1 \\ 1\;0\;0 \\ 1\;0\;0 \end{pmatrix}. \tag{4.2.114}$$

The elastic strains are obtained from the stress $\boldsymbol{\sigma}$ via Hooke's law

$$\boldsymbol{\epsilon}^{el} = 2(1+\nu)\frac{\sigma_0}{E} \begin{pmatrix} 0\;1\;1 \\ 1\;0\;0 \\ 1\;0\;0 \end{pmatrix}. \tag{4.2.115}$$

The total strains in terms of the displacements (u_x, u_y, u_z) read

$$\boldsymbol{\epsilon}^{tot} = \begin{pmatrix} \dfrac{\partial u_x}{\partial x} & \dfrac{\partial u_x}{\partial y} + \dfrac{\partial u_y}{\partial x} & \dfrac{\partial u_x}{\partial z} + \dfrac{\partial u_z}{\partial x} \\[2ex] \dfrac{\partial u_y}{\partial x} + \dfrac{\partial u_x}{\partial y} & \dfrac{\partial u_y}{\partial y} & \dfrac{\partial u_y}{\partial z} + \dfrac{\partial u_z}{\partial y} \\[2ex] \dfrac{\partial u_z}{\partial x} + \dfrac{\partial u_x}{\partial z} & \dfrac{\partial u_z}{\partial y} + \dfrac{\partial u_y}{\partial z} & \dfrac{\partial u_z}{\partial z} \end{pmatrix} \tag{4.2.116}$$

$$= \boldsymbol{\epsilon}^{el} + \boldsymbol{\epsilon}^{cr} = \left(2(1+\nu)\frac{\sigma_0}{E} + 54N\sigma_0^5 t\right) \begin{pmatrix} 0 \ 1 \ 1 \\ 1 \ 0 \ 0 \\ 1 \ 0 \ 0 \end{pmatrix}.$$

The displacements (u_x, u_y, u_z) will next be obtained from the total strains.

$$\frac{\partial u_x}{\partial x} = \frac{\partial u_y}{\partial y} = \frac{\partial u_z}{\partial z} = 0 \tag{4.2.117}$$

yield

$$\begin{aligned} u_x &= u_x(y, z, t)\,, \\ u_y &= u_y(x, z, t)\,, \\ u_z &= u_z(x, y, t)\,, \end{aligned} \tag{4.2.118}$$

thus reducing the number of independent variables. Because $u_x(y, z, t)$ does not depend on x and the face $x = 0$ is entirely fixed

$$u_x(y, z, t) = 0\,. \tag{4.2.119}$$

Then

$$\frac{\partial u_x}{\partial y} + \frac{\partial u_y}{\partial x} = \frac{\partial}{\partial x} u_y(x, z, t) = \frac{2(1+\nu)}{E}\sigma_0 + 54N\sigma_0^5 t\,, \tag{4.2.120}$$

and due to the fixities at the face $x = 0$

$$u_y(x, t) = x\left[2(1+\nu)\frac{\sigma_0}{E} + 54N\sigma_0^5 t\right]. \tag{4.2.121}$$

Because

$$\frac{\partial u_x}{\partial z} + \frac{\partial u_z}{\partial x} = \frac{\partial}{\partial x} u_z(x, y, t) = \frac{2(1+\nu)}{E}\sigma_0 + 54N\sigma_0^5 t\,, \tag{4.2.122}$$

the fixities at the face $x = 0$ yield

$$u_z(x, t) = x\left[2(1+\nu)\frac{\sigma_0}{E} + 54N\sigma_0^5 t\right]. \tag{4.2.123}$$

The displacement vector (u_x, u_y, u_z) becomes

$$\begin{aligned} u_x &= 0, \\ u_y(x, t) &= x\left[2(1+\nu)\frac{\sigma_0}{E} + 54N\sigma_0^5 t\right], \\ u_z(x, t) &= x\left[2(1+\nu)\frac{\sigma_0}{E} + 54N\sigma_0^5 t\right]. \end{aligned} \tag{4.2.124}$$

The plate undergoes shear in the x-y-plane and in the x-z-plane, the deformations increase with time.

4.2.6 Due to increasing surface loads a plate of Norton material undergoes shear in two planes

The setup of this exercise has been adopted from the previous example, however, the specified surface loads depend linearly on time. The domain is a rectangular plate located in the first octant with three faces on the coordinate planes. It is $H = 2$ m thick, has an extent of $L = 10$ m in x- and y-direction and is discretized by $8 \times 8 \times 2$ equally sized hexahedral elements. The plate is represented by a Norton material. Young's modulus $E = 25,000$ MPa and Poisson's ratio $\nu = 0.25$ have been assigned, gravity is neglected via zero material density. The additional parameters involved in the rheological model are identical to those of the previous examples. The face $x = 0$ is entirely fixed, specified loads $P(x, y, z, t)$ prevail along the remaining faces for times $t > 0$. The stress $\sigma_0 \cdot t$ ($\sigma_0 = 40$ MPa/d) depends linearly on time t; in terms of this stress the specified loads read along the face $x = L$

$$P(L, y, z, t) = \sigma_0 t \begin{pmatrix} 0 \\ 1 \\ 1 \end{pmatrix}, \tag{4.2.125}$$

along the faces $y = L$ and $y = 0$

$$P(x, L, z, t) = \sigma_0 t \begin{pmatrix} 1 \\ 0 \\ 0 \end{pmatrix}, \quad P(x, 0, z, t) = -\sigma_0 t \begin{pmatrix} 1 \\ 0 \\ 0 \end{pmatrix}, \tag{4.2.126}$$

and along the faces $z = H$ and $z = 0$

$$P(x, y, H, t) = \sigma_0 t \begin{pmatrix} 1 \\ 0 \\ 0 \end{pmatrix}, \quad P(x, y, 0, t) = -\sigma_0 t \begin{pmatrix} 1 \\ 0 \\ 0 \end{pmatrix}. \tag{4.2.127}$$

Starting from an initial setup free of load the simulation evaluates stresses, strains, and displacements through time with output after 0.5 and 1.0 days (Fig. 4.2.3).

The rheological model of the Norton material and its underlying theory have already been outlined before; we focus on the special features of the present example. The stress tensor

$$\boldsymbol{\sigma} = \begin{pmatrix} \sigma_{11} & \sigma_{12} & \sigma_{13} \\ \sigma_{12} & \sigma_{22} & \sigma_{23} \\ \sigma_{13} & \sigma_{23} & \sigma_{33} \end{pmatrix} = \sigma_0 t \begin{pmatrix} 0 & 1 & 1 \\ 1 & 0 & 0 \\ 1 & 0 & 0 \end{pmatrix} \tag{4.2.128}$$

satisfies the equation of mechanical equilibrium
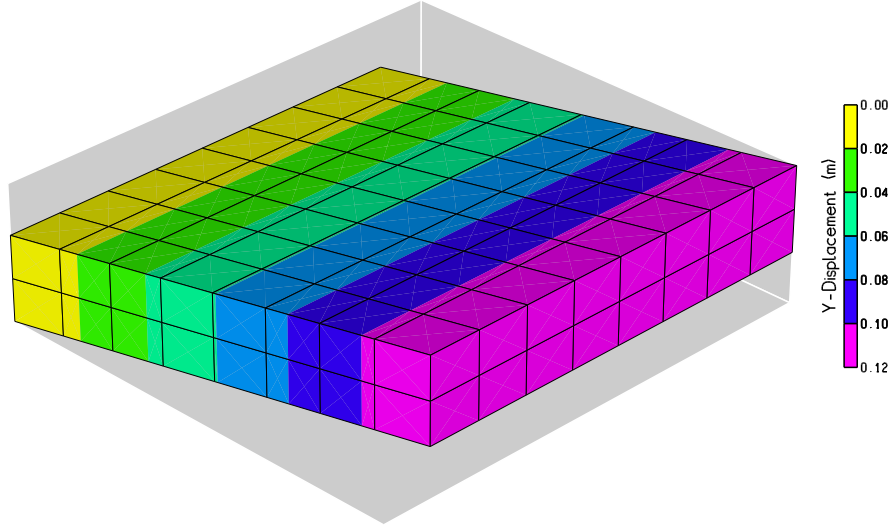
$$\nabla \cdot \boldsymbol{\sigma} = 0 \tag{4.2.129}$$

Fig. 4.2.3: Deformations scaled up, y-displacements after one day

as well as the specified surface loads because along the face $x = L$

$$\sigma \begin{pmatrix} 1 \\ 0 \\ 0 \end{pmatrix} = \begin{pmatrix} \sigma_{11} \\ \sigma_{12} \\ \sigma_{13} \end{pmatrix} = \sigma_0 t \begin{pmatrix} 0 \\ 1 \\ 1 \end{pmatrix}, \qquad (4.2.130)$$

along the faces $y = L$ and $y = 0$

$$\sigma \begin{pmatrix} 0 \\ 1 \\ 0 \end{pmatrix} = -\sigma \begin{pmatrix} 0 \\ -1 \\ 0 \end{pmatrix} = \begin{pmatrix} \sigma_{12} \\ \sigma_{22} \\ \sigma_{23} \end{pmatrix} = \sigma_0 t \begin{pmatrix} 1 \\ 0 \\ 0 \end{pmatrix}, \qquad (4.2.131)$$

and along the faces $z = H$ and $z = 0$

$$\sigma \begin{pmatrix} 0 \\ 0 \\ 1 \end{pmatrix} = -\sigma \begin{pmatrix} 0 \\ 0 \\ -1 \end{pmatrix} = \begin{pmatrix} \sigma_{13} \\ \sigma_{23} \\ \sigma_{33} \end{pmatrix} = \sigma_0 t \begin{pmatrix} 1 \\ 0 \\ 0 \end{pmatrix}. \qquad (4.2.132)$$

The stress tensor

$$\sigma = \sigma_0 t \begin{pmatrix} 0 & 1 & 1 \\ 1 & 0 & 0 \\ 1 & 0 & 0 \end{pmatrix} \qquad (4.2.133)$$

yields the trace of σ

$$\mathrm{tr}\,\sigma = 0, \qquad (4.2.134)$$

the stress deviator

$$\boldsymbol{\sigma}^D = \sigma_0 t \begin{pmatrix} 0 & 1 & 1 \\ 1 & 0 & 0 \\ 1 & 0 & 0 \end{pmatrix}, \tag{4.2.135}$$

the v. Mises or effective stress

$$\sigma_{\text{eff}} = \sqrt{6}\,\sigma_0 t\,, \tag{4.2.136}$$

and the time derivative of the creep strains

$$\frac{\partial}{\partial t}\boldsymbol{\epsilon}^{cr} = 54N\sigma_0^5 t^5 \begin{pmatrix} 0 & 1 & 1 \\ 1 & 0 & 0 \\ 1 & 0 & 0 \end{pmatrix}. \tag{4.2.137}$$

The entire domain is initially free of creep strains. Integrating with respect to time t the creep strains become

$$\boldsymbol{\epsilon}^{cr} = 9N\sigma_0^5 t^6 \begin{pmatrix} 0 & 1 & 1 \\ 1 & 0 & 0 \\ 1 & 0 & 0 \end{pmatrix}. \tag{4.2.138}$$

The elastic strains are obtained from the stress $\boldsymbol{\sigma}$ via Hooke's law

$$\boldsymbol{\epsilon}^{el} = 2(1+\nu)\frac{\sigma_0}{E}t \begin{pmatrix} 0 & 1 & 1 \\ 1 & 0 & 0 \\ 1 & 0 & 0 \end{pmatrix}. \tag{4.2.139}$$

The total strains in terms of the displacements (u_x, u_y, u_z) read

$$\boldsymbol{\epsilon}^{tot} = \begin{pmatrix} \dfrac{\partial u_x}{\partial x} & \dfrac{\partial u_x}{\partial y} + \dfrac{\partial u_y}{\partial x} & \dfrac{\partial u_x}{\partial z} + \dfrac{\partial u_z}{\partial x} \\[2mm] \dfrac{\partial u_y}{\partial x} + \dfrac{\partial u_x}{\partial y} & \dfrac{\partial u_y}{\partial y} & \dfrac{\partial u_y}{\partial z} + \dfrac{\partial u_z}{\partial y} \\[2mm] \dfrac{\partial u_z}{\partial x} + \dfrac{\partial u_x}{\partial z} & \dfrac{\partial u_z}{\partial y} + \dfrac{\partial u_y}{\partial z} & \dfrac{\partial u_z}{\partial z} \end{pmatrix} \tag{4.2.140}$$

$$= \boldsymbol{\epsilon}^{el} + \boldsymbol{\epsilon}^{cr} = \left(2(1+\nu)\frac{\sigma_0}{E}t + 9N\sigma_0^5 t^6\right) \begin{pmatrix} 0 & 1 & 1 \\ 1 & 0 & 0 \\ 1 & 0 & 0 \end{pmatrix}.$$

The displacements (u_x, u_y, u_z) will next be obtained from the total strains.

$$\frac{\partial u_x}{\partial x} = \frac{\partial u_y}{\partial y} = \frac{\partial u_z}{\partial z} = 0 \tag{4.2.141}$$

yield

$$u_x = u_x(y, z, t) \,,$$
$$u_y = u_y(x, z, t) \,, \qquad (4.2.142)$$
$$u_z = u_z(x, y, t) \,,$$

thus reducing the number of independent variables. Because $u_x(y, z, t)$ does not depend on x and the face $x = 0$ is entirely fixed

$$u_x(y, z, t) = 0 \,. \qquad (4.2.143)$$

Then

$$\frac{\partial u_x}{\partial y} + \frac{\partial u_y}{\partial x} = \frac{\partial}{\partial x} u_y(x, z, t) = \frac{2(1 + \nu)}{E} \sigma_0 t + 9N\sigma_0^5 t^6, \qquad (4.2.144)$$

and due to the fixities at the face $x = 0$

$$u_y(x, t) = x \left[2(1 + \nu)\frac{\sigma_0}{E} t + 9N\sigma_0^5 t^6 \right] \,. \qquad (4.2.145)$$

Because

$$\frac{\partial u_x}{\partial z} + \frac{\partial u_z}{\partial x} = \frac{\partial}{\partial x} u_z(x, y, t) = \frac{2(1 + \nu)}{E} \sigma_0 t + 9N\sigma_0^5 t^6, \qquad (4.2.146)$$

the fixities at the face $x = 0$ yield

$$u_z(x, t) = x \left[2(1 + \nu)\frac{\sigma_0}{E} t + 9N\sigma_0^5 t^6 \right] \,. \qquad (4.2.147)$$

The displacement vector (u_x, u_y, u_z) becomes

$$u_x = 0,$$
$$u_y(x, t) = x \left[2(1 + \nu)\frac{\sigma_0}{E} t + 9N\sigma_0^5 t^6 \right] \,, \qquad (4.2.148)$$
$$u_z(x, t) = x \left[2(1 + \nu)\frac{\sigma_0}{E} t + 9N\sigma_0^5 t^6 \right] \,.$$

The plate undergoes shear in the x-y-plane and in the x-z-plane, the deformations increase with time.

4.3 Thick walled pipe

Norbert Böttcher and Thomas Nagel

4.3.1 Definition

This problem considers a thick walled pipe exposed to internal and external pressure. The test is equivalent to the description in benchmark book volume II Kolditz et al. (2015), except that the current example considers a three dimensional domain. The aim of this study in the first place is to verify the implementation of a traction boundary condition for arbitrarily oriented surfaces in 3D space. The pipe in this example represents a standard hydraulic tube made of steel certified as EN 10305-4 (DIN 2445/2). It is made of E235+N steel with an elastic modulus of E = 210 GPa. Due to symmetry, the model grid is reduced to a quarter of the cross section of the pipe. Inner and outer diameter are 2 mm and 4 mm, respectively. The maximum internal pressure for this kind of pipe is indicated to be 52.2 MPa.

4.3.2 Solution

To evaluate the internal stresses of the pipe at full load pressure, the pressure at the outer boundary is set to atmospheric level (≈ 0.1 MPa). The vertical and horizontal sides are fixed in both x and y directions. Since the model considers a pipe of virtually infinite length, the plain strain assumption can be made. Thus, the displacements along the z direction are constrained. Fig. 4.3.1a shows the model geometry and all applied boundary conditions. The finite element grid has been created using the preprocessing software Gina (Kunz, 2012) and Gmsh (Geuzaine and Remacle, 2009): Starting from a two dimensional geometry of the cross section, a 2D mesh consisting of triangular elements has been made using Gmsh. This planar grid was then extruded along the z axis by 0.5 mm using Gina. The final mesh consists of 5430 prism elements, see Fig. 4.3.1b.

4.3.3 Results

Figures 4.3.2a and 4.3.2b show the first and the third principal stresses in the pipe wall. The third principal stress corresponds to the normal stress in radial direction. At the inside and outside walls, the normal stress is approaching the applied boundary conditions. The maximum principal stress of about

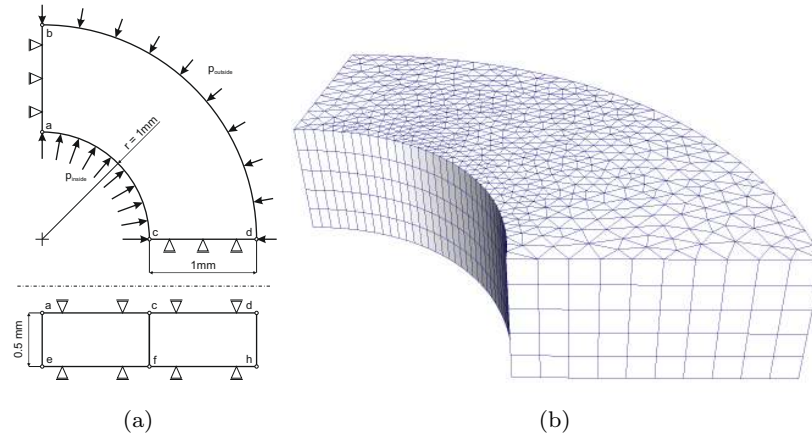(a)   (b)

Fig. 4.3.1: Geometry and boundary conditions for the pipe benchmark (a) and FE-Grid for the thick walled pipe problem (b).

85 MPa occurs in circumferential direction at the inner tube wall. This value corresponds roughly to 30 % of the yield stress of the pipe material.

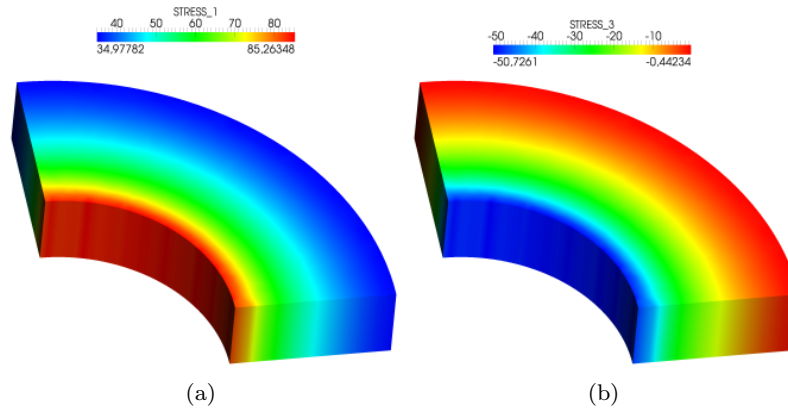(a)   (b)

Fig. 4.3.2: First principal stress along the tube wall (a) and third principal stress along the tube wall (b).

4.4 Cylinder stress test

Norbert Böttcher and Thomas Nagel

4.4.1 Definition

Parameters for visco-elastoplastic constitutive material models are often obtained by performing laboratory triaxial tests on small material samples. This benchmark is based on creep tests performed on a cylindrical salt sample with a height of $h = 25\,\mathrm{cm}$ and a radius of $r = 5\,\mathrm{cm}$, as denoted by *BGR-4131* found in Pudewills (2007). Due to total friction between the mounting and the sample at the top and the bottom faces of the cylinder, the displacement in radial direction at these locations was constrained. The stress test has been driven by displacement in axial direction using a constant strain rate of $\dot{\epsilon} = 1.0 \cdot 10^{-5}\,\mathrm{s}^{-1}$, and a cell pressure of $p = 1\,\mathrm{MPa}$ was applied. The maximum compression at the upper surface is $8.4\,\%$, so the test duration is $8400\,\mathrm{s}$. Because of its radial symmetry, the domain has been reduced to two dimensions in cylinder coordinates. For the simulation of this experiment, the Lubby2 material model (Heusermann et al., 1983, 2003) has been utilized. Table 4.4.1 shows the parameters used to define the material behaviour.

Table 4.4.1: Parameters for the Lubby2 material model

G_M	MPa	$8.0{\cdot}10^3$
K_M	MPa	$2.16{\cdot}10^4$
η_M0	MPa d	$4.03{\cdot}10^7$
m_1	MPa^{-1}	-0.327
G_K0	MPa	$6.27{\cdot}10^4$
m_G	MPa^{-1}	-0.254
η_K0	MPa d	$8.37{\cdot}10^4$
m_2	MPa^{-1}	-0.285

4.4.2 Results

Results in terms of effective stress and effective creep strain (Fig. 4.4.1) are compared to similar simulations described in Pudewills (2007). In these examples, a different visco-elastic material model has been utilized, so the results are not identical. However, the comparison shows qualitatively analogous effective stresses and and creep strains in both simulations.
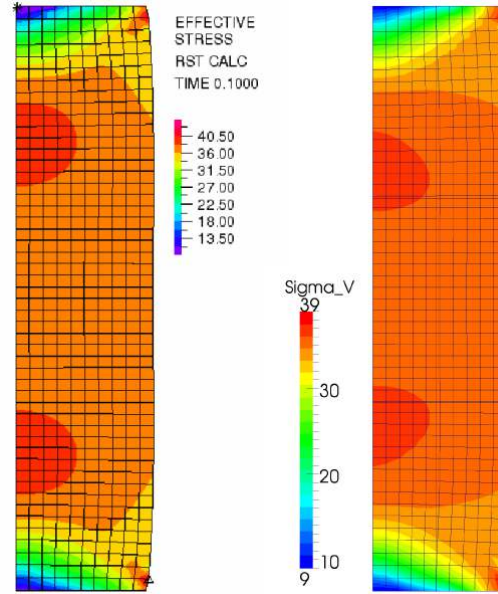
(a)
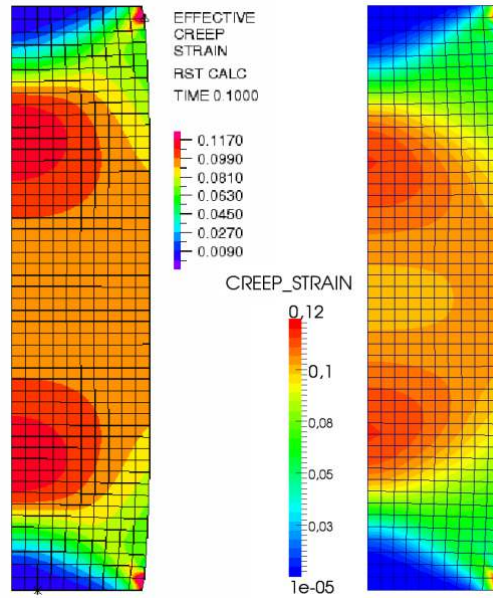
(b)

Fig. 4.4.1: Comparison of effective stress (a) and creep strain (b). Left: Results found in Pudewills (2007), right: this study. Differences in the results are primarily consequences of different material models.

4.5 Sondershausen Drift

Norbert Böttcher and Thomas Nagel
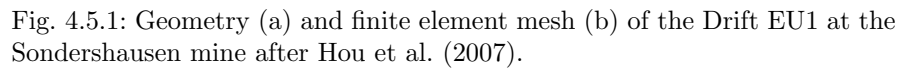

(a)   (b)

Fig. 4.5.1: Geometry (a) and finite element mesh (b) of the Drift EU1 at the Sondershausen mine after Hou et al. (2007).

4.5.1 Definition

For the prediction of long-term behaviour of rock salt, a study performed by Hou et al. (2007) examined a horizontal drift in the Sondershausen mine, drilled in the 1960's. The drift is located in a depth of 720 m in the lower part of the Staßfurt rock salt formation. This benchmark test simulates the long term mechanical behaviour of the rock salt formation over a period of 35 years.

4.5.2 Solution

The original model domain from Hou et al. (2007) is a quadratic cross section with a size of 200 m by 200 m with the drift in its centre. For bench-

marking purposes, the domain has been reduced to a size of 30 m by 30 m, see Fig. 1(a). The finite element mesh shown in Fig. 1(b) was created using the preprocessing software Gina (Kunz, 2012) and Gmsh (Geuzaine and Remacle, 2009). A coarse mesh consisting of only 358 elements has been chosen to guarantee a fast computation with regards to the benchmarking process. The drift is long enough to justify the plain strain approach. The overburden pressure is applied at the upper boundary of the domain by a given stress of $\sigma_{zz} = 18.065$ MPa. The left boundary serves as reflection symmetry axis. Left, bottom and right boundary displacements are restrained. The initial stress condition was $\sigma_1 = \sigma_2 = \sigma_3 = 0$ MPa. The inner and outer boundaries as well as the bottom of the domain are fixed, so that $u_{x(x=0\,\mathrm{m})} = u_{x(x=15\,\mathrm{m})} = u_{z(z=0\,\mathrm{m})} = 0$.

The overburden stress is applied as ramp function over the first ten loading steps, where each time step has a duration of $\Delta t = 0.1$ d. After the overburden pressure is fully applied, the remaining time step lengths are increasing linearly, starting from $\Delta t = 1$ d to $\Delta t = 160$ d, with an increment of one day. The final simulation time ends at 12881 days (about 35 years) after 170 time steps. The Lubby2 material model (Heusermann et al., 1983, 2003) is used for the description of the salt behaviour, material parameters are given in Table 4.4.1. The density of the rock salt is $\rho = 2200\,\mathrm{kg} \cdot \mathrm{m}^{-3}$.

4.5.3 Results

Fig. 4.5.2 shows the *von Mises* equivalent stress of the domain after 10 d, 100 d, 1000 d, and 10000 d. The equivalent stress is computed by

$$\sigma_{\mathrm{V}} = \sqrt{\frac{3}{2}\boldsymbol{\sigma}^{\mathrm{D}} : \boldsymbol{\sigma}^{\mathrm{D}}} \qquad (4.5.1)$$

Equivalent stress versus equivalent strain is shown in Fig. 4.5.3 at for 4 points a, b, c, and d. The locations of these points can be found in Fig. 1(a). First and third principal stresses along a horizontal line starting in point b are plotted in Fig. 4.5.4 and Fig. 4.5.5.
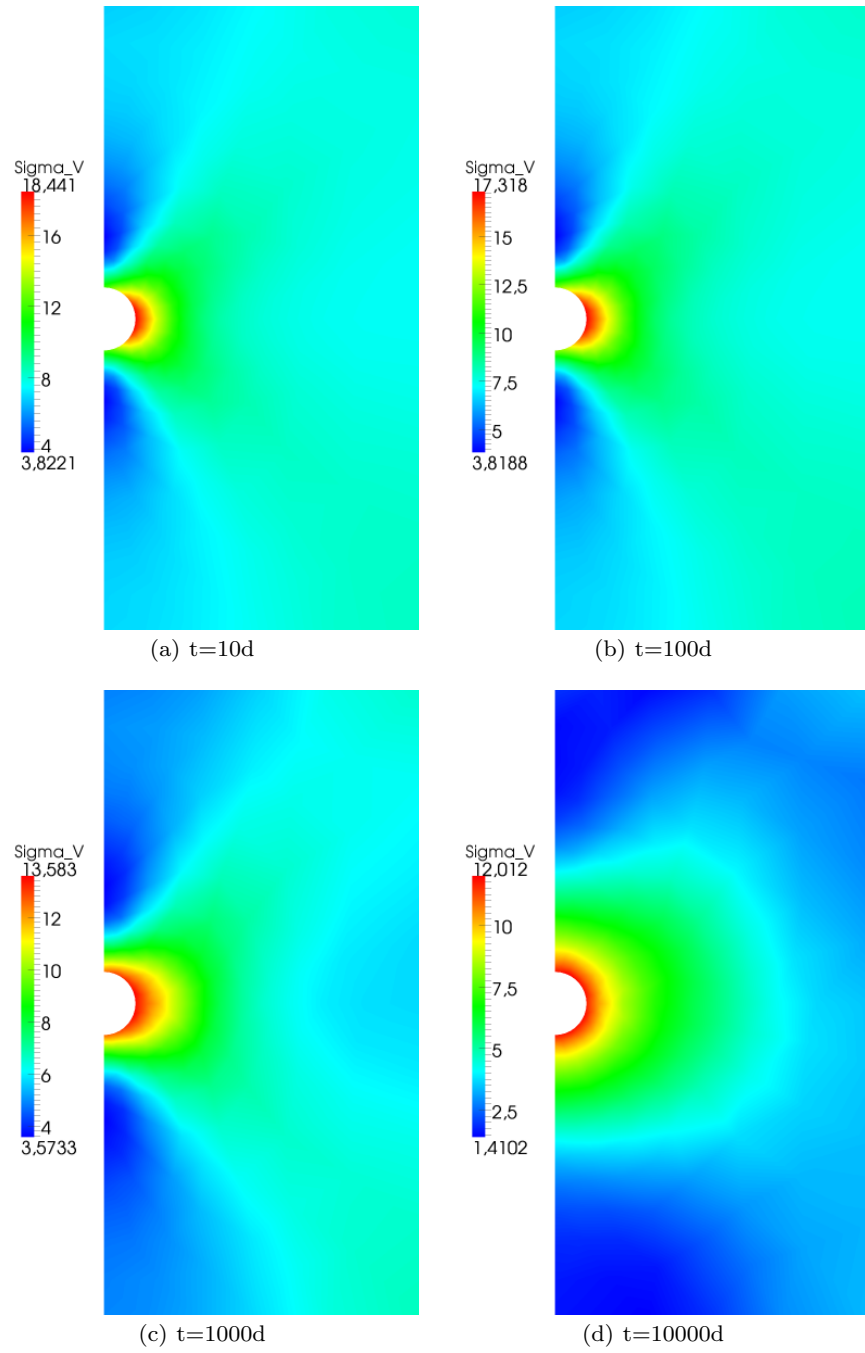
(a) t=10d

(b) t=100d

(c) t=1000d

(d) t=10000d

Fig. 4.5.2: von Mises equivalent stress after t=10 d (a), t=100 d (b), t=1000 d(≈ 2.7 a) (c), and t=10000 d(≈ 27 a) (d).
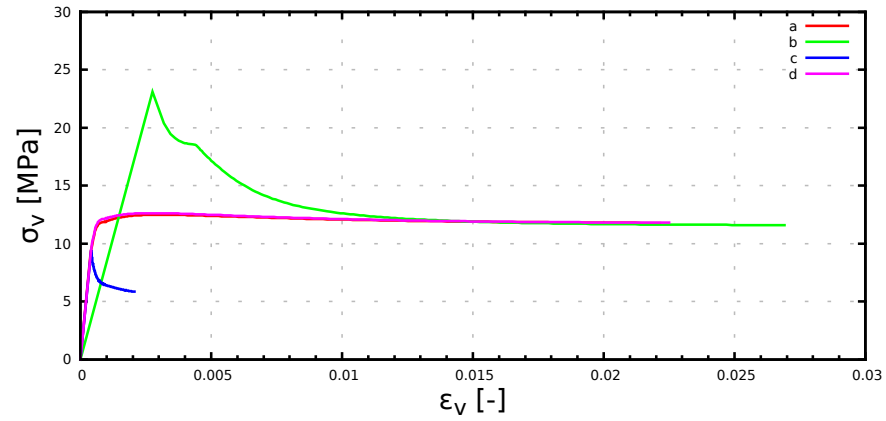
Fig. 4.5.3: Equivalent stress versus equivalent strain at points a, b, c, and d.
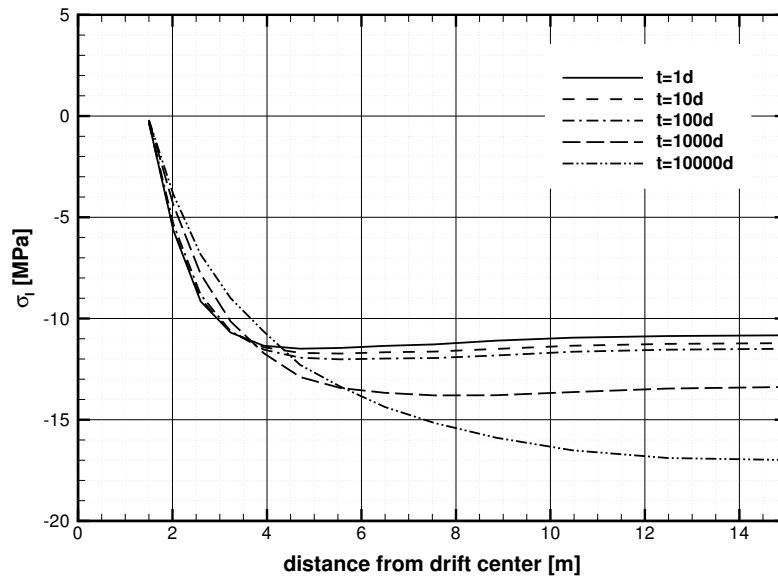

Fig. 4.5.4: First principal stress along horizontal line starting at point b for different points in time.
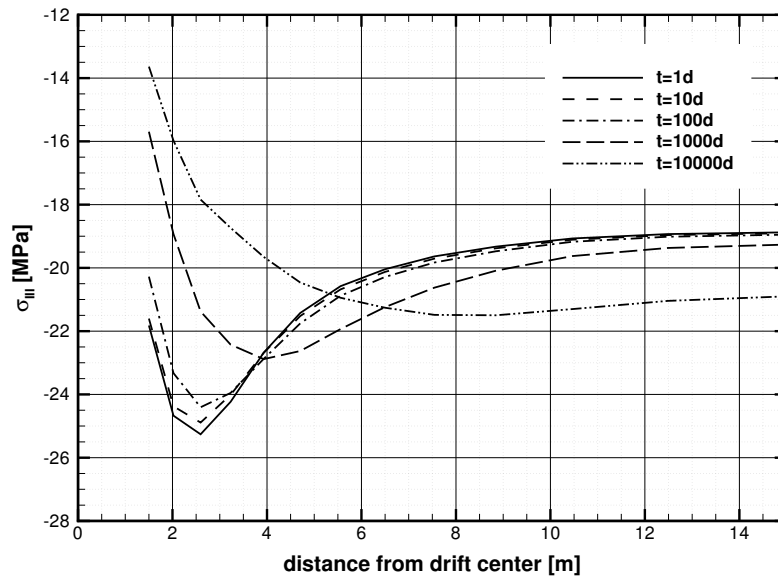
Fig. 4.5.5: Third principal stress along horizontal line starting at point b for different points in time.

4.6 Lubby2 and Minkley models under simple shear loading
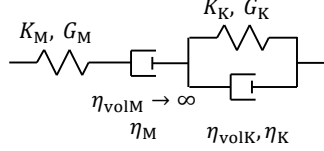
Norbert Böttcher and Thomas Nagel

Fig. 4.6.1: Generalised linear Burgers model.

The Burgers model comprises a Maxwell-element in series with a Kelvin element (Fig. 4.6.1). Following a stress jump the analytical solution for the shear strain developing in such a model reads:

$$\epsilon_{xy}(t) = \frac{1}{2}\gamma_{xy}(t) = \frac{1}{2}\left[\left(\frac{1}{G_M} + \frac{1}{\eta_M}t\right)\sigma_{xy} + \frac{1}{G_K}\left(1 - e^{-\frac{G_K}{\eta_K}t}\right)\sigma_{xy}\right] \quad (4.6.1)$$

Note, that in the Lubby2 formulation the viscosities and the Kelvin shear modulus are functions of the current stress state

$$\eta_M = \eta_{M0}e^{m_1\sigma_{eff}} \qquad (4.6.2)$$

$$\eta_K = \eta_{K0}e^{m_2\sigma_{eff}} \qquad (4.6.3)$$

$$G_K = G_{K0}e^{m_G\sigma_{eff}} \qquad (4.6.4)$$

where

$$\sigma_{eff} = \sqrt{3\sigma_{xy}^2} \qquad (4.6.5)$$

The parameters in table 4.4.1 are used. A shear stress of $\sigma_{xy} = 5\,\text{MPa}$ is numerically imposed in $0.01\,\text{d}$ and held for $15\,\text{d}$. Analytical and numerical solution fit well (Fig. 4.6.2a).

In the Minkley formulation, only the Maxwell viscosity is stress-dependent with

$$\eta_M = \frac{\eta_{M0}}{\sinh(m\sigma_{eff}^n)} \qquad (4.6.6)$$

The material parameters used can be found in table 4.6.1. A shear stress of $\sigma_{xy} = 2\,\text{MPa}$ is numerically imposed in $1\,\text{d}$ and held for $1500\,\text{d}$. Analytical and numerical solution fit well (Fig. 4.6.2b).

Both numerical solutions were obtained by subjecting a single 2D eight-node quadrilateral finite element to simple shear loading using the boundary conditions described above.

Table 4.6.1: Parameters for the viscous part of the Minkley material model.

G_M / MPa	$12.0{\cdot}10^3$
K_M / MPa	$18.0{\cdot}10^3$
η_M0 / MPa d	$10.0{\cdot}10^{10}$
m / MPa^{-1}	4.9
n	0.33
G_K / MPa	$63.0{\cdot}10^3$
η_K / MPa d	$14.0{\cdot}10^6$
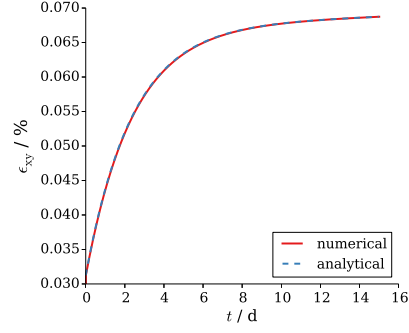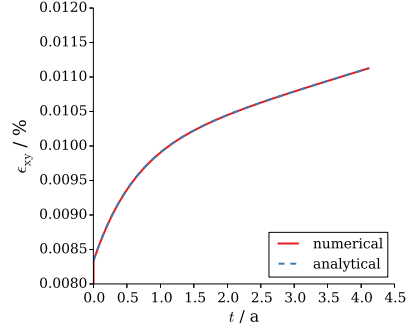
(a) LUBBY2   (b) Minkley

Fig. 4.6.2: Lubby2 model with parameters from Sondershausen Drift (sec. 4.5) and Minkley model with parameters from table 4.6.1. Comparison of numerical and analytical (Eq. (4.6.1)) solutions.

Part III Coupled Processes

Chapter 5
Variable Density Flow

by Marc Walther, James W. Heiss, Fabien Magri, Jens-Olaf Delfs, Thomas Graf

5.1 Tidal forcing in a sandy beach aquifer

5.1.1 Overview and Problem Description

The purpose of this benchmark is to verify the new directional transport boundary condition in OpenGeoSys. Therefore, a variable-density groundwater flow and solute transport model of an unconfined coastal aquifer under tidal influence was developed.

The model represents a 2-D cross-section of an isotropic and homogenous sandy beach aquifer with fresh groundwater and saltwater sources. Groundwater flow and solute transport are investigated once the simulation reached dynamic-steady state with respect to hydraulic head and concentration.

Previous modeling studies in SEAWAT have demonstrated that the direction of groundwater flow across a sloping beach reverses from into the seabed near high tide to out of the seabed near low tide (Heiss and Michael, 2014; Robinson et al., 2007). The transport boundary condition along the shoreface must coincide with the time-varying flow behavior; the concentration of inflowing water near high tide must match that of the sea water, and the concentration of discharging groundwater near low tide must be equal to that calculated at the node adjacent to the point of discharge across the seabed. The example model incorporates this direction-dependent transport boundary condition.

5.1.2 Model Setup

Methods

Following Walther et al. (2012) and Kolditz et al. (2012c), we adopt an approach originally presented by Sugio and Desai (1987) to represent an unconfined groundwater surface. RICHARDS_FLOW and MASS_TRANSPORT processes are coupled iteratively by a linear curve relating the calculated concentrations to density (compare Walther et al. (2015)). The correlation assumed a freshwater density of $1000\,\mathrm{kg \cdot m^{-3}}$ and a saltwater density of $1025\,\mathrm{kg \cdot m^{-3}}$.

Model Domain and Boundary Conditions

The model domain, boundary, and initial conditions are shown in Fig. 5.1.1. The homogeneous domain extends $50\,\mathrm{m}$ seaward and $150\,\mathrm{m}$ landward of the intersection between the shoreface and mean sea level. The left vertical boundary is set as a constant head with a concentration $c = 0$ to represent fresh water flow into the coastal aquifer. A time-varying head is applied to the shoreface boundary to simulate the movement of the tide across the sloping beach. The sinusoidal head signal has a period of $0.5\,\mathrm{d}$ and a $1\,\mathrm{m}$ amplitude. The sea-side mass transport boundary is defined as an adaptive boundary condition, which is governed by the flow direction: if the flow velocity vector is pointing into the model domain, i.e. for high tide when sea water is intruding into the fresh water aquifer, the mass transport BC is set to $c = 1$; if flow vectors are pointing outwards, i.e. for low tide when the aquifer is discharging into the sea, the mass transport BC is switched to a zero-dispersive flux BC (compare Mulligan et al. (2011)). The top and bottom boundaries were no NO-FLOW with a zero concentration gradient.
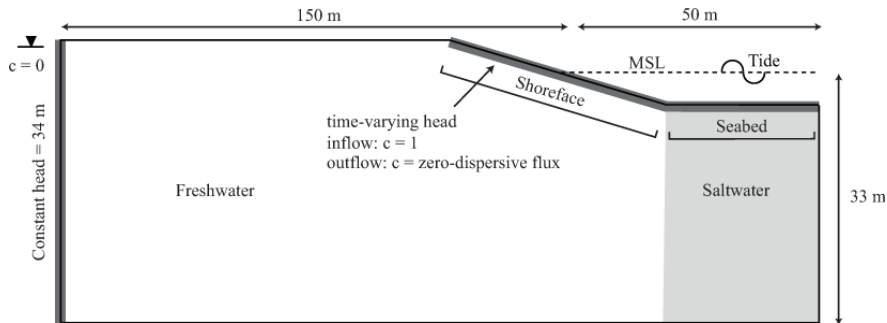

Fig. 5.1.1: Conceptual model.

Initial Conditions

The initial pressure distribution is hydrostatic throughout the aquifer which takes into account the undisturbed situation, ie. without sea water intrusion and tidal activity, of fresh and saltwater that evolve from the application of the boundary conditions shown in Fig. 5.1.1.

The aquifer system had has an initial concentration of $c = 0$ except beneath the seabed where the concentration is $c = 1$. These initial conditions represent an aquifer without tidal activity, density driven flows, or mixing processes.

Spatial and Temporal Discretization

The triangular mesh is non-uniform with higher discretization along the shoreface and seabed boundaries where high flow rates and large concentration gradients exist. The mesh size ranges from $\Delta x = \Delta z = 5\,\text{m}$ along the landward boundary to $\Delta x = \Delta z = 0.3\,\text{m}$ along the shoreface and seabed boundaries.

COURANT Cr and mesh PÉCLET Pe numbers are minimized to omit numerical oscillations. The numbers' values are within a reasonable range of the recommended criteria. Also, an automatic time stepping is employed.

Fluid and Aquifer Properties

Model parameters are listed in Table 5.1.1. Due to the dominantly advective regime, diffusion is assumed to be negligible in comparison to dispersion and, thus, diffusion coefficient was set to zero.

Table 5.1.1: Fluid and aquifer properties

Parameter	Value
Intrinsic permeability (m^2)	$0.355 \cdot 10^{-12}$
Porosity $(-)$	0.300
Dynamic viscosity ($\text{kg} \cdot \text{m} \cdot \text{s}^{-1}$)	$1.000 \cdot 10^{-3}$
Freshwater density ($\text{kg} \cdot \text{m}^{-3}$)	$1.000 \cdot 10^{3}$
Saltwater density ($\text{kg} \cdot \text{m}^{-3}$)	$1.025 \cdot 10^{3}$
Longitudinal dispersivity (m)	0.150
Transversal dispersivity (m)	0.015

5.1.3 Results

The oscillating tide along the sloping shoreface caused saltwater to infiltrate across the upper intertidal zone which modified the salinity distribution in the coastal aquifer. The inflowing seawater mixed with underlying fresh groundwater in the intertidal zone to form a secondary saltwater-freshwater mixing zone in addition to the lower density-driven traditional interface located farther seaward (Fig. 5.1.2). The intertidal mixing zone extended horizontally from the high tide mark seaward to the zone of discharging fresh groundwater and vertically to a depth of 15 m below the sand surface. Flow through the intertidal mixing zone was driven primarily by tidal fluctuations, which led to a tidally averaged beach water table that was higher than would occur without tides. The resulting seaward-directed hydraulic gradient caused infiltrating saltwater to flow downward and seaward until discharging near the lower end of the intertidal zone, forming a cell of circulating seawater.
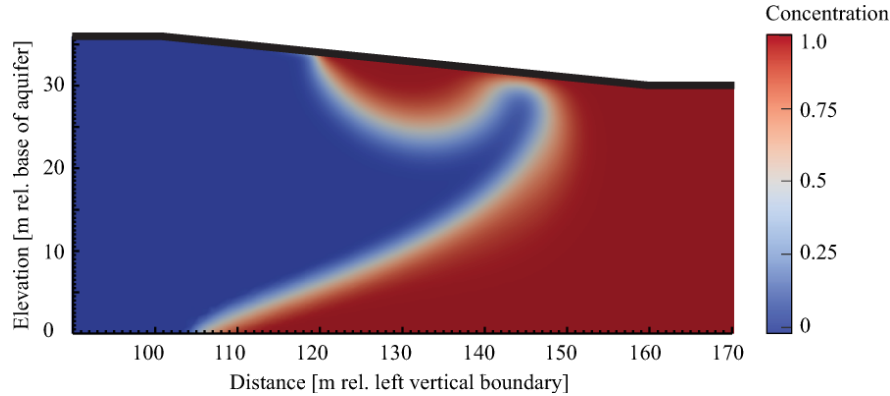

Fig. 5.1.2: Salinity distribution beneath the intertidal mixing zone.

Tidal forcing led to infiltration and discharge cycles along the aquifer-ocean interface. Near high tide, the seaward originally falling hydraulic potential was reduced and flow was directed into the seabed. Concentrations in the shallow sediments near these recharge zones were correspondingly higher as a result of inflowing saltwater (Fig. 5.1.3). Conversely at low tide, the seaward-directed falling hydraulic potential was stronger and flow was directed out of the system (Fig. 5.1.4). As a result of the flow reversal, the transport boundary condition automatically switched from constant concentration when water was inflowing to calculated concentration at the boundary during outflow. The stronger hydraulic gradient at low tide flushed saltwater out of the system, leading to more realistic concentrations along the boundary than would otherwise be calculated by implementing a constant concentration boundary for both flow into and out of the aquifer.
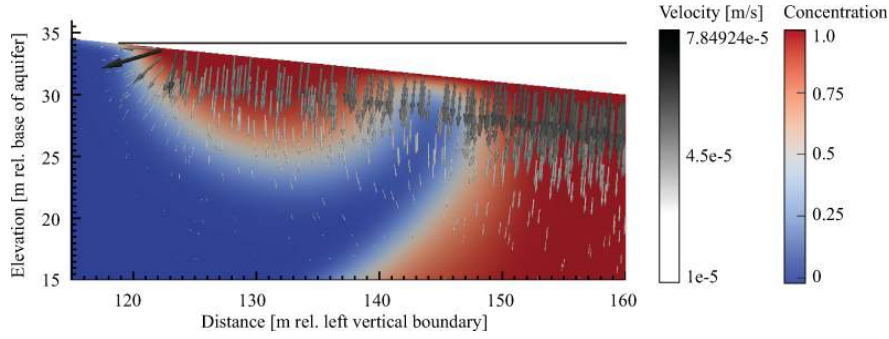
Fig. 5.1.3: Salinity distribution and flow vectors at high tide. Inflowing seawater caused by a weaker hydraulic gradient increased concentrations directly beneath the seabed in the fresh discharge zone. Horizontal black line is the tide level.
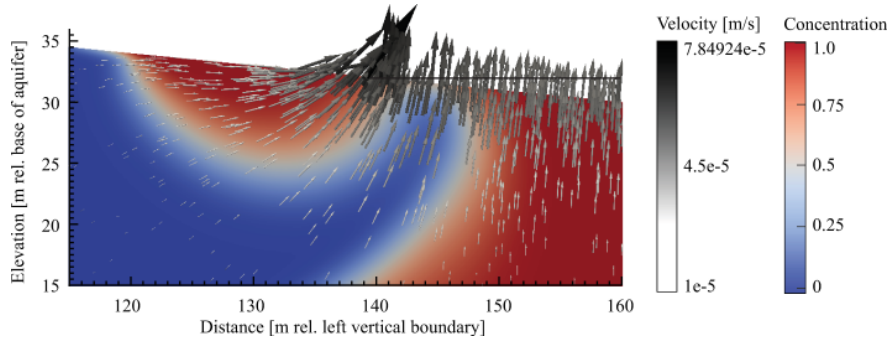

Fig. 5.1.4: Salinity distribution and flow vectors at low tide. Concentrations directly beneath the seabed in the fresh discharge zone decreased as the hydraulic gradient increased, allowing greater freshwater to discharge, which diluted and flushed saltwater out of the system. Horizontal black line is the tide level.

The oscillating flows into and out of the aquifer over individual tidal cycles is shown in Fig. 5.1.5. Inflow was highest at a rate of $1.3 \cdot 10^{-3} \, \mathrm{m^3 \cdot s^{-1} \cdot m^{-1}}$ near high tide. As the tide lowered, the rate of inflow decreased until midway through ebb tide when discharge began. At low tide, discharge from the aquifer was highest at $1.2 \cdot 10^{-3} \, \mathrm{m^3 \cdot s^{-1} \cdot m^{-1}}$ as porewater drained from the aquifer.
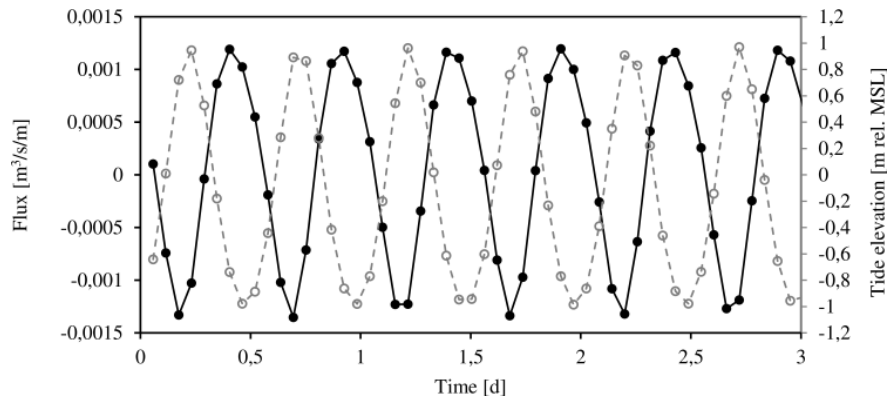
Fig. 5.1.5: Flux per meter length of shoreline over three days (black solid line) and tidal elevation (gray dotted line). A positive flux indicates discharge.

5.2 Investigations on Mesh Convergence

5.2.1 Overview

The result of a numerical simulations should not depend on the spatial discretization that is chosen to investigate a given problem. The term "mesh convergence" refers to the spatial resolution of a mesh, at which the simulation result does not change significantly in comparison to the next coarser resolution. Finding the point of mesh convergence is therefore important to ensure high prediction quality of a numerical model.

For variable-density flow, mesh convergence (sometimes also referred to as grid, or net convergence) has been a subject for a multitude of studies and different setups, e.g. Ataie-Ashtiani and Aghayi (2006); Graf and Degener (2011); Lan et al. (2003); Oltean et al. (2008); Stern (1969). It has been shown, that for a given setup there may or may not exist a resolution, where mesh convergence can be found. Besides the numerical aspect, in most applied studies, the choice for the size of the elements in a given setup strongly depends on the process that is investigated, i.e. whether local, regional, or large-scale phenomena are of interest.

We assess mesh convergence for variable-density flow on a laboratory-scale setup. Investigations are based on the GOSWAMI-CLEMENT problem, which has been used as a benchmark for OPENGEOSYS for steady-state and transient cases before (compare Kolditz et al. (2012c), Walther et al. (2014)). We employ different mesh resolutions with triangular and quadrilateral elements and evaluate corresponding changes of the intrusion length of the salt water, and of the transition zone between fresh and salt water.

5.2.2 Problem Description

Model Setup

Goswami and Clement (2007) describe a physical, Henry-like salt water intrusion benchmark on a laboratory scale and use numerical software (SEAWAT) as a modeling tool in a x-z-domain ($x = 0.53\,\mathrm{m}$, $z = 0.26\,\mathrm{m}$). Figure 5.2.1 shows the conceptual setup of the problem, for which we use an identical parameter set, as well as the same initial and boundary conditions (BC) for the steady state SS1 as described in Kolditz et al. (2012c), except for one difference: the salt-water-side BC is set to a variable concentration c, which is set to $c = 1$ when water is entering the model domain ($v_x > 0$), and $c = c'$ for the opposite case ($v_x \leq 0$), where c' resembles the actual concentration of the exiting fluid.
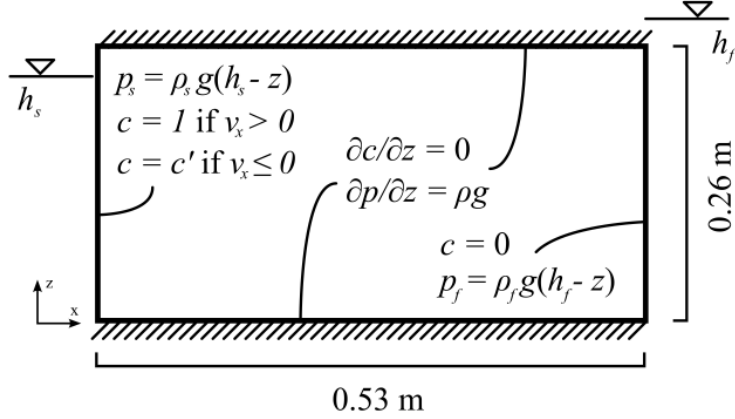
Fig. 5.2.1: Conceptual setup of the GOSWAMI-CLEMENT problem, after Kolditz et al. (2012c).

Temporal and Spatial Discretization

The time step is set to a constant size of $1\,\text{s}$ for the first 100 steps, and afterwards to $10\,\text{s}$.

All meshes use a homogeneous element size throughout the domain. Following equation 5.2.1 to calculate the element edge length ϵ, triangular meshes are generated with GMSH (Geuzaine and Remacle, 2009), while quadrilateral meshes are obtained from ogs[6] (Fischer et al., 2015).

$$\epsilon = \frac{x}{n_x \cdot i} \tag{5.2.1}$$

with $n_x = 26$ as the number of discretizations for the coarsest mesh (i.e. $i = 1$), and $1 \leq i \leq 20$ as the refinement step.

Figure 5.2.2 shows the properties of the generated different meshes for which the simulations are carried out with respect to the refinement step i. The figure only shows setups that successfully generated a solution for SS1.

5.2.3 Results

We evaluate the horizontal position of the toe, i.e. $x(c, z = 10^{-4}\,\text{m})$, of the saline intrusion for the concentrations $c = \{0.1, 0.5, 0.9\}$. Figure 5.2.3 shows
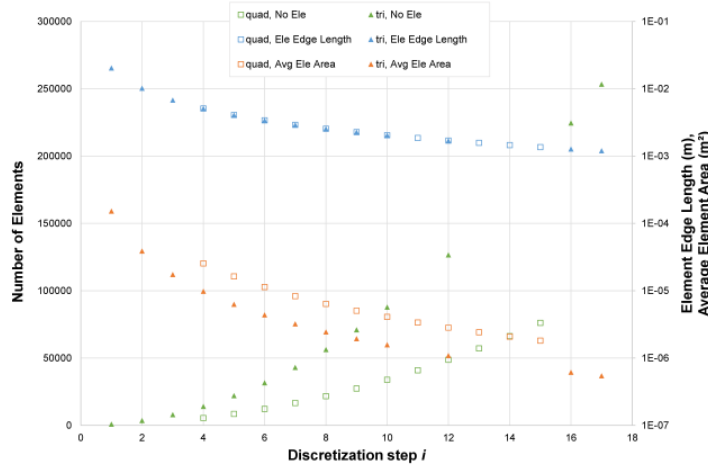
Fig. 5.2.2: Mesh properties; 'quad' and 'tri' for quadrilateral and triangular elements; 'No Ele' for number of elements, 'Ele Edge Length' for element edge length, and 'Avg Ele Area' for average element area.

the simulated intrusion length over the mean area of the elements in a base 2 single-logarithmic plot. Results show, that

1. for decreasing element sizes, the intrusion length increases, while the size of the transition zone decreases;
2. decreasing the element size by a factor of two for an element with the area $A \approx 1.28 \cdot 10^{-5}\,\mathrm{m}^2$ (i.e. $3 < i < 4$) will increase the intrusion length by less than $10\,\%$ ($\Delta x < 0.01\,\mathrm{m}$), which is well at the limit of laboratory observation accuracy;
3. at the refinement step $3 < i < 4$, the toe position for $c = 0.1$ already shows an oscillating behaviour, which is most likely due to interpolation artefacts;
4. quadrilateral element types seem to reach mesh convergence at earlier discretization steps than triangular elements.
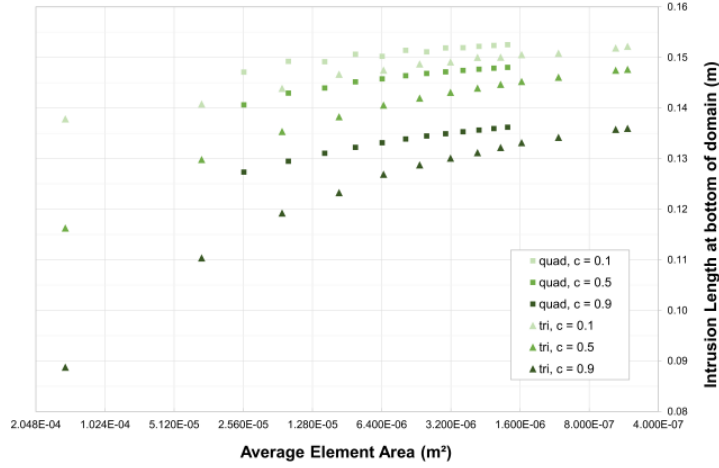
Fig. 5.2.3: Simulated intrusion lengths over the average area of the elements.

5.2.4 Conclusions & Outlook

For GOSWAMI-CLEMENT problem, one might define mesh convergence for the situation where the factor of change in element size yields a difference in the simulation result that lies within or below the limit of laboratory observation accuracy. Although an asymptotic behaviour has not yet been reached, it may still be concluded that, for this example, an average element area $A \approx 1.28 \cdot 10^{-5}\,\mathrm{m}^2$ can be used to adequately resemble variable-density flow processes. Even more, it needs to be acknowledged that this area is already at the verge of representing the size of a pore, i.e. the concept of a representative elementary volume may become questionable for higher resolutions.

It seems advisable to use quadrilateral element types, as mesh convergence seems to be achieved with larger, i.e. less elements, thus, faster and with using less computing power.

It may be of interest to investigate the impact of sensitive modelling parameters, and whether errors of experimental measurement techniques result in larger deviations than those that can be observed with mesh refinement.

Chapter 6
Multiphase Flow

Yonghui Huang and Haibing Shao

In this chapter, we consider two-phase two-component transport process with phase transition phenomenon.

6.1 Gas injection and migration in fully water saturated column

The background of this benchmark is the production of hydrogen gas due to the corrosion of the metallic container in the nuclear waste repository. Numerical model is built to illustrate such gas appearance phenomenon. The model domain is a two dimensional horizontal column representing the bentonite backfill in the repository tunnel, with hydrogen gas injected on the left boundary. This benchmark was proposed in the GNR MoMaS project by French National Radioactive Waste Management Agency. Several research groups has made contributions to test the benchmark and provided their reference solutions Ben Gharbia and Jaffré (2014); Bourgeat et al. (2009); Marchand and Knabner (2014b); Neumann et al. (2013). Here we adopted the results proposed in Marchand and Knabner (2014b) for comparison.

6.1.1 Physical scenario

Here a 2D rectangular domain $\Omega = [0, 200] \times [-10, 10]$ m (see Figure 6.1.1) was considered with an impervious boundary at $\Gamma_{imp} = [0, 200] \times [-10, 10]$ m, an inflow boundary at $\Gamma_{in} = \{0\} \times [-10, 10]$ m and an outflow boundary at $\Gamma_{out} = \{200\} \times [-10, 10]$ m. The domain was initially saturated with water, hydrogen gas was injected on the left-hand-side boundary within a certain

time span ($[0, 5 \times 10^4 \text{century}]$). After that the hydrogen injection stopped and no flux came into the system. The right-hand-side boundary is kept open throughout the simulation. The initial condition and boundary conditions were summarized as

- $X(t=0) = 10^{-5}$ and $P_L(t=0) = P_L^{out} = 10^6$ [Pa] on Ω.
- $q^w \cdot \nu = q^h \cdot \nu = 0$ on Γ_{imp}.
- $q^w \cdot \nu = 0, q^h \cdot \nu = Q_d^h = 0.2785$ [mol century^{-1}m^{-2}] on Γ_{in}.
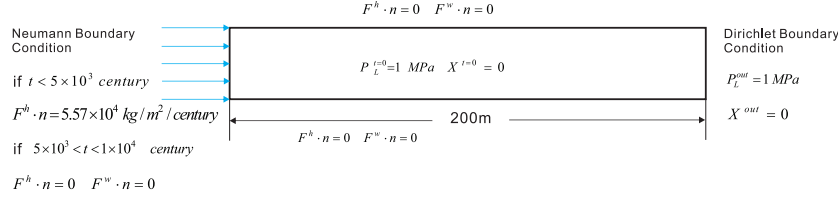- $X = 0$ and $P_l = P_L^{out} = 10^6$ [Pa] on Γ_{out}.

Fig. 6.1.1: Geometry and boundary condition for the H$_2$ injection benchmark.

6.1.2 Model parameters and numerical settings

The capillary pressure P_c and relative permeability functions are given by the van-Genuchten model (Van Genuchten, 1980).

$$P_c = P_r \left(S_{le}^{-\frac{1}{m}} - 1 \right)^{\frac{1}{n}}$$

$$K_{r_L} = \sqrt{S_{le}} \left(1 - \left(1 - S_{le}^{\frac{1}{m}} \right)^m \right)^2$$

$$K_{r_G} = \sqrt{1 - S_{le}} \left(1 - S_{le}^{\frac{1}{m}} \right)^{2m}$$

where $m = 1 - \frac{1}{n}$, P_r and n are van-Genuchten model parameters and the effective saturation S_{le} is given by

$$S_{le} = \frac{1 - S_g - S_{lr}}{1 - S_{lr} - S_{gr}} \tag{6.1.1}$$

here S_{lr} and S_{gr} indicate the residual saturation in liquid and gas phases, respectively. Values of parameters applied in this model are summarized in Table 6.1.1.

We created a 2D triangular mesh here with 963 nodes and 1758 elements. The mesh element size varies between 1m and 5m. A fixed time step size of

Table 6.1.1: Fluid and porous medium properties applied in the H_2 migration benchmark.

Parameters	Symbol	Value	Unit
Intrinsic Permeability	K	5×10^{-20}	$[m^2]$
Porosity	Φ	0.15	-
Residual Saturation of liquid phase	S_{lr}	0.4	[-]
Residual Saturation of gas phase	S_{gr}	0	[-]
Viscosity of liquid	μ_l	10^{-3}	$[Pa \cdot s]$
Viscosity of gas	μ_g	9×10^{-6}	$[Pa \cdot s]$
van Genuchten parameter	P_r	2×10^6	$[Pa]$
van Genuchten parameter	n	1.49	-

1 century is applied. The entire simulated time from 0 to 10^4 centuries were simulated. The entire execution time is around 3.241×10^4s.

6.1.3 Results and analysis

The results of this benchmark are depicted in Figure 6.1.2. The evolution of gas phase saturation and the gas/liquid phase pressure over the entire time span are shown. In additional, we compare results from our model against those given in Marchand and Knabner (2014b). In Figure 6.1.2, solid lines are our simulation results while the symbols are the results from Marchand et al. It can be seen that a good agreement has been achieved. Furthermore, the evolution profile of the gas phase saturation S_g, the liquid phase pressure P_L, and the total molar fraction of hydrogen X are plotted at different time ($t = 150, 1 \times 10^3, 5 \times 10^3, 6 \times 10^3$ centuries) in Figure 3(a), 3(b) and 3(c) respectively.

 By observing the simulated saturation and pressure profile, the complete physical process of H_2 injection can be categorized into five subsequent stages.

1) The dissolution stage: After the injection of hydrogen at the inflow boundary, the gas first dissolved in the water. This was reflected by the increasing concentration of hydrogen in Figure 3(c). Meanwhile, the phase pressure did not vary much and was kept almost constant (see Figure 3(b)).

2) Capillary stage: Given a constant temperature, the maximal soluble amount of H_2 in the water liquid is a function of pressure. In this MoMaS benchmark case, our simulation showed that this threshold value was about 1×10^{-3} mol H_2 per mol of water at a pressure of 1×10^6 [Pa]. Once this pressure was reached, the gas will emerge and formed a continuous phase. As shown in Figure 3(a), at approximately 150 centuries, the first phase transition happens. Beyond this point, the gas and liquid phase pressure quickly increase, while hydrogen gas is transported towards the right boundary driven by the pressure and concentration gradient. In the meantime, the location of
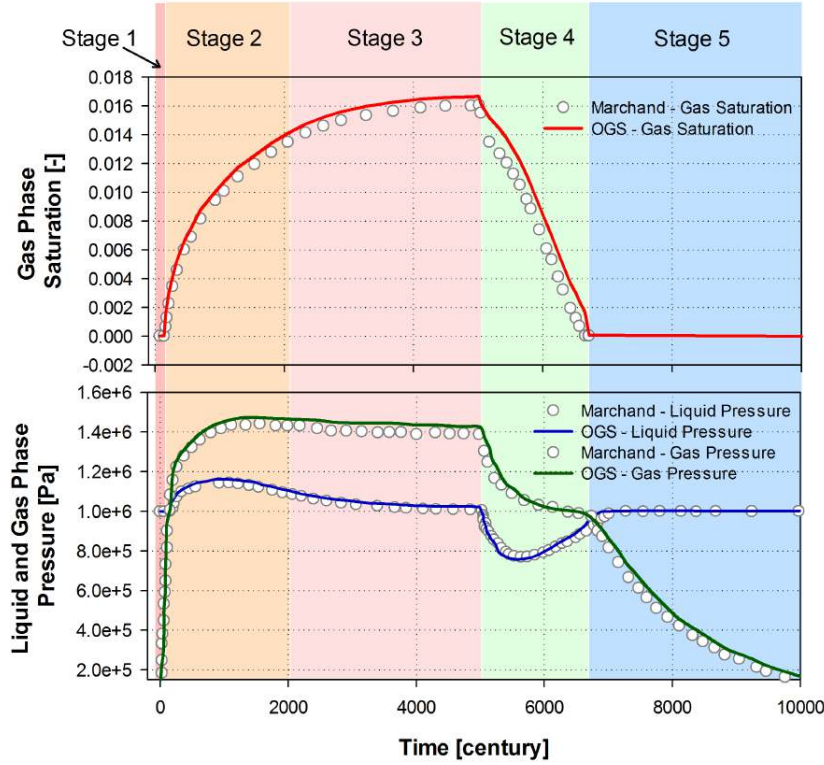
Fig. 6.1.2: Evolution of pressure and saturation over time.

this phase transition point also slowly shifted towards the middle of the domain.

3) Gas migration stage: The hydrogen injection process continued until the 5000-th century. Although the gas saturation continues to increase, pressures in both phases begin to decline due to the existence of the liquid phase gradient. Eventually, the whole system will reach steady state with no liquid phase gradient.

4) Recovery stage: After hydrogen injection was stopped at the 5000-th century, the water came back from the outflow boundary towards the left, which was driven by the capillary effect to occupy the space left by the disappearing gas phase. During this stage, the gas phase saturation begins to decline, and both phase pressures drop even below the initial pressure. The whole process will not stop until the gas phase completely disappeared.

5) Equilibrium stage: After the complete disappearance of the gas phase, the saturation comes to zero again, and the whole system will reach steady state, with pressure and saturation values same as the ones given in

the initial condition.

(a) Evolution of saturation

(b) Evolution of liquid phase pressure

(c) Evolution of total hydrogen molar fraction
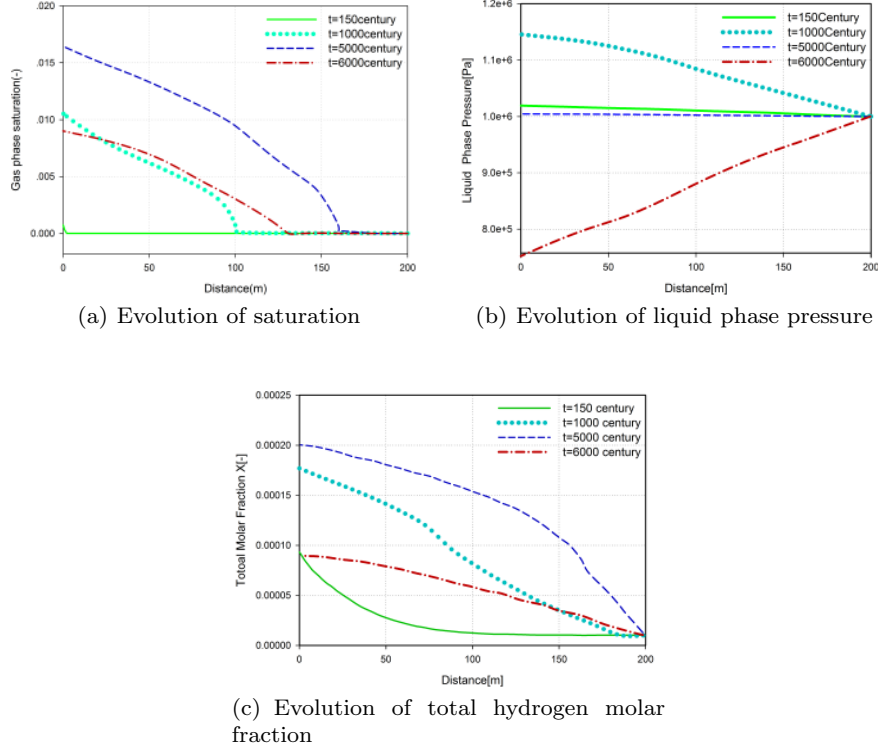
Fig. 6.1.3: Evolution of (a) gas phase saturation (b) liquid phase pressure and (c) total hydrogen molar fraction over the whole domain at different time.

6.2 MoMaS Benchmark 2: Gas injection and migration in partially water saturated column

The physical setting of this benchmark is very similar to the previous one. The only difference is the column is initially partially saturated with water, which indicates the gas exist at the beginning of the simulation.

6.2.1 Physical scenario

The physical scenario of this benchmark is exactly the same as the first Mo-MaS benchmark. However, the initial and boundary condition will be altered, and the total simulation time will be different as well. The initial gas phase pressure was set to be $1.1e + 6$[Pa] which is bigger than the liquid phase pressure($1.e + 6$[Pa]) to ensure the presence of gas phase in the whole domain, while on the inflow boundary Γ_{in} the Dirichlet boundary was chosen the same as the initial condition in order to keep the presence of gas phase on the boundary. A constant hydrogen gas flux was imposed on the left-hand-side boundary. The initial condition and boundary conditions were summarized as:

- $X(t = 0) = 0.018762136579995 \quad$ and $\quad P_L(t = 0) = P_L^{out} = 10^6$ [Pa] on Ω.
- $q^w \cdot \nu = q^h \cdot \nu = 0$ on Γ_{imp}.
- $q^w \cdot \nu = 0, q^h \cdot \nu = Q_d^h = 2.785$ [mol century^{-1}m^{-2}] on Γ_{in}.
- $X = 0.018762136579995$ and $P_l = P_L^{out} = 10^6$ [Pa] on Γ_{out}.

The model parameters can be referred to Table.6.1.1.

6.2.2 Results and analysis

The results of this benchmark are depicted in Figure 6.2.1, 6.2.2, 6.2.3. The evolution profile of the gas phase saturation S_g, the liquid phase pressure P_L, and the total molar fraction of hydrogen X are plotted at different time respectively. We compare results from our model against those given in Bourgeat et al. (2013). In all these figures, solid lines are our simulation results while the symbols are the results from Bourgeat et al. It can be seen that a good agreement has been achieved.

By observing the simulated saturation and pressure profile, the complete physical process of H_2 injection can be categorized into four subsequent stages.

1) up to t < 1,400 years, the two phases are present in the whole domain (see time t =500 years in Fig. 6.2.1). The injection of hydrogen flux increases the gas saturation in the vicinity of inflow boundary Γ_{in}. The drop of gas saturation is due to the difference in relative mobilities between the two phases: the lower liquid mobility leads to a bigger liquid pressure accumulation, compared to the increase of the gas pressure, which is finally resulting in a decrease of capillary pressure and a liquid saturated zone is generated(see Fig.6.2.2).

2) At time t = 1,400 years, the gas phase starts to disappear in some region of the porous domain (see time t = 1,500 years, in Fig.6.2.1a). Then, a fully saturated liquid region (Sg = 0) will exist until time t = 17,000 years (see

Fig.6.2.1a), and during this period of time, the saturated region is pushed by the injected hydrogen, from Γ_{in} to Γ_{out}.

3) After the time t = 17,000 years, due to the Dirichlet conditions imposed on Γ_{out}, the liquid saturated region disappears and all together the phases' pressure and the gas saturation are growing in the whole domain (see the time t = 20,000 years in Figs. 6.2.1b and 6.2.2b).

4) Finally, the liquid pressure reaches its maximum at time t = 20,000 years and then decreases in the whole domain (see Fig. 6.2.2b). This is caused, like in the benchmark 1, by the evolution of the system towards a stationary state.
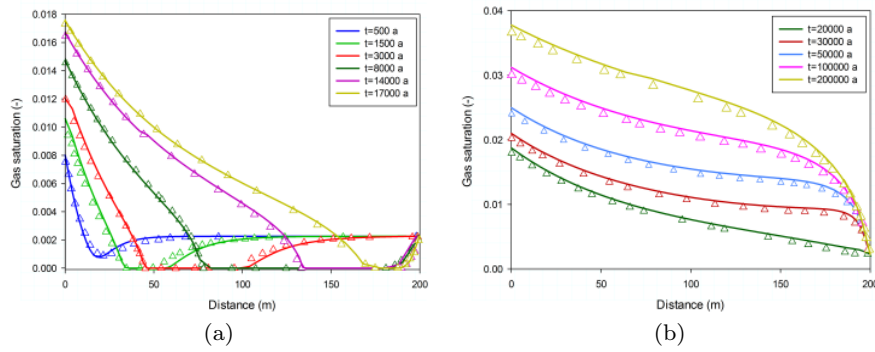

(a)   (b)

Fig. 6.2.1: Evolution of gas phase saturation over the whole domain at different time.
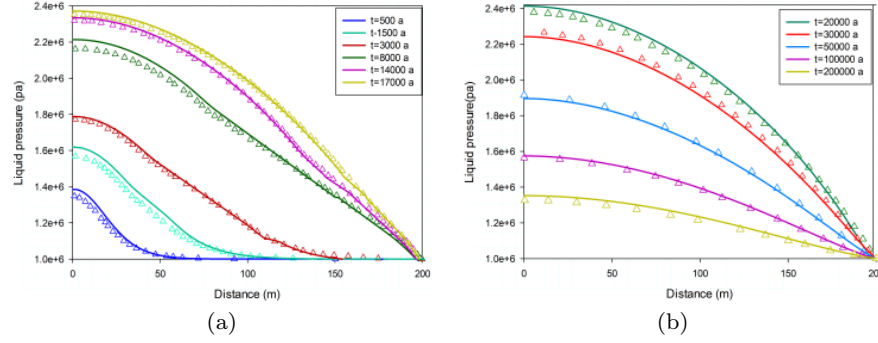
Fig. 6.2.2: Evolution of Liquid phase pressure over the whole domain at different time.
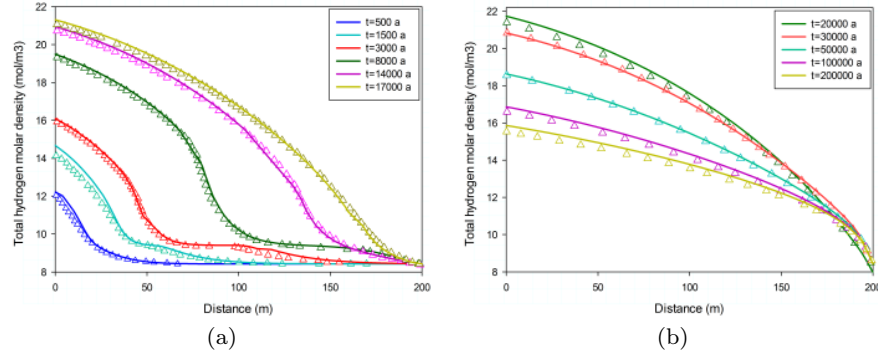

Fig. 6.2.3: Evolution of total hydrogen molar density over the whole domain at different time.

6.3 Heat pipe problem with phase appearance and disappearance

The thermal effects on multiphase formulation with phase transition phenonmena are investigated. We adopted the heat pipe problem proposed by Udell and Fitch Udell and Fitch (1985). They have provided a semi-analytical solution for a non-isothermal water-gas system in porous media, where heat convection, heat conduction as well as capillary forces were considered. A heater installed on the right-hand-side of the domain generated constant flux of heat, and it was then transferred through the porous media by conduction, as well as the enthalpy transport of the fluids. The semi-analytical solution

was developed for the steady state condition, and the liquid phase flowed in
the opposite direction to the gas phase. If gravity was neglected, the system
can be simplified to a system of six ordinary differential equations (ODE), the
solution of which was then be obtained in the form of semi-analytical solu-
tion. Detailed derivation procedure is available in Helmig (1997) and Huang
et al. (2015b), and the parameters used in our comparison are listed in Table
6.3.1.

Table 6.3.1: Parameters applied in the Heat Pipe problem

Parameters Name	Symbol	Value	Unit
Permeability	K	10^{-12}	$[\mathrm{m}^2]$
Porosity	Φ	0.4	$[-]$
Residual liquid phase saturation	S_{lr}	0.4	$[-]$
Heat conductivity of fully saturated porous medium	$\lambda_{pm}^{S_w=1}$	1.13	$[\mathrm{W\ m^{-1}\ K^{-1}}]$
Heat conductivity of dry porous medium	$\lambda_{pm}^{S_w=0}$	0.582	$[\mathrm{W\ m^{-1}\ K^{-1}}]$
Heat capacity of the soil grains	c_s	700	$[\mathrm{J\ kg^{-1}\ K^{-1}}]$
Density of the soil grain	ρ_s	2600	$[\mathrm{kg\ m^{-3}}]$
Density of the water	ρ_w	1000	$[\mathrm{kg\ m^{-3}}]$
Density of the air	ρ	0.08	$[\mathrm{kg\ m^{-3}}]$
Dynamic viscosity of water	μ_w	2.938×10^{-4}	$[\mathrm{Pa \cdot s}]$
Dynamic viscosity of air	μ_g^a	2.08×10^{-5}	$[\mathrm{Pa \cdot s}]$
Dynamic viscosity of steam	μ_g^w	1.20×10^{-5}	$[\mathrm{Pa \cdot s}]$
Diffusion coefficient of air	D_g^a	2.6×10^{-5}	$[\mathrm{m^2\ s^{-1}}]$
van Genuchten parameter	P_r	1×10^4	$[\mathrm{Pa}]$
van Genuchten parameter	n	5	$[-]$

6.3.1 Physical scenario

As shown in Figure 6.3.1, the heat pipe was represented by a 2D hori-
zontally column (2.25m in length and 0.2m in diameter) of porous media,
which was partially saturated with a liquid phase saturation value of 0.7 at
the beginning. A constant heat flux ($Q_T = 100$ [W m^{-2}]) was imposed on
the right-hand-side boundary Γ_{in}, representing the continuously operating
heating element. At the left-hand-side boundary Γ_{out}, Dirichlet boundary
conditions were imposed for Temperature $T = 70°$C, liquid phase pressure
$P_G = 1 \times 10^5$ [Pa], effective liquid phase saturation $S_{le} = 1$, and air molar
fraction in the gas phase $X_G^a = 0.71$. Detailed initial and boundary condition
are summarized as follows.

- $P(t = 0) = 1 \times 10^5$ [Pa], $S_L(t = 0) = 0.7$, $T(t = 0) = 70$ [°C]   on the entire domain.
- $q^w \cdot \nu = q^h \cdot \nu = 0$ on Γ_{imp}.

- $q^w \cdot \nu = q^h \cdot \nu = 0, \quad q^T \cdot \nu = Q_T \quad$ on Γ_{in}.
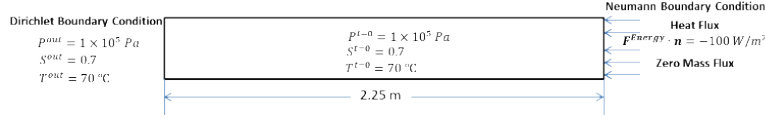- $P = 1 \times 10^5$ [Pa], $\quad S_L = 0.7, T = 70$ [°C] $\quad$ on Γ_{out}.

Fig. 6.3.1: Geometry and boundary condition for the H₂ injection benchmark.

6.3.2 Model parameters and numerical settings

For the capillary pressure-saturation relationship, van Genuchten model was applied. The parameters used in the van Genuchten model are listed in Table 6.3.1. The water-air relative permeability relationships were described by the Fatt and Klikoffv formulations Fatt et al. (1959).

$$K_{rG} = (1 - S_{le})^3$$
$$K_{rL} = S_{le}^3$$

where S_{le} is the effective liquid phase saturation, referred to Eq(6.1.1).

We created a 2D triangular mesh here with 206 nodes and 326 elements. The averaged mesh element size is around 6m. A fixed size time stepping scheme has been adopted, with a constant time step size of 0.01 day. The entire simulated time from 0 to 10^4 day were simulated.

6.3.3 Results and analysis

The results of our simulation were plotted along the central horizontal profile over the model domain at y=0.1m, and compared against semi-analytical solution. Temperature and saturation profiles at day 1, 10, 100, 1000 are depicted in Figure 6.3.2(a) and 6.3.2(b) respectively. As the heat flux was imposed on the right-hand-side boundary, the temperature kept rising there. After 1 day, the boundary temperature already exceeded 100 °C, and the water in the soil started to boil. Together with the appearance of steam, water saturation on the right-hand-side began to decrease. After 10 days, the boiling point has almost moved to the middle of the column. Meanwhile, the steam front kept boiling and shifted to the left-hand-side, whereas liquid

water was drawn back to the right. After about 1000 days, the system reached a quasi-steady state, where the single phase gas, two phase and single phase liquid regions co-exist and can be distinguished. A pure gas phase region can be observed on the right and liquid phase region dominates the left side.
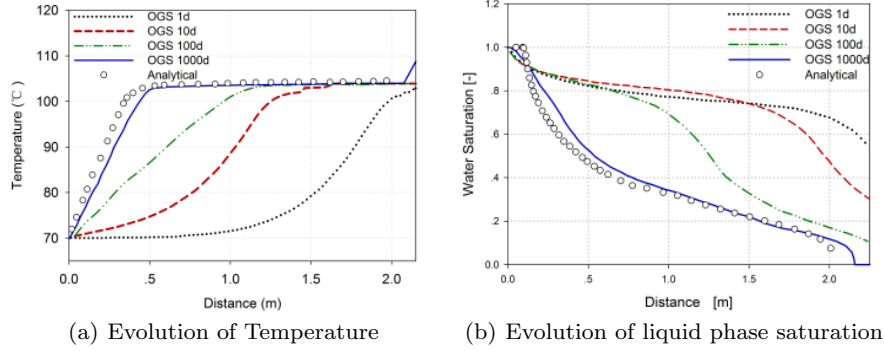

(a) Evolution of Temperature   (b) Evolution of liquid phase saturation

Fig. 6.3.2: Evolution of (a) temperature and (b) liquid phase saturation over the whole domain at different time.

Chapter 7
Hydro-Mechanical (Consolidation) Processes

Peter Vogel, Jobst Maßmann, Gesa Ziefle, Hongwei Zhou

7.1 Mandel-Cryer effects

Peter Vogel and Jobst Maßmann

The presence of a fluid pressure affects the mechanical behaviour of the porous matrix and vice versa. This interaction constitutes the subject of Biot's theory, see Biot (1941) or see Jaeger and Cook (1971). Based on the ideas of Mandel (1953) and Cryer (1963) we present a few transient problems, which exhibit an increase in liquid pressure due to increased mechanical load on the porous matrix. We focus on the closed form solutions. The associated simulation exercises have been checked by OGS; they may serve as verification tests.

7.1.1 Increasing axial load on a liquid-filled elastic column causes an increase in liquid pressure

Given size $H = 0.1$ m and length $L = 1$ m the domain represents the rectangular beam $[0, L] \times [0, H] \times [0, H]$. It is discretized by hexahedral elements with section $0 \leq x \leq 0.6\,L$ composed of $10 \times 1 \times 1$ and section $0.6\,L \leq x \leq L$ composed of $60 \times 1 \times 1$ elements. The solid material has been selected elastic with Poisson's ratio $\nu = 0.2$, Young's modulus $E = 30,000$ Pa, and Biot number equal one. An isotropic permeability $k = 10^{-10}$ m^2 and zero porosity is assumed for the material, liquid viscosity is $\mu = 1$ mPa·s and gravity is neglected via zero material and liquid densities. Zero pressure is specified along the face $x = L$, the other faces of the beam are no-flow faces by de-

fault. Except from the face $x = L$ all faces of the beam are sliding planes. Starting from zero initial pressure and zero mechanical load the compressive stress $\sigma_0 \cdot t\,(\sigma_0 = -1000$ Pa/s$)$ is applied at the face $x = L$ for times $t > 0$. The simulation evaluates the transient pressure distribution $p(x, t)$ as well as stresses, strains, and displacements with output after 6 and 12 s (Fig. 7.1.1).
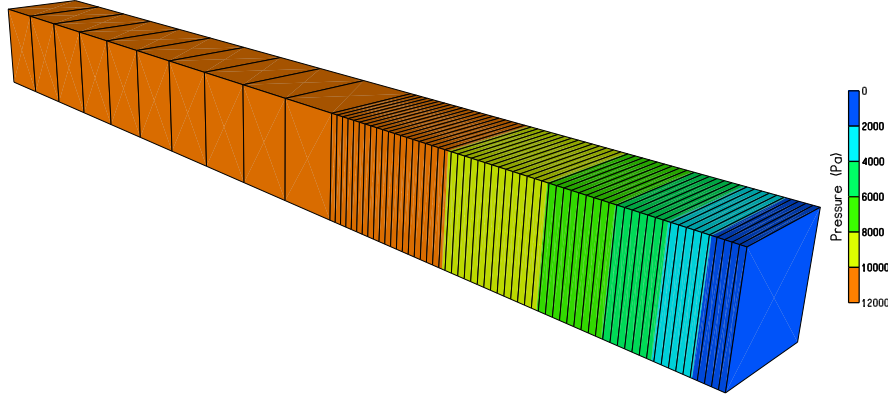

Fig. 7.1.1: Pressure distribution after 12 s

Let $\boldsymbol{\sigma}$ denote the stress tensor and $\mathbf{I}$ the unit tensor. Employing Biot's simplified theory (i.e. Biot number equal one) the equation of mechanical equilibrium reads

$$0 = \nabla \cdot (\boldsymbol{\sigma} - p\,\mathbf{I})\,. \qquad (7.1.1)$$

It is satisfied by zero shear, if the stresses σ_{22} and σ_{33} are functions of x only and the horizontal stress σ_{11} satisfies

$$\frac{\partial}{\partial x}(\sigma_{11} - p) = 0\,. \qquad (7.1.2)$$

With respect to the prescribed boundary conditions at $x = L$ the last equation yields

$$\sigma_{11} = \sigma_0 t + p\,. \qquad (7.1.3)$$

Due to the y- and z-fixities along the front, rear, top, and bottom and with principal axes equal to coordinate axes, Hooke's law gives for the strains

$$\begin{aligned} E \cdot \epsilon_{11} &= \sigma_{11} - \nu(\sigma_{22} + \sigma_{33})\,, \\ 0 = E \cdot \epsilon_{22} &= \sigma_{22} - \nu(\sigma_{11} + \sigma_{33})\,, \\ 0 = E \cdot \epsilon_{33} &= \sigma_{33} - \nu(\sigma_{11} + \sigma_{22})\,. \end{aligned} \qquad (7.1.4)$$

The strain ϵ_{11} and the stresses σ_{22} and σ_{33} are obtained in terms of the prescribed stress $\sigma_0 \cdot t$ and the pressure p

$$\epsilon_{11} = \left(1 - \frac{2\nu^2}{1-\nu}\right) \frac{1}{E}(\sigma_0 t + p)\,,$$

$$\sigma_{22} = \sigma_{33} = \frac{\nu}{1-\nu}(\sigma_0 t + p)\,. \tag{7.1.5}$$

Integrating the strains with respect to the fixities at the coordinate planes yields the displacement vector (u_x, u_y, u_z)

$$u_x(x,t) = \left(1 - \frac{2\nu^2}{1-\nu}\right) \frac{1}{E}\left[\sigma_0 t x + \int_0^x p(x',t)dx'\right]\,,$$

$$u_y = u_z = 0\,. \tag{7.1.6}$$

Therefore, once that the pressure p is known, the displacements and the entire mechanical load may be obtained from the above.

Let q denote the specific discharge via Darcy's law

$$q = -\frac{k}{\mu}\nabla p\,. \tag{7.1.7}$$

Conservation of momentum yields

$$0 = \nabla \cdot \left(q + \frac{\partial}{\partial t}(u_x, u_y, u_z)\right)\,. \tag{7.1.8}$$

For the present example this reduces to

$$0 = -\frac{k}{\mu}\frac{\partial^2 p}{\partial x^2} + \frac{\partial \epsilon_{11}}{\partial t}\,. \tag{7.1.9}$$

Introducing the notation

$$\chi = \frac{\mu}{kE}\left(1 - \frac{2\nu^2}{1-\nu}\right) \tag{7.1.10}$$

the pressure distribution $p(x,t)$ is governed by the parabolic equation

$$\frac{\partial^2 p}{\partial x^2} - \chi\frac{\partial p}{\partial t} = \chi\sigma_0\,, \tag{7.1.11}$$

subject to the initial condition

$$p(x,0) = 0 \qquad \text{for } 0 \le x \le L\,, \tag{7.1.12}$$

the no-flow boundary condition at $x = 0$

$$\frac{\partial p}{\partial x}(0, t) = 0 \qquad \text{for } t > 0 \,, \tag{7.1.13}$$

and zero pressure at $x = L$

$$p(L, t) = 0 \qquad \text{for } t > 0 \,. \tag{7.1.14}$$

Applying the Laplace transform with respect to t yields the ordinary differential equation

$$\bar{p}'' - \chi s \bar{p} = \chi \frac{\sigma_0}{s} \,, \tag{7.1.15}$$

where $\bar{p}$ is the transform of p, s is the transformation parameter, and the prime denotes the derivative with respect to the argument x. This equation has to be solved with respect to the transformed boundary conditions. The Laplace transform of the pressure distribution becomes

$$\bar{p}(x, s) = \sigma_0 \frac{\cosh(\sqrt{\chi s}x) - \cosh(\sqrt{\chi s}L)}{s^2 \cosh(\sqrt{\chi s}L)} \,. \tag{7.1.16}$$

The transform $\bar{p}(x, s)$ may also serve to evaluate the required integral of the pressure. We have for the transformed integral

$$\begin{aligned}
L\left\{ \int_0^x p(x', t)dx' \right\} &= \int_0^x \bar{p}(x', s)dx' \\
&= \sigma_0 \frac{\sinh(\sqrt{\chi s}x)/(\sqrt{\chi s}) - x\cosh(\sqrt{\chi s}L)}{s^2 \cosh(\sqrt{\chi s}L)} \,,
\end{aligned} \tag{7.1.17}$$

and the last expression, as well as the Laplace transform of the pressure itself, are well suited for numerical inversion. The numerical inversion scheme by Crump (1976) may easily be applied to give the required values of pressure $p(x, t)$ and the entire mechanical load.

7.1.2 Instant axial load on a liquid-filled elastic column causes an increase in liquid pressure

Given size $H = 0.1$ m and length $L = 1$ m the domain represents the rectangular beam $[0, L] \times [0, H] \times [0, H]$. It is discretized by hexahedral elements with section $0 \leq x \leq 0.6\,L$ composed of $10 \times 1 \times 1$ and section $0.6\,L \leq x \leq L$ composed of $60 \times 1 \times 1$ elements. The solid material has been selected elastic with Poisson's ratio $\nu = 0.2$, Young's modulus $E = 30,000$ Pa, and Biot number equal one. An isotropic permeability $k = 10^{-10}$ m^2 and zero porosity is assumed for the material, liquid viscosity is $\mu = 1$ mPa·s and gravity is neglected via zero material and liquid densities. Zero pressure is specified along the face $x = L$, the other faces of the beam are no-flow faces by de-

fault. Except from the face $x = L$ all faces of the beam are sliding planes. Starting from zero initial pressure and zero mechanical load the compressive stress $\sigma_0 = -1000$ Pa is instantly applied at the face $x = L$ for times $t > 0$. The simulation evaluates the transient pressure distribution $p(x, t)$ as well as stresses, strains, and displacements with output after 4 and 10 s (Fig. 7.1.2).
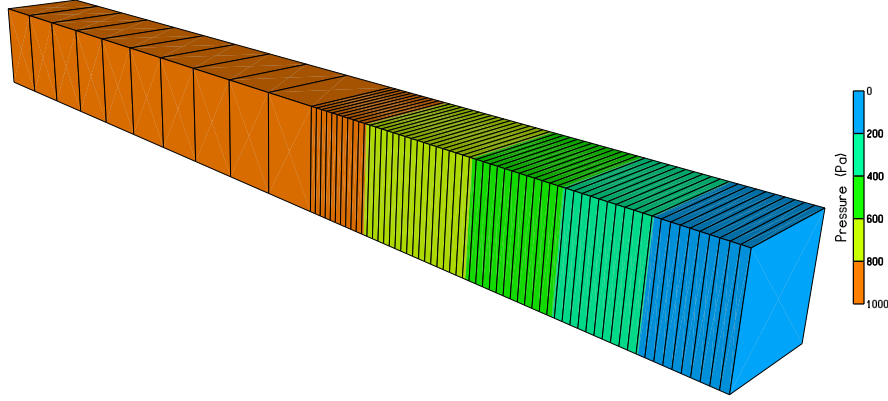

Fig. 7.1.2: Pressure distribution after 10 s

Let $\boldsymbol{\sigma}$ denote the stress tensor and $\mathbf{I}$ the unit tensor. Employing Biot's simplified theory (i.e. Biot number equal one) the equation of mechanical equilibrium reads

$$0 = \nabla \cdot (\boldsymbol{\sigma} - p\,\mathbf{I})\,. \tag{7.1.18}$$

It is satisfied by zero shear, if the stresses σ_{22} and σ_{33} are functions of x only and the horizontal stress σ_{11} satisfies

$$\frac{\partial}{\partial x}(\sigma_{11} - p) = 0\,. \tag{7.1.19}$$

With respect to the prescribed boundary conditions at $x = L$ the last equation yields

$$\sigma_{11} = \sigma_0 U(t) + p\,, \tag{7.1.20}$$

where $U(t)$ denotes the unit step function. Due to the y- and z-fixities along the front, rear, top, and bottom and with principal axes equal to coordinate axes, Hooke's law gives for the strains

$$E \cdot \epsilon_{11} = \sigma_{11} - \nu(\sigma_{22} + \sigma_{33}),$$
$$0 = E \cdot \epsilon_{22} = \sigma_{22} - \nu(\sigma_{11} + \sigma_{33}), \qquad (7.1.21)$$
$$0 = E \cdot \epsilon_{33} = \sigma_{33} - \nu(\sigma_{11} + \sigma_{22}).$$

The strain ϵ_{11} and the stresses σ_{22} and σ_{33} are obtained in terms of the prescribed stress $\sigma_0 U(t)$ and the pressure p

$$\epsilon_{11} = \left(1 - \frac{2\nu^2}{1 - \nu}\right) \frac{1}{E}(\sigma_0 U(t) + p),$$
$$\sigma_{22} = \sigma_{33} = \frac{\nu}{1 - \nu}(\sigma_0 U(t) + p). \qquad (7.1.22)$$

Integrating the strains with respect to the fixities at the coordinate planes yields the displacement vector (u_x, u_y, u_z)

$$u_x(x, t) = \left(1 - \frac{2\nu^2}{1 - \nu}\right) \frac{1}{E} \left[\sigma_0 U(t)x + \int_0^x p(x', t)dx'\right], \qquad (7.1.23)$$
$$u_y = u_z = 0.$$

Therefore, once that the pressure p is known, the displacements and the entire mechanical load may be obtained from the above.

Let q denote the specific discharge via Darcy's law

$$q = -\frac{k}{\mu}\nabla p. \qquad (7.1.24)$$

Conservation of momentum yields

$$0 = \nabla \cdot \left(q + \frac{\partial}{\partial t}(u_x, u_y, u_z)\right). \qquad (7.1.25)$$

For the present example this reduces to

$$0 = -\frac{k}{\mu}\frac{\partial^2 p}{\partial x^2} + \frac{\partial \epsilon_{11}}{\partial t}. \qquad (7.1.26)$$

Introducing the notation

$$\chi = \frac{\mu}{kE}\left(1 - \frac{2\nu^2}{1 - \nu}\right) \qquad (7.1.27)$$

the pressure distribution $p(x, t)$ is governed by the parabolic equation

$$\frac{\partial^2 p}{\partial x^2} - \chi\frac{\partial p}{\partial t} = \chi\sigma_0\frac{d}{dt}U(t), \qquad (7.1.28)$$

subject to the initial condition

$$p(x,0) = 0 \qquad \text{for } 0 \le x \le L \,, \tag{7.1.29}$$

the no-flow boundary condition at $x = 0$

$$\frac{\partial p}{\partial x}(0,t) = 0 \qquad \text{for } t > 0 \,, \tag{7.1.30}$$

and zero pressure at $x = L$

$$p(L,t) = 0 \qquad \text{for } t > 0 \,. \tag{7.1.31}$$

Applying the Laplace transform with respect to t yields the ordinary differential equation

$$\bar{p}'' - \chi s \bar{p} = \chi \sigma_0 \,, \tag{7.1.32}$$

where $\bar{p}$ is the transform of p, s is the transformation parameter, and the prime denotes the derivative with respect to the argument x. This equation has to be solved with respect to the transformed boundary conditions. The Laplace transform of the pressure distribution becomes

$$\bar{p}(x,s) = \sigma_0 \frac{\cosh(\sqrt{\chi s}x) - \cosh(\sqrt{\chi s}L)}{s \cosh(\sqrt{\chi s}L)} \,. \tag{7.1.33}$$

The transform $\bar{p}(x,s)$ may also serve to evaluate the required integral of the pressure. We have for the transformed integral

$$
\begin{aligned}
L\left\{ \int_0^x p(x',t)dx' \right\} &= \int_0^x \bar{p}(x',s)dx' \\
&= \sigma_0 \frac{\sinh(\sqrt{\chi s}x)/(\sqrt{\chi s}) - x\cosh(\sqrt{\chi s}L)}{s \cosh(\sqrt{\chi s}L)} \,,
\end{aligned}
\tag{7.1.34}
$$

and the last expression, as well as the Laplace transform of the pressure itself, are well suited for numerical inversion. The numerical inversion scheme by Crump (1976) may easily be applied to give the required values of pressure $p(x,t)$ and the entire mechanical load.

7.1.3 Mandel's setup: Instant squeezing of a liquid-filled elastic column perpendicular to its central axis causes an increase in liquid pressure

Given size $H = 0.1$ m and length $L = 1$ m the domain represents the rectangular beam $[0,L] \times [0,H] \times [0,H]$. It is discretized by hexahedral elements with section $0 \le x \le 0.6\,L$ composed of $10 \times 2 \times 2$ and section $0.6\,L \le x \le L$ composed of $60 \times 2 \times 2$ elements. The solid material has been selected elastic

with Poisson's ratio $\nu = 0.2$, Young's modulus $E = 30,000$ Pa, and Biot number equal one. An isotropic permeability $k = 10^{-10}$ m^2 and zero porosity is assumed for the material, liquid viscosity is $\mu = 1$ mPa·s and gravity is neglected via zero material and liquid densities. Zero pressure is specified along the face $x = L$, the other faces of the beam are no-flow faces by default. The faces on the coordinate planes and the face $y = H$ are sliding planes. Starting from zero initial pressure and zero mechanical load the vertical displacement $w = -10^{-2}$ m is instantly applied along the top face $z = H$ for times $t > 0$. The simulation evaluates the transient pressure distribution $p(x, t)$ as well as stresses, strains, and displacements with output after 2 and 8 s (Fig. 7.1.3).
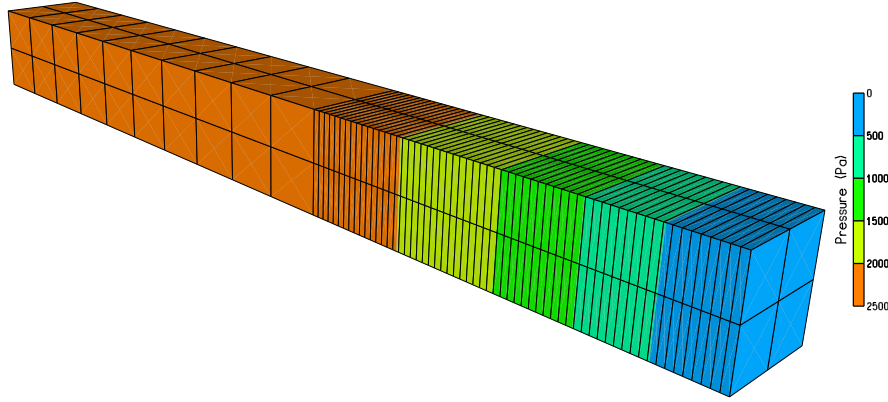

Fig. 7.1.3: Pressure distribution after 8 s

Let $\boldsymbol{\sigma}$ denote the stress tensor and $\mathbf{I}$ the unit tensor. Employing Biot's simplified theory (i.e. Biot number equal one) the equation of mechanical equilibrium reads

$$0 = \nabla \cdot (\boldsymbol{\sigma} - p\,\mathbf{I})\,. \tag{7.1.35}$$

It is satisfied by zero shear, if the stresses σ_{22} and σ_{33} are functions of x only and the horizontal stress σ_{11} satisfies

$$\frac{\partial}{\partial x}(\sigma_{11} - p) = 0\,. \tag{7.1.36}$$

With respect to the prescribed boundary conditions at $x = L$ the last equation yields

$$\sigma_{11} = p\,. \tag{7.1.37}$$

The strains ϵ_{22} and ϵ_{33} are obtained from the problem setup. Due to the y-fixities along the faces $y = 0$ and $y = H$

$$\epsilon_{22} = 0 \,. \tag{7.1.38}$$

Due to the z-fixity along the face $z = 0$ and the specified z-displacement along the face $z = H$

$$\epsilon_{33} = \frac{w}{H} U(t) \,, \tag{7.1.39}$$

where $U(t)$ denotes the unit step function. Then, with principal axes equal to coordinate axes, Hooke's law reads for the strains

$$\epsilon_{11} = \frac{1}{E}[\sigma_{11} - \nu(\sigma_{22} + \sigma_{33})] = \frac{1}{E}[p - \nu(\sigma_{22} + \sigma_{33})] \,,$$
$$0 = \epsilon_{22} = \frac{1}{E}[\sigma_{22} - \nu(\sigma_{11} + \sigma_{33})] = \frac{1}{E}[\sigma_{22} - \nu(p + \sigma_{33})] \,, \tag{7.1.40}$$
$$\frac{w}{H}U(t) = \epsilon_{33} = \frac{1}{E}[\sigma_{33} - \nu(\sigma_{11} + \sigma_{22})] = \frac{1}{E}[\sigma_{33} - \nu(p + \sigma_{22})] \,.$$

The strain ϵ_{11} and the stresses σ_{22} and σ_{33} are obtained in terms of the prescribed vertical displacement and the pressure p

$$\epsilon_{11} = -\frac{\nu}{1-\nu}\frac{w}{H}U(t) + (1 - \frac{2\nu^2}{1-\nu})\frac{p}{E} \,,$$

$$\sigma_{22} = \frac{E\nu}{1-\nu^2}\frac{w}{H}U(t) + \frac{\nu}{1-\nu}p \,, \tag{7.1.41}$$

$$\sigma_{33} = \frac{E}{1-\nu^2}\frac{w}{H}U(t) + \frac{\nu}{1-\nu}p \,.$$

Integrating the strains with respect to the fixities at the coordinate planes yields the displacement vector (u_x, u_y, u_z)

$$u_x(x,t) = -\frac{\nu}{1-\nu}\frac{w}{H}U(t)x + (1 - \frac{2\nu^2}{1-\nu})\frac{1}{E}\int_0^x p(x',t)dx' \,,$$

$$u_y = 0 \,, \tag{7.1.42}$$

$$u_z(z,t) = z\frac{w}{H}U(t) \,.$$

Therefore, once that the pressure p is known, the displacements and the entire mechanical load may be obtained from the above.

Let q denote the specific discharge via Darcy's law

$$q = -\frac{k}{\mu}\nabla p \,. \tag{7.1.43}$$

Conservation of momentum yields

$$0 = \nabla \cdot \left(q + \frac{\partial}{\partial t}(u_x, u_y, u_z) \right). \tag{7.1.44}$$

For the present example this reduces to

$$0 = -\frac{k}{\mu}\frac{\partial^2 p}{\partial x^2} + \frac{\partial}{\partial t}(\epsilon_{11} + \epsilon_{33}). \tag{7.1.45}$$

Introducing the notation

$$\chi = \frac{\mu}{kE}\left(1 - \frac{2\nu^2}{1 - \nu} \right) \tag{7.1.46}$$

the pressure distribution $p(x,t)$ is governed by the parabolic equation

$$\frac{\partial^2 p}{\partial x^2} - \chi\frac{\partial p}{\partial t} = \frac{\mu}{k}\frac{1 - 2\nu}{1 - \nu}\frac{w}{H}\frac{d}{dt}U(t), \tag{7.1.47}$$

subject to the initial condition

$$p(x, 0) = 0 \qquad \text{for } 0 \leq x \leq L, \tag{7.1.48}$$

the no-flow boundary condition at $x = 0$

$$\frac{\partial p}{\partial x}(0, t) = 0 \qquad \text{for } t > 0, \tag{7.1.49}$$

and zero pressure at $x = L$

$$p(L, t) = 0 \qquad \text{for } t > 0. \tag{7.1.50}$$

Applying the Laplace transform with respect to t yields the ordinary differential equation

$$\bar{p}'' - \chi s\bar{p} = \frac{\mu}{k}\frac{1 - 2\nu}{1 - \nu}\frac{w}{H}, \tag{7.1.51}$$

where $\bar{p}$ is the transform of p, s is the transformation parameter, and the prime denotes the derivative with respect to the argument x. This equation has to be solved with respect to the transformed boundary conditions. The Laplace transform of the pressure distribution becomes

$$\bar{p}(x, s) = \frac{E}{1 + \nu}\frac{w}{H}\frac{\cosh(\sqrt{\chi s}x) - \cosh(\sqrt{\chi s}L)}{s\cosh(\sqrt{\chi s}L)}. \tag{7.1.52}$$

The transform $\bar{p}(x, s)$ may also serve to evaluate the required integral of the pressure. We have for the transformed integral

$$L\left\{\int_0^x p(x',t)dx'\right\} = \int_0^x \bar{p}(x',s)dx'$$

$$= \frac{E}{1+\nu}\frac{w}{H}\frac{\sinh(\sqrt{\chi s}x)/(\sqrt{\chi s}) - x\cosh(\sqrt{\chi s}L)}{s\cosh(\sqrt{\chi s}L)}, \tag{7.1.53}$$

and the last expression, as well as the Laplace transform of the pressure itself, are well suited for numerical inversion. The numerical inversion scheme by Crump (1976) may easily be applied to give the required values of pressure $p(x,t)$ and the entire mechanical load.

7.2 Mont Terri Project - HM-behaviour in the EZB niche

by Gesa Ziefle

This benchmark focuses on coupled hydromechanical processes in a low permeable, anisotropic claystone formation with swelling and shrinkage behaviour. Significant research concerning the behaviour of this kind of material due to various thermal and mechanical loads is carried out in the Mont Terri URL in Switzerland. Here, numerous partners of different countries investigate the behaviour of claystone in various experiments. The focus of the following benchmark is laid on the CD/LP experiment which deals with the hydromechanical effects due to seasonal oscillations of the climatic atmosphere in an uncovered niche (EZB-niche). Long-term measurements of temperature, relative humidity and the convergence of the niche are carried out. Furthermore, crackmeter as well as jointmeter observe the geometric alterations of cracks at the surface of the niche. The measurements for the relative humidity and temperature are presented in Figure 7.2.1; more information can be found in e.g. (Möri et al., 2010), (Girardin and Nussbaum, 2006) and (Matray and Möri, 2012). The model setup for the OGS simulation is done for a 2D-model, representing the near field of the niche.

7.2.1 Model setup

To picture the effects in the EZB niche a fully coupled hydromechanical simulation is carried out in a staggered scheme. Coupling effects from the hydraulic to the mechanical process as well as from the mechanical to the hydraulic process are of significant interest in this benchmark. Consequently, the presented model focuses on the coupling, the hydraulic and mechanical orthotropy as well as shrinkage and swelling effects in the claystone formation. The grav-
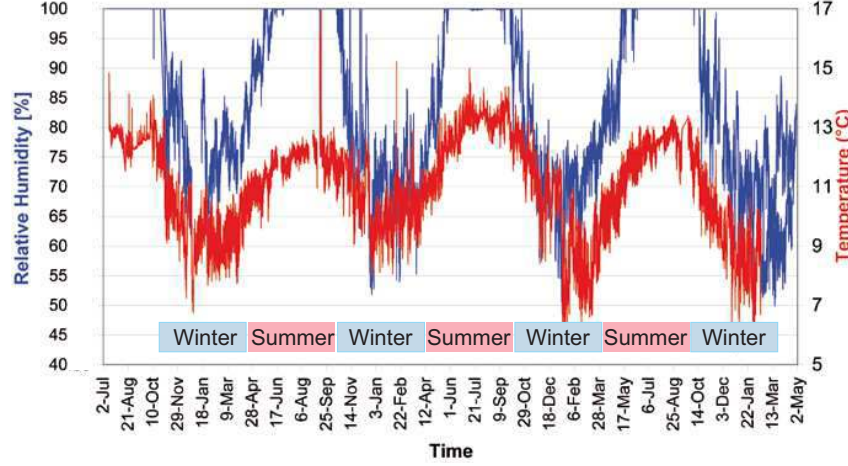
Fig. 7.2.1: Temporal evolution of the relative humidity and the temperature.

ity and the excavation process are neglected. The simulation is carried out on a 2–dimensional domain with an extent of 50 m times 50 m. The initial conditions imply a fully saturated area of Opalinus clay. The boundaries are assumed to remain fully saturated. The detailed model setup as well as the FE–mesh are presented in Figure 7.2.2.

The far–field compressive stresses are specified as initial stresses and assumed to be 7 MPa in the vertical direction and 5 MPa in the horizontal direction. More information about the in–situ stress field at the Mont Terri rock laboratory can be found in (Martin and Lanyon, 2003). The bedding plane has an inclination of 10° in this part of the laboratory and the displacements are prevented in the horizontal direction at the left boundary and in the vertical direction at the bottom of the presented area. Furthermore, a pressure boundary condition at the boundary of the niche represents the seasonal changes of the temperature and the relative humidity in the niche. This boundary condition is characterized by negative pore pressures (suction) and is based on the measurements of the relative humidity and the temperature in the niche as presented in Figure 7.2.1. The Kelvin equation is used to derive the pressure boundary condition. It is given by

$$p = \frac{\rho_l R T}{M_v} \cdot \ln h_{rel} \qquad (7.2.1)$$

with the liquid density ρ_l, the perfect gas constant R, the temperature T, the molecular weight of water M_v and the relative humidity h_{rel}. The relation between capillary pressure and saturation is defined by the van Genuchten model
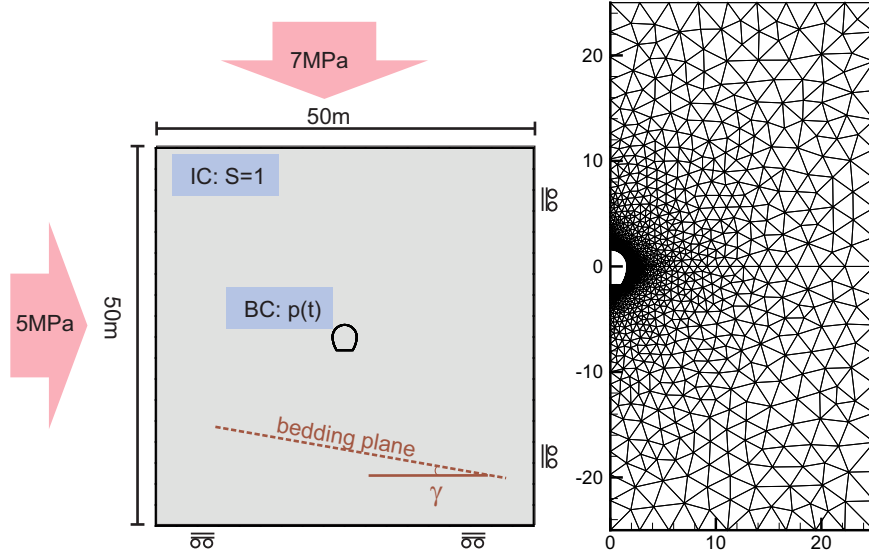
Fig. 7.2.2: Geometry and model setup (left) and part of the FE–mesh (right).

$$S = \left[1 + \left(\frac{p}{P_0}\right)^{1/(1-\beta)}\right]^{-\beta} \tag{7.2.2}$$

with the saturation S, the suction pressure p and the van Genuchten fitting parameters P_0 and β according to Wild et al. (2014). The hydraulic and mechanical parameters are summarized in Table 7.2.1.

The flow process in the hydraulically orthotropic claystone is simulated by the Richard's approach while the mechanical effects are depicted by an orthotropic, linear elastic material model. As the initial pore pressure would cause additional strains, the initial pore pressure is neglected in the stress calculation. The desaturation of the Opalinus clay implies shrinkage and swelling behaviour. This effect is incorporated in the model by an isotropic, linear swelling model, proposed by (Rutqvist et al., 2001). Information about the swelling behaviour of the claystone can be found in (Martin and Lanyon, 2003). The coupling effects are considered using the well–known Biot constant and furthermore the Bishop coefficient. A similar model is used and presented in detail in section 9.1. This model approach implies that classical Terzaghi coupling effects are restricted to the fully saturated case. For the unsaturated case the coupling is mainly caused by the swelling and shrinkage behaviour. The material parameters are summarized in Table 7.2.1. More information can be found in (Wild et al., 2014) and (Bock, 2008) amongst others.

Table 7.2.1: Hydraulic and mechanical material parameters

| Parameter	Value	Unit
Angle of inclination, γ	10.0	$\circ$
Porosity, n	0.16	-
Perm. in the plane of isotropy, $k_\parallel$	$3.91 \cdot 10^{-20}$	m^2
Perm. normal to the plane of isotropy, $k_\perp$	$7.82 \cdot 10^{-21}$	m^2
$k_\parallel / k_\perp$	5	-
Liquid density, ρ_l	1000	kg/m^3
Perfect gas constant, R	8.314	$J/(K\ mol)$
Molecular weight water, M_s	0.018	kg/mol
Biot constant, α	1.0	-
Bishop coefficient, χ	1.0 - 0.0	-
Grain density claystone, ρ_s	2500	kg/m^3
Poisson number normal to the plane of isotropy, $\nu_\perp$	0.16	-
E in the plane of isotropy, $E_\parallel$	$3.6 \cdot 10^9$	N/m^2
E normal to the plane of isotropy, $E_\perp$	$1.1 \cdot 10^9$	N/m^2
G normal to the plane of isotropy, $G_\perp$	$1.2 \cdot 10^9$	N/m^2
Max. swelling pressure, $p_{sw,max}$	$1.1 \cdot 10^7$	N/m^2
Van Genuchten parameter, P_0	$44.4 \cdot 10^6$	Pa
Van Genuchten parameter, β	0.54	-
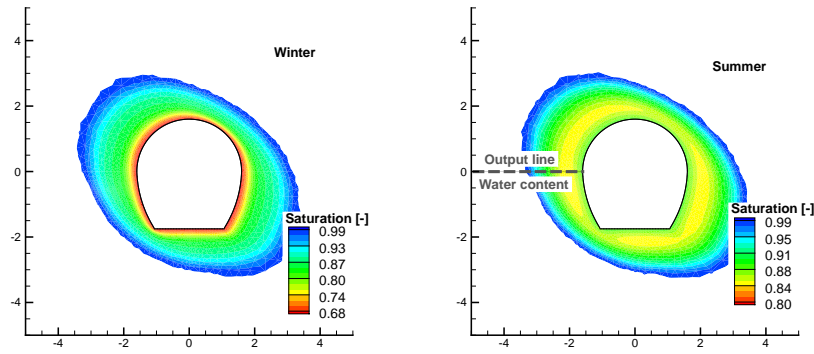
Fig. 7.2.3: Desaturated area in winter (left) and summer (right) after 7 years of atmospheric influences.

7.2.2 Results

The presented model represents a desaturation of the claystone due to the climatic conditions in the niche. While the desaturated zone increases in the cold and dry wintertime, there exists a temporary resaturation close to the tunnel in the warm, wet summer months. The desaturated zone for the summer as well as the winter case is presented in Figure 7.2.3 after 7 years of atmospheric influences. The extent of the desaturated zone reaches its maximum in the direction of the bedding and has an extent of nearly 2 m at

this time. Figure 7.2.4 shows the water content versa the distance from the niche (the output line is defined in Figure 7.2.3 (right)) for the summer as well as the winter time. While the seasonally influenced desaturated zone is characterized by the ongoing change between desaturation and resaturation, the water content in the longterm desaturated zone undergoes only minor changes due to the long term development.
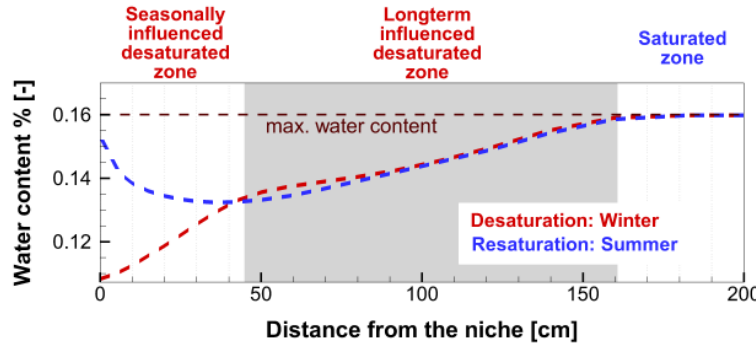

Fig. 7.2.4: Water content versa the distance from the niche for the horizontal line given in Figure 7.2.3 (right).

Concerning the mechanical processes, the desaturation implies an area of compaction due to the shrinkage of the material. The resulting stress state is given in Figure 7.2.5 for the winter time. Here, a decrease of the compressive stresses can be observed in the near field of the niche. The related vertical and horizontal displacements are given in Figure 7.2.6 for the winter time and indicate a comparatively large affected zone with movements towards the desaturated area. They correspond to the deformation of the niche profile presented in Figure 7.2.7. The comparison of the presented results with measurements indicates that the hydraulic behaviour can be pictured well. The mechanical model fits the trend of the niche deformation quite well, but it underestimates the measured deformation of the niche quantitatively.
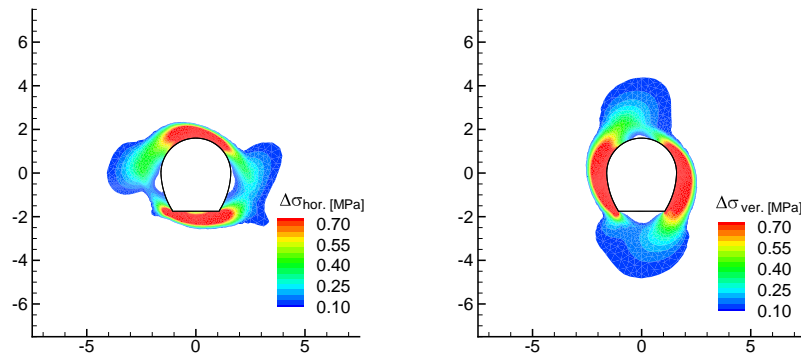
Fig. 7.2.5: Decrease of the compressive stresses after 7 years of atmospheric influences (left: horizontal stresses; right: vertical stresses).
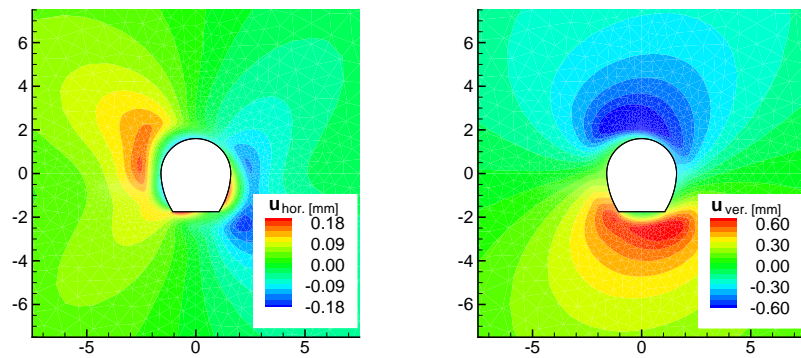

Fig. 7.2.6: Horizontal (left) and vertical (right) displacements after 7 years of atmospheric influences.
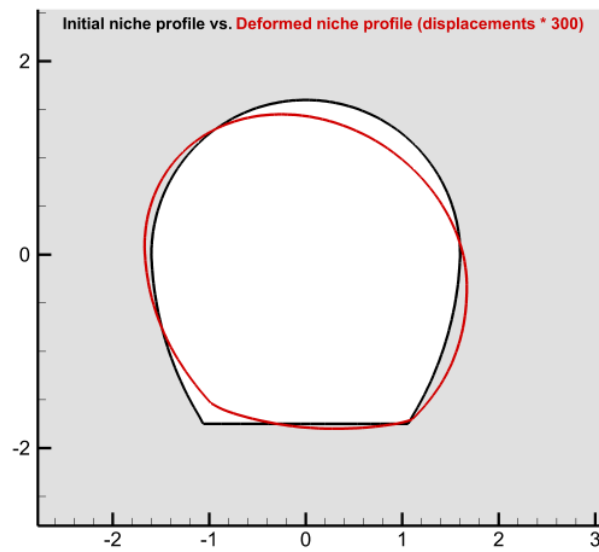
Fig. 7.2.7: Deformed niche (scaling factor: 300) in comparison with the original tunnel profile

7.3 Hydro-mechanical application: SEALEX Experiment

by Haiyang Yi, Wenqing Wang, Hongwei Zhou

This section includes numerical modeling of compression tests under suction control and small scale hydro-mechanical coupled tests of bentonite/sand mixture. These two tests are parts of the SEALEX experiment, which are aimed at hydro-mechanical properties of bentonite/sand mixture. The numerical modeling is based on the task description of Task A of the DECOVALEX-2015 project.

7.3.1 Governing equations

A constitutive equation based on Richard's equation is given as(Kolditz et al., 2012b)

$$-\eta\rho_w\frac{\partial S}{\partial p_\mathrm{c}}\frac{\partial p}{\partial t} - \nabla\cdot\left[\rho_w\frac{\mathbf{K}k_\mathrm{rel}}{\mu}\left(\nabla p - \rho g\right)\right] + S\rho_w\nabla\cdot\dot{\mathbf{u}} = Q_w \qquad (7.3.1)$$

where n represents the porosity, S stands for the saturation, p and P_c mean pressure and capillary pressure, respectively, ρ is the density, μ is the viscosity, k_rel is the relative permeability, $\mathbf{K}$ is the intrinsic permeability, $\mathbf{u}$ denotes the displacement, and Q_w is the source/sink term. The deformation process is described on the basis of momentum balance as (Wang et al., 2009)

$$\nabla\cdot\left(\boldsymbol{\sigma}' - Sp\mathbf{I}\right) + \rho_s\,\mathbf{g} = 0 \qquad (7.3.2)$$

$$\dot{\boldsymbol{\sigma}}' = \mathbf{D}\,\dot{\boldsymbol{\epsilon}} + \dot{\boldsymbol{\sigma}}^{sw}qa \qquad (7.3.3)$$

$$\dot{\boldsymbol{\sigma}}^{sw} = \sigma_\mathrm{max}^{sw}\dot{S}\mathbf{I} \qquad (7.3.4)$$

$\mathbf{D}$ is a fourth order elasto-plastic tensor, $\dot{\boldsymbol{\sigma}}^{sw}$ indicates the stress ratio induced by the swelling and σ_max^{sw} represents the maximum swelling stress in tests.

The generalized Cam-Clay model is adopted for the plastic deformation which is defined as

$$f = g = q^2 + M^2 p_\mathrm{s}\left(p_\mathrm{s} - p_\mathrm{scn}\right), \qquad (7.3.5)$$

where f is the yield function, g is the plastic potential, q, p_s and p_scn are the shear stress, the mean stress and isotropic pre-consolidation pressure, respectively, M denotes the slope of the critical state line. The mean stress and volume plastic strain have the relationship of

$$\frac{dp_\mathrm{s}}{d\epsilon_\mathrm{v}} = \frac{(1+e)\,p_\mathrm{s}}{\lambda_\mathrm{c} - k_\mathrm{c}} \tag{7.3.6}$$

where e is the void ratio, ϵ_v is the volume plastic strain, λ_c denotes the virgin compression index, k_c represents swelling/recompression index.

7.3.2 Parameter identification

According to the gravimetric water content versus suction data in reference (Wang et al., 2013a), we get effective saturation versus suction data as shown in Fig. 7.3.1. The porosity and residual saturation are calculated as 0.279 and 0.2 based on the data in reference (Wang et al., 2013a), respectively. The initial saturation is 0.2828 corresponding to initial water content of 11 %.

The van Genuchten model was employed for fitting the effective saturation-suction curve. The fitting equation is

$$P = \frac{\rho g}{\alpha}((S_\mathrm{e})^{-\frac{1}{m}} - 1)^{\frac{1}{\eta}} \tag{7.3.7}$$

$$m = 1 - \frac{1}{\eta} \tag{7.3.8}$$
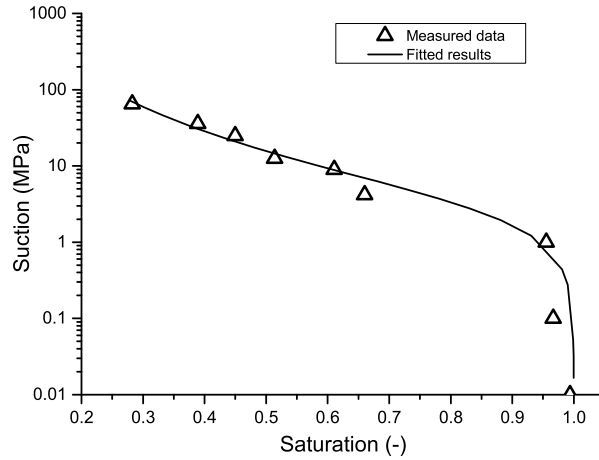
The fitting parameters are m=0.2857 and α=0.0033.

Fig. 7.3.1: Saturation-suction curves

The permeability-saturation curve is defined as:

$$k_\mathrm{rel} = (S_\mathrm{e})^3 \tag{7.3.9}$$

Model setup and calculation in detail are described in following sections. All the models in this report adopted quadrilateral element mesh. Liquid in the tests is water which has a density of $1000\,\mathrm{kg/m^3}$ and viscosity of $0.001\,\mathrm{Pa \cdot s}$.

Two groups of parameters for bentonite were applied corresponding to different densities in calculations. In which, the sample with density of $1970\,\mathrm{kg/m^3}$ has a porosity of 0.279, intrinsic permeability of $4.3 \times 10^{-21}\,\mathrm{m^2}$, passion ratio of 0.3, Young's modulus of $8.6\,\mathrm{MPa}$ and maximum swelling stress of $4.68\,\mathrm{MPa}$ MPa. The sample with density of $1670\,\mathrm{kg/m^3}$ has a porosity of 0.389, intrinsic permeability of $1.3 \times 10^{-21}\,\mathrm{m^2}$ and others are the same as that of sample with density of $1970\,\mathrm{kg/m^3}$.

7.3.3 Compression under suction control

The detailed description of the compression tests under suction control can be found in reference (Wang et al., 2013c). The analyzed models for free swell and compression are still axisymmetric. Firstly, for sample SO-02 04, the out ring edge was fixed in displacement of vertical direction and bottom edge in displacement of radial direction, water inlet from the bottom edge. When suction of the detecting point arrived at $4.2\,\mathrm{MPa}$, $12.6\,\mathrm{MPa}$ and $38\,\mathrm{MPa}$, load a pressure of $50\,\mathrm{MPa}$ at top edge within 100 steps, and then unload the top pressure in another 100 steps. For sample SO-01, let it free swell until fill the oedometric cell, then following with the same as SO-02, 03 and 04.

After the suction of detected points reach to $0.001\,\mathrm{MPa}$, $4.2\,\mathrm{MPa}$, $12.6\,\mathrm{MPa}$ and $38\,\mathrm{MPa}$, the stress conditions were recorded for the initial stress of the Cam-Clay model in the compression process. The virgin compression index and slop of swelling line were determined by fitting work as shown in Fig. 7.3.2. The initial void ratios were calculated from the deformation in the swelling stage. Slope of the critical state line is 1.94 for SO-01 and 1.84 for SO-02, 03 and 04.

7.3.4 1/10 scale mock-up tests

The small scale mock-up tests aim at laboratory investigating in the hydro-mechanical properties of bentonite/sand mixture. Reference Wang et al. (2013b) gives a detailed description on the setup of those tests. In brief, there are three phases involving in the tests. There is a technical void existing between the bentonite and load cell initially.

An axisymmetric model was employed for simulating the mock-up tests. In the first phase, water inlet from the bottom and out ring edge (water fill the gap), and then fix the out ring edge in radial displacement and let water
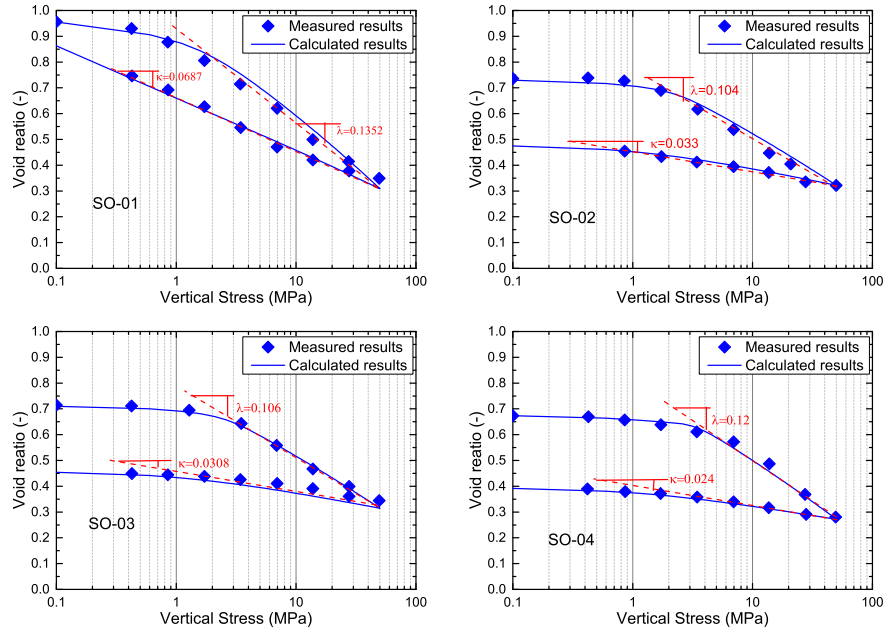
Fig. 7.3.2: Measured and calculated void ratio-vertical stress data

only inlet from the bottom edge when the out ring edge reach the inner face of the cell. In the second phase, free top displacement initially for 14 days (2.8 % in displacement), then let water inlet from both top and bottom edge. In the third phase, the axial displacement of top edge is fixed.

In the mock-up tests, the pressure was measured at the top face. Initially, as water filled in the gap, then the force sensor would detect the pressure around out ring of top end, then the maximum vertical stress will move towards the center in calculation. Therefore the stresses at both points of out ring edge and middle node at top end were calculated, and their proposition in the total stress is 75:25. In phase 1, after 9 days' free swell, the load cell was filled with the sample. The durations of phase 1, 2 and 3 are 350 days, 50 days and 100 days, respectively. The vertical pressure-time results are shown in Fig. 7.3.3(a) and (c). The axial displacement versus time of phase 2 is plotted in Fig. 7.3.3(b).

7.3.5 Conclusion

Although the calculated results of mock up test seem a little different from the experimental data, the tendency is still similar. Interestingly, the calculated
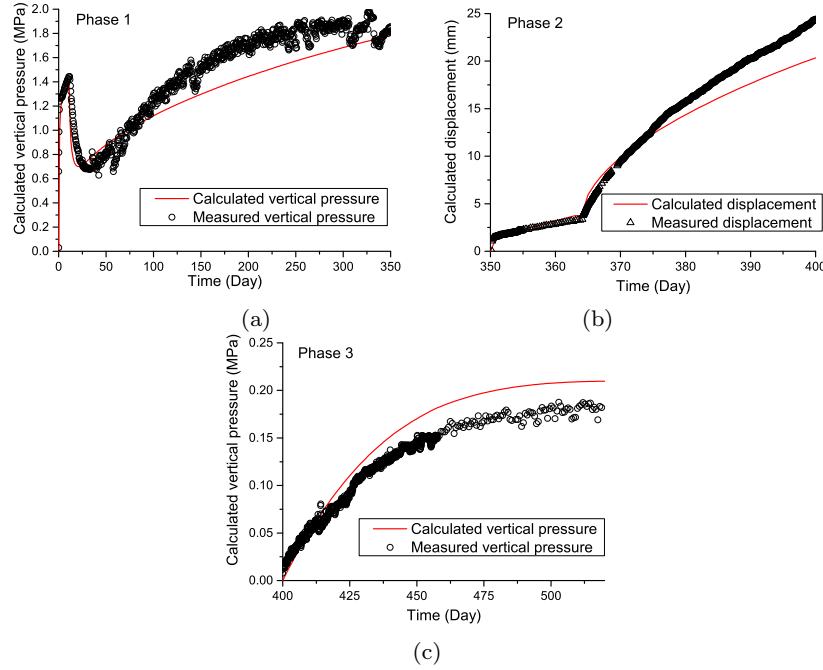
Fig. 7.3.3: Experimental and calculated results of mock-up tests (a)-(c) corresponding to phase 1-3

results of compression test under suction control fit the experimental data greatly. In addition, The parameters are identified from the SEALEX experiment. All of these indicate that the model, especial the Cam-Clay model, and parameters are capable for describing the hydro-mechanical coupling processes of the bentonite/sand mixture.

Acknowledgments

Chapter 8
Thermomechanics

by Thomas Nagel, Peter Vogel, Jobst Maßmann

8.1 Heated beams and plates

Peter Vogel and Jobst Maßmann

This section presents a set of closed form solutions of 3D steady-state problems on heated beams and plates which have been adopted from Kneschke (1960). The associated simulation exercises have been checked by OGS; they may serve as verification tests. We focus on the closed form solutions; for the underlying theory of linear thermoelasticity see Carlson (1972) or see Melan and Parkus (1953).

8.1.1 An elastic beam deformes due to an instant temperature change

Given length $2L = 20$ m and thickness $2H = 1$ m the domain represents the rectangular beam $[-L, L] \times [-H, H] \times [-H, H]$. It is discretized by $20 \times 4 \times 4$ equally sized hexahedral elements. The solid material has been selected elastic with Young's modulus $E = 10,000$ MPa, Poisson's ratio $\nu = 0.2$, zero heat capacity, and thermal expansion $\alpha = 10^{-3}$ 1/K. Gravity is neglected via zero material density. The faces $y = H$ and $y = -H$ are sliding planes, the remaining faces are free of load by default. Fixities have been prescribed in the interior of the domain with zero x-displacement along the plane $x = 0$, and zero z-displacement at the origin. The simulation starts from zero initial temperature and comprises one timestep applying an instant temperature

change with temperature $T_1 = -10\,^\circ\mathrm{C}$ at $z = H$ and temperature $T_0 = 10\,^\circ\mathrm{C}$ at $z = -H$.

The formal solution proceeds in two steps, first to solve for the temperature distribution and then to evaluate stresses, strains, and displacements (u_x, u_y, u_z) (Fig. 8.1.1 and 8.1.2). The Laplace equation is the governing
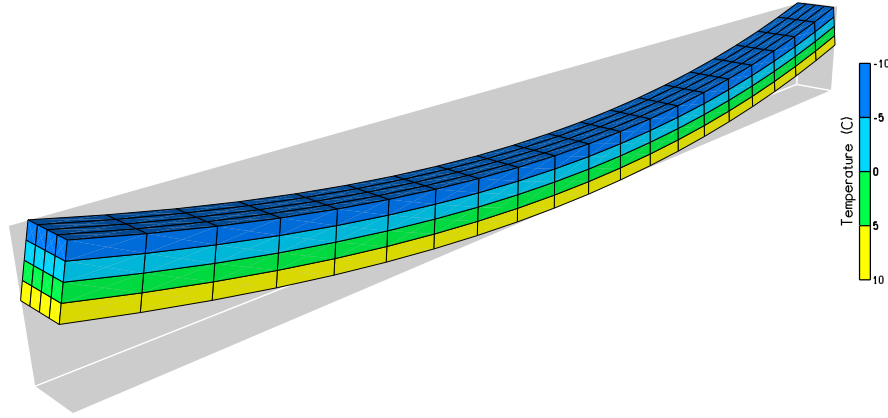

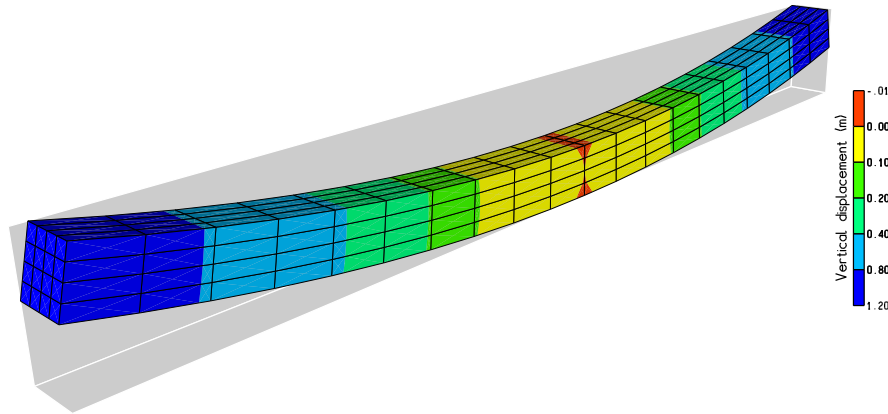Fig. 8.1.1: Deformed mesh, temperature distribution

Fig. 8.1.2: Deformed mesh, vertical displacements

equation describing the steady-state temperature distribution. It reads

$$\frac{d^2T}{dz^2} = 0 \qquad (8.1.1)$$

for 1D heat flow along the z-axis. The temperature distribution

$$T(z) = \frac{T_1 - T_0}{2H}z \qquad (8.1.2)$$

satisfies the Laplace equation and the specified temperature boundary conditions, hence, this is the closed form solution of the temperature problem.

For the closed form solution of the mechanical problem note, that due to the simulation setup, the applied temperature change is identical to the above $T(z)$. The constitutive equations relate the strains $\epsilon_{11}, \epsilon_{22}, \epsilon_{33}$ (in x-, y-, and z-direction, respectively) and the associated stresses $\sigma_{11}, \sigma_{22}, \sigma_{33}$ via

$$\begin{aligned}
\epsilon_{11} - \alpha\frac{T_1 - T_0}{2H}z &= \frac{1}{E}[\sigma_{11} - \nu(\sigma_{22} + \sigma_{33})]\,, \\
\epsilon_{22} - \alpha\frac{T_1 - T_0}{2H}z &= \frac{1}{E}[\sigma_{22} - \nu(\sigma_{11} + \sigma_{33})]\,, \qquad (8.1.3)\\
\epsilon_{33} - \alpha\frac{T_1 - T_0}{2H}z &= \frac{1}{E}[\sigma_{33} - \nu(\sigma_{11} + \sigma_{22})]\,.
\end{aligned}$$

Because the problem setup does not depend on the y-coordinate and due to the y-fixities along the faces $y = H$ and $y = -H$ the y-direction is free of strain

$$\epsilon_{22} = 0\,. \qquad (8.1.4)$$

The top face and the bottom face as well as the faces $x = L$ and $x = -L$ are free of load, hence, they are free of normal stress. These boundary conditions are satisfied by

$$\sigma_{11} = \sigma_{33} = 0\,. \qquad (8.1.5)$$

The remaining diagonal elements of stress tensor and strain tensor become

$$\begin{aligned}
\sigma_{22} &= -E\alpha\frac{T_1 - T_0}{2H}z\,, \\
\epsilon_{11} &= \frac{\partial u_x}{\partial x} = (1+\nu)\alpha\frac{T_1 - T_0}{2H}z\,, \qquad (8.1.6)\\
\epsilon_{33} &= \frac{\partial u_z}{\partial z} = (1+\nu)\alpha\frac{T_1 - T_0}{2H}z\,.
\end{aligned}$$

Integrating the strains yields the displacement vector (u_x, u_y, u_z)

$$u_x(x, z) = (1 + \nu)\alpha \frac{T_1 - T_0}{2H} xz + f(z) \,,$$

$$u_y = 0 \,, \tag{8.1.7}$$

$$u_z(x, z) = (1 + \nu)\frac{\alpha}{2}\frac{T_1 - T_0}{2H} z^2 + g(x) \,,$$

where $f(z)$ and $g(x)$ have to be determined from the specified fixities and the default boundary conditions. Due to the x-fixities along the plane $x = 0$

$$f(z) = 0 \,. \tag{8.1.8}$$

The shear strains become

$$\epsilon_{12} = \frac{\partial u_x}{\partial y} + \frac{\partial u_y}{\partial x} = 0 \,,$$

$$\epsilon_{23} = \frac{\partial u_y}{\partial z} + \frac{\partial u_z}{\partial y} = 0 \,, \tag{8.1.9}$$

$$\epsilon_{13} = \frac{\partial u_x}{\partial z} + \frac{\partial u_z}{\partial x} = (1 + \nu)\alpha \frac{T_1 - T_0}{2H} x + \frac{dg}{dx} \,.$$

The top face and the bottom face as well as the faces $x = L$ and $x = -L$ are free of load, hence, they are free of shear stresses, and therefore

$$\epsilon_{13} = 0 \,. \tag{8.1.10}$$

This yields

$$g(x) = -(1 + \nu)\frac{\alpha}{2}\frac{T_1 - T_0}{2H} x^2 + C \,, \tag{8.1.11}$$

and the entire domain is free of shear

$$\epsilon_{12} = \epsilon_{13} = \epsilon_{23} = 0, $$
$$\sigma_{12} = \sigma_{13} = \sigma_{23} = 0. \tag{8.1.12}$$

The free constant C has to be determined from the z-fixity at the origin. The displacement vector (u_x, u_y, u_z) becomes

$$u_x(x, z) = (1 + \nu)\alpha \frac{T_1 - T_0}{2H} xz \,,$$

$$u_y = 0 \,, \tag{8.1.13}$$

$$u_z(x, z) = (1 + \nu)\frac{\alpha}{2}\frac{T_1 - T_0}{2H}(z^2 - x^2) \,.$$

These displacements yield the volumetric strain

$$e = \frac{\partial u_x}{\partial x} + \frac{\partial u_y}{\partial y} + \frac{\partial u_z}{\partial z} = (1+\nu)\alpha \frac{T_1 - T_0}{2H} 2z \,, \qquad (8.1.14)$$

the Laplacian of u_x, u_y, and u_z

$$\frac{\partial^2 u_x}{\partial x^2} + \frac{\partial^2 u_x}{\partial y^2} + \frac{\partial^2 u_x}{\partial z^2} = 0 \,,$$

$$\frac{\partial^2 u_y}{\partial x^2} + \frac{\partial^2 u_y}{\partial y^2} + \frac{\partial^2 u_y}{\partial z^2} = 0 \,, \qquad (8.1.15)$$

$$\frac{\partial^2 u_z}{\partial x^2} + \frac{\partial^2 u_z}{\partial y^2} + \frac{\partial^2 u_z}{\partial z^2} = 0 \,,$$

and the displacement-temperature equations of equilibrium

$$\frac{\partial^2 u_x}{\partial x^2} + \frac{\partial^2 u_x}{\partial y^2} + \frac{\partial^2 u_x}{\partial z^2} + \frac{1}{1-2\nu} \frac{\partial e}{\partial x} = 0 = \frac{2(1+\nu)}{1-2\nu} \alpha \frac{\partial T}{\partial x} \,,$$

$$\frac{\partial^2 u_y}{\partial x^2} + \frac{\partial^2 u_y}{\partial y^2} + \frac{\partial^2 u_y}{\partial z^2} + \frac{1}{1-2\nu} \frac{\partial e}{\partial y} = 0 = \frac{2(1+\nu)}{1-2\nu} \alpha \frac{\partial T}{\partial y} \,, \qquad (8.1.16)$$

$$\frac{\partial^2 u_z}{\partial x^2} + \frac{\partial^2 u_z}{\partial y^2} + \frac{\partial^2 u_z}{\partial z^2} + \frac{1}{1-2\nu} \frac{\partial e}{\partial z} = \frac{2(1+\nu)}{1-2\nu} \alpha \frac{T_1 - T_0}{2H} = \frac{2(1+\nu)}{1-2\nu} \alpha \frac{\partial T}{\partial z}$$

are satisfied.

8.1.2 An elastic plate deformes in 3D due to an instant temperature change

Given length $2L = 20$ m and thickness $2H = 2$ m the domain represents the rectangular plate $[-L, L] \times [-L, L] \times [-H, H]$. It is discretized by $20 \times 20 \times 4$ equally sized hexahedral elements. The solid material has been selected elastic with Young's modulus $E = 10,000$ MPa, Poisson's ratio $\nu = 0.2$, zero heat capacity, and thermal expansion $\alpha = 10^{-3}$ 1/K. Gravity is neglected via zero material density. The entire surface of the domain is free of load by default. Fixities have been prescribed in the interior of the domain with zero x-displacement along the plane $x = 0$, zero y-displacement along the plane $y = 0$, and zero z-displacement at the origin. The simulation starts from zero initial temperature and comprises one timestep applying an instant temperature change with temperature $T_1 = -10\,°$C at $z = H$ and temperature $T_0 = 10\,°$C at $z = -H$.

The formal solution proceeds in two steps, first to solve for the temperature distribution and then to evaluate stresses, strains, and displacements (u_x, u_y, u_z)(Fig. 8.1.3 and 8.1.4).
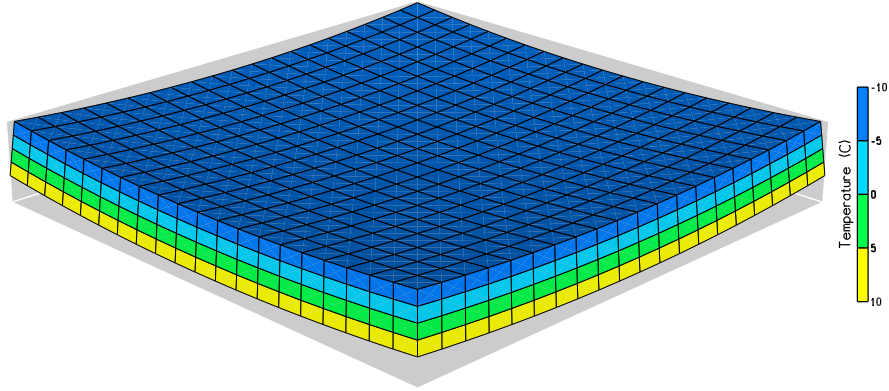
Fig. 8.1.3: Deformed mesh, temperature distribution
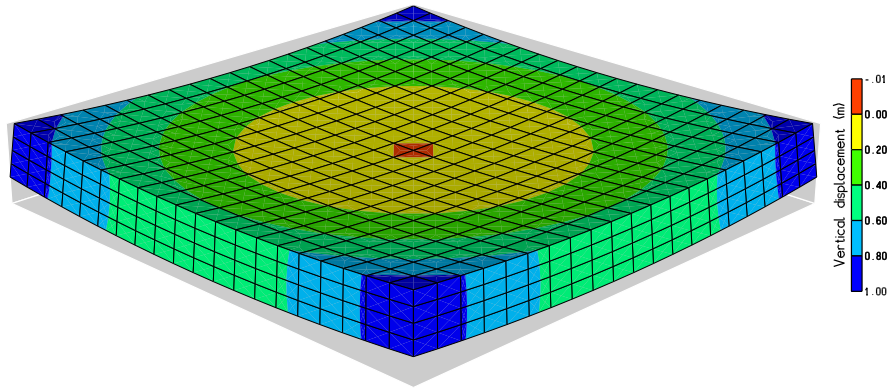
Fig. 8.1.4: Deformed mesh, vertical displacements

The Laplace equation is the governing equation describing the steady-state temperature distribution. It reads

$$\frac{d^2 T}{dz^2} = 0 \tag{8.1.17}$$

for 1D heat flow along the z-axis. The temperature distribution

$$T(z) = \frac{T_1 - T_0}{2H} z \tag{8.1.18}$$

satisfies the Laplace equation and the specified temperature boundary conditions, hence, this is the closed form solution of the temperature problem.

For the closed form solution of the mechanical problem note, that due to the simulation setup, the applied temperature change is identical to the above $T(z)$. The constitutive equations relate the strains $\epsilon_{11}, \epsilon_{22}, \epsilon_{33}$ (in x-, y-, and z-direction, respectively) and the associated stresses $\sigma_{11}, \sigma_{22}, \sigma_{33}$ via

$$
\begin{aligned}
\epsilon_{11} - \alpha \frac{T_1 - T_0}{2H} z &= \frac{1}{E}\left[\sigma_{11} - \nu(\sigma_{22} + \sigma_{33})\right], \\
\epsilon_{22} - \alpha \frac{T_1 - T_0}{2H} z &= \frac{1}{E}\left[\sigma_{22} - \nu(\sigma_{11} + \sigma_{33})\right], \\
\epsilon_{33} - \alpha \frac{T_1 - T_0}{2H} z &= \frac{1}{E}\left[\sigma_{33} - \nu(\sigma_{11} + \sigma_{22})\right].
\end{aligned}
\tag{8.1.19}
$$

All faces of the domain are free of load, hence, they are free of normal stress. These boundary conditions are satisfied by

$$
\sigma_{11} = \sigma_{22} = \sigma_{33} = 0, \tag{8.1.20}
$$

and the diagonal elements of the strain tensor become

$$
\begin{aligned}
\epsilon_{11} &= \frac{\partial u_x}{\partial x} = \alpha \frac{T_1 - T_0}{2H} z, \\
\epsilon_{22} &= \frac{\partial u_y}{\partial y} = \alpha \frac{T_1 - T_0}{2H} z, \\
\epsilon_{33} &= \frac{\partial u_z}{\partial z} = \alpha \frac{T_1 - T_0}{2H} z.
\end{aligned}
\tag{8.1.21}
$$

Integrating the strains yields the displacement vector (u_x, u_y, u_z)

$$
\begin{aligned}
u_x(x, y, z) &= \alpha \frac{T_1 - T_0}{2H} xz + f(y, z), \\
u_y(x, y, z) &= \alpha \frac{T_1 - T_0}{2H} yz + g(x, z), \\
u_z(x, y, z) &= \frac{\alpha}{2} \frac{T_1 - T_0}{2H} z^2 + h(x, y),
\end{aligned}
\tag{8.1.22}
$$

where $f(y, z)$, $g(x, z)$, and $h(x, y)$ have to be determined from the specified fixities and the default boundary conditions. Due to the x-fixities along the plane $x = 0$

$$
f(y, z) = 0, \tag{8.1.23}
$$

and due to the y-fixities along the plane $y = 0$

$$
g(x, z) = 0. \tag{8.1.24}
$$

The shear strains become

$$\epsilon_{12} = \frac{\partial u_x}{\partial y} + \frac{\partial u_y}{\partial x} = 0 \, ,$$

$$\epsilon_{13} = \frac{\partial u_x}{\partial z} + \frac{\partial u_z}{\partial x} = \alpha \frac{T_1 - T_0}{2H} x + \frac{\partial h}{\partial x} \, , \qquad (8.1.25)$$

$$\epsilon_{23} = \frac{\partial u_y}{\partial z} + \frac{\partial u_z}{\partial y} = \alpha \frac{T_1 - T_0}{2H} y + \frac{\partial h}{\partial y} \, .$$

All faces are free of load, hence, they are free of shear stresses, and therefore

$$\epsilon_{13} = \epsilon_{23} = 0 \, . \qquad (8.1.26)$$

This yields

$$h(x, y) = -\frac{\alpha}{2} \frac{T_1 - T_0}{2H} (x^2 + y^2) + C \, , \qquad (8.1.27)$$

and the entire domain is free of shear

$$\epsilon_{12} = \epsilon_{13} = \epsilon_{23} = 0 \, ,$$
$$\sigma_{12} = \sigma_{13} = \sigma_{23} = 0 \, . \qquad (8.1.28)$$

The free constant C has to be determined from the z-fixity at the origin. The displacement vector (u_x, u_y, u_z) becomes

$$u_x(x, z) \quad = \alpha \frac{T_1 - T_0}{2H} xz \, ,$$

$$u_y(y, z) \quad = \alpha \frac{T_1 - T_0}{2H} yz \, , \qquad (8.1.29)$$

$$u_z(x, y, z) = \frac{\alpha}{2} \frac{T_1 - T_0}{2H} [z^2 - (x^2 + y^2)] \, .$$

These displacements yield the volumetric strain

$$e = \frac{\partial u_x}{\partial x} + \frac{\partial u_y}{\partial y} + \frac{\partial u_z}{\partial z} = \alpha \frac{T_1 - T_0}{2H} 3z \, , \qquad (8.1.30)$$

the Laplacian of u_x, u_y, and u_z

$$\frac{\partial^2 u_x}{\partial x^2} + \frac{\partial^2 u_x}{\partial y^2} + \frac{\partial^2 u_x}{\partial z^2} = 0 \, ,$$

$$\frac{\partial^2 u_y}{\partial x^2} + \frac{\partial^2 u_y}{\partial y^2} + \frac{\partial^2 u_y}{\partial z^2} = 0 \, , \qquad (8.1.31)$$

$$\frac{\partial^2 u_z}{\partial x^2} + \frac{\partial^2 u_z}{\partial y^2} + \frac{\partial^2 u_z}{\partial z^2} = -\alpha \frac{T_1 - T_0}{2H} \, ,$$

and the displacement-temperature equations of equilibrium

$$\frac{\partial^2 u_x}{\partial x^2} + \frac{\partial^2 u_x}{\partial y^2} + \frac{\partial^2 u_x}{\partial z^2} + \frac{1}{1-2\nu}\frac{\partial e}{\partial x} = 0 = \frac{2(1+\nu)}{1-2\nu}\alpha\frac{\partial T}{\partial x} \,,$$

$$\frac{\partial^2 u_y}{\partial x^2} + \frac{\partial^2 u_y}{\partial y^2} + \frac{\partial^2 u_y}{\partial z^2} + \frac{1}{1-2\nu}\frac{\partial e}{\partial y} = 0 = \frac{2(1+\nu)}{1-2\nu}\alpha\frac{\partial T}{\partial y} \,, \qquad (8.1.32)$$

$$\frac{\partial^2 u_z}{\partial x^2} + \frac{\partial^2 u_z}{\partial y^2} + \frac{\partial^2 u_z}{\partial z^2} + \frac{1}{1-2\nu}\frac{\partial e}{\partial z} = \frac{2(1+\nu)}{1-2\nu}\alpha\frac{T_1-T_0}{2H} = \frac{2(1+\nu)}{1-2\nu}\alpha\frac{\partial T}{\partial z}$$

are satisfied.

8.1.3 A modification of the previous example with focus on the vicinity of the origin

Given length $2L = 2$ m and thickness $2H = 0.6$ m the domain represents the cuboid $[-L, L] \times [-L, L] \times [-H, H]$. It is discretized by $10 \times 10 \times 6$ equally sized hexahedral elements. The solid material has been selected elastic with Young's modulus $E = 10,000$ MPa, Poisson's ratio $\nu = 0.2$, zero heat capacity, and thermal expansion $\alpha = 10^{-3}$ 1/K. Gravity is neglected via zero material density. The entire surface of the domain is free of load by default. Fixities have been prescribed in the interior of the domain with zero x-displacement along the plane $x = 0$, zero y-displacement at the origin, and zero z-displacement along the plane $z = 0$. The simulation starts from zero initial temperature and comprises one timestep applying an instant temperature change with temperature $T_1 = 10\,°\text{C}$ at $y = L$ and temperature $T_0 = -10\,°\text{C}$ at $y = -L$.

The formal solution proceeds in two steps, first to solve for the temperature distribution and then to evaluate stresses, strains, and displacements (u_x, u_y, u_z)(Fig. 8.1.5 and 8.1.6).

The Laplace equation is the governing equation describing the steady-state temperature distribution. It reads

$$\frac{d^2 T}{dy^2} = 0 \qquad (8.1.33)$$

for 1D heat flow along the y-axis. The temperature distribution

$$T(y) = \frac{T_1 - T_0}{2L}y \qquad (8.1.34)$$

satisfies the Laplace equation and the specified temperature boundary conditions, hence, this is the closed form solution of the temperature problem.

For the closed form solution of the mechanical problem note, that due to the simulation setup, the applied temperature change is identical to the above $T(y)$. The constitutive equations relate the strains $\epsilon_{11}, \epsilon_{22}, \epsilon_{33}$ (in x-, y-, and

z-direction, respectively) and the associated stresses $\sigma_{11}, \sigma_{22}, \sigma_{33}$ via

$$
\begin{aligned}
\epsilon_{11} - \alpha \frac{T_1 - T_0}{2L} y &= \frac{1}{E} \left[\sigma_{11} - \nu(\sigma_{22} + \sigma_{33}) \right], \\
\epsilon_{22} - \alpha \frac{T_1 - T_0}{2L} y &= \frac{1}{E} \left[\sigma_{22} - \nu(\sigma_{11} + \sigma_{33}) \right], \\
\epsilon_{33} - \alpha \frac{T_1 - T_0}{2L} y &= \frac{1}{E} \left[\sigma_{33} - \nu(\sigma_{11} + \sigma_{22}) \right].
\end{aligned}
\tag{8.1.35}
$$

All faces of the domain are free of load, hence, they are free of normal stress. These boundary conditions are satisfied by

$$
\sigma_{11} = \sigma_{22} = \sigma_{33} = 0,
\tag{8.1.36}
$$

and the diagonal elements of the strain tensor become

$$
\begin{aligned}
\epsilon_{11} &= \frac{\partial u_x}{\partial x} = \alpha \frac{T_1 - T_0}{2L} y, \\
\epsilon_{22} &= \frac{\partial u_y}{\partial y} = \alpha \frac{T_1 - T_0}{2L} y, \\
\epsilon_{33} &= \frac{\partial u_z}{\partial z} = \alpha \frac{T_1 - T_0}{2L} y.
\end{aligned}
\tag{8.1.37}
$$

Integrating the strains yields the displacement vector (u_x, u_y, u_z)

$$
\begin{aligned}
u_x(x, y, z) &= \alpha \frac{T_1 - T_0}{2L} xy + f(y, z), \\
u_y(x, y, z) &= \frac{\alpha}{2} \frac{T_1 - T_0}{2L} y^2 + g(x, z), \\
u_z(x, y, z) &= \alpha \frac{T_1 - T_0}{2L} yz + h(x, y),
\end{aligned}
\tag{8.1.38}
$$

where $f(y, z)$, $g(x, z)$, and $h(x, y)$ have to be determined from the specified fixities and the default boundary conditions. Due to the x-fixities along the plane $x = 0$

$$
f(y, z) = 0,
\tag{8.1.39}
$$

and due to the z-fixities along the plane $z = 0$

$$
h(x, y) = 0.
\tag{8.1.40}
$$

The shear strains become

$$\epsilon_{12} = \frac{\partial u_x}{\partial y} + \frac{\partial u_y}{\partial x} = \alpha \frac{T_1 - T_0}{2L} x + \frac{\partial g}{\partial x} \,,$$

$$\epsilon_{13} = \frac{\partial u_x}{\partial z} + \frac{\partial u_z}{\partial x} = 0 \,, \tag{8.1.41}$$

$$\epsilon_{23} = \frac{\partial u_y}{\partial z} + \frac{\partial u_z}{\partial y} = \alpha \frac{T_1 - T_0}{2L} z + \frac{\partial g}{\partial z} \,.$$

All faces are free of load, hence, they are free of shear stresses, and therefore

$$\epsilon_{12} = \epsilon_{23} = 0 \,. \tag{8.1.42}$$

This yields

$$g(x, z) = -\frac{\alpha}{2} \frac{T_1 - T_0}{2L} (x^2 + z^2) + C \,, \tag{8.1.43}$$

and the entire domain is free of shear

$$\epsilon_{12} = \epsilon_{13} = \epsilon_{23} = 0 \,,$$
$$\sigma_{12} = \sigma_{13} = \sigma_{23} = 0 \,. \tag{8.1.44}$$

The free constant C has to be determined from the y-fixity at the origin. The displacement vector (u_x, u_y, u_z) becomes

$$u_x(x, z) \quad = \alpha \frac{T_1 - T_0}{2L} xy \,,$$

$$u_y(x, y, z) = \frac{\alpha}{2} \frac{T_1 - T_0}{2L} [y^2 - (x^2 + z^2)] \,, \tag{8.1.45}$$

$$u_z(y, z) \quad = \alpha \frac{T_1 - T_0}{2L} yz \,.$$

Similar to the previous example it may be shown that these displacements satisfy the displacement-temperature equations of equilibrium.
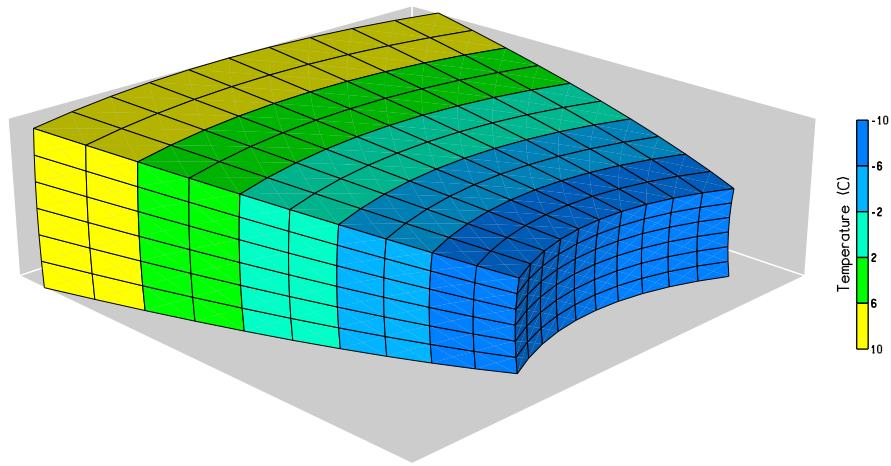
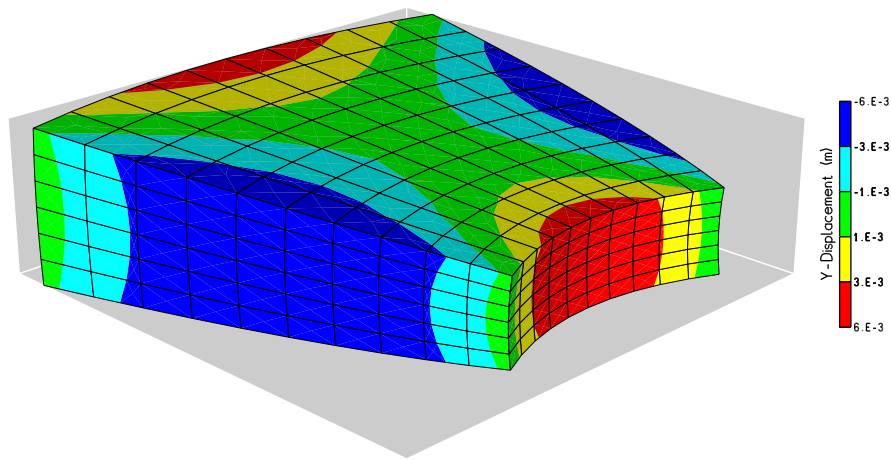Fig. 8.1.5: Deformations scaled up, temperature distribution

Fig. 8.1.6: Deformations scaled up, y-displacements

8.2 Thermoelasticity of a pipe in cement

by Xing-Yuan Miao and Thomas Nagel

In this section, the analytical solution of a two-layered ring subjected to pressure loading on its internal and external surfaces as well as a spatially homogeneous temperature increase is obtained under plane strain conditions.

8.2.1 Basic equations

The derivation is based on cylindrical coordinates (radius r, polar angle ϕ, axial coordinate z). Body forces are not considered.

- Kinematic relations:

$$
\begin{aligned}
\epsilon_{rr} &= u_{r,r}, \\
\epsilon_{\phi\phi} &= \frac{1}{r}u_{\phi,\phi} + \frac{u_r}{r}, \\
\epsilon_{zz} &= 0 \\
\epsilon_{r\phi} &= \frac{1}{2}\left(u_{\phi,r} + \frac{1}{r}u_{r,\phi} - \frac{u_\phi}{r}\right).
\end{aligned}
\tag{8.2.1}
$$

- Equilibrium conditions:

$$
\begin{aligned}
\sigma_{rr,r} + \frac{1}{r}\sigma_{r\phi,\phi} + \frac{1}{r}\left(\sigma_{rr} - \sigma_{\phi\phi}\right) &= 0, \\
\sigma_{r\phi,r} + \frac{1}{r}\sigma_{\phi\phi,\phi} + \frac{2}{r}\sigma_{r\phi} &= 0, \\
\sigma_{zz,z} &= 0.
\end{aligned}
\tag{8.2.2}
$$

- Constitutive equations for isotropic linear thermoelasticity:

$$
\begin{aligned}
\epsilon_{rr} &= \frac{1}{\bar{E}}\left(\sigma_{rr} - \bar{\nu}\sigma_{\phi\phi}\right) + \bar{\alpha}\vartheta, \\
\epsilon_{\phi\phi} &= \frac{1}{\bar{E}}\left(\sigma_{\phi\phi} - \bar{\nu}\sigma_{rr}\right) + \bar{\alpha}\vartheta, \\
\epsilon_{r\phi} &= \frac{1+\bar{\nu}}{\bar{E}}\sigma_{r\phi},
\end{aligned}
\tag{8.2.3}
$$

where $\bar{E} = \dfrac{E}{1-\nu^2}$, $\bar{\nu} = \dfrac{\nu}{1-\nu}$, $\bar{\alpha} = (1+\nu)\alpha$, $\vartheta = T - T_0$.

Furthermore, E is the Young's modulus, ν the Poisson's ratio, and α the linear thermal expansion coefficient.

The above can be simplified by making use of the axisymmetry inherent in the considered problem, i.e.

$$
\begin{aligned}
\sigma_{r\phi} &= 0, \\
\epsilon_{r\phi} &= 0, \\
u_\phi &= 0, \\
\frac{\partial}{\partial \phi} &= 0.
\end{aligned}
\tag{8.2.4}
$$

Based on the above, the stress compatibility equation can be obtained:

$$
\nabla^2 \left(\sigma_{rr} + \sigma_{\phi\phi} \right) = 0,
\tag{8.2.5}
$$

where $\nabla^2 = \nabla \cdot \nabla = \dfrac{\partial^2}{\partial r^2} + \dfrac{1}{r}\dfrac{\partial}{\partial r} + \dfrac{1}{r^2}\dfrac{\partial^2}{\partial \phi^2}$.

Assuming the stress coordinates are related to a stress function ψ in the following manner

$$
\begin{aligned}
\sigma_{rr} &= \frac{1}{r}\psi_{,r} + \frac{1}{r^2}\psi_{,\phi\phi}, \\
\sigma_{\phi\phi} &= \psi_{,rr}, \\
\sigma_{zz} = \nu \left(\frac{1}{r}\psi_{,r} + \psi_{,rr} + \frac{1}{r^2}\psi_{,\phi\phi} \right) &- E\alpha\vartheta, \\
\sigma_{r\phi} &= - \left[\frac{1}{r}\psi_{,\phi} \right]_{,r},
\end{aligned}
\tag{8.2.6}
$$

the stress compatibility equation can be rewritten as a bipotential equation

$$
\Delta\Delta\psi = 0,
\tag{8.2.7}
$$

Intentionally, the two-layer ring is composed of two linear thermoelastic materials. The outer is characterised by an outer radius r_2 and an inner radius r_1, the inner has the outer radius r_1 and an inner radius r_0 (see Fig. 8.2.1a).

8.2.2 Boundary conditions

Considering an axisymmetric problem, the following continuity and boundary conditions apply

$$u_r^1|_{r_1} = u_r^2|_{r_1},$$
$$\sigma_{rr}^1|_{r_1} + \sigma_{rr}^2|_{r_1} = 0,$$
$$\sigma_{rr}^1|_{r_0} = -p_0,$$
$$\sigma_{rr}^2|_{r_2} = -p_2$$

(8.2.8)

where superscripts 1, 2 indicate the inner and outer material of the ring, respectively. The geometry and the boundary conditions are displayed in Fig. 8.2.1.
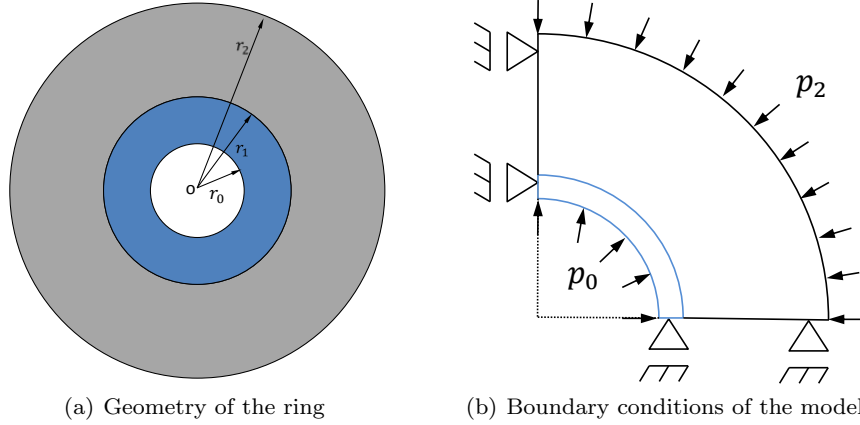

(a) Geometry of the ring

(b) Boundary conditions of the model

Fig. 8.2.1: Schematic view and boundary conditions

8.2.3 Analytical Solution

Assuming the stress function ψ is only dependent on r, Eq. (8.2.7) becomes an ordinary differential equation

$$\left\{ r \left[\frac{1}{r} (r\psi_{,r})_{,r} \right]_{,r} \right\}_{,r} = 0.$$

(8.2.9)

Substituting the general solution of Eq. (8.2.9) into Eq. (8.2.6), and involving the radial momentum balance for axisymmetric conditions, the stress coordinates can be found for both material regions. For the inner ring, $r_0 \leq r \leq r_1$, we have

$$\sigma_{rr}^1 = \frac{A_1}{r^2} + 2C_1,$$

$$\sigma_{\phi\phi}^1 = -\frac{A_1}{r^2} + 2C_1,$$

$$\sigma_{zz}^1 = 4\nu^1 C_1 - E^1 \alpha^1 \vartheta,$$

$$\sigma_{r\phi}^1 = 0,$$

(8.2.10)

while for the outer ring, $r_1 \le r \le r_2$,

$$\sigma_{rr}^2 = \frac{A_2}{r^2} + 2C_2,$$

$$\sigma_{\phi\phi}^2 = -\frac{A_2}{r^2} + 2C_2,$$

$$\sigma_{zz}^2 = 4\nu^2 C_2 - E^2 \alpha^2 \vartheta,$$

$$\sigma_{r\phi}^2 = 0$$

(8.2.11)

is obtained.

Then, substituting Eqs. (8.2.10) and (8.2.11) into Eq. (8.2.3) yields the strain coordinates. Using the kinematic relationships, the displacement u_r can be obtained for the inner ring

$$u_r^1 = \frac{1}{\bar{E}^1} \left[-\left(1 + \bar{\nu}^1\right) \frac{A_1}{r} + 2\left(1 - \bar{\nu}^1\right) C_1 r \right] + \bar{\alpha}^1 \vartheta r,$$

(8.2.12)

as well as the outer ring

$$u_r^2 = \frac{1}{\bar{E}^2} \left[-\left(1 + \bar{\nu}^2\right) \frac{A_2}{r} + 2\left(1 - \bar{\nu}^2\right) C_2 r \right] + \bar{\alpha}^2 \vartheta r.$$

(8.2.13)

Using the boundary and continuity relations from Eq. (8.2.8), the four undetermined constants A_1, A_2, C_1, C_2 can be determined,

$$A_1 = \frac{\bar{E}^2 \left(1 - \bar{\nu}^1\right) r_0^2 r_1^2 r_2^2 p_0 + \bar{E}^1 r_0^2 \left[-r_1^2 r_2^2 p_2 - R_1 \left(r_1^2 + r_2^2\right)\right]}{\bar{E}^1 r_0^2 R_0 \left[r_2^2 + r_1^2 + \bar{\nu}^2 \left(r_2^2 - r_1^2\right)\right] - \bar{E}^2 r_2^2 \left[r_0^2 + r_1^2 + \bar{\nu}^1 \left(r_0^2 - r_1^2\right)\right]} +$$
$$\frac{\bar{E}^1 \bar{\nu}^2 r_0^2 \left[r_1^2 r_2^2 p_2 + R_1 \left(r_1^2 - r_2^2\right)\right] + \bar{E}^1 \bar{E}^2 r_0^2 r_1^2 r_2^2 \left(\bar{\alpha}^2 - \bar{\alpha}^1\right) \vartheta}{\bar{E}^1 r_0^2 R_0 \left[r_2^2 + r_1^2 + \bar{\nu}^2 \left(r_2^2 - r_1^2\right)\right] - \bar{E}^2 r_2^2 \left[r_0^2 + r_1^2 + \bar{\nu}^1 \left(r_0^2 - r_1^2\right)\right]},$$

$$A_2 = R_0 A_1 + R_1,$$

$$C_1 = -\frac{1}{2} \left(p_0 + \frac{A_1}{r_0^2}\right),$$

$$C_2 = -\frac{1}{2} \left(p_2 + \frac{A_2}{r_2^2}\right),$$

(8.2.14)

where $R_0 = \dfrac{r_2^2 \left(r_0^2 - r_1^2\right)}{r_0^2 \left(r_1^2 - r_2^2\right)}$ and $R_1 = -\dfrac{r_1^2 r_2^2 \left(p_0 + p_2\right)}{r_1^2 - r_2^2}$.

8.2.4 Numerical simulation

This benchmark investigates the mechanical loading of the interface region between a composite pipe surrounded by cement under coupled thermo-mechanical loading. The temperature difference ϑ is set to $80\,\text{K}$, radii to $r_2 = 25\,\text{mm}$, $r_1 = 15\,\text{mm}$, $r_0 = 12.5\,\text{mm}$. The pressures $p_0 = 1\,\text{MPa}$ and $p_2 = 2\,\text{MPa}$ are applied on the inner and outer boundary, respectively. The material properties are listed in Table 8.2.1.

Table 8.2.1: Material properties

Parameters	Cement	Pipe
α / K^{-1}	1.5×10^{-5}	2.8×10^{-5}
E / Pa	5.354×10^{9}	6.89×10^{10}
ν	0.17	0.4

The analytical solution is compared against two numerical approximations obtained using OpenGeoSys. The comparison focuses on stresses and displacements in the cross section of the object. The first mesh uses the plane strain implementation (Fig. 8.2.2a). Due to symmetry, the numerical analysis considered only a quarter of the full ring (see Fig. 8.2.1a) while symmetry boundary conditions were applied on the appropriate boundaries. The second mesh used the OGS implementation of axisymmetric meshes and is shown in

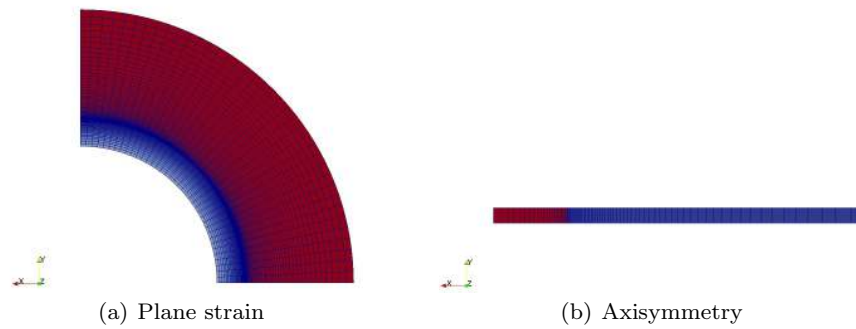(a) Plane strain   (b) Axisymmetry

Fig. 8.2.2: Finite element discretisation of the model.

Fig. 8.2.2b. Both geometries were meshed using quadrilateral elements with biquadratic shape functions and were refined towards the interface.

Fig. 8.2.3 shows the stress and displacement distribution within the two-layered ring. It can be seen that the numerical approximations are consistent with the analytical solutions. Further, on account of the different mechanical properties of the two materials, changes in the slope of the radial stress and displacement distributions occur at the interface, while a jump in the curves for the circumferential and axial stress appears. In addition, maximum compressive stresses occur in the circumferential direction at the inner surface of the inner pipe.
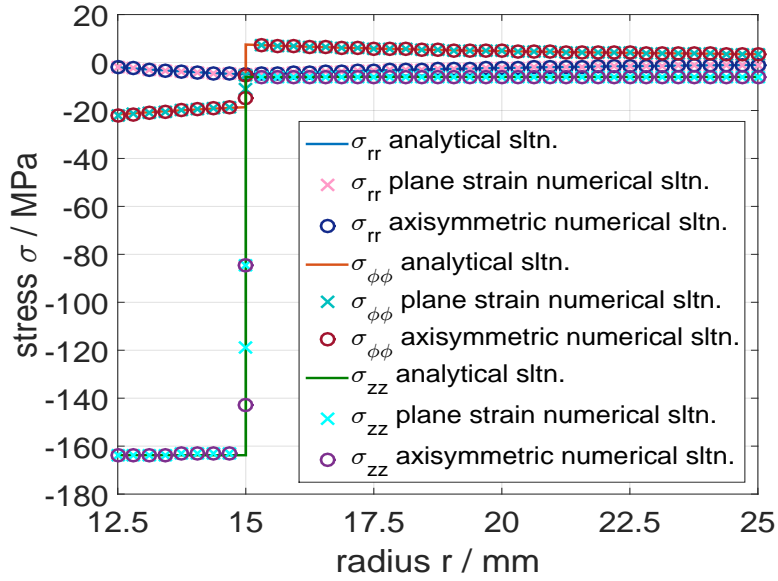
(a) Stress distribution
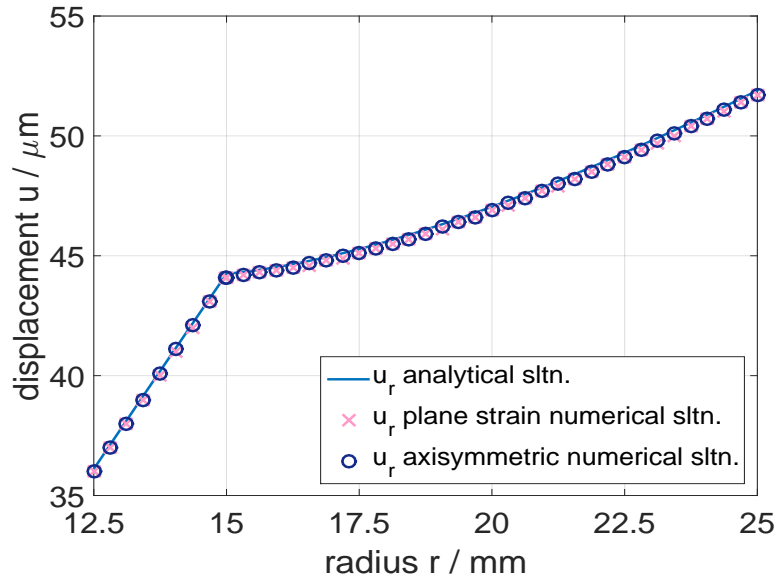
(b) Radial displacement

Fig. 8.2.3: Principal stress distribution and radial displacement along the radius.

Chapter 9
Coupled THM-Processes

by Jobst Maßmann, Fabien Magri, Wenqing Wang

9.1 2D axially symmetric and 3D simulations of THM processes at the EBS experiment, Horonobe URL (Japan)

Jobst Maßmann

9.1.1 Introduction

The DECOVALEX project is an international research and model comparison collaboration in the field of coupled THM simulations of processes concerning the safe geological storage of nuclear waste (DEC, 2015). In the current project phase "DECOVALEX2015", one of the tasks is proposed by the Japan Atomic Energy Agency (JAEA). It focuses on THM simulations for the full-scale Engineering Barrier System (EBS) experiment as a part of the Horonobe Underground Research Laboratory (URL) project in Japan (Sugita and Nakama, 2012).

In the following 2D axially symmetric and 3D simulations, performed with OGS, will be presented. The main emphasis is laid on the desaturation and resaturation processes in the near field of the heater and the THM coupled effects.

9.1.2 Model setup

The model of the EBS experiment comprises the surrounding claystone, an open drift, a plug, support and floor, backfill and buffer and the heater. The material of the plug, support and floor is concrete with the same properties. The buffer and the backfill consist of different kinds of bentonite. This model approach considers the heating phase only. The general model setup, including the initial (IC) and boundary conditions (BC), is depicted in Fig. 9.1.1. The material properties are listed in Table 9.1.1. The material properties and geometries have been provided within the DECOVALEX2015 project and are mainly based on Sugita and Nakama (2012), Sugita (2013), Sugita (2014) and JNC (2000). The initial and boundary conditions in the 2D model are set accordingly to the 3D model. As a matter of course, the open drift and the plug cannot be considered in a 2-dimensional approach. Furthermore, the shape of the backfill and concrete area are simplified in the axially symmetric model.
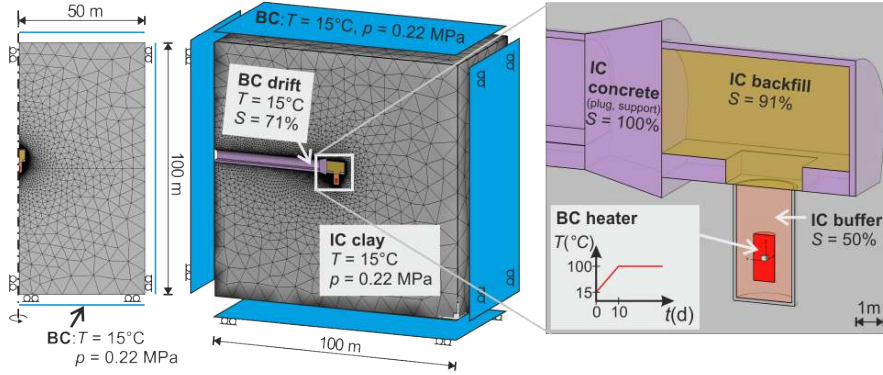

Fig. 9.1.1: Model setups of the 2D axially symmetric (left) and the 3D model (center and right)

The hydraulic problem is described by a non-isothermal Richard's flow in a deformable porous medium considering vapour diffusion. The water retention curves are depicted in Fig. 9.1.2. The fluid viscosity and the fluid density are defined as non linear functions of temperature. The values for the fluid density are taken from the NIST database (Lemmon et al., retrieved Oct, 2014). Since the thermal expansion of the fluid is defined by the derivative of the density with respect to temperature, the thermal expansion of the fluid depends on temperature, too. The viscosity μ is calculated by a function published by Yaws et al. (1976) with the absolute temperature T_{abs}:

$$\ln \mu = -24.7 + \frac{421}{T_{\mathrm{abs}}} + 0.0453\,T_{\mathrm{abs}} - 0.0000338\,T_{\mathrm{abs}}^2\,. \qquad (9.1.1)$$

Table 9.1.1: Material properties, based on Sugita and Nakama (2012), Sugita (2013), Sugita (2014) and JNC (2000).

| parameter	clay	buffer	backfill	concrete	fluid	unit
particle density, ρ	2454.0	2680.0	2593.0	2621.0	$f(T)$	kg/m^3
porosity, n	0.45	0.4	0.46	0.13	-	-
intrinsic permeability, k	1.33e-15	1.4e-20	1.76e-19	1.0e-17	-	m^2
Young's modulus, E	1820.0	37.0	3.0	20,000.0	-	MPa
Poisson's ratio, ν	0.21	0.3	0.3	0.3	-	-
specific heat capacity, c_p	626.0	341.0	300.6	871.7	4180.0	J/(kg·K)
cubic th. exp. coeff., β	1.3e-5	1.0e-6	8.0e-6	1.3e-5	$f(\rho_w)$	1/K
thermal conductivity, κ	$f(Sw)$	$f(Sw)$	1.7	2.85	0.6	W/(m·K)
Biot's coefficient, α	1.0	1.0	1.0	1.0	-	-
max. swell. press., $p_{sw,max}$	0.0	5.0e5	8.6e5	0.0	-	-
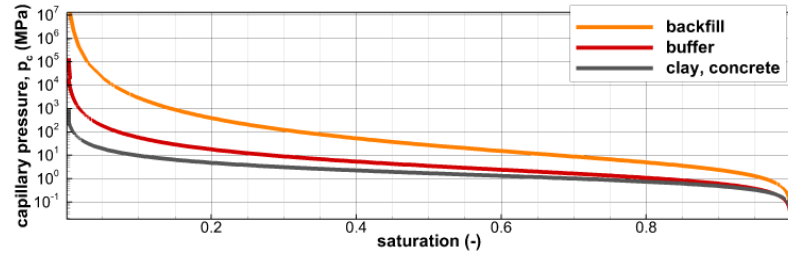
Fig. 9.1.2: Water retention curves for the clay and buffer (both based on Sugita (2013)), backfill (based on Sugita (2014)) and concrete

The deformation behaviour is simulated by a linear elastic model taking into account thermal expansion, saturation dependent swelling/shrinkage and the pore water pressure. Thus, the conservation of linear momentum can be stated as:

$$\nabla \cdot (\boldsymbol{\sigma} - \alpha\chi p\mathbf{1} - S_w p_{sw,max}\mathbf{1} - \beta_s\mathbf{C}\Delta T) = 0\,, \qquad (9.1.2)$$

where $\boldsymbol{\sigma}$ represents the tensor of effective stresses, α the Biot coefficient, p the pore water pressure, S_w the degree of water saturation, $p_{sw,max}$ the maximum swelling stress, β_s the cubic thermal expansion coefficient of the solid phase, $\mathbf{C}$ the tensor of elasticity and T the temperature. The Bishop coefficient χ is defined as:

$$\chi = \begin{cases} 0, & \text{if } S_w < 1 \\ 1, & \text{else} \end{cases}. \qquad (9.1.3)$$

Consequently, in the unsaturated case the coupling between pore water pressure and total stresses by the effective stress approach is neglected and the HM coupling is modelled by the linear swelling model only.

The thermal conductivities of the porous media κ_{m} of the buffer and the clay are presented in Fig. 9.1.3. The general mixture theory is applied in the backfill and the concrete with the porosity n and the indices s and w for solid and water, respectively:

$$\kappa_{\mathrm{m}} = (1 - n)\kappa_{\mathrm{s}} + nS_{\mathrm{w}}\kappa_{\mathrm{w}} . \tag{9.1.4}$$
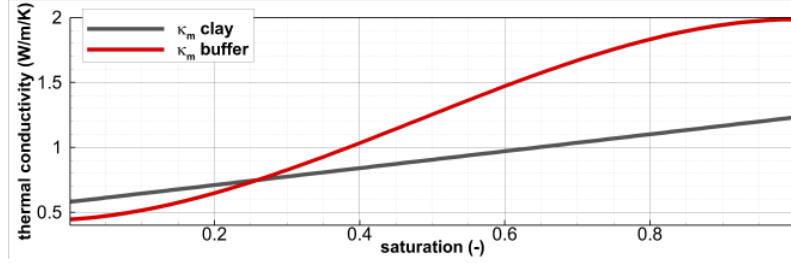

Fig. 9.1.3: Thermal conductivities of the porous media clay and buffer

9.1.3 Discussion of results

The simulated temperature and degree of water saturation are depicted in Figs. 9.1.4 and 9.1.5. A comparison between the results of the 3D model and the 2D axially symmetric model approach along a vertical line shows a good agreement. After 7 years the temperature above the heater calculated by the 2D model is slightly higher. This can be explained by the influence of the open drift in the 3D model, where a temperature boundary condition ($T = 15\,^\circ\mathrm{C}$) acts as a heat sink. Nearby the heater, the saturation is decreased due to vapour diffusion. After 7 years, the backfill is nearly saturated but the buffer only partially.

The heating and resaturation induce a change of pore water pressure and the stress field (Fig. 9.1.6). The results are strongly influenced by the wide-ranging mechanical and hydraulic material properties. Some THM coupling effects can be observed: the temperature rise leads to compression, strengthened by swelling due to increase of saturation, and thus, negative stresses occur. This phenomena is observable in the buffer as well as in the parts of the claystone and the comparatively stiff concrete, where a noticeable increase in temperature takes place. Close to the heater, this effect is superimposed by shrinkage, due to a decrease of saturation, which leads to tensional stresses. In the upper parts of the concrete the temperature change is small
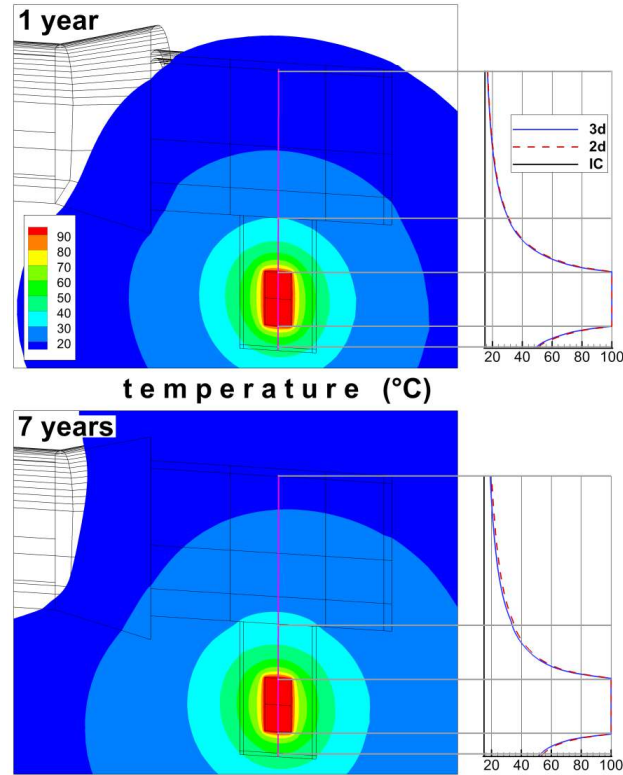
Fig. 9.1.4: Simulated temperature after 1 and 7 years of heating; right: results
along a vertical line

and the pore water pressure increases because of the initial and boundary con-
ditions of the rock. In these areas tensional stresses can be observed, caused
by the effective stress principle.

Overall it can be stated that different THM coupling effects takes place
due to heating and resaturation. In some areas, they are mutually reinforcing,
in others they are mutually weakening.
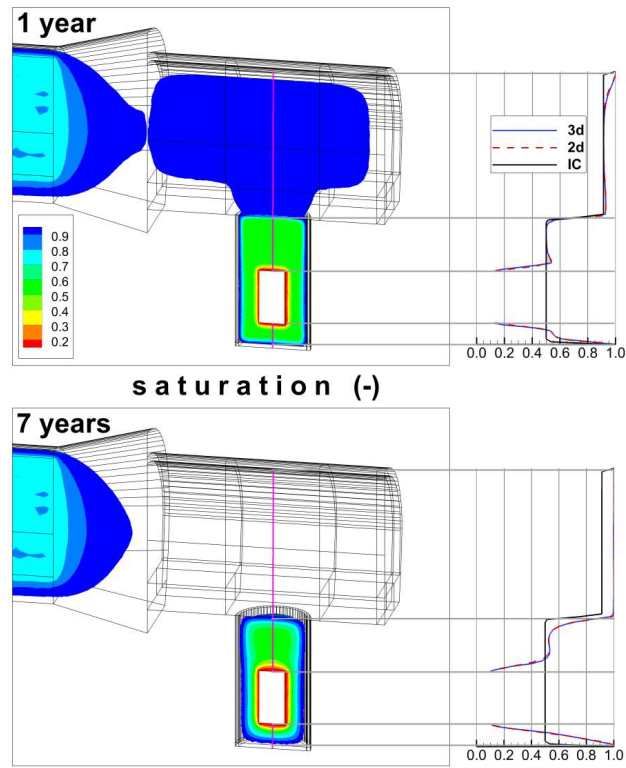
Acknowledgments

Fig. 9.1.5: Simulated saturation after 1 and 7 years of heating; right: results along a vertical line

tion(s). Also, no responsibility is assumed by the authors for any damage to property or persons as a result of operation or use of this publication and/or the information contained herein.
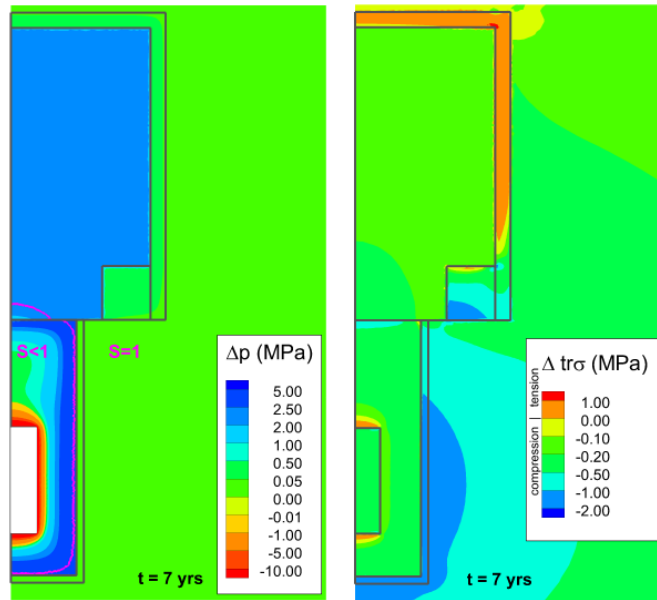
Fig. 9.1.6: Simulated changes in the pore water pressure and stresses due to
7 years of heating

9.2 HM/THM processes in a faulted aquifer

by Fabien Magri, Elena Tillner, Thomas Kempka, Norihiro Watanabe, Wen-qing Wang, Günter Zimmermann

Hydro–Mechanical (HM) and transient Thermo–Hydro–Mechanical (THM) simulations in a faulted aquifer are presented. Both 2D and 3D scenarios are illustrated. OpenGeoSys (OGS) results are compared with those obtained using ABAQUS Abaqus (2007), a commercial finite element software with wide material modeling capability, including coupled hydraulic and mechanical processes in porous media. To some extent, the results comparison validates OGS numerical capabilities in solving 2D and 3D HM and THM problems.

9.2.1 Definition

The model geometry is shown in Fig. 9.2.1. The model is a 900×900 m cube including a 100 m thick storage aquifer embedded in a sedimentary fill. A 20 m wide fault with a dip angle of 80° cuts all units. The fault is conceptually modeled as an equivalent porous media, i.e. a unit made of solid elements with their own hydraulic and mechanical physical properties. Both ABAQUS and OGS numerical simulations use the same 3D mesh. For the HM case, the grid consists of 62,818 nodes and 359,566 tetrahedral elements. Elements near the fault are 10 m wide as shown in Fig. 9.2.2. For THM simulations instead, ABAQUS requires hexahedral elements. Here 30 m wide first order cubes (i.e. 8 nodes) are used to discretize the sedimentary fill, whereas in the fault the resolution is still 10 m.

9.2.2 Initial and Boundary conditions

A hydrostatic pore pressure distribution is used to initialize the simulation. For simplicity zero stress field is set over the whole model. In the paragraph "Initial conditions effects", a simulation importing a stress state as initial conditions is illustrated. Constant pore pressure (3×10^6 Pa) and stress (7.36×10^6 Pa load) are assumed as boundary conditions at the top. No flow is set on the remaining sides of the model. Null displacement conditions are applied normal to the vertical and bottom boundaries. A constant pressure of 10^8 Pa is set in the hanging wall aquifer (i.e. at the left side of the fault) in order to simulate the overpressure resulting from fluid injection. Though 10^8 Pa is not a realistic value it allows to test the software capabilities with regard to extreme pressures in a heterogeneous system.
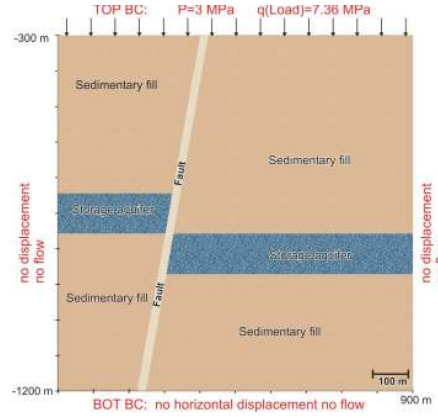
Fig. 9.2.1: Model geometry displaying three different units (sedimentary fill, fault and storage aquifer) and the boundary conditions of the HM problem. In the 2D simulations, the vertical profile is referred to the XY reference frame (i.e. depth in the Y direction).
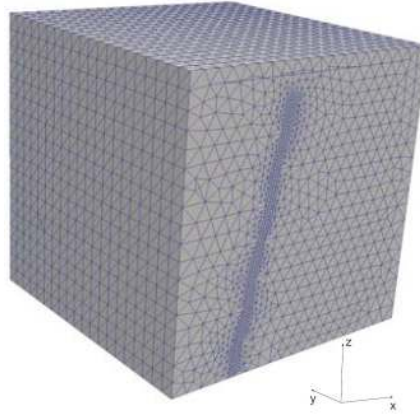

Fig. 9.2.2: : Example of 3D finite element mesh used for HM simulations (62,818 nodes and 359,566 tetrahedral elements) in OGS and ABAQUS.

9.2.3 Material properties

Hydraulic and mechanical properties are given in Tables 9.2.1, 9.2.2 and 9.2.3, where each unit is considered isotropic and homogeneous. The fluid properties are: viscosity $= 1{\times}10^{-3}$ Pa s, density $= 998$ kg m^{-3}. Properties of the sedimentary fill and the storage aquifer represent sandstones according to data from the book by Jaeger et al. (2007).

Property	Value	Unit
Density	2500	kg/m^3
Young's modulus	2.964×10^{10}	N/m^2
Poisson's ratio	0.12	$-$
Permeability	2×10^{-16}	m^2
Storage coefficient	8.63×10^{-11}	Pa^{-1}
Porosity	0.04	$-$

Table 9.2.1: Material properties of sedimentary fill.

Property	Value	Unit
Density	2200	kg/m^3
Young's modulus	1.44×10^{10}	N/m^2
Poisson's ratio	0.20	$-$
Permeability	1.5×10^{-13}	m^2
Storage coefficient	8.36×10^{-11}	Pa^{-1}
Porosity	0.19	$-$

Table 9.2.2: Material properties of storage aquifer.

Property	Value	Unit
Density	2200	kg/m^3
Young's modulus	1.44×10^{10}	N/m^2
Poisson's ratio	0.20	$-$
Permeability	1.5×10^{-12}	m^2
Storage coefficient	1.96×10^{-10}	Pa^{-1}
Porosity	0.19	$-$

Table 9.2.3: Material properties of fault.

9.2.4 Results

The calculated 2D steady state pressure, pore fluid velocity, displacement and stress fields are illustrated and directly compared with the results obtained with ABAQUS in the following.

A pressure buildup induced by the highly pressurized hanging aquifer (Fig. 9.2.3) develops within the fault owing to its higher hydraulic permeability (Table 9.2.3). Consequently, the fault acts as a preferential pathway for groundwater flow (Fig. 9.2.4). Deep seated fluids can flow therein at velocities ranging between 4×10^{-6} ms^{-1} to 1.4×10^{-5} ms^{-1} (i.e. 0.3 to 1.2 mday^{-1}), the peak velocities being observed at the boundary between the storage aquifer and the fault zone. Owing to the no displacement conditions at the lateral and bottom boundaries, major structural deformations are observed within the sedimentary fill above the hanging storage aquifer (Fig. 9.2.5). The calculated
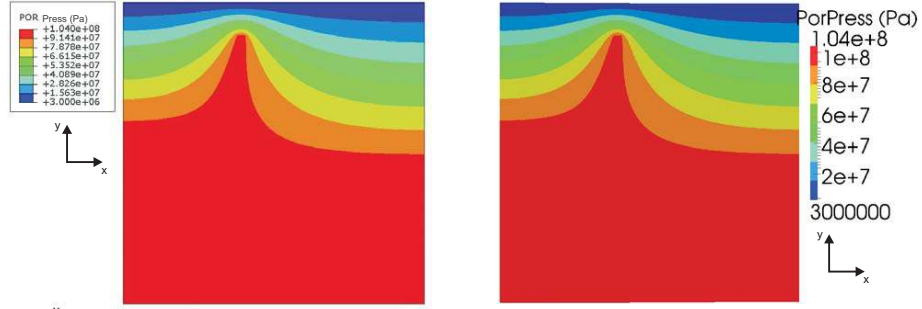
Fig. 9.2.3: Pore pressure (Pa) distribution calculated with ABAQUS (left) and OGS (right)
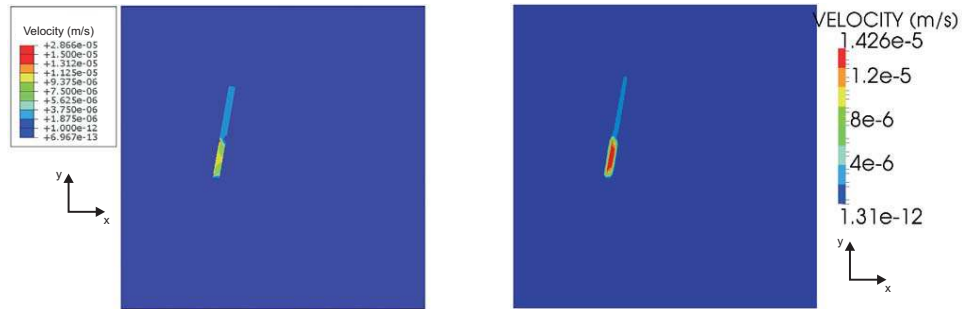

Fig. 9.2.4: Pore fluid velocity (ms^{-1}) calculated with ABAQUS (left) and OGS (right). Please note the different scales.

Fig. 9.2.5: : Displacement in the y direction (m) calculated with ABAQUS (left) and OGS (right)

uplift of the surface is 2.58 m, in good agreement with ABAQUS calculations. The sliding of the hanging wall occurs along the fault plane because of the differences in the material properties between the sedimentary fill and fault, in particular the density and the elastic properties. The physical properties
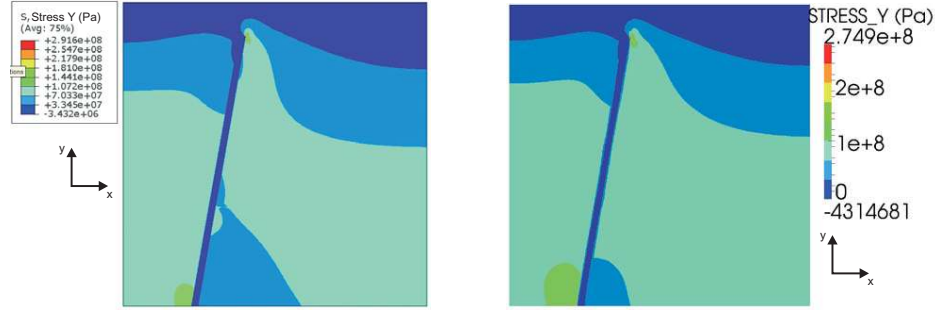

Fig. 9.2.6: Y component of the stress field (Pa) calculated ABAQUS (left) and OGS (right)

contrast between the fault and surrounding sediments are also reflected in the calculated stress (Fig. 9.2.6). In general, the stress should increase roughly linear with depth due to the increase of lithostatic pressure with depth. Here, this trend is intensely perturbed by the fault. Jumps in stress magnitude at both the top and bottom interface of the fault may reach maximum values of several hundreds of MPa. Abrupt changes in stress magnitude also occur along the fault sides, as therein the stress reaches its minimal values.

9.2.5 Initial conditions effects

Here the stress and hydraulic pressure calculated with the previously described simulation are used as IC to verify whether or not the system is at hydro-mechanical equilibrium. If the mechanical equilibrium between the applied boundary conditions and the state of stress in the units has been reached, no displacement should be observed in this test case.

As a first test, a simulation is initialized with stress and hydraulic pressure fields that were calculated a priori with a two time-steps simulation. The vertical displacement is illustrated in Fig. 9.2.7. It can be seen that a vertical displacement exists though in the order of few millimeter (Fig. 9.2.7), suggesting that the stress field calculated with two time-steps is very close to mechanical equilibrium. An additional simulation initialized with stress and hydraulic pressure fields calculated with three iterations display no vertical displacement (i.e. 0 m everywhere).
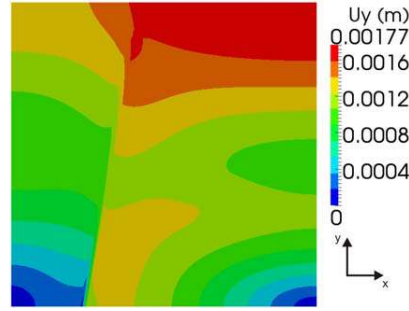
Fig. 9.2.7: : Initial conditions effects: Displacement in the y direction (m) calculated using initial stress and hydraulic pressure fields. The IC were derived a priori with a two time-steps simulation.

9.2.6 Temperature effects THM simulation

Here the results obtained from a transient Thermo–Hydro–Mechanical (THM) simulation are illustrated. Flow and mechanical boundary conditions are those pictured in Fig. 9.2.1. Additionally, a constant temperature of 17 °C and 44 °C are set at the top and bottom boundaries, respectively, leading to a thermal gradient of 30 K/km. For simplicity, the whole model is homogeneous with respect to thermal properties (Table 9.2.4). The simulation is conducted for 7.4×10^7 s (856 days) with a time step size of varying between 10^5 to 10^6 s (1 to 10 days). To ensure higher flow motion, the porosity of

Layers	Specific heat capacity $[J\,kg^{-1}\,K^{-1}]$	Thermal conductivity $[W\,m^{-1}\,K^{-1}]$	Thermal expansion coefficient $[K^{-1}]$
Solid	900	0.6	10^{-5}
Fluid	4280	3	−

Table 9.2.4: Thermal properties of the solid and fluid used to simulate 2D and 3D THM problem.

the sedimentary fill and fault are increased to 0.2 and 0.43 respectively. The other physical properties are those given in Tables 9.2.1, 9.2.2 and 9.2.3.

Results of temperature The hanging aquifer is saturated with fluid at 30 °C approximately. Driven by the imposed pressure gradient, groundwater flows from the storage aquifer to the fault. As a result, fluid moving upward (downward) increases (decreases) the temperature within the fold, as illustrated by convex (concave) isotherms in Fig. 9.2.8.

3D Results

Fig. 9.2.8: Temperature (°C) calculated with ABAQUS (left) and OGS (right). Temperature increase (decrease) can be observed in the fold as a result of fluid outflow from the storage aquifer into the fault.

The same set of simulations has been run for the 3D cases. OGS results well compare to those obtained with ABAQUS which validates OGS capabilities in solving 3D pressure induced stress field.
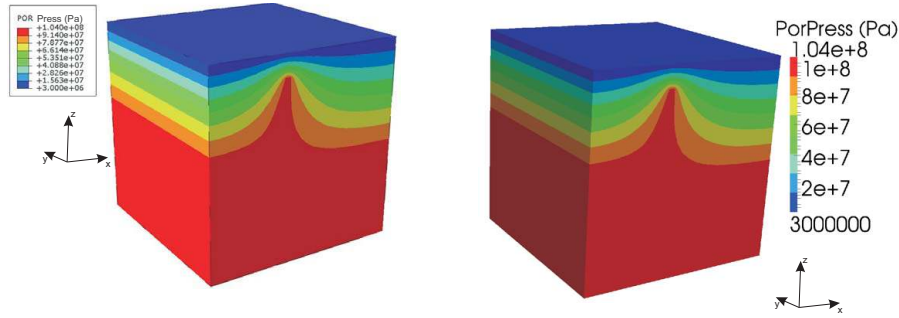

Fig. 9.2.9: Pore pressure (Pa) distribution calculated with ABAQUS (left) and OGS (right).

OGS and ABAQUS results are compared at an observation point (located with the star in Fig. 9.2.13) for the simulated period. The temporal trends of vertical displacement (U_z) and temperature (T) are illustrated in Fig. 9.2.14. It can be seen that whereas the vertical displacements calculated with both software match within the error allowance, heat transport in OGS is more vigorous. The observed differences can be explained as follow: In ABAQUS, the elastic part of the volumetric behavior is proportional to the logarithm of the pressure stress (Chap 19.3.1. ABAQUS User's manual Abaqus (2007)) whereas in OGS we assume that the elastic modulus are constant. Therefore
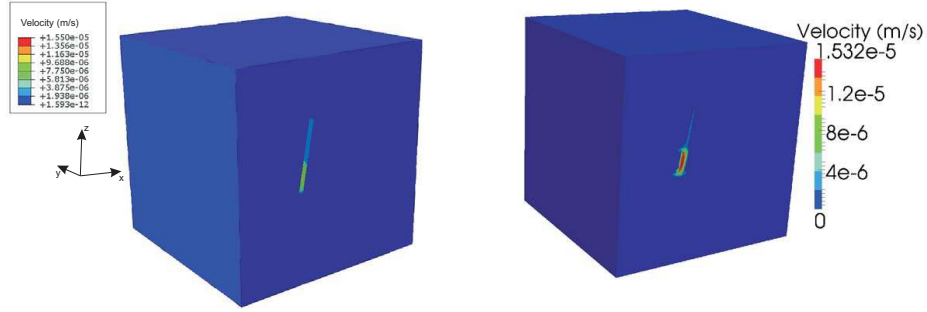
Fig. 9.2.10: Pore fluid velocity (m/s) calculated with ABAQUS (left) and OGS (right).
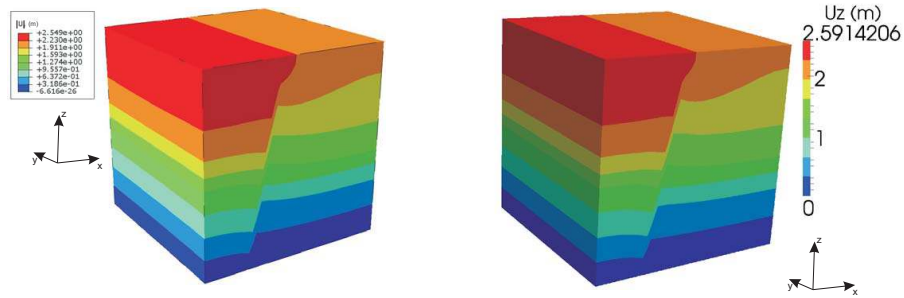

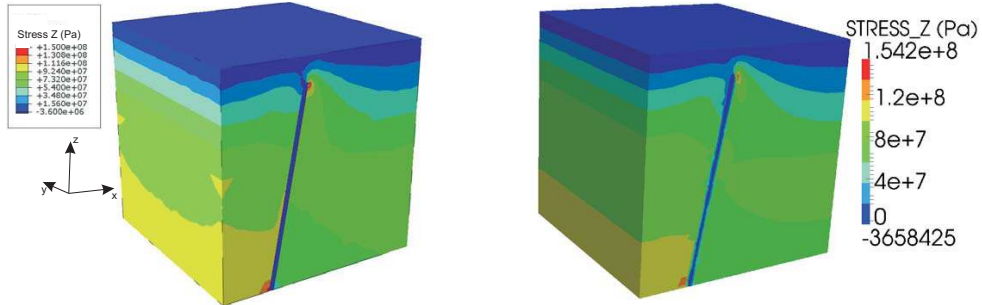Fig. 9.2.11: Displacement (m) calculated with ABAQUS (left) and OGS (right).

Fig. 9.2.12: Z component of the stress field (Pa) calculated with ABAQUS (left) and OGS (right).
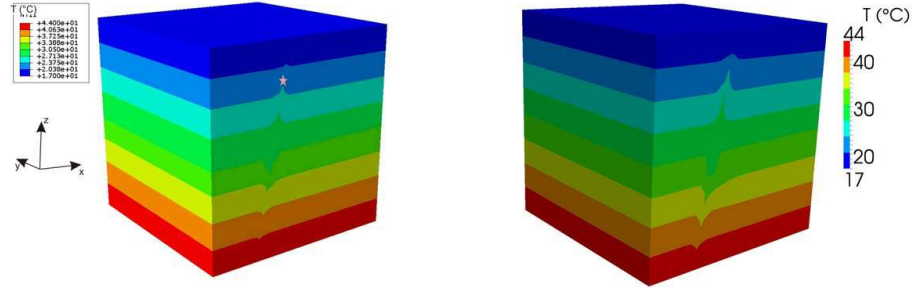
Fig. 9.2.13: Temperature ($^\circ$C) calculated at 3×10^7 s with ABAQUS (left) and OGS (right). The star locates the observation point for the comparative graphs in Fig. 9.2.14 and fig. 9.2.15.

the important fluid pressure modeled here will induce slightly different stress and displacements. In ABAQUS porosity is strain dependent. In this problem, the calculated strain increases porosity in the fold as flow evolves. Increasing porosity values lead to higher heat storage which in turn slows down heat flow. By contrast, in OGS, porosity is constant during all the simulation. OGS and ABAQUS pore pressure and pore velocity perfectly fit (Fig. 9.2.15)
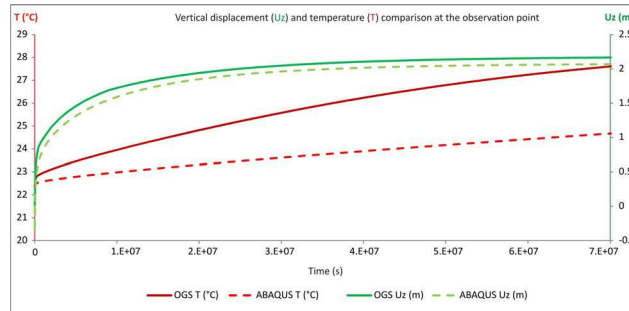
Fig. 9.2.14: OGS and ABAQUS comparison: Temporal trends at the observation point of the temperature (T, in $^\circ$C left axis) and vertical displacement (U_z, in m, right axis)

Additionally, results are provided for an observation point located inside the model at the (x, y, z) coordinates (343, -540, -400) m (Fig. 9.2.16)

Fig. 9.2.15: OGS and ABAQUS comparison: Temporal trends pore velocity (v in m/s left axis) and pressure (P, in Pa, right axis), at the observation point in Fig. 9.2.13

Fig. 9.2.16: Temperature (°C) calculated at 3×10^7 s with: OGS. The star locates the observation point for the comparative graphs in Fig. 9.2.17 and Fig. 9.2.18.

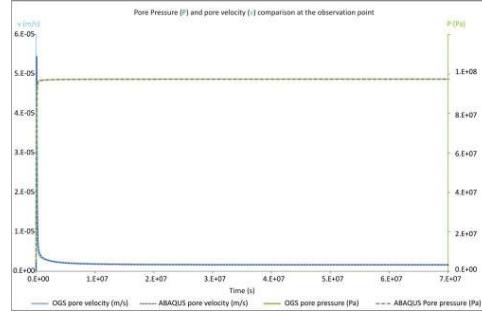Fig. 9.2.17: OGS and ABAQUS comparison: Temporal trends of pore velocity (v in m/s left axis) and pressure (P, in Pa right axis) at the observation point in Fig. 9.2.16
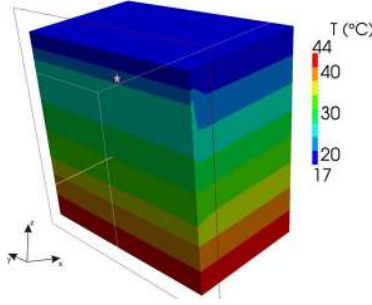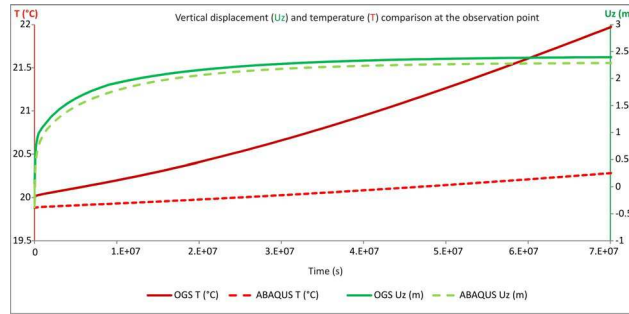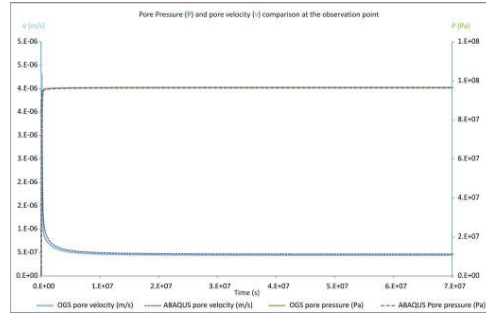
Fig. 9.2.18: OGS and ABAQUS comparison: Temporal trends of the temperature (T, in °C left axis) and vertical displacement (U_z, in m right axis) at the internal observation point in Fig. 9.2.16

9.3 Consolidation around a point heat source

by Xuerui Wang, Son Nguyen, Hua Shao and Wenqing Wang

When a saturated porous medium is subjected to heating, a series of thermo-hydraulic-mechanical (THM) interactions will be generated. The temperature rise will lead to the expansion of pore water and solid skeleton, which will cause the increase of the pore pressure. The increase of pore pressure can then cause reduction of effective stress. If the porous medium is sufficient permeable, consolidation will occur and the excess pore pressure will dissipate.

9.3.1 Governing equations

The equations governing the non-isothermal consolidation of a saturated porous media are:

$$c\rho\frac{\partial T}{\partial t} + c\rho\mathbf{v}\cdot\nabla T - \nabla\cdot(K\nabla T) = Q \qquad (9.3.1)$$

$$G\nabla^2 u_i + (\lambda + G)\frac{\partial\varepsilon_i}{\partial x_i} + \alpha\frac{\partial p}{\partial x_i} - \beta K_D\frac{\partial T}{\partial x_i} + F_i = 0 \qquad (9.3.2)$$

$$\left(\frac{n}{K_f} + \frac{a-n}{K_s}\right)\frac{\partial p}{\partial t} + \nabla\left(\frac{k_{ij}}{\mu}(\nabla p - \rho_f\mathbf{g})\right) + \frac{\partial}{\partial t}\frac{\partial u_i}{\partial x_i}$$
$$- \left((1-a)\beta - (1-n)\beta_s - n\beta_f\right)\frac{\partial T}{\partial t} = 0 \qquad (9.3.3)$$

where temperature T, pore pressure p and displacement u_i are chosen as the primary variables. c is the specific heat capacity; ρ and ρ_f are the density of bulk medium and of fluid respectively; $\mathbf{v}$ is the advection velocity; K is the thermal conductivity of porous medium; Q is the external thermal source; λ, G are the Lamé constants of the soil skeleton; K_D , K_s , K_f are the bulk moduli of drained material, solid, fluid respectively. $\alpha = 1 - K_D/K_s$ is the Biot-coefficient; F is the volumetric body force; n is porosity; β_s and β_f are the coefficients of volume expansion of soil grain and water respectively; β_s is the coefficient of volume expansion of soil. It is assumed that no structural changes occur, then $\beta_v = \beta_s$; $\mathbf{k}$ is the permeability tensor; μ is viscosity and $\mathbf{g}$ is the gravity vector.

Problem definition: We consider a point heat source of constant heat input which is located in the centre of an infinite saturated and homogenous porous medium.

9.3.2 Analytical solution

An analytical solution for consolidation of an infinite homogenous saturated porous medium around a constant point heat source Q [W] was provided by Booker and Savvidou (1985a). The temperature, pore pressure, displacement and stress can be given by:

$$T = \frac{Q}{4\pi K R} f(\frac{\kappa t}{R^2}) \tag{9.3.4}$$

$$p = \frac{X}{1 - c_v/\kappa} \frac{Q}{4\pi K R} \left(f(\frac{\kappa t}{R^2}) - f(\frac{ct}{R^2}) \right) \tag{9.3.5}$$

$$u_i = a_u i \frac{Q}{4\pi K R} g* \tag{9.3.6}$$

$$\sigma_{ii} = 2G a_u \frac{Q}{4\pi K R} \left(f* -g* + \frac{r^2}{R^2}(3f* -g*) \right) \tag{9.3.7}$$

$$\sigma_{ij} = 2Ga - u \frac{Q}{4\pi K R} \frac{ij}{R^2}(3f* -g*) \tag{9.3.8}$$

where κ is given by:

$$\kappa = \frac{K}{\rho c} \tag{9.3.9}$$

$$c_v = k_f(\lambda + 2G)/\gamma_w \quad \text{is the coefficient of consolidation} \tag{9.3.10}$$

$$a_u = \beta_s(1 - n) + \beta_w n \tag{9.3.11}$$

K_f is the hydraulic conductivity, γ_w is the specific weight of pore water. And

$$R = \left((x - x_i)^2 + (y - y_i)^2 + (z - z_i)^2\right) \tag{9.3.12}$$

$$f(\frac{\kappa t}{R^2}) = \text{erfc}(\frac{R}{2\sqrt{\kappa t}}) \tag{9.3.13}$$

$$g(\frac{\kappa t}{R^2}) = \frac{\kappa t}{R^2} + (\frac{1}{2} - \frac{\kappa t}{R^2})\text{erfc}(\frac{R}{2\sqrt{\kappa t}}) - \sqrt{\frac{\kappa t}{\pi R^2}}\exp^{-R^2/4\kappa t} \tag{9.3.14}$$

where

$$f* = \Gamma f(\frac{\kappa t}{R^2}) - Z f(\frac{ct}{R^2}) \tag{9.3.15}$$

$$g* = \Gamma g(\frac{\kappa t}{R^2}) - Z g(\frac{ct}{R^2}) \tag{9.3.16}$$

$$X = \left(\beta_s(1 - n) + \beta_f n\right)(\lambda + 2G) - (\lambda + 2G/3)\beta_u \tag{9.3.17}$$

$$Y = \frac{1}{\lambda + 2G}\left(\frac{X}{(1 - c_v/\kappa)a_u} + \frac{b'}{a_u}\right) \tag{9.3.18}$$

$$Z = \frac{1}{\lambda + 2G}\left(\frac{X}{(1 - c_v/\kappa)a_u}\right) \tag{9.3.19}$$

$i, j = x_s, y_s, z_s (i \neq j)$ are the coordinates of the point heat source and

$$b' = \left(\lambda + \frac{2G}{3}\right)\beta_u \tag{9.3.20}$$

9.3.3 Numerical solution

A 3D eighth-model has been generated to analyse the aforementioned THM processes. The model domain and the boundary conditions are showed in Figure 9.3.1. Symmetric conditions are specified in the model. This 3D model has a geometry of 10 m × 10 m × 10 m. The point heat source is located at the coordinate of (0, 0, 0) with the constant heat output of 300/8 W. The initial temperature and pore pressure are set as 0 ^{0}C and 0 Pa respectively. The model parameters are listed in Table 9.3.1. Homogenous and isotropic material properties were applied in the model. Pore water and solid are assumed as incompressible.

For the THM coupling, solid and fluid equations are solved in a monolithic manner. And the thermal equation is solved separately and iteratively with solid and fluid matrix.
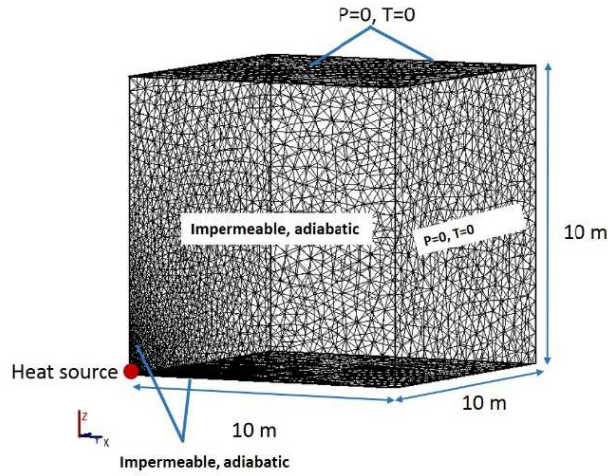
Fig. 9.3.1: 3D model for consolidation around a point heat source

9.3.4 Results

In Fig. 9.3.2 the evolution of temperature (left) and pore pressure (right) at three points are depicted. All points are along the Z-axis and have a distance of 0.25 m (node 1), 0.5 m (node 2) and 1 m (node3) to the heat point. The calculated temperature by OGS shows a very accurate agreement with the analytical solution as well as with the calculated temperature by COMSOL. At the early stage, the pore pressure increase caused by the thermal expansion

Table 9.3.1: Model parameters

Property	Symbol	Unit	Value
Bulk density	ρ	kg/m3	2450
Young's modulus	E	GPa	5
Poisson ratio	ν	-	0.3
Biot coefficient	α	-	1
Thermal conductivity	K	W/m/K^{-1}	1.64
Specific heat capacity	c	J/kg/K^{-1}	1000
Porosity	n	-	0.16
Permeability	$\mathbf{k}$	m^2	210^{-20}
Volumetric thermal expansion coefficient			
Pore water	β_w	K^{-1}	410^{-4}
Solid grain	β_s	K^{-1}	4.510^{-5}
Porous medium	β_u	K^{-1}	4.510^{-5}

of solid and water can be numerically exactly simulated. After that consolidation occurred, during which the excess pore pressure dissipated successively. All the results show the consistence tendency. There is only slight difference among each result.
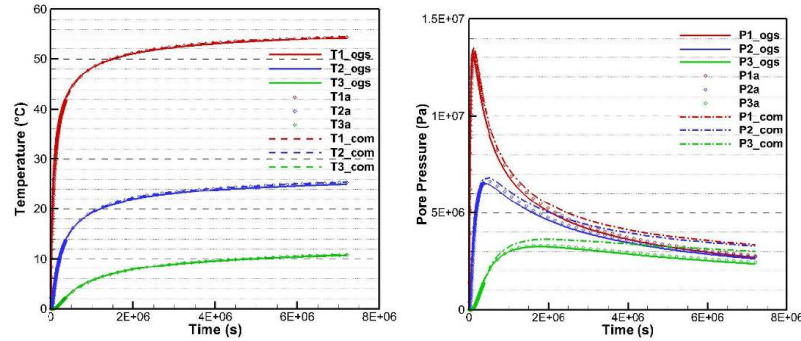
Fig. 9.3.2: Temperature (left) and pore pressure (right) evolutions at three different points. Comparison of the results calculated by code OGS with those of COMSOL and the analytical solution

Besides, one additional point of coordinate (0.4, 0.5, 0.4) outside the symmetrical axis was selected to present the mechanical results (Fig. 9.3.3). This point has a distance of about 0.75 m to the heat point. A fair good agreement has been achieved between the calculated results and the analytical solution. The thermal induced strain and the change of pore pressure caused firstly tensile stress in all the direction and also displacement in direction

away from the heat point. After that consolidation occurred resulted in the dissipation of pore pressure, reduce of the displacement and reduce of the tensile stress.
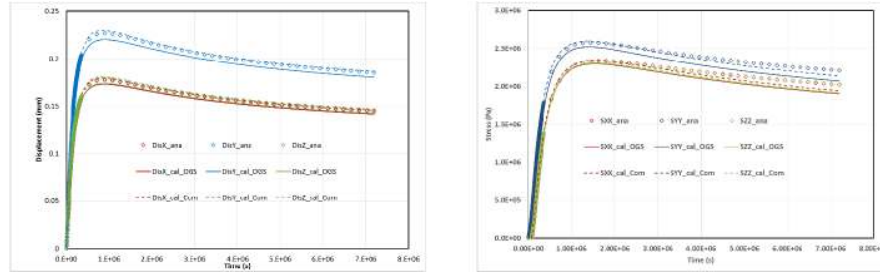
Fig. 9.3.3: Displacement (left) and stress (right) evolutions in X-, Y-, Z-direction at the select point. Comparison of the results calculated by code OGS with those of COMSOL and the analytical solution

Chapter 10
Reactive Transport

by Wenkui He, Jenna Poonoosamy, Georg Kosakowski, Luc R. Van Loon, Urs Mäder

10.1 Sequential chlorinated hydrocarbons degradation

by Wenkui He and Thomas Kalbacher

This benchmark problem is based on the reactive transport example presented in Chapter 15.6 of benchmark book volume I (Kolditz et al., 2012c), which was originally described in van Breukelen et al. (2005). It simulates the sequential dechlorination of chlorinated hydrocarbons (CHCs) from tetrachloroethene (PCE) to ethane (ETH) along an around 800 m long aquifer with a period of 20 years. Here, we use the benchmark to validate the coupling interface OGS#IPhreeqc described in He et al. (2015a).

10.1.1 Definition

The hydraulic conductivity and porosity of the aquifer are $10\,\text{m}\,\text{d}^{-1}$ and $0.25\,\text{m}\,\text{d}^{-1}$, respectively. The groundwater flow velocity is $0.1\,\text{m}\,\text{d}^{-1}$. Initially there is no CHC in the aquifer. The concentrations of PCE and its heavy isotope in the infiltration water are $0.9892\,\text{mol}\,\text{m}^{-3}$ and $0.0108\,\text{mol}\,\text{m}^{-3}$, respectively. The whole dechlorination chain is as follows:

PCE $\Rightarrow$ TCE (trichloroethylene) $\Rightarrow$ DCE (dichloroethylene) $\Rightarrow$ VC (vinyl chloride) $\Rightarrow$ ETH (ethylene)

The ^{12}C and ^{13}C isotopes of each CHC are modeled as separate species. Totally there are 11 chemical species including one tracer chloride, which is produced in each dechlorination reaction. All degradation reactions are simulated as first-order kinetics. For each CHC the kinetic isotope fractionation factor α_k is assumed to be constant during the whole degradation process, which can be calculated by equation (10.1.1):

$$\alpha_k = 1 + \frac{\epsilon}{1000} \tag{10.1.1}$$

where ϵ is the isotope enrichment factor. The kinetic of each ^{12}C as well as ^{13}C CHC can be calculated by equation (10.1.2) and (10.1.3), respectively.

$$\frac{d\text{CHC}_l}{dt} = -\gamma_l \ \text{CHC}_l \tag{10.1.2}$$

$$\frac{d\text{CHC}_h}{dt} = -\gamma_l \ \text{CHC}_h(1 + \frac{\epsilon}{1000}) \tag{10.1.3}$$

The first-order degradation rate and enrichment factor for each CHC are listed in Table 10.1.1.

Table 10.1.1: The first-order degradation rate and enrichment factor for CHCs

Parameter	Unit	PCE	TCE	DCE	VC	ETH
First-order rate	day^{-1}	$5.5 \cdot 10^{-3}$	$2.7 \cdot 10^{-3}$	$1.9 \cdot 10^{-3}$	$1.1 \cdot 10^{-3}$	0
Enrichment factor	-	-5.2	-8.5	-17.8	-23.2	-

10.1.2 Results

The concentration profiles of the light CHC as well as the $\delta^{13}C$ isotope signatures along the model domain simulated by PHREEQC (from van Breukelen et al. (2005)) and OGS#IPhreeqc are illustrated in Figure 10.1.1. As we can see, there is a very good agreement between the results simulated by both codes. More details of the coupling interface OGS#IPhreeqc and its applications can be found in He et al. (2015a).
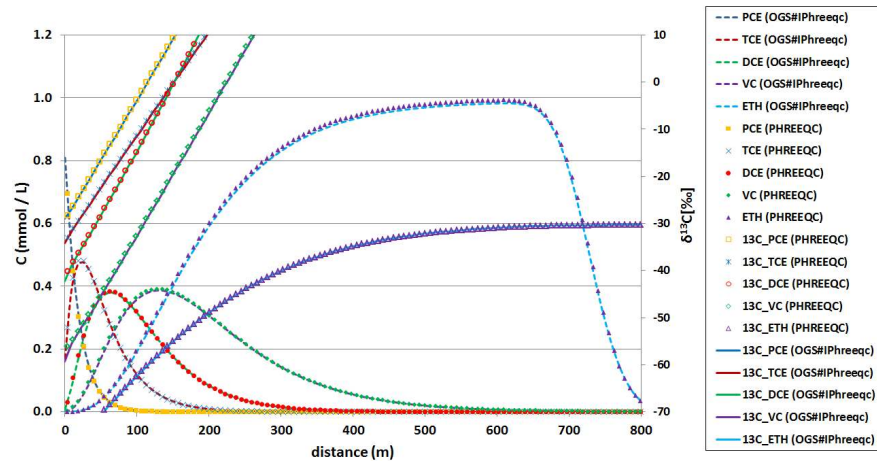
Fig. 10.1.1: Concentration profiles of the light CHCs and $\delta^{13}C$ isotope signatures along the model domain simulated by PHREEQC (symbols) and OGS#IPhreeqc (lines) after 20 a (from He et al. (2015a)).

10.2 PSI - Reactive transport benchmark

Jenna Poonoosamy, Georg Kosakowski, Luc R. Van Loon, Urs Mäder

In this chapter we briefly summarize the reactive transport experiments we conducted in a flow cell and which are described in Poonoosamy et al. (2015). Then we present our numerical simulations whose results were benchmarked against our experimental work. We considered three case studies with increasing complexity: case 1 considers a 2D system with density driven flow and conservative mass transport, case 2 in addition includes the dissolution and precipitation of mineral phases leading to porosity changes and case 3 extends the case 2 by considering the formation of solid solutions. We used the OpenGeoSys-GEM simulator, which uses finite element solvers for fluid flow and mass transport implemented in OpenGeoSys, coupled with GEMS for chemical equilibrium calculations (Kosakowski and Wanatabe, 2014). The numerical calculation with OpenGeosys-GEM will be compared with other reactive transport codes within the framework of SeS benchmark projects (se section 1.2).

10.2.1 Definition of the problem set-up

We designed a 2D reactive transport experimental benchmark which aims to be reproducible, fast to conduct and with a simple chemical set up. In what follows, we briefly summarize the experiment formulated to benchmark numerical simulations of flow of a fluid with variable density coupled with reactive transport (Poonoosamy et al., 2015). The experiment was conducted using the flow cell depicted in Fig. 10.2.1, which allowed us to visualize dye tracer tests. It consists of a reactive porous layer of strontium sulphate ($SrSO_4$) between two inert porous layers composed of silicon dioxide (SiO_2). The flow cell has dimensions of $0.1 \times 0.1 \times 0.01$ m, and it contains several ports for fluid injection and sampling. The inlet and outlet positions were chosen to create an asymmetric flow field. The chemical transformations in the flow cell were monitored by taking samples of the pore solution at ports 'c' and 'd', as well as by collecting the effluent at the outlet. The pressure difference between ports 'a' and 'b' was also measured. We performed post mortem analysis to determine the nature and location of the mineralogical transformations of the reactive media. Our numerical simulations will follow up this setup, and we will use our experimental measurements to quantitatively benchmark them. A qualitative benchmark will also be shown using images of the dye tracer distribution throughout the flow cell.

In Table 10.2.1, we list the properties of the different regions Q1, Q2, and Q3 shown in Fig. 10.2.1, as well as properties of the fluid and initial conditions used for the numerical calculations. The coordinates (x, z) of the
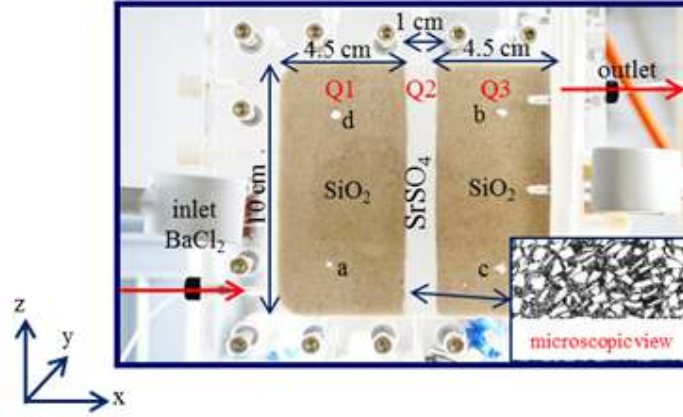
Fig. 10.2.1: Geometry of the numerical benchmark.

ports 'a' and 'b', where pressure sensors were installed, are (0.02 m, 0.02 m) and (0.08 m, 0.08 m) respectively. The ports 'c' and 'd', where sampling was performed, are located at (0.08 m, 0.02 m) and (0.02 m, 0.08 m) respectively. These are the coordinates one should use to compare numerical results with the experimental measurements presented in Poonoosamy et al. (2015).

Table 10.2.1: Properties of the different regions of porous media

Characteristics	Q1	Q2	Q3
Length [m] case 1 & 2	0.045	0.01	0.045
Length [m] case 3	0.045	0.005	0.055
Initial porosity (w_0) [-] case 1 & 2	0.34	0.33	0.40
Initial porosity (w_0) [-] case 3	0.34	0.40	0.40
Initial permeability k_0 [m^2] case 1, 2	1.82×10^{-11}	1.8×10^{-14}	1.82×10^{-11}
Initial permeability k_0 [m^2] case 3	1.82×10^{-11}	3.0×10^{-14}	1.82×10^{-11}
Dispersivity α [m]	10^{-5}	10^{-5}	10^{-5}
Diffusion coefficient D_w[m^{2}s^{-1}]	10^{-9}	10^{-9}	10^{-9}
Volume fraction of silicon dioxide case 1, 2 & 3 [-]	0.66	0	0.60
Total volume fraction of SrSO$_4$ case 1 & 2 [-]		0.67	
Volume fraction small strontium sulphate grains case 2 [-]	0	0.223	0
Volume fraction large strontium sulphate grains case 2 [-]	0	0.447	0
Total volume fraction of SrSO$_4$ case 3 [-] (one strontium sulphate grain size only.)		0.60	
Initial pH (fixed by initial chemical set up.)	5.6	5.6	5.6

In case 2, the Q2 region is composed of bimodal grain size distribution of SrSO$_4$ crystals (mixture of large and small grains).

We define three different benchmark cases with increasing complexity. In Case 1, we study density driven flow with conservative mass transport. In Case 2, we in addition consider dissolution and precipitation of mineral phases leading to porosity changes. Finally, Case 3 extends the Case 2 by inclusion of the possible formation of solid solutions. Table 10.2.2 provides additional information on the inlet and outlet conditions for the three case studies. For all simulations, we considered a discretization of the squared geometry in Fig. 10.2.1 by triangular elements. For Cases 1 and 3, a node distance of 1 mm was chosen, while for Case 2 a more refined mesh was adopted, with a node distance of 0.5 mm.

Table 10.2.2: Characteristics of the inlet and outlet.

| Characteristics	Case 1	Case 2	Case 3
Inlet (x=0 m; z from 0.008 to 0.0113 m) [m]	0.0033	0.0033	0.0033
Outlet (x=0.1 m; z from 0.08855 to 0.09185 m) [m]	0.0033	0.0033	0.0033
Source term [μL min^{-1}] at inlet	20.0	20.0	10.0
NaCl concentration [mol L^{-1}] at inlet	1.4	NA	NA
BaCl$_2$ concentration [mol L^{-1}] at inlet	NA	0.3	0.001
SrCl$_2$ concentration [mol L^{-1}] at inlet	NA	NA	0.099
Pressure at outlet [Pa]	101325	101325	101325
Amount [mL] of 3 g L^{-1}dye tracer injected	0.5	NA	NA
Modelling time duration [hours]	24	200	600

NA: not applicable

Case 1: *Conservative mass transport coupled with a density driven flow.*
Here we consider the injection of a highly concentrated solution of sodium chloride (NaCl of density 1.056 kg dm^{-3}) in a flow cell, initially saturated with water (density 1 kg dm^{-3}). An injection of 0.5 mL of a conservative tracer at the inlet is carried out at a rate of 20 μL min^{-1}, followed by the inflow of a NaCl solution for 24 hours. This NaCl solution was saturated with strontium sulphate (SrSO$_4$). The Q2 region, composed of SrSO$_4$, was assumed to be unreactive in this case study. The system was simulated for 24 hours.

Case 2: *Reactive transport with porosity changes.*
A highly concentrated solution of barium chloride (BaCl$_2$) is injected in a flow cell. The injection of BaCl$_2$ enhances the dissolution of SrSO$_4$ and causes barium sulphate (BaSO$_4$) to precipitate according to the reaction:

$$BaCl_{2(aq)} + SrSO_{4(s)} \rightarrow BaSO_{4(s)} + SrCl_{2(aq)} \qquad (10.2.1)$$
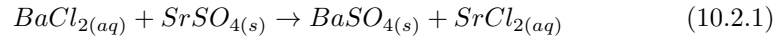
Porosity changes are likely to occur given that BaSO$_4$has a larger molar volume than SrSO$_4$. As a result, material medium properties such as permeability and diffusivity will equally change. The reactive layer Q2 has an

initial porosity of 33% and is composed of two grain size populations of $SrSO_4$ (i.e., celestite 1 and celestite 2). Celestite 1 corresponds to $SrSO_4$ with a grain size of 10-63 μm, while celestite 2 has a much higher grain size in the range 250-400 μm. Different kinetic rates of dissolution are used for these two grain populations (see section 10.2.2). The following reactive surface areas (per volume unit) were attributed to the small and large crystals respectively: 20000 m^2 m^{-3} and 100 m^2 m^{-3}. We assumed no kinetic constraints on the precipitated barite ($BaSO_4$(s)) phase. The simulation time is set to 200 hours.

Case 3: *Reactive transport involving the formation of a solid solution.* Here the reactive media is composed of celestite with a single grain size population of 63-125 μm. The reactive surface area (per volume unit), $a_{(SrSO4)}$, is 10000 m^2 m^{-3}. A solution composed of 0.099 mol L^{-1} $SrCl_2$ and 0.001 mol L^{-1} $BaCl_2$ is injected at the inlet at a flow rate of 10 μL min^{-1}. The simulation time is set to 600 hours.

The chemical configurations for Case 1, Case 2 and Case 3 are summarized in Table 10.2.4, Table 10.2.5 and Table 10.2.6 in the annex.

10.2.2 Description of the coupled code

The fluid flow and mass transport equations are solved by OpenGeoSys, and the chemical processes by the GEMS3K kernel code of GEM-Selektor V3 (Kulik et al., 2013). The coupling of these two codes is referred as OpenGeoSys-GEM, and its capabilities are described in Shao et al. (2009) and Kosakowski and Wanatabe (2014). Mass transport and chemical reactions are solved in a sequential non-iterative approach (SNIA), i.e. the transport and reaction equations are solved separately in a sequential manner without iteration between them.

The GEM approach consists of calculating the equilibrium state of a chemical system via minimization of its Gibbs free energy. The minimization is constrained by mass balance equations where the given total amounts of chemical elements are conserved. An additional charge balance equation is also imposed to enforce the electrically neutral condition of the system. The calculated equilibrium state by GEMS3K not only provides the molar amounts of every species in the system, which indicates which phases are stable or unstable, but also important chemical quantities such as species activities that are needed for calculation of kinetic rates of mineral dissolution. The thermodynamic data (standard Gibbs energy of formation [kJ mol^{-1}]) of aqueous, gaseous and solid species considered in our chemical system and the molar volumes [m^3 mol^{-1}] based on the PSI/NAGRA thermodynamic database (Hummel et al., 2002), are given in Table 10.2.3.

In OpenGeosys-GEM the density of the aqueous phase is calculated by GEM3K. This is done by calculating the partial molar volumes of each

aqueous species at the temperature and pressure of interest, and summing the product of these partial molar volumes by the corresponding molar amounts of the aqueous species to obtain the volume of the aqueous phase. The total mass of the phase divided by this volume gives the density of the aqueous phase, which is dependent on its molar composition. This density is updated after each chemical equilibrium calculation and passed along to the fluid flow solver.

Density flow

During the numerical simulations, the velocity field is calculated by solving the flow equation (equation 14.16 in Kolditz (2002)). The concentrations of all chemical species are determined by solving the mass transport equation (equation 3.46 in Kolditz (2002)) for the components (i.e. chemical elements) followed by equilibrium calculations by the chemical solver at every node of the mesh using the result of the transported components. The equilibrated concentrations are retrieved for the next time step of mass transport calculation. In OpenGeoSys, the Boussinesq approximation is considered, i.e the density variation is neglected in the mass conservation equation of the fluid phase. Density variations are included by the buoyancy term of the Darcy equation only. For variable-density flow in porous medium the Darcy velocity $\mathbf{q}$(m s^{-1}) is given as:

$$\mathbf{q} = -\frac{\mathbf{k}}{\mu}\left(\nabla p - \rho\mathbf{g}\right), \tag{10.2.2}$$

where $\mathbf{k}$ is the permeability tensor (m^2), μ is the dynamic viscosity (Pa s) of fluid, ∇p (Pa) is the pressure gradient, ρ is density of fluid (kg m^{-3}) and $\mathbf{g}$ is the gravity vector (m s^{-2}).

Porosity, diffusivity and permeability

As a result of dissolution/precipitation reactions, porosity changes occur. Transport properties such as effective diffusion coefficients, D_e,and the permeability, k_s, of the medium are parameterized as a function of porosity.

For the dependence of the effective diffusion coefficient, D_e, on porosity we used a simplified Archie's law (Archie (1942)):

$$D_e = D_w n^m \tag{10.2.3}$$

where D_w [m^{2}s^{-1}] is the diffusion coefficient in water, n [-] is the porosity and m [-] is an empirical coefficient. In our case m was set to 1.

Changes of permeability k_s [m^2] with porosity are given by a modified Kozeny – Carman equation:

$$k_s = k_0 \left(\frac{n}{n_0} \right)^3 \tag{10.2.4}$$

where k_0 [m^2] is the initial permeability, and w and w_0 are the current and initial porosities, respectively.

Activity corrections

Activity coefficients for all dissolved species γ_i are calculated by the extended Debye-Hückel equation (Helgeson et al. (1981)). A detailed description is reported in Wagner et al. (2012). Equation (5) relates the activity coefficients of an aqueous ion to its charge (Z_i) and ionic strength (I):

$$log_{10}\gamma_i = \frac{-A_\gamma Z_i^2 \sqrt{I}}{1 + \dot{a}_i B_\gamma \sqrt{I}} + b_{\gamma_i}\ I \tag{10.2.5}$$

Where $\dot{a}_i$ (in 10^{-8} cm) is an average distance of approach of two ions of opposite charges, b_γ is a semi-empirical coefficient, either individual for a given electrolyte or common for all charged species. $\dot{a}_i$ and $b_{\gamma i}$ were set to 3.72 and 0.064 respectively for all the ionic species (Helgeson et al. (1981)). These are values for the well calibrated sodium chloride electrolyte. A_γ and B_γ are temperature dependent coefficients obtained internally from SUPCRT92 subroutines (Johnson et al. (1992)) incorporated into the GEMS code. At a temperature of 25 ^{o}C and pressure of 1 bar, $A_\gamma \approx 0.5114$ and $B_\gamma \approx 0.3288$. Activity coefficients, $\gamma_{(i)}$ for neutral species (dissolved gasses) and water were set to unity.

Kinetics of precipitation and dissolution reactions of minerals

The temporal quantities of strontium and barium sulphate, and consequently also the porosity evolution, depend on the reaction kinetics. The kinetic rates dm/dt [mol s^{-1}] are calculated following Palandri and Kharaka (2004a). In our simulations, the simplest reactive surface area SA [m^2] model of those implemented in OGS-GEM was chosen:

$$SA = V_i a_i \tag{10.2.6}$$

where V_i [m^3] is the volume of the mineral and a_i [m^2 m^{-3}] is the relative surface area per volume unit.

In our simulations, barium sulphate was assumed to precipitate instantaneously (very fast kinetics) and only the kinetic dissolution of strontium sulphate was taken into account. The dissolution rate of strontium sulphate at pH = 5.6 (pH of the experiment) is calculated based on the equation given

in Palandri and Kharaka (2004a) with parameters from Dove and Czank (2005).

$$\frac{dm}{dt} = -SA \; k^\circ \, (1 - \Omega) \qquad (10.2.7)$$

where $SA[\text{m}^2]$ is the reactive surface area of the strontium sulphate mineral phase, $k^\circ = 10^{-5.66}\text{mol m}^{-2}\text{ s}^{-1}$ is the dissolution rate constant at 298.15 K and Ω is the mineral saturation index.

Solid solution

A solid solution phase is defined as a mixture of solids forming a homogeneous crystalline structure. The thermodynamics of a solid solution has been described in details by Bruno et al. (2007). Briefly, the Gibbs energy of a solid solution (composed of n-components) that deviates from ideality ($\Delta G_{total}{}^{real}$), can be split into the Gibbs energy of pure end-members ($G_i^0 X_i$), the ideal Gibbs energy of mixing ($\Delta G_{mix}{}^{id}$), and the excess Gibbs energy of mixing (G^{ex}):

$$\Delta G_{total}^{real} = \sum_{i=1}^{n} G_i^0 X_i + \Delta G_{mix}^{id} + G^{ex} \qquad (10.2.8)$$

The $\Delta G_{mix}{}^{id}$ is given by the following formula:

$$\Delta G_{mix}^{id} = qRT \sum_{i=1}^{n} X_i ln X_i \qquad (10.2.9)$$

where q is the site multiplicity factor and X_i the mole fraction of component i, R and T are the gas constant and temperature respectively.

The G^{ex} term depends on the mixing model of choice. In our approach, the subregular mixing model is considered (Bruno et al., 2007). The excess Gibbs energy of a binary subregular solution with component A and B mixing randomly is given by the Margules formula:

$$\Delta G^{ex} = X_A X_B (X_A w_{BA} + X_B w_{AB}) \qquad (10.2.10)$$

where X_A and X_B are the molar fractions of the end-members and w_{AB} and w_{BA} are the Margules interaction parameters, $w_{AB} \neq w_{BA}$. Note that this model reduces to the regular model when $w_{AB} = w_{BA}$. The Margules parameters (in J mol^{-1}) are usually defined as linear functions of temperature, T, and pressure, P,

$$w_{AB} = w_{u,AB} - T w_{s,AB} + P w_{v,AB} \qquad (10.2.11)$$

where w_u, w_s and w_v are empirical coefficients related to excess internal energy, entropy and volume of mixing, respectively. The Margules parameters w_{AB}, w_{BA} for barium and strontium sulphate solid solution at 298.15 K were set to 3787 J mol^{-1} and 3665 J mol^{-1} according to Zhu (2004). Corrections to pressure and temperature were neglected in our model.

Table 10.2.3: Thermodynamic database of aqueous, gaseous and solid species present under standards conditions.

Phase	Component	Standard Gibbs energy of formation $\Delta G^0{}_f$ [kJ mol^{-1}]	Molar volume [10^{-5}m^{3}mol^{-1}] under standard conditions
Aqueous	Ba(CO$_3$)	-1104.251	-1.1798542
	Ba(HCO$_3$)$^+$	-1153.325	1.917225
	Ba(SO$_4$)	-1320.652	0.818138
	Ba^{+2}	-560.782	-1.2901389
	BaOH$^+$	-721.077	0.91585235
	Sr(CO$_3$)	-1107.830	-1.5228401
	Sr(HCO$_3$)$^+$	-1157.538	1.4082323
	Sr(SO$_4$)	-1321.366	0.50248447
	Sr^{+2}	-563.836	-1.7757955
	SrOH$^+$	-725.159	0.70988636
	CO$_2$	-386.015	3.2806681
	CO$_3{}^{-2}$	-527.982	-0.60577246
	HCO$_3{}^-$	-586.940	2.4210897
	Cl$^-$	-131.290	1.7340894
	H$_2$	17.729	2.5264358
	O$_2$	16.446	3.0500889
	HSO$_4{}^-$	-755.805	3.484117
	SO$_4{}^{-2}$	-744.459	1.2917656
	OH$^-$	-157.27	-0.470784
	H$^+$	0.00	0.00
	H$_2$O	-237.18138	1.807
Gaseous	CO$_2$	-394.393	2478.9712
	H$_2$	0.00	2478.9712
	O$_2$	0.00	2478.9712
Solid	Ba(CO$_3$)	-1137.634	5.03
	BaCl$_2$	-810.400	5.40
	BaCl$_2$ • 2H$_2$O	-1296.320	8.186
	BaCl$_2$ • H$_2$O	-1055.630	7.208
	Ba(SO$_4$)	-1362.152	5.21
	Quartz	-854.793	2.2688
	Sr(CO$_3$)	-1144.735	3.901
	SrCl$_2$	-781.10	5.194
	SrCl$_2$ • 2H$_2$O	-1281.6798	7.283
	SrCl$_2$ • 6H$_2$O	-2240.8033	13.814
	Sr(SO$_4$)	-1346.15	4.625

10.2.3 Results

In this part we present the reference solution for the different case studies.

Case 1

Case 1 considers the injection of a concentrated non-reacting sodium chloride solution into a porous medium initially saturated with a liquid of lower density (water). Fig. 10.2.2 compares, at different times, the experimentally observed dye tracer distribution in a highly concentrated NaCl solution (bottom figures) with results from our numerical simulations (top figures). The simulated tracer profile is in good qualitative agreement with the experimental observation. A quantitative tracer concentration comparison could not be performed because of large uncertainties on the experimental tracer concentration calibration. Fig. 10.2.3 gives the simulated breakthrough curve of the tracer at ports 'c' and 'd', and at the outlet for comparison with other transport codes.
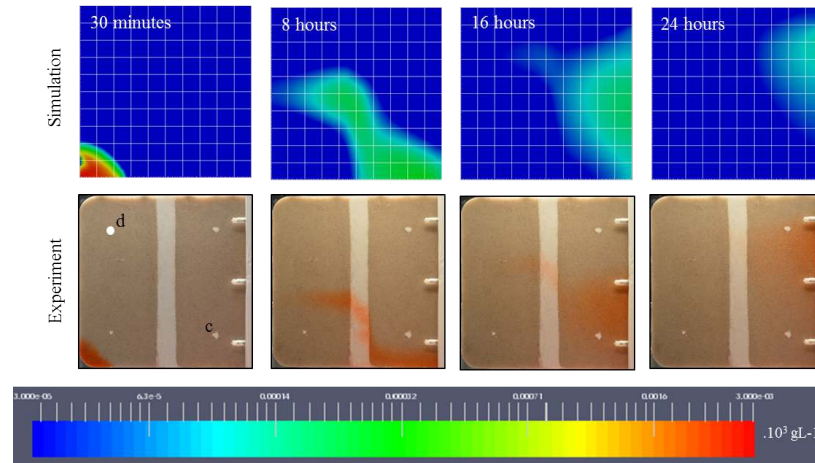

Fig. 10.2.2: The temporal evolution of the tracer profiles of the model (top) and the experiment (bottom).
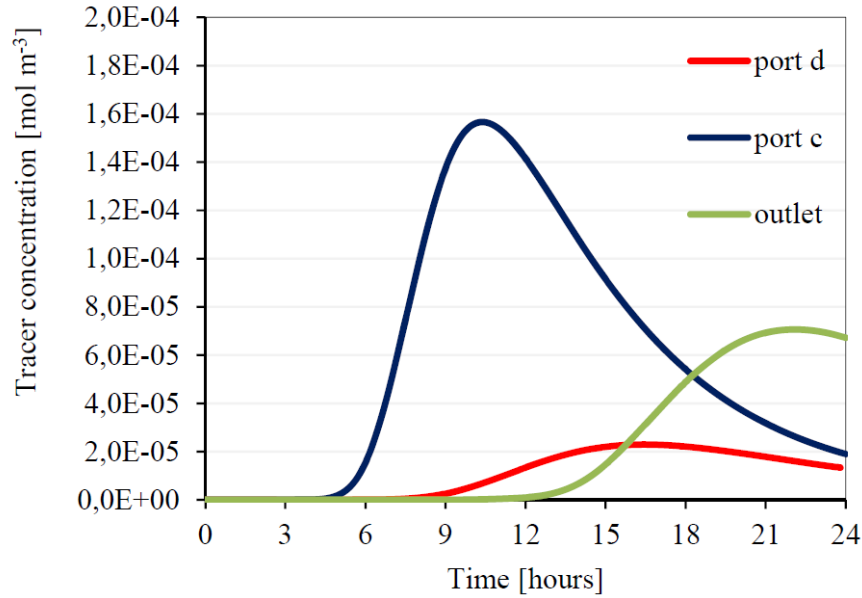
Fig. 10.2.3: The simulated tracer concentration at port 'd', 'c' and the outlet as a function of time.

Case 2

Case 2 extends Case 1 by considering dissolution and precipitation of minerals that change porosity and permeability in the flow cell. When a concentrated $BaCl_2$ solution reaches the reactive $SrSO_4$ layer Q2, the dissolution of $SrSO_4$ is triggered and barium sulphate ($BaSO_4$) precipitates. Fig. 10.2.4 shows the total amount of $BaSO_4$ and $SrSO_4$ in the flow cell with time, which changes due to either mineral dissolution or precipitation. During the first 150 hours, dissolution of $SrSO_4$ at a constant rate of 0.2 mmol per hour is observed. After 150 hours, this dissolution rate slows down. Similarly the total amount of precipitated barium sulphate increases for the first 150 hours and slowly builds up to 0.036 mol at 200 hours. The initial fast precipitation of barium sulphate for the first 150 hours results from the dissolution of the smaller strontium sulphate particles (celestite 1). As the smaller strontium sulphate grains are consumed, aqueous SO_4^{2-} is supplied by the dissolution of larger dissolution strontium sulphate (celestite 2) which is much slower due to its lower reactive surface area. The simulated results reproduced well the experimental data. In the experiments, small strontium sulphate crystals dissolved completely, while larger strontium sulphate grains were coated by a layer of barium sulphate, which prevented further dissolution. These observations
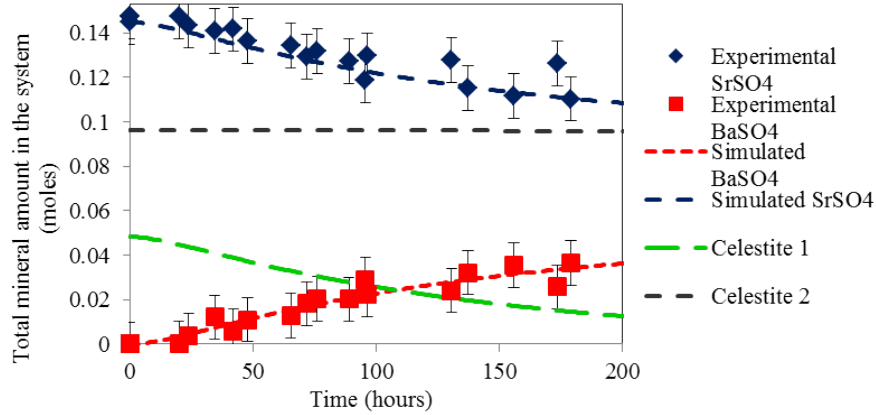
Fig. 10.2.4: Time evolution of the total bulk amount [mol] of barium sulphate and strontium sulphate in the flow cell.

were approximated in our model by applying a different reactive surface area for small and big strontium sulphate grains. The reactive surface areas attributed to celestite 1 and celestite 2 are fitted values, because the measured BET surface area overestimated strontium sulphate dissolution. The experimental observation also showed the absence of a precipitation front of barium sulphate at 200 hours. This was reproduced in our simulation as shown in Fig. 10.2.5.

The transformation of strontium sulphate to barium sulphate involves a volume increase of about 12%. The resulting porosity decrease and associated permeability changes are shown in Fig. 10.2.6. This model does not reproduce the experimentally observed 100% net pressure increase (between port
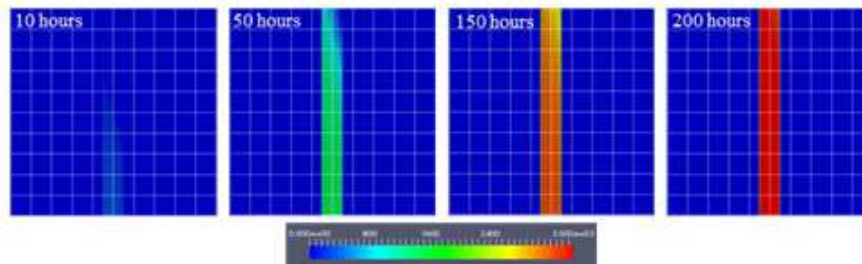

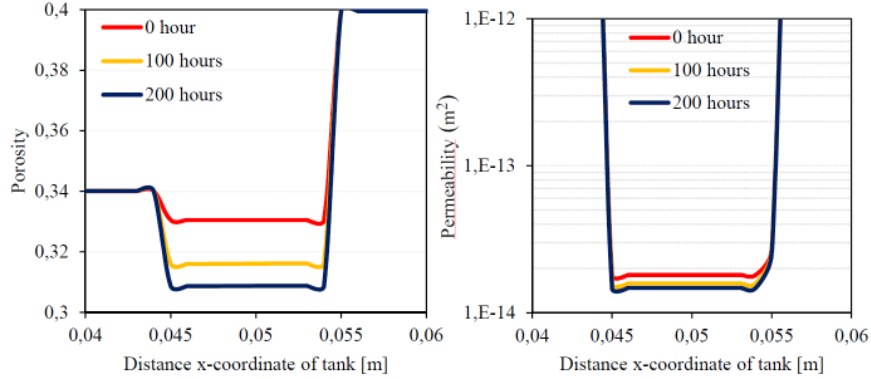Fig. 10.2.5: Time evolution of barium sulphate profiles [mol m-3] in the flow cell.

Fig. 10.2.6: Porosity (left) and associated permeability changes (right) across z = 0.01 m at 0, 100 and 200 hours.

'a' and port 'b') measured during the experiment (Poonoosamy et al., 2015), because the calculated porosity change is too small to significantly change the permeability as calculated by the Kozeny-Carman porosity – permeability relation (Equation 10.2.4). In Poonoosamy et al. (2015), a second scenario that involved the insertion of a 1mm thick zone at the quartz/ strontium sulphate interface (between the Q1 and Q2 region) with an initial lower porosity of 0.1 reproduced the experimental pressure changes. This scenario is not included here.

Fig. 10.2.7 shows the calculated and simulated ion concentrations at port 'c' and at the outlet as a function of time. Note that the uncertainties on the measured concentration at port 'c' are relatively high because it involved the sampling of small volumes of liquid (100μL) that were afterwards diluted for measurement by ion chromatography. The simulated breakthrough curves of Cl^-, Sr^{2+} and Ba^{2+} differ significantly from the experimental data. The chloride concentration of the liquid samples collected at port 'c' exceeds its injecting concentration (0.6 mol L^{-1}). This can be due to sampling artefacts at the ports. As such, the experimental ion concentrations at the port cannot be used for comparison. On the other hand, the calculated ion concentrations at the outlet are in good agreement qualitatively and quantitatively with experimental data.

Case 3

Case 3 is a hypothetical case study that considers the formation of a solid solution between barium sulphate and strontium sulphate. It still needs to be
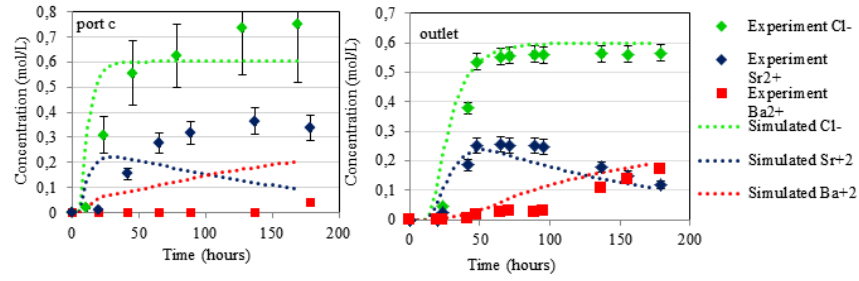
Fig. 10.2.7: Measured and calculated ion concentrations at port 'c' and at the outlet as a function of time.

tested experimentally. In this case, the pure mineral phase strontium sulphate is replaced by a solid solution. No pure barium sulphate phase is likely to precipitate. The injection of a solution composed of 1 mmol/L barium chloride and 99 mmol/L of strontium chloride, likely triggers a barium rich solid solution. Fig. 10.2.8 shows the total amount of mineral phases present in the flow cell with time. After 600 hours, 0.0330 mol of pure strontium sulphate phase has reacted to form 0.032 mol of a $(Sr_{1-x}Ba_x)SO_4$ solid solution. The composition of the formed solid solution changes with time. During the first 400 hours, the solid solution is enriched with barium (about 70%). Afterwards, the solid solution enriches itself in strontium (about 45% at 600 hours). This behavior is also reproduced in Fig. 10.2.8, where the total amount of the barium sulphate end member increases sharply for the first 400 hours and then only slightly increases afterwards.

Fig. 10.2.9 shows the porosity change between 0 and 600 hours and the associated permeability decrease across line $z = 0.01$m. The porosity decrease and the corresponding permeability change are negligible. It is also worth noting that for approximately the same amount of newly formed phase (0.032 mol of solid solution for Case 3 and 0.036 mol of pure barium sulphate for Case 2), the corresponding porosity decreases, and thus permeability is bigger for case 2 (1% in case 3 versus 6% in case 2). This is because the molar volume occupied by barium sulphate is higher than the molar volume of a solid solution composed of barium and strontium sulphate.

Fig. 10.2.8: The evolution of mineralogical changes in the flow cell.
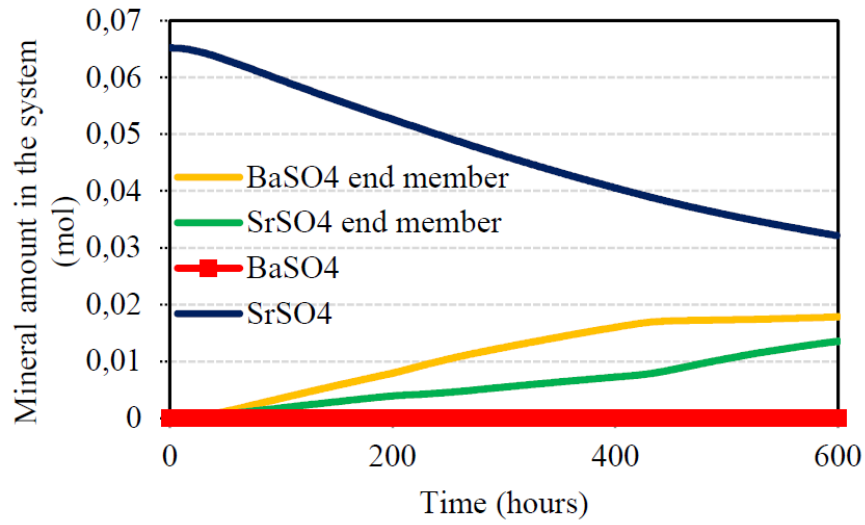
10.2.4 Summary

We conducted 2D experiments to benchmark fluid flow and reactive transport calculations. Barium chloride was injected in a flow cell filled with a porous reactive layer of strontium sulphate sandwiched between two layers of inert
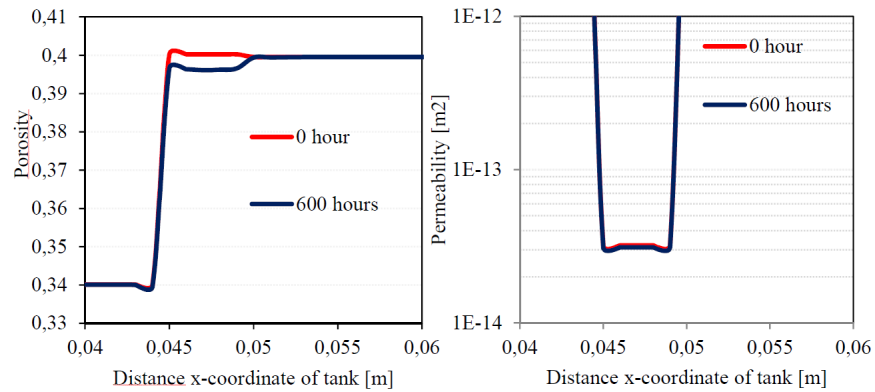

Fig. 10.2.9: Porosity (left) and associated permeability changes (right) across $z = 0.01$ m at 0 and 600 hours.

porous material, silicon dioxide. Our experiments are flexible enough to investigate several process couplings such as the effect of the liquid phase density on advective-diffusive transport of solutes, kinetically controlled dissolution/precipitation reactions causing porosity changes, and mineral changes involving formation of solid solution. We thus present 3 case studies with increasing level of complexity as a benchmark for reactive transport codes. In Case 1 tests with a non-reactive tracer and density-driven flow (due to the high concentration of a sodium chloride solution), were well reproduced by the numerical model. Case 2 involved the dissolution and precipitation of mineral phases that caused changes in porosity and permeability of the porous media. The presented model could reproduce well the temporal mineral bulk composition in the flow cell, but failed to reproduce the measured net pressure increase with the implemented Kozeny-Carman equation. However, by modifying the initial medium properties of the interface in the simulation, the experimental results could be fitted. This scenario described in Poonoosamy et al. (2015) is not presented here. Case 3 extends the problem of case 2 by considering the formation of a non-ideal solid solution and still needs to be verified experimentally. The presented cases are based on the benchmark study in the framework of the SeS benchmark initiative (Xie et al. (2014)).

Annex

Table 10.2.4: Equilibrium amount of solutes and phases (mol) for boundary (BC) and initial conditions (IC) for case 1.

Case 1	Inlet_BC (mol)	Q1_IC (mol)	Q2_IC (mol)	Q3_IC (mol)
$Na(CO_3)^-$	9.26E-010	8.72E-19	9.04E-19	8.72E-19
$Na(HCO_3)(aq)$	9.41E-007	1.38E-15	1.32E-15	1.38E-15
$Na(SO_4)^-$	4.74E-010	5.03E-18	2.42E-12	5.03E-18
Na^+	1.3999991	1.00E-09	9.98E-10	1.00E-09
$NaOH(aq)$	1.77E-009	2.69E-18	2.60E-18	2.69E-18
$Sr(CO_3)(aq)$	2.30E-018	2.99E-17	1.50E-11	2.99E-17
$Sr(HCO_3)^+$	5.82E-015	3.76E-14	1.94E-08	3.76E-14
$Sr(SO_4)(aq)$	1.33E-018	1.95E-16	4.54E-05	1.95E-16
Sr^{+2}	1.00E-009	1.00E-09	5.99E-04	1.00E-09
$SrOH^+$	3.13E-018	2.09E-17	1.09E-11	2.09E-17
$CO_2(aq)$	1.11E-005	1.36E-05	1.34E-05	1.36E-05
CO_3^{-2}	2.77E-010	4.67E-11	6.03E-11	4.67E-11
HCO_3^-	2.97E-006	2.45E-06	2.62E-06	2.45E-06
Cl-	1.4	1.00E-09	1.00E-09	1.00E-09
$H_2(aq)$	0	0.00E+00	0.00E+00	0.00E+00
tracer (aq)	0.003	1.00E-10	1.00E-10	1.00E-10
$O_2(aq)$	0.00019	2.30E-04	2.30E-04	2.30E-04
HSO_4^-	2.57E-014	2.39E-13	1.18E-07	2.39E-13
SO_4^{-2}	5.26E-010	1.00E-09	5.99E-04	1.00E-09
OH^-	4.75E-009	4.05E-09	4.39E-09	4.05E-09
H^+	3.92E-006	2.45E-06	2.52E-06	2.45E-06
$H_2O(aq)$	5.41 E+01	5.53E+01	5.53E+01	5.53E+01
CO_2	0	0.00E+00	0.00E+00	0.00E+00
O_2	0	0.00E+00	0.00E+00	0.00E+00
SiO_2	8.55E+01	8.55E+01	1.00E-09	6.47E+01
$SrCO_3$	0	0.00E+00	0.00E+00	0.00E+00
$SrCl_2$	0	0.00E+00	0.00E+00	0.00E+00
$SrCl_2.2H_2O$	0	0.00E+00	0.00E+00	0.00E+00
$SrCl_2.6H_2O$	0	0.00E+00	0.00E+00	0.00E+00
$SrSO_4$	0	0.00E+00	4.380E+01	0.00E+00

Table 10.2.5: Equilibrium amount of solutes and phases (mol) for boundary (BC) and initial conditions (IC) for case 2.

Case 2	Inlet_BC (mol)	Q1_IC (mol)	Q2_IC (mol)	Q3_IC (mol)
$Ba(CO_3)(aq)$	6.44E-10	2.42E-17	1.69E-17	2.42E-17
$Ba(HCO_3)^+$	1.24E-06	2.35E-14	1.69E-14	2.35E-14
$Ba(SO_4)(aq)$	7.33E-10	5.02E-16	1.63E-10	5.02E-16
Ba^{+2}	3.00E-01	1.00E-09	8.37E-10	1.00E-09
$BaOH^+$	7.31E-10	1.38E-17	1.01E-17	1.38E-17
$Sr(CO_3)(aq)$	2.65E-18	2.99E-17	1.50E-11	2.99E-17
$Sr(HCO_3)^+$	6.60E-15	3.76E-14	1.94E-08	3.76E-14
$Sr(SO_4)(aq)$	9.51E-19	1.95E-16	4.54E-05	1.95E-16
Sr^{+2}	1.00E-09	1.00E-09	5.99E-04	1.00E-09
$SrOH^+$	3.69E-18	2.09E-17	1.09E-11	2.09E-17
$CO_2(aq)$	1.17E-05	1.35E-05	1.34E-05	1.35E-05
CO_3^{-2}	2.28E-10	4.67E-11	6.04E-11	4.67E-11
HCO_3^-	2.97E-06	2.45E-06	2.62E-06	2.45E-06
Cl^-	6.00E-01	2.00E-09	2.00E-09	2.00E-09
$H_2(aq)$	0.00E+00	0.00E+00	0.00E+00	0.00E+00
$O_2(aq)$	2.00E-04	2.30E-04	2.30E-04	2.30E-04
HSO_4^-	1.59E-14	2.39E-13	1.18E-07	2.39E-13
SO_4^{-2}	2.67E-10	1.00E-09	5.99E-04	1.00E-09
OH^-	4.95E-09	4.06E-09	4.39E-09	4.06E-09
H^+	4.22E-06	2.45E-06	2.52E-06	2.45E-06
$H_2O(aq)$	5.50E+01	5.54E+01	5.53E+01	5.54E+01
CO_2	0.00E+00	0.00E+00	0.00E+00	0.00E+00
H_2	0.00E+00	0.00E+00	0.00E+00	0.00E+00
O_2	0.00E+00	0.00E+00	0.00E+00	0.00E+00
$BaCO_3$	0.00E+00	0.00E+00	0.00E+00	0.00E+00
$BaCl_2$	0.00E+00	0.00E+00	0.00E+00	0.00E+00
$BaCl_2.2H_2O$	0.00E+00	0.00E+00	0.00E+00	0.00E+00
$BaCl_2.H_2O$	0.00E+00	0.00E+00	0.00E+00	0.00E+00
$BaSO_4$	0.00E+00	0.00E+00	0.00E+00	0.00E+00
SiO_2	8.551E+01	8.551E+01	1.00E-09	6.657E+01
$SrCO_3$	0.00E+00	0.00E+00	0.00E+00	0.00E+00
$SrCl_2$	0.00E+00	0.00E+00	0.00E+00	0.00E+00
$SrCl_2.2H_2O$	0.00E+00	0.00E+00	0.00E+00	0.00E+00
$SrCl_2.6H_2O$	0.00E+00	0.00E+00	0.00E+00	0.00E+00
Celestite 1	0.00E+00	0.00E+00	1.466E+01	0.00E+00
Celestite 2	0.00E+00	0.00E+00	2.931E+01	0.00E+00

Table 10.2.6: Equilibrium amount of solutes and phases (mol) for boundary and initial conditions for case 3.

Case 3	Inlet_BC (mol)	Q1_IC (mol)	Q2_IC (mol)	Q3_IC (mol)
$Ba(CO_3)(aq)$	2.98E-12	1.62E-17	3.43E-18	1.63E-17
$Ba(HCO_3)^+$	5.52E-09	1.96E-14	4.20E-15	1.97E-14
$Ba(SO_4)(aq)$	1.23E-11	5.02E-16	4.78E-11	5.02E-16
Ba^{+2}	1.00E-03	1.00E-09	2.46E-10	1.00E-09
$BaOH^+$	3.33E-12	1.11E-17	2.41E-18	1.11E-17
$Sr(CO_3)(aq)$	3.65E-10	2.01E-17	1.03E-11	2.01E-17
$Sr(HCO_3)^+$	8.72E-07	3.13E-14	1.63E-08	3.15E-14
$Sr(SO_4)(aq)$	4.73E-10	1.95E-16	4.54E-05	1.95E-16
Sr^{+2}	9.90E-02	1.00E-09	5.99E-04	1.00E-09
$SrOH^+$	4.99E-10	1.68E-17	8.91E-12	1.67E-17
$CO_2(aq)$	1.25E-05	1.40E-05	1.38E-05	1.41E-05
CO_3^{-2}	1.21E-10	3.13E-11	4.17E-11	3.14E-11
HCO_3^-	2.57E-06	2.04E-06	2.21E-06	2.05E-06
Cl^-	2.00E-01	1.00E-06	1.00E-06	1.00E-06
$H_2(aq)$	0.00E+00	0.00E+00	0.00E+00	0.00E+00
$O_2(aq)$	2.52E-04	2.52E-04	2.50E-04	2.50E-04
HSO_4^-	5.00E-14	2.96E-13	1.45E-07	2.98E-13
SO_4^{-2}	5.15E-10	1.00E-09	5.99E-04	1.00E-09
OH^-	4.40E-09	3.27E-09	3.59E-09	3.25E-09
H^+	4.46E-06	3.04E-06	3.08E-06	3.06E-06
$H_2O(aq)$	5.53E+01	5.53E+01	5.53E+01	5.53E+01
CO_2	0.00E+00	0.00E+00	0.00E+00	0.00E+00
H_2	0.00E+00	0.00E+00	0.00E+00	0.00E+00
O_2	0.00E+00	0.00E+00	0.00E+00	0.00E+00
$BaSO_4$ end member	0.00E+00	0.00E+00	7.07E-10	0.00E+00
$SrSO_4$ end member	0.00E+00	0.00E+00	3.64E-06	0.00E+00
$BaCO_3$	0.00E+00	0.00E+00	0.00E+00	0.00E+00
$BaCl_2$	0.00E+00	0.00E+00	0.00E+00	0.00E+00
$BaCl_2.2H_2O$	0.00E+00	0.00E+00	0.00E+00	0.00E+00
$BaCl_2.H_2O$	0.00E+00	0.00E+00	0.00E+00	0.00E+00
$BaSO_4$	0.00E+00	0.00E+00	0.00E+00	0.00E+00
SiO_2	8.55E+01	8.55E+01	1.00E-09	6.62E+01
$SrCO_3$	0.00E+00	0.00E+00	0.00E+00	0.00E+00
$SrCl_2$	0.00E+00	0.00E+00	0.00E+00	0.00E+00
$SrCl_2.2H_2O$	0.00E+00	0.00E+00	0.00E+00	0.00E+00
$SrCl_2.6H_2O$	0.00E+00	0.00E+00	0.00E+00	0.00E+00
$SrSO_4$	0.00E+00	0.00E+00	3.24E+01	0.00E+00

Chapter 11
Mechanical-Chemical (MC) Processes

by Norihiro Watanabe and Renchao Lu

11.1 Permeability evolution of a quartz fracture due to free-face dissolution and pressure solution

Norihiro Watanabe and Joshua Taron

   This benchmark focuses on permeability evolution of a quartz fracture due to water-rock interaction under confining pressure. Free-face mineral dissolution/precipitation at pore walls and pressure solution (i.e. stress enhanced dissolution) at asperity contacts are assumed as dominant mechanisms to alter the fracture void space geometry and its permeability. Effects of a rock matrix on flow and solute transport are ignored in the current model.

11.1.1 Theory

We consider a quartz fracture having upper and lower surfaces in contact. In a macroscopic view, the fracture can be statistically represented using the mean mechanical aperture b_m [m] and the contact area ratio R_c [-]. Corresponding to water flow through the fracture, the fracture void space geometry can be altered by the following water-quartz interaction at the fracture surfaces:

$$\text{SiO}_2 + 2\text{H}_2\text{O} \leftrightarrow \text{H}_4\text{SiO}_4(\text{aq}) \tag{11.1.1}$$
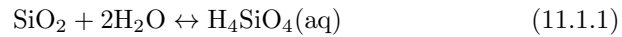
Since the fracture is under confining stress, the reaction rate will be different at hydrostatically stressed pore walls and at non-hydrostatically stressed asperity contacts. At the pore-walls, the reaction is free-face quartz dissolution

and precipitation as

$$\dot{m}_p = 2(1 - R_c)k^+ \left(1 - \frac{C_p}{C_{eq}^h} \right). \tag{11.1.2}$$

with the free-face dissolution rate m_p [mol/m^2/s], the dissolution rate constant k^+ [mol/m^2/s], solute concentration in the pore space C_p [mol/m^3], and the solubility under hydrostatic pressure C_{eq}^h [mol/m^3]. At fracture asperity contacts, pressure solution process can be dominant. Following a pressure solution model for intergranular contacts in Taron and Elsworth (2010a,b), the stress-enhanced reaction rate m_i can be expressed as

$$\dot{m}_i = 2\alpha R_c a^\sigma k^+ \left(1 - \frac{C_i}{a^\sigma C_{eq}^h} \right) \tag{11.1.3}$$

with the intergranular roughness α, the activity of solid silica under stress a^σ, and the intergranular concentration C_i [mol/m^3]. The activity of stressed solid silica is given as

$$a^\sigma = \exp \left(\frac{\max(\sigma_a - \sigma_c \beta_c^2, 0)}{\alpha RT} V_m \right). \tag{11.1.4}$$

where σ_a is the contact stress [Pa], σ_c is the critical stress [Pa], β_c is the burial constant, R is the gas constant [J/K/mol], T is temperature [K], V_m is the molar volume [m^3/mol]. If the contact stress is below the critical threshold $\sigma_c \beta_c^2$, the activity becomes unity and no enhancement is applied to the intergranular reaction.

Including the above reaction rates and solute exchange between the pore space and the intergranular zones, solute mass balances in a fracture void space and intergranular zones can be given as

$$b_m \frac{\partial C_p}{\partial t} + \nabla \cdot b_m \left(-\mathbf{D}' \nabla C_p + \mathbf{q} C_p \right) = 2(1 - R_c)k^+ \left(1 - \frac{C_p}{C_{eq}^h} \right) + 8R_c D_f \omega (C_i - C_p) \tag{11.1.5}$$

$$\omega R_c \frac{dC_i}{dt} = 2\alpha R_c a^\sigma k^+ \left(1 - \frac{C_i}{a^\sigma C_{eq}^h} \right) - 8R_c D_f \omega (C_i - C_p), \tag{11.1.6}$$

with the dispersion tensor $\mathbf{D}'$ [m^2/s], the flow velocity $\mathbf{q}$ [m/s], the intergranular water film thickness ω [m], and the intergranular molecular diffusivity D_f [m^2/s]. The dispersion tensor is given as

$$D'_{ij} = D_m \delta_{ij} + \alpha_T |\mathbf{v}| \delta_{ij} + (\alpha_L - \alpha_T) \frac{v_i v_j}{|\mathbf{v}|} \tag{11.1.7}$$

with the molecular diffusivity D_m [m^2/s], the longitudinal and transversal dispersion coefficients α_L, α_T [m]. The intergranular molecular diffusivity can be estimated by the Stokes-Einstein equation (Renard et al., 1999).

Fracture void space will be altered as a result of the free-face reaction and pressure solution at asperity contacts. Total aperture change can be estimated as a linear combination of the above effects

$$\Delta b_m = \frac{\Delta m_p V_m}{A_p} - \frac{\Delta m_i V_m}{A_i} \qquad (11.1.8)$$

where A_p and A_i are the surface area of pore walls and intergranular zones, respectively. As it is clear from the equation, the free-face dissolution tries to increase the aperture while the pressure solution has the opposite influence. Contact area ratio will also be updated corresponding to the aperture changes.

The void space geometry has an significant impact on the fracture permeability. In the case of laminar flow without gravitational effects, groundwater flow through the fracture can be expressed as

$$b_m S_s \frac{\partial p}{\partial t} + \nabla \cdot b_h (-\frac{k}{\mu} \nabla p) = 0 \qquad (11.1.9)$$

where b_h denote the hydraulic aperture [m], S_s is the specific storage [1/Pa], p is water pressure [Pa], k is the fracture permeability [m^2], and μ is the fluid dynamic viscosity [Pa s]. The fracture permeability is given from the cubic law (Snow, 1969)

$$k = \frac{b_h^2}{12}, \qquad (11.1.10)$$

and the hydraulic aperture can be estimated from the mean mechanical aperture and the contact area ratio as Walsh (1981)

$$b_h^3 = \frac{1 - R_c}{1 + R_c} b_m^3. \qquad (11.1.11)$$

11.1.2 Example

This example simulates a flow-through experiment of a novaculite fracture under confining pressure reported in Yasuhara et al. (2006). In particular, we focus on the experiment result until 1292 hours when a monotonic decrease of the fracture permeability was observed. The experimental fracture has a length of 89.5 mm and a width of 50 mm. Its initial hydraulic aperture was estimated as 18.5 μm from the cubic law. The fracture is under confining pressure of 1.38 MPa. Deionized water at 20°C is injected with time-dependent flow rates (Table 11.1.1) and the outlet pressure is fixed to 345 kPa.

In this example, we simplify the fracture geometry as a 1D homogenized model along a flow path (Fig. 11.1.1). The contact area ratio can be calculated

from the mean aperture using the aperture–contact area ratio relationship given in Yasuhara et al. (2006)

$$b_m = 2.5 \cdot 10^{-6} + 16.0 \cdot 10^{-6} \exp\left(-\frac{R_c - 5}{20}\right). \qquad (11.1.12)$$

Using the relationship and the Walsh's hydraulic aperture model, the initial mean aperture and contact area ratio can be calculated as 19.04 μm and 4.3 %, respectively. For quartz dissolution, we take the dissolution rate constant from Rimstidt (1997); Rimstidt and Barnes (1980)

$$\log_{10} k^+ = -0.7324 - 3705.12/T \qquad (11.1.13)$$

and solubility [mol/kg-w] from Rimstidt (1997)

$$\log_{10} m = -0.0254 - 1107.12/T. \qquad (11.1.14)$$

Reactive surface area is assumed to be equal to the geometric fracture surface area. Because of limited data availability, there is considerable uncertainty in the geochemical parameters in the experimented system. To match the simulation result with the experiment, the dissolution rate had to be enhanced by a factor of $7 \cdot 10^5$. All the other material parameters are listed in Table 11.1.2.
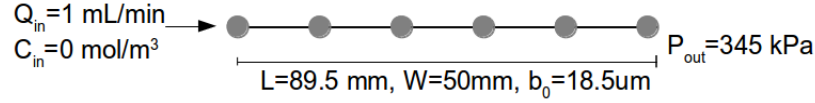

Fig. 11.1.1: 1D fracture model

Table 11.1.1: Time dependent boundary conditions

t [h]	T [°C]	Q_{in} [mL/min]	p_{out} [kPa]	C_{in} [ppm]
0 - 121	20	1.0	345	0
121 - 380	20	0.5	345	0
380 - 858	20	0.25	345	0
858 - 930	20	0	-	-
930 - 1266	20	0.25	345	0
1266 - 1292	20	0.125	345	0

Numerical solution of the problem can be obtained by using the finite element method to both the flow and transport equations. The numerical

model employs a mesh with linear line elements having a length of 1.1 mm and the implicit backward Euler method with an adaptive time stepping.

Table 11.1.2: Model parameters at $T = 20°C$

Parameter	Value
Quartz dissolution rate constant	$4.25 \cdot 10^{-14}$ mol/m^2/s
Quartz solubility	4.4 ppm
Dissolution rate enhancement	$7 \cdot 10^5$
Water density	998.3 kg/m^3
Water dynamic viscosity	0.001 Pa s
Molecular diffusion coefficient	10^{-9} m^2/s
Specific storage	$4.6 \cdot 10^{-10}$ 1/Pa
Initial mean aperture	19.04 μm
Initial contact ratio	4.3 %
Intergranular thickness	4 nm
Intergranular roughness	0.3
Intergranular diffusion coefficient	$0.43 \cdot 10^{-9}$ m^2/s
Burial constant	0.1

The simulation result as well as the experimental results are presented in terms of the fracture hydraulic aperture and effluent silica concentrations in Fig. 11.1.2 and Fig. 11.1.3. The fracture hydraulic aperture was calculated by

$$< b_h > = \sqrt[3]{\frac{12\mu LQ}{W(p_{\text{in}} - p_{\text{out}})}} \qquad (11.1.15)$$

with the fracture length L and the width W. Effluent concentrations were taken from concentrations at the outlet (x=L). The simulation reproduces both the monotonic decrease of the fracture permeability and effluent concentrations observed in the experiment.
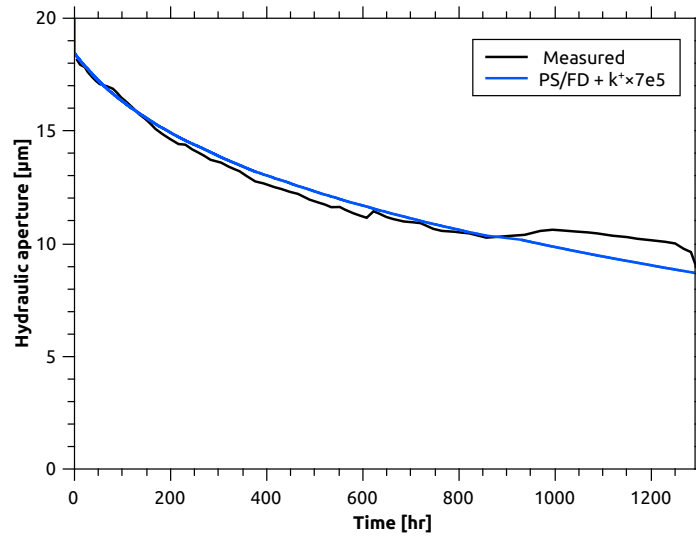
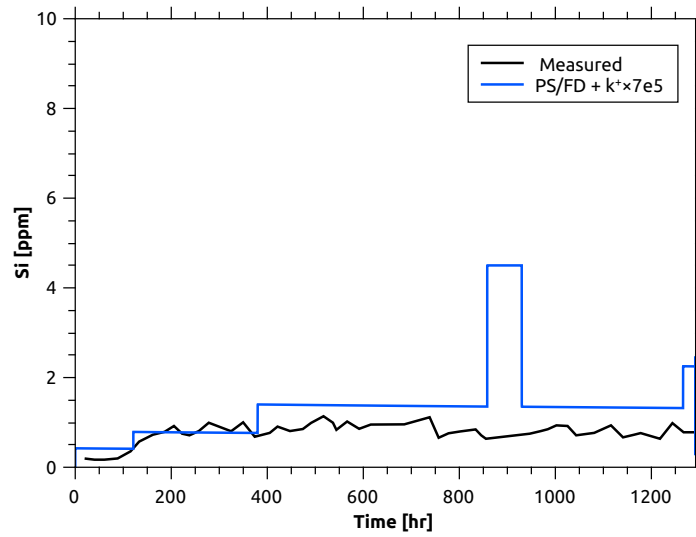Fig. 11.1.2: Simulated fracture hydraulic aperture evolution

Fig. 11.1.3: Simulated effluent Si concentrations

11.2 Free-face dissolution from granite fracture surfaces

by Renchao Lu, Wenkui He, Eunseon Jang, Haibing Shao, Norihiro Watanabe

In this benchmark, we focus on free-face dissolution from granite fracture surfaces when deionized water flows through the fracture surface. Laboratory-scale batch experiments are detailedly presented in Yasuhara et al. (2011). To better understand chemical weathering in a multi-mineral-constituted system with flowing water, a 1D reactive transport model is simulated using OpenGeoSys#IPhreeqc simulator. The simulated results are verified against Phreeqc (Parkhurst et al. (1999)).

11.2.1 Theory

Granite is composed of quartz and feldspar (k-feldspar, albite and anorthite) with minor amounts of biotite (annite and phlogopite). When deionized water flows through the fracture surfaces, water-granite interactions will result in continuous mineral dissolution. The involved kinetic reactions and corresponding logarithmic equilibrium constants are listed in Table 11.2.1.

Table 11.2.1: Kinetic reactions involved in the water-granite interactions and corresponding logarithmic equilibrium constants

Mineral	Kinetic reactions	[a] $\log K_{eq}$
Quartz	$SiO_2 + 2H_2O \rightarrow H_4SiO_4(aq)$	-4.00
K-feldspar:	$KAlSi_3O_8 + 4H^+ + 4H_2O \rightarrow Al^{3+} + K^+ + 3H_4SiO_4(aq)$	0.92
Albite	$NaAlSi_3O_8 + 4H^+ + 4H_2O \rightarrow Al^{3+} + Na^+ + 3H_4SiO_4(aq)$	2.76
Anorthite	$CaAl_2(SiO_4)_2 + 8H^+ \rightarrow 2Al^{3+} + Ca^{2+} + 2H_4SiO_4(aq)$	26.58
Annite	$KFe_3AlSi_3O_10(OH)_2 + 10H^+ \rightarrow Al^{3+} + K^+ + 3Fe^{2+} + 3H_4SiO_4(aq)$	29.47
Phlogopite	$KAlMg_3Si_3O_10(OH)_2 + 10H^+ \rightarrow Al^{3+} + K^+ + 3Mg^{2+} + 3H_4SiO_4(aq)$	37.44

[a] $\log K_{eq}$ is the temperature-dependent logarithmic equilibrium constant. 25°C is prescribed as reference temperature and given values are extracted from PHREEQC llnl database.

Dissolution-precipitation rates follow the widely used kinetic rate equation for multiple mechanisms

$$\dot{m} = \sum_i k_i^+ \left(1 - \left(\frac{Q}{K_{eq}} \right)^{p_i} \right)^{q_i},$$

(11.2.1)

where $\dot{m}$ [mol/m^2/s] is the mass removal rate per unit area, k_i^+ [mol/m^2/s] is the dissolution rate constant in the ith mechanism, Q [-] is the activity

product, K_{eq} [-] is the equilibrium constant, p_i [-] and q_i [-] are chemical affinity parameters in the ith mechanism.

The dissolution rate constant k^+ has Arrhenius-type dependence with temperature, and pH value, namely the negative logarithmic form of activity of hydrogen ion a_{H^+}, also has an impact on it which takes the form

$$k^+ = Ae^{-\frac{E}{RT}} a_{H^+}^{n_{H^+}}, \qquad (11.2.2)$$

where A [mol/m^2/s] is the Arrhenius pre-exponential factor, E [J/mol] is the Arrhenius activation energy, a_{H^+} [-] is the activity of hydrogen ion, n_{H^+} [-] is the H^+ catalysis constant. Generally, acid mechanism, neutral mechanism and base mechanism are considered.

Introducing roughness factor for minerals as f_r [-], the solute transport equation for a product j produces the relationship

$$b\frac{\partial C_j}{\partial t} + \nabla \cdot (-\mathbf{D}\nabla C_j + b\mathbf{q}C_j) = \sum_{m=1}^{n} \phi_m s_{mj} f_{r,m} \dot{m}_m \qquad (11.2.3)$$

with the fracture aperture b [m], the dispersion tensor $\mathbf{D}$ [m^2/s], the flow velocity $\mathbf{q}$ [m/s], the surface area ratio for mineral m in a unit area ϕ_m and the stoichiometric coefficient of the product j in the reaction m s_{mj}. The dispersion tensor is given as

$$D_{ij} = bD_m\delta_{ij} + b\alpha_T|\mathbf{v}|\delta_{ij} + b(\alpha_L - \alpha_T)\frac{v_i v_j}{|\mathbf{v}|} \qquad (11.2.4)$$

with the molecular diffusivity D_m [m^2/s], the longitudinal and transveral dispersion coefficients α_L, α_T [m]. The roughness factor for mineral m is

$$f_{r,m} = \frac{S_m d_m \rho_m}{6}, \qquad (11.2.5)$$

where S_m [m^2], d_m [m] and ρ_m [kg/m^3] are specific surface area, grain diameter and density of mineral m, respectively.

In the case of laminar flow without gravitational effects, groundwater flow through the parallel fracture can be expressed as

$$bS_s\frac{\partial p}{\partial t} + \nabla \cdot b\left(-\frac{k}{\mu}\nabla p\right) = 0 \qquad (11.2.6)$$

where S_s [1/Pa] is the specific storage, p [Pa] is water pressure, k [m^2] is the fracture permeability, and μ [Pa s] is the fluid dynamic viscosity. The fracture permeability is given from the cubic law (Snow (1969))

$$k = \frac{b^2}{12} \tag{11.2.7}$$

11.2.2 Problem definition

Granite samples used for the experiments are collected from a borehole, roughly 200m in depth, at the construction site of the Mizunami Underground Research Laboratory (MIU) in central Japan. Reactive surface area ratios for minerals at the fracture surface pairings are approximated by counting representative particles in a square-shape thin-section sample with a side length of 2mm (Table 11.2.2). The grain diameter and specific surface area are 178 μm and 0.51 m^2/g, respectively, revealed from the BET analysis. The experimental fracture induced by the Brazilian test has a length of 60 mm and a width of 30 mm. In the model, the fracture is approximated as a parallel plate with a uniform aperture, 5.7 μm. The differential pressure between the inlet and outlet is prescribed as 0.04 MPa to drive deionized water flow through the fracture. The experimental temperature is 25 °C. Figure 11.2.1 is a schematic of the 1D fracture model.

Table 11.2.2: Kinetic reactions involved in the water-granite interactions and corresponding logarithmic equilibrium constants

Mineral	Density (kg/m^3)	Surface area ratio (%)
Quartz	2.65 $\times 10^3$	50
K-feldspar	2.55 $\times 10^3$	25
Albite	2.62 $\times 10^3$	10
Anorthite	2.75 $\times 10^3$	10
Annite	2.10 $\times 10^3$	5
Phlogopite	2.10 $\times 10^3$	5

P_{in} = 0.04 MPa P_{out} = 0 MPa
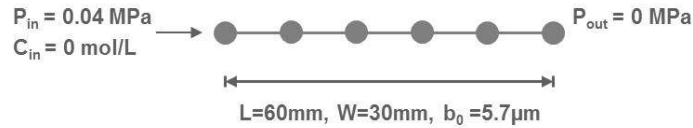C_{in} = 0 mol/L

L=60mm, W=30mm, b_0 =5.7μm

Fig. 11.2.1: a schmatic of the 1D fracture model

All the reaction parameters are taken from U.S. Geological Survey Open File Report 2004- 1068 as shown in Table 11.2.3 (Palandri and Kharaka (2004b)).

Table 11.2.3: Parameters used for calculating dissolution rate constants at given temperature and pH value

Mineral	Acid			Neutral		Base		
	$\log k_1$ mol/m^2/s	n_1 -	E_1 kJ/mol	$\log k_2$ mol/m^2/s	E_2 kJ/mo	$\log k_3$ mol/m^2/s	n_3 -	E_3 kJ/mol
Quartz	-	-	-	-13.34	90.10	-	-	-
K-feldspar	-10.06	0.50	51.70	-12.41	38.00	-21.20	-0.82	94.10
Albite	-10.16	0.46	65.00	-12.56	69.80	-15.60	-0.57	71.00
Anorthite	-3.50	1.41	16.60	-9.12	17.80	-	-	-
Annite	-9.84	0.53	22.00	-12.55	22.00	-	-	-

[1] Chemical affinity parameters p and q default to unity if not specified.

[2] log k computed at 25°C and pH = 0.

11.2.3 OGS-IPQC solution

The fracture is meshed into 60 line elements with a length of 1 mm. The initial concentrations, pH value and pe value at each element are 0 mol/m^3, 7.0 and 4.0, respectively. Dirichlet-type boundary conditions are set at the inlet. Element concentrations are assigned as 0 mol/m^3. PH value and pe value are assigned as 7.0 and 4.0, respectively. Hydraulic pressure is prescribed as 0.04 MPa. The .pqc file is responsible for preparing the input file for Phreeqc.The automatically-generated phinp.dat file sends the solution composition calculated at the last time step and configurations of mineral dissolution/precipitation rates to the Phreeqc for batch-reaction calculations. It is noteworthy that the water volume in a discretized fracture element is 1.70763×10^{-7} kg.

11.2.4 Phreeqc solution

Time step is a key parameter in the transport module in Phreeqc which is used to control the fluid velocity. Before activating kinetic reactions, some tracers are put into the water at the inlet and the arrival time at the outlet is recorded. By this way, we can calculate the fluid velocity in the fracture and make sure it has a same value in the OGS#IPQC simulator.
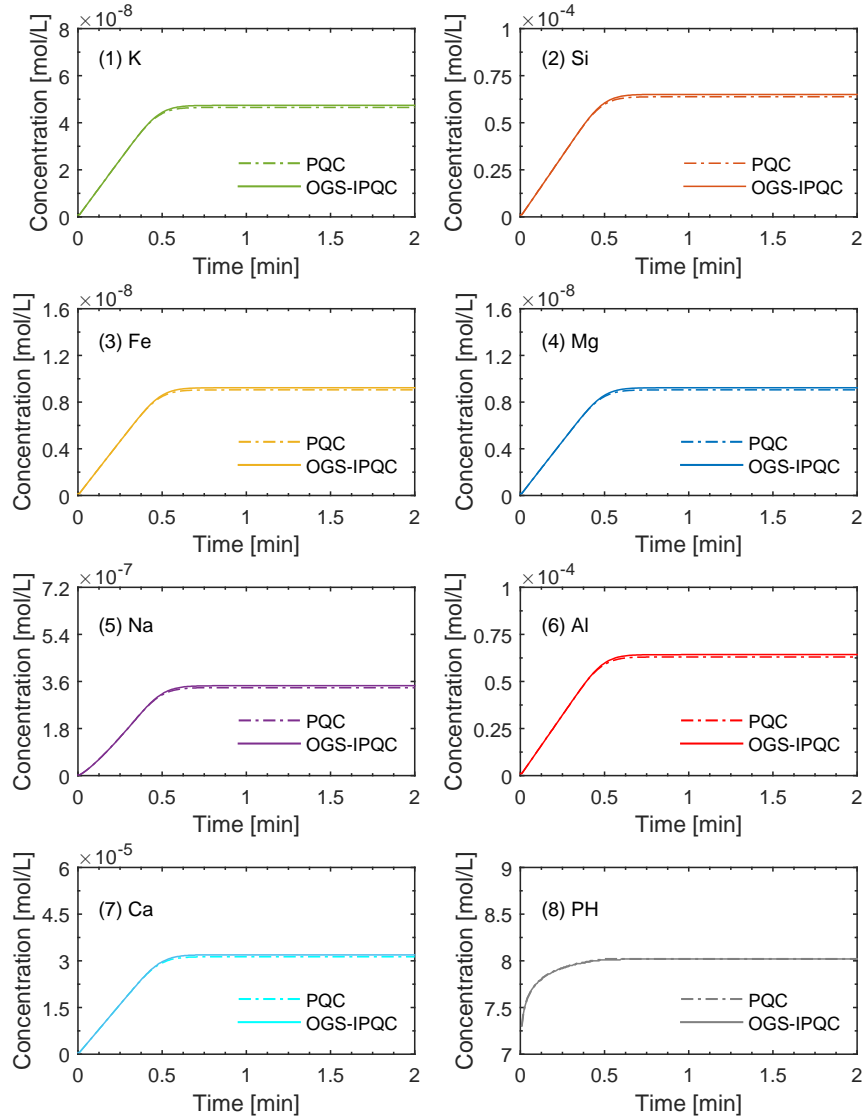
Fig. 11.2.2: Evolution of element concentrations (K, Si, Fe, Mg, Na, Al and Ca) and pH value at the outlet

11.2.5 Results

The evolution of element concentrations (K, Si, Fe, Mg, Na, Al and Ca) and pH value at the outlet simulated by Phreeqc and OGS#IPhreeqc are illustrated in Figure 11.2.2. Element concentrations and the pH value are in a good agreement. Before the water front arrives at the outlet, element concentrations grow linearly due to continuous mineral dissolution. After that, the new-formed aqueous species will be taken away with the flowing water.

Acknowledgments

Chapter 12
THC Processes in Energy Systems

by Christoph Lehmann and Thomas Nagel

12.1 Water adsorption to zeolites

Water adsorption to zeolites is a promising means for heat storage, including the seasonal storage of solar energy. We have added a material model to OpenGeoSys that calculates the equilibrium water loading of the zeolite and the heat of adsorption using the Dubinin-Polanyi theory of adsorption to microporous solids.

12.1.1 Experimental Data

Exemplary adsorption data parameterizing the material model are taken from measurements on binderless granulated 13X zeolite spheres (KÖSTROLITH® 13XBFK by Chemiewerk Bad Köstritz GmbH, Germany), which were performed by Dr.-Ing. H. Kerskes at Universität Stuttgart, Germany.

12.1.2 Theory

Zeolites are microporous aluminosilicate minerals which can be used, among others, for gas purification, as catalysts, for water softening, or for energy storage. It is the latter that we are focused on. Water adsorption to and desorption from zeolites constitute a completely reversibly cycle which is accompanied by the uptake and release of heat:

$$Z(s) + n\,H_2O(g) \rightleftharpoons Z \cdot n\,H_2O(s); \quad -\Delta H_{ads}$$
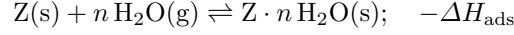
which makes zeolites a candidate for a thermochemical energy storage process.

The equilibrium of the adsorbate loading C at a certain temperature T and pressure p can be described as a two-dimensional surface in the three-dimensional C–p–T space:

$$f(C, p, T) = 0.$$

Polanyi found out that for a wide range of adsorbents the equilibrium loading can be described by the specific adsorption potential A_m, i. e. the amount of heat realeased per unit mass of adsorptive that gets adsorbed. Later on Dubinin extended this theory to the case of adsorption to microporous adsorbents, cf. Dubinin (1960).

The specific adsorption potential A_m can be calculated as

$$A_m = \frac{R}{M_V} T \ln \frac{p_S}{p_V} \tag{12.1.1}$$

where p_S is the saturation vapour pressure of the adsorptive and p_V is the current partial pressure of the adsorptive (here: water vapour) and M_V is the molar mass of the adsorptive. According to Dubinin, the equilibrium loading can be calculated from a single characteristic curve $W(A)$ which is a fixed functional relation for each adsorptive/adsorbent pair. Therein, W is the specific occupied pore volume of the adsorbent, i. e. the volume per unit mass of adsorbent that is occupied by the adsorbate. It relates to the dimensionless loading as

$$C = \varrho_{ads}(T) \cdot W \tag{12.1.2}$$

where $\varrho_{ads}(T)$ is the density of the adsorbate phase. The adsorbate density is not the same as the density of the free liquid, and it is not easy to determine experimentally. Hence, there are several density models for the adsorbate in literature. The one currently implemented in OpenGeoSys is taken from Hauer (2002)

$$\varrho_{ads}(T) = \varrho_0 \cdot \big(1 - \alpha_0 \cdot (T - T_0)\big) \tag{12.1.3}$$

with $T_0 = 293.15\,\mathrm{K}$, $\alpha_0 = 2.07 \cdot 10^{-4}\,\mathrm{K}^{-1}$ and $\varrho_0 = 998.08\,\mathrm{kg\,m^{-3}}$.

Using equations (12.1.1)–(12.1.3) the measured adsorption isotherms can be transformed into the characteristic curve, cf. Fig. 12.1.1. Afterwards a suitable model function can be fit to the mapped data. We employed a rational function as suggested by Núñez (2002), which reproduces the shape of the data very well:

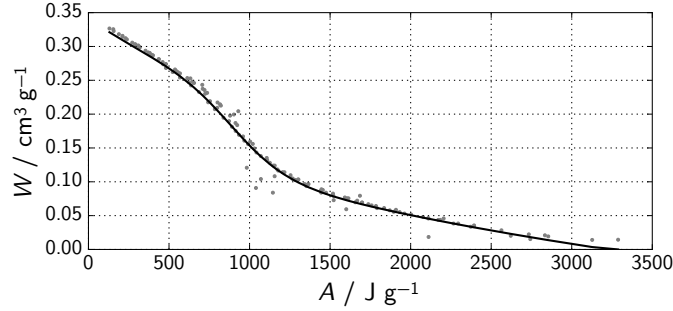$$W(A) \sim \frac{c_0 + c_2 A + c_4 A^2 + c_6 A^3}{1 + c_1 A + c_3 A^2 + c_5 A^3} \tag{12.1.4}$$

Fig. 12.1.1: Characteristic curve. It is clearly visible that the data points (A, W) obey a functional relation $W(A)$. The model (12.1.4) nicely fits the data

12.1.3 Benchmark: In equilibrium

The purpose of this and the other benchmarks is to show that the sorption equilibrium is implemented correctly. The simulations are performed using a one-element mesh and employ OpenGeoSys' TES process. The primary variables fluid pressure p, temperature T and water vapour mass fraction x_m are fixed at each node at the same value. Thus, heat conductivity, diffusion coefficient and permeability do not influence the simulations, and only adsorption takes place.

In the first benchmark, initial conditions are chosen in such a way, that the simulation already starts at equilibrium. Hence, we expect the reaction rate to be zero. The applied initial and boundary conditions are given in Tab. 12.1.1. For the sorption process the loading C and the vapour partial pressure are important. They relate to the values given in the table via

$$C = \frac{\varrho_{\mathrm{SR}}}{\varrho_{\mathrm{SR,\ dry}}} - 1, \tag{12.1.5}$$

where here $\varrho_{\mathrm{SR,\ dry}} = 1150\,\mathrm{kg\,m^{-3}}$, and via Dalton's law

$$p_{\mathrm{V}} = p \cdot x_{n\mathrm{V}} = p \cdot \frac{x_{m\mathrm{V}} \cdot M_{\mathrm{N}}}{x_{m\mathrm{V}} \cdot M_{\mathrm{N}} + (1 - x_{m\mathrm{V}}) \cdot M_{\mathrm{V}}}. \tag{12.1.6}$$

The reaction is driven by first-order kinetics

$$\dot{C} = k \cdot (C_{\mathrm{eq}} - C) \tag{12.1.7}$$

with a constant coefficient k.

The simulation results are plotted in Fig. 12.1.2. The reaction rate $\hat{\varrho}_{\mathrm{S}}$, which is given by

$$\hat{\varrho}_{\mathrm{S}} = \varrho_{\mathrm{SR,\ dry}} \cdot \dot{C} \cdot (1 - \phi), \qquad\qquad (12.1.8)$$

and also the difference between the equilibrium loading C_{eq} and the loading C_{num} obtained from OpenGeoSys are zero to the precision required for practical applications.

Table 12.1.1: Initial and boundary conditions for the benchmark starting in equilibrium

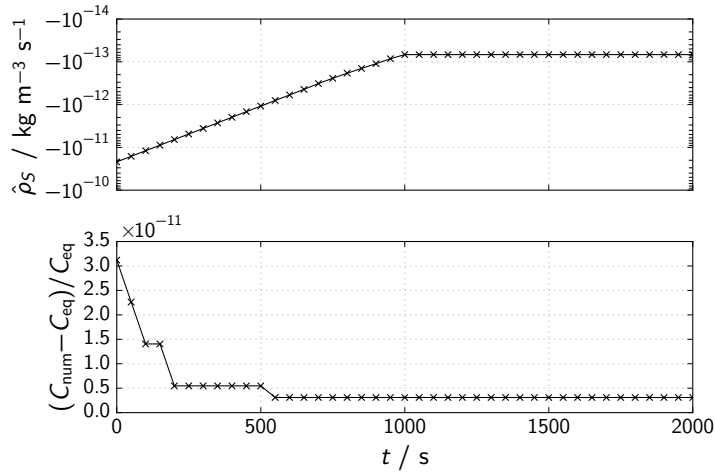|		
p	$500.0\,\mathrm{Pa}$	initial and
T	$130.0\,^{\circ}\mathrm{C}$	boundary
x_m	0.5	condition
ϱ_{SR}	$1266.6\,\mathrm{kg\,m^{-3}}$	initial condition only

Fig. 12.1.2: Change of reaction rate and relative difference to equilibrium loading when zeolite loading is in equilibrium initially. The reaction rate at later timesteps stays at $\approx -10^{-13}$ because of the limited output accuracy of 10^{-12}. That is also the reason for the steps in the plot of the relative difference between analytically and numerically obtained loading.

12.1.4 Benchmark: Starting at 99% of equilibrium loading

In the second benchmark it shall be verified that the zeolite loading correctly relaxes to its equilibrium value when it is initially out of equilibrium. The initial and boundary values have been changed compared to the first benchmark (cf. Tab. 12.1.2), such that now the initial loading corresponds to 99 % of the equilibrium value.

Table 12.1.2: Initial and boundary conditions for the benchmark starting out of equilibrium

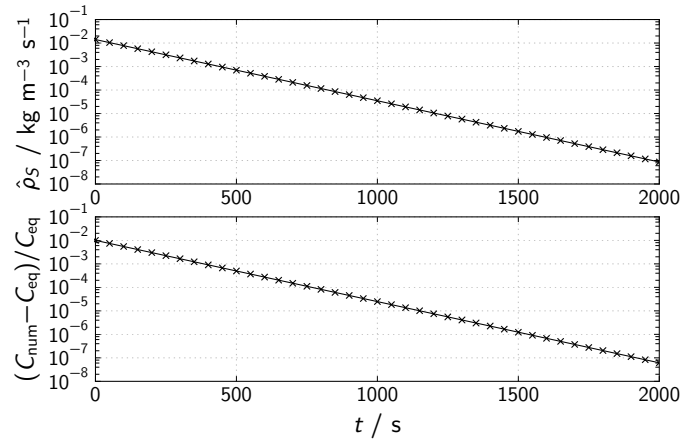|		
p	$500.0\,\mathrm{Pa}$	initial and
T	$76.9\,^{\circ}\mathrm{C}$	boundary
x	0.5	condition
ρ_{SR}	$1382.4\,\mathrm{kg\,m^{-3}}$	initial condition only

Fig. 12.1.3: Reaction rate and relative difference to equilibrium loading when the zeolite loading is at 99 % of its equilibrium value initially. While the loading approaches its equilibrium value over time, the reaction slows down accordingly.

## *12.1.5 Benchmark: Trajectories in pressure-temperature space*

Finally two trajectories in p-T space have been imposed as time-dependent boundary conditions: The first one comprises the isotherms from the experimental data (cf. Fig 4(a)), the second one proceeds diagonally through p-T space (cf. Fig 5(a)).

In both cases we begin with a completely dry zeolite sample, then every $1000\,\mathrm{s}$ a new (p, T) pair is imposed as a boundary condition, so the system has $1000\,\mathrm{s}$ to relax to equilibrium until new boundary conditions are imposed.

The loadings at the end of each of those $1000\,\mathrm{s}$ sections and the relative difference between them and the current equilibrium loading have been plotted in Fig. 4(b) and Fig. 5(b). It can be seen, that the equilibrum values are reproduced very well.
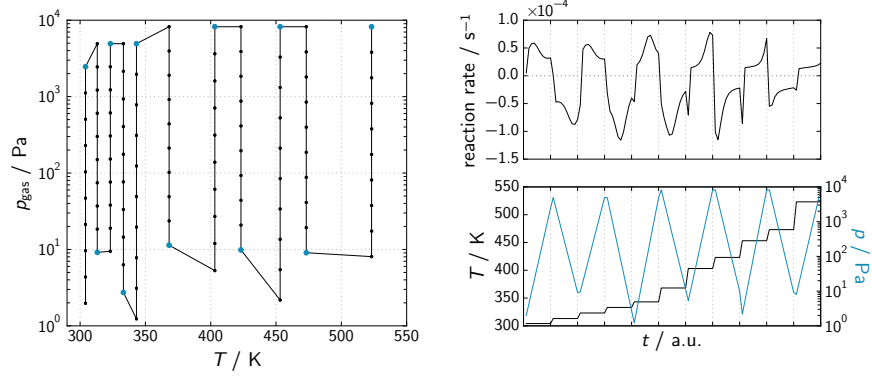
(a) Each coloured point in the diagram on the left corresponds to a grid line in the diagrams on the right. The start of the trajectory is at small p and small T.
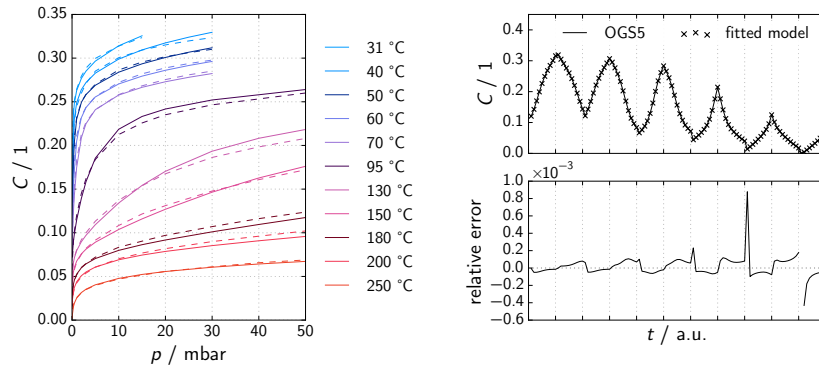
(b) Simulation results. In the diagram on the left the dashed lines are the isotherms from experimental data. The solid curves are the isotherms as obtained from the simulation. They exactly match the isotherms taken from the characteristic curve (cf. Fig. 12.1.1).

Fig. 12.1.4: Trajectory in p-T space comprising the measured isotherms.
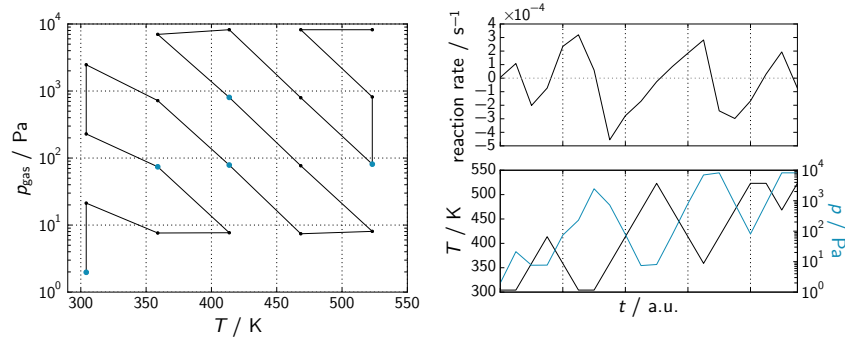
(a) Each coloured point in the diagram on the left corresponds to a grid line in the diagrams on the right. The start of the trajectory is at small p and small T.
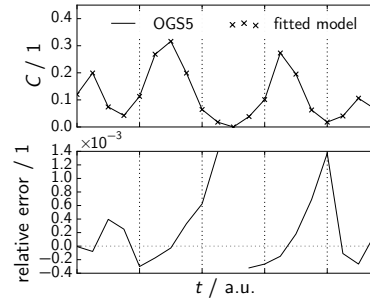

(b) Simulation results.

Fig. 12.1.5: Diagonal trajectory in p-T space.

Appendices

Appendix A
GINA_OGS

by Herbert Kunz (BGR)

In the field of the deep geological disposal of radioactive waste, a coupled THMC process modelling is inalienable for planning and evaluation of experiments in underground laboratories. Modelling helps to understand the processes and to assess the long-term safety of different disposal concepts. During the development of the numerical code OpenGeoSys (OGS), a pre- and post- processing tool, program GINA, is continuously developed by the BGR to match the requirements of the users.
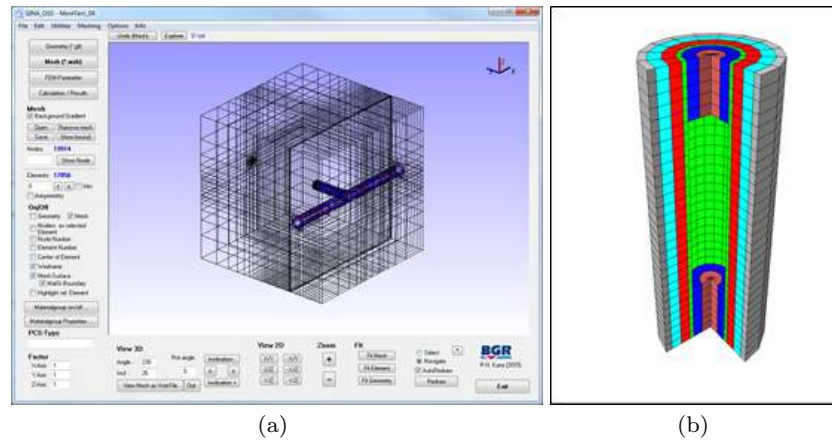

(a) (b)

Fig. A.1: Basic layout of GINA with a generated mesh for a rock-EDZ-tunnel system (a) and multi-barrier-system of a borehole concept (b)

The main features of this interactive graphical user interface GINA can be summarised:

A.1 Pre-processing

- Setting-up the geometrical data for FE meshing: The geometrical objects (points, polylines, surfaces and volumes) can be defined by entering coordinates or with the graphical user interface by mouse. These objects are the basic information for a FE-mesh generation, the definition of initial and boundary conditions, and the definition of result output in the post-processing.
- Preparation of control data for finite element calculations: The necessary control data (i.e. initial and boundary conditions, material properties, time step control) can be interactively defined using keyboard or mouse.

A.2 Mesh generation

A mesh generator for structured meshes in 2-D (quad element) and 3-D (prism and hexahedron element) is implemented in GINA (Fig. A.1). A special feature for the generation of finite element meshes is the tool for fracture networks including the rock mass (matrix). This feature was developed in the course of BGR's activities in fractured crystalline rock (Fig. A.1)

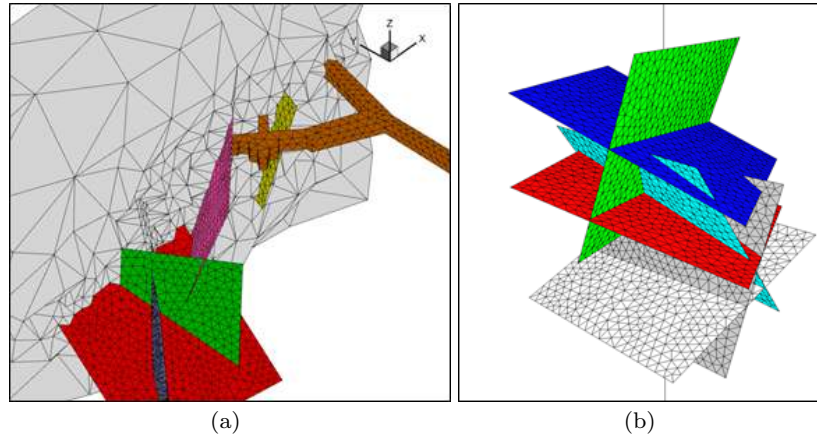(a)   (b)

Fig. A.1: Finite element mesh for a fracture network including rock mass (a) and for a fracture-borehole system (b)

For the unstructured meshes in 2-D and 3-D an interface to open source software, e.g. GMSH (`www.geuz.org/gmsh`) for unstructured meshes with triangles and quads and TetGen (`http://tetgen.berlios.de`) for meshes

with tetrahedrons. With the help of these programs even complex geological structures can be meshed in 2-D and 3-D. A special export function to GMSH allowed the re-meshing of triangle with bad aspect ratio (Fig. A.2).

(a)   (b)
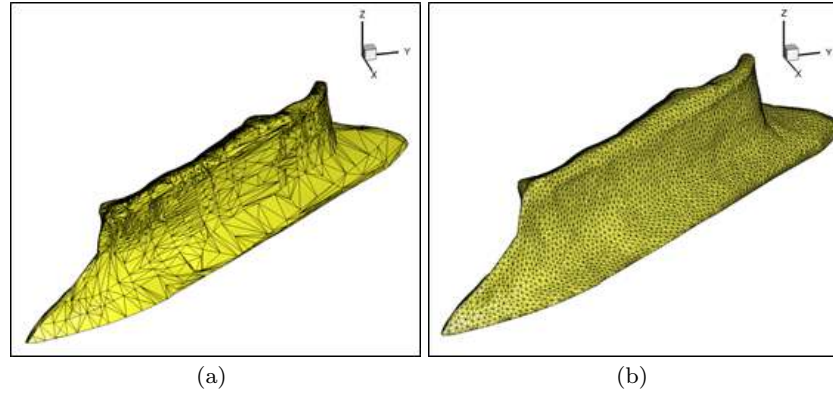
Fig. A.2: Triangles with bad aspect ratio (a) and the re-meshed geological model (b)

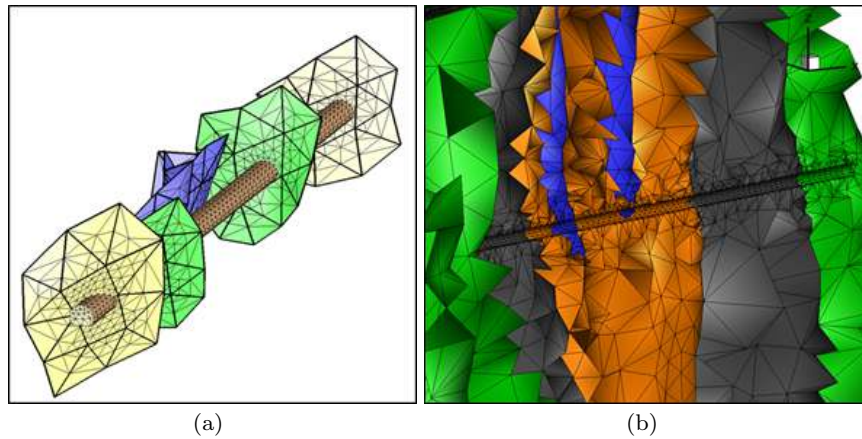

(a)   (b)

Fig. A.3: Intersection between a underground gallery (a) and different geological layers (b)

For the geotechnical modelling of, e.g. the heat generation of radioactive waste, holes, tunnels and even shafts must be integrated into a geological model. Hence a special feature in GINA has been developed to create galler-

ies along a path and calculate the intersection between the gallery and the
geological layers (Fig. A.3).

A.3 Post-processing

Before the simulated results are exported to another format for detailed eval-
uation, several post-processing functions are implemented for a quick view of
the results:

- Contour, colour, and isoline plots,
- X/Y-diagrams versus time or along a polyline,
- Calculation of principle stresses from a stress field and visualisation in
  vector form.

A.4 Data Interface

For data exchange with other programs, GINA supports following import and
export functions:

- Import file formats: GMSH, TetGen, VTK, Tecplot, DXF, ASCII
- Export file formats: GMSH, TetGen, JPG, VRML, Excel

   Contact: e-mail: `Herbert.Kunz@bgr.de`

Appendix B
ogs^6 Overview

by Dmitri Naumov, Lars Bilke, Thomas Fischer, Christoph Lehmann, Karsten Rink, Marc Walther, Wenqing Wang, Norihiro Watanabe

OpenGeoSys5 (ogs5) is a numerical simulator for coupled multifield problems based on the finite element method (FEM) which has been successfully applied in various fields. In ogs5, the current level of code flexibility allows the implementation of numerical algorithms specialized for the solution of numerous coupled problems such as groundwater flow systems, geotechnical systems, energy conversion technologies, *etc*. An overview of ogs5 applications is given in this book or see for example Kolditz et al. (2012c).

This success of the code, which is largely based on community efforts, also created some difficulties. Based on the experiences made, the new version OpenGeoSys6 (ogs6) is being developed with the aim of avoiding these difficulties and in order to supply the user with state-of-the-art and highly flexible numerical software. In the sequel, common difficulties encountered in the current version are described along with the new strategies applied in ogs6.

Major changes to fundamental parts of the ogs5 code, for example changing the time-stepping scheme, substantial reordering of parts of certain algorithms, or changing the coupling of subsystems, require substantial effort on the users' side. The ogs5 code structure is organized in several libraries like the `MeshLib` library dealing with mesh creation and access, or the `FileIO` library responsible for the reading of different file formats, *etc*. This approach was successful as long as a certain set of processes was used and users were interested in comparatively minor changes, such as implementing new constitutive relationships or modifying individual coefficients of local finite element matrices. Larger changes to numerical methods or fundamental modeling concepts are, however, complicated by the fact that key aspects of a physical model such as the state (referring to the physical and algorithmic state of the simulation) of a running simulation are spread across different

parts of the code (and thus libraries) making it difficult to implement such changes in one part of the code without causing ripples in others.

One of the problems common in software community projects having large interdependent parts of code is frequent "branching" of the code base without back-contributions to the main development trunk of the software. This happens because changes in one part of the code break some of the functionalities in others, as indicated earlier. Because complex code dependencies make a correction very difficult, developers often ignore flaws in parts of the software outside their sphere of interest, thus prohibiting the merging of branches into a common version with combined functionality.

This lack of modularization also leads to code replication based on small changes to existing code instead of an algorithm's generalization. In other words, instead of using or implementing a generalized algorithm for their current needs, programmers often copy and paste the entire algorithm and make minor changes to the copy. This rapidly leads to code duplication. In a modular code, such redundancies should be avoided: the behaviour of an algorithm can be changed without introducing changes to the data structures (representing a physical or abstract state, for example) to which that algorithm is being applied. Most of the algorithms available for example in the Standard Template Library (ISO, 2011) share this property.[1] Such an approach is at the core of ogs6 development.

Testing and benchmarking are important assets in the quality assurance of a scientific code, especially in a community project. A lack of code modularity will, in addition to complicating the actual code, make all tests, in particular unit-tests, significantly more difficult to write and maintain. Testing a single aspect of an algorithm requires some setup, which is usually accomplished by creating "dummy" objects—mockups. The mockups isolate the part of the system they are representing as required for testing a specific algorithm. As a consequence of a program's state being spread out through different parts of the code, *i.e.* a lack of modularity, the creation of mockups leads to the replication of many parts of the system, which do not have any influence on the test being performed but are merely an inconvenient consequence of the interdependent code structures.

One of the current goals for ogs6 development is parallelization. The implementation of algorithms operating on data structures, whose state is spread over different regions of the code is usually more difficult than for algorithms which depend on a system's state. In this respect, the modularization of the code also aids its efficient parallelization: algorithms without any side-effects (*i.e.* which do not change the system's state) can be executed in parallel without any further ado; parallel algorithms changing only small and well-defined portions of the state need synchronization only with that data portion; algorithms dependent on many parts of the system are very difficult to parallelize and their correct execution is hard to verify. These concepts are

---

[1] Many more algorithms can be found in the Boost C++ library (Boost).

reflected in the code structure of ogs6 and based on lessons learnt by using and developing parallel versions of ogs5.

Considering the above reflections on the ogs5 code base and the experience gained in recent years with this code, one can conclude that the modularization of the code is the most important aspect of current code development. Consequently, the idea of modularization is implemented on several levels in addition to the separation of libraries:

- using algorithms provided by the Standard Template Library and Boost library, for example, and implementing algorithms which do not depend on a particular state[2]
- using common linear algebra interfaces allowing for the use of different linear algebra solver libraries like Eigen (Guennebaud et al., 2015), LIS (LIS), or PETSc (Balay et al., 2015)[3]
- strict separation of types, their capabilities (which operations are supported by values/objects of this type), and their semantics (the relations between types). See for example "a concept design for the STL." (Stroustrup and Sutton, 2012)
- localization of data required for a single common computation; for example local assembler data can include shape matrices of the current finite element and a set of primary/secondary variables required for the assembly of a local matrix. The ideas of localized data structures are known under the names "cache-aware" (Aggarwal and Vitter, 1988) and "cache-oblivious algorithms" (Frigo et al., 1999; Prokop, 1999), or "data-driven design."[4]

Imposing much stricter requirements in the development process of tests for all new code contributed to ogs6 is also influencing the design of ogs6. Tests of algorithms with very versatile interfaces are difficult to write and usually result in a large number of cases to be covered by these tests. Difficulties encountered by a developer when writing tests can be recognized as a problem of the newly written code itself and lead to its refactorization. Thus, tests do not only ensure the functionality of the code but also improve its quality.

Unit-tests in ogs6 are implemented in the google testing framework "gtest" (Google Test). For unit-tests of numerical algorithms the automatic test creation suite "autocheck" (Autocheck) has proven helpful.[5] With "autocheck" it is possible to write concise tests checking invariants of an algorithm with

---

[2] Algorithms without side-effects are also known as pure functions in functional languages such as Haskell (Haskell).

[3] PETSc is a library for parallel computations including a parallelized suite of linear solvers. Using parallelized and non-parallelized libraries interchangeably further increases code reusability.

[4] Localization of the local assembler data yielded approximately a two-fold improvement in computation time of the local matrices of the Laplace operator in comparison to the ogs5 code. See Naumov et al. (2014) for more details.

[5] The autocheck library written in C++ has its roots in the Haskell libraries quickcheck (Claessen and Hughes, 2015) and SmallCheck (Runciman and Cheplyaka, 2015).

random input data. Random-value generators starting with simplest types for floating point numbers for example, are step by step extended to user specific types like points in 3 dimensional space with constraints such as points lying on a sphere of a given radius.

In addition to the unit-tests there are end-to-end tests (formerly called benchmarks) executing whole simulations starting with reading of input files, then reading geometry, assembling and solving the linear system of equations, and finally writing the results. The results are then compared to an analytical solution of the problem or to a very accurate numerical reference solution. The comparison is based on absolute and relative maximum errors specific for the test being run.

The test suite including end-to-end tests is run on continuous basis. The unit-tests are run on all supported platforms (with their respective compilers: Visual Studio C++ compiler for Windows OS, and gcc and clang compilers on linux and Mac OS) before any changes are merged into the main development line. All tests are executed after every change introduced to the main development line including time-measurements and other indicators of the submitted code's quality.

Not all of the code quality requirements can be tested automatically. The code structure, the introduction of new interfaces, the correct choice of data structures and algorithms operating on that data are verified in a peer review process by at least two developers. The review process and the corresponding discussions are publicly available on GitHub—a web based project hosting platform based on the distributed revision control system git—at `https://www.github.com/ufz/ogs`.

Existing and planned releases `http://docs.opengeosys.org/releases`:

- 6.0.01 (02/15): Basic elliptic solver
  `http://docs.opengeosys.org/releases/6-0-1`
- 6.0.02 (07/15): General Neumann boundary conditions
  `http://docs.opengeosys.org/releases/6-0-2`
- 6.0.03 (09/15): Heterogeneous material properties, Unstrut case study (Fig. B.1)
  `http://docs.opengeosys.org/releases/6-0-3`

- 6.0.04 [WW]: PETSc interface for parallel applications (Fig. B.2)
- 6.0.05 [CL]: Coupled non-linear process: Energy storage applications
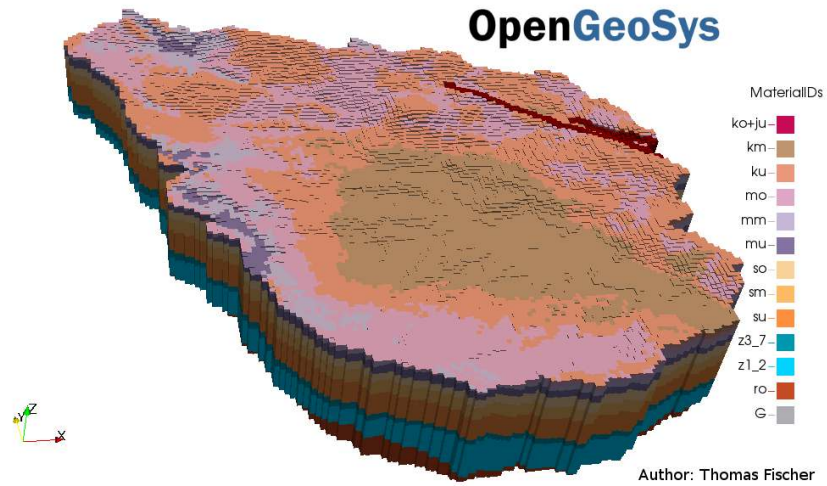
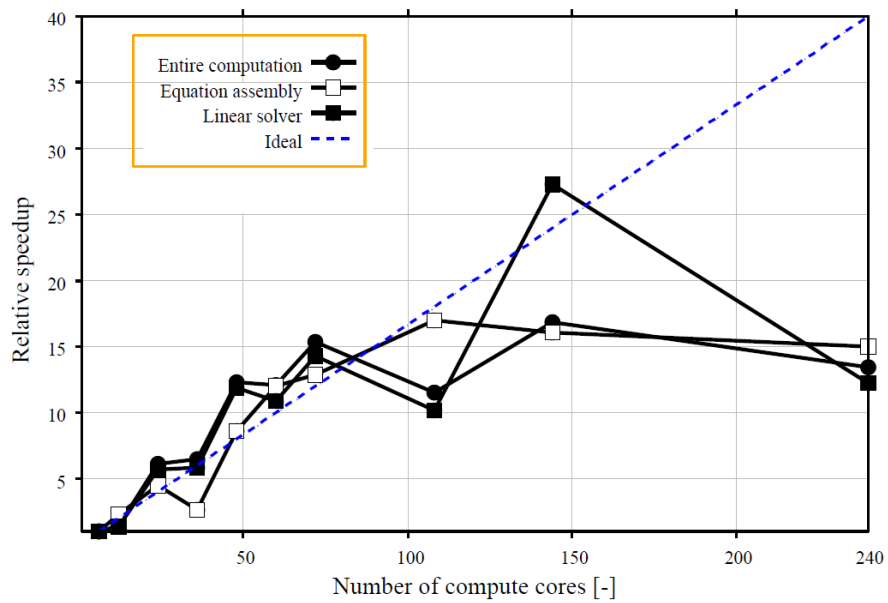Fig. B.1: ogs[6] simulation for the Unstrut catchment in the Thuringian Basin

Fig. B.2: Parallel ogs[6] simulation - preliminary OGS#PETSc results (based on 6 cores, i.e. multiply relative speed-up by factor 6)

Symbols

Table B.1: Table of Symbols

Symbol	Parameter	Unit
Greek symbols		
α	Biot constant	$-$
α	Thermal expansion coefficient	K^{-1}
α	Intergranular radius	$-$
α	Van Genuchten parameter	m^{-1}
α_k	Kinetic isotope fractionation factor	$-$
α_L	Longitudinal dispersion length	m
α_T	Transversal dispersion length	m
β	Cubic thermal expansion coefficient	K^{-1}
β_c	Burial constant	$-$
χ	Bishop coefficient	$-$
γ	Activity coefficient for dissolved species	$-$
Γ	Domain boundary	$-$
$\boldsymbol{\epsilon}$	Strain tensor	$-$
$\dot{\epsilon}$	Strain rate	s^{-1}
ϵ	Isotope enrichment factor	$-$
ϵ	Strain	$-$
ϵ_v	Volume plastic strain	$-$
η	Porosity	$-$
η_M	Maxwell viscosity	$\mathrm{Pa}\cdot\mathrm{d}$
η_K	Kelvin viscosity	$\mathrm{Pa}\cdot\mathrm{d}$
γ	Activity coefficient for dissolved species	$-$
γ_l	First-order degradation rate	day^{-1}
κ	Thermal conductivity	$\mathrm{W}\cdot\mathrm{m}^{-1}\,\mathrm{K}^{-1}$
λ_c	Virgin compression index	$-$
λ_p	Hardening parameter	$-$
λ	Thermal conductivity	$\mathrm{W}\cdot\mathrm{m}^{-1}\,\mathrm{K}^{-1}$
μ	Dynamic viscosity	$\mathrm{Pa}\cdot\mathrm{s}$
μ	Viscosity	$\mathrm{Pa}\cdot\mathrm{s}$
ν	Poisson number	$-$
Q_ω	source/sink term	$\mathrm{kg}\cdot\mathrm{m}^{-3}\cdot\mathrm{s}{-}1$

ω	Intergranular thickness	m
ω	Saturation index	–
ϕ	Porosity	–
ρ	Density	$kg \cdot m^{-3}$
ρ_s	Density of solid	$kg \cdot m^{-3}$
ρ_w	Density of water	$kg \cdot m^{-3}$
ρ_d^s	Density of bentonite bulk	$kg \cdot m^{-3}$
$\boldsymbol{\sigma}$	Cauchy stress tensor	Pa
σ_V	Von Mises equivalent stress	Pa
σ_{eff}	Effective stress	Pa
σ	Effective stress	Pa
σ_{max}^{sw}	Tested maximum swelling stress	Pa
σ_a	Contact stress	Pa
σ_c	Critical stress	Pa

Roman symbols

a	Specific surface area	$m^2 \cdot m^{-3}$
a^σ	Activity of stressed solid	–
$\dot{a}$	Effective diameter of ion	m
b_h	Fracture hydraulic aperture	m
b_m	Fracture mechanical aperture	m
c	Normalized concentration	–
c	Concentration	$kg \cdot m^{-3}$
C_{eq}^h	Solubility under hydrostatic pressure	$mol \cdot m^{-3}$
C_i	Intergranular concentration	$mol \cdot m^{-3}$
C_p	Pore-space concentration	$mol \cdot m^{-3}$
Cr	Courant number	–
c_p	Heat capacity	$J \cdot kg^{-1} \cdot K^{-1}$
Cp	Heat capacity	$J \cdot kg^{-1} \cdot K^{-1}$
D	Diffusivity coefficient	$m^2 \cdot s^{-1}$
D_f	Intergranular diffusion coefficient	$m^2 \cdot s^{-1}$
E	Young's modulus	–
e	Void ratio	–
g	Gravitational coefficient	$m \cdot s^{-2}$
g	plastic potential	J
$\mathbf{g}$	Gravity vector	$m \cdot s^{-2}$
$\mathbf{g}$	Gravitational acceleration	$m \cdot s^{-2}$
G	Gibbs energy	J
G	Gibbs energy	$J \cdot mol^{-1}$
G_M	Maxwell shear modulus	–
G_K	Kelvin shear modulus	–
h_f	Freshwater hydraulic head	m
h_s	Saltwater hydraulic head	m
I	Ionic strength	–
$\mathbf{k}$	Permeability tensor	m^2
$\mathbf{k}$	Permeability tensor	$m \cdot s^{-1}$
$\mathbf{K}$	Intrinsic permeability	m^2
k_c	Swelling/recompression index	–
K_M	Maxwell bulk modulus	–
$K_r el$	Relative permeability	m^2
k_s	Saturated hydraulic conductivity	$m \cdot d^{-1}$
k^+	Dissolution rate constant	$mol \cdot m^{-2} \cdot s^{-1}$
k°	Reaction rate constant	$mol \cdot m^{-2} \cdot s^{-1}$

M	Slope of critical state line	$-$
M_w	Molecular mass of water vapor	$18.016\,\mathrm{g} \cdot \mathrm{mol}^{-1}$
n	Porosity	$\mathrm{m}^3 \cdot \mathrm{m}^{-3}$
n	Van Genuchten parameter	$-$
p	Pressure	$\mathrm{kg} \cdot \mathrm{s}^{-1} \cdot \mathrm{m}^{-1}$
p	Pressure	Pa
P_c	Capillary pressure	Pa
p_s	Mean stress	Pa
p_{scn}	Isotropic pre-consolidation pressure	Pa
Pe	Péclet number	$-$
q	Source/sink term	$-$
q	Shear stress	Pa
q	Heat source	W
q	Darcy velocity	$\mathrm{m} \cdot \mathrm{s}^{-1}$
$\mathbf{q}$	Darcy velocity vector	$\mathrm{m} \cdot \mathrm{s}^{-1}$
R	Universal gas constant	$8.31432\,\mathrm{J} \cdot \mathrm{mol}^{-1} \cdot \mathrm{K}^{-1}$
R_c	Contact area ratio	$-$
s	soil suction	kPa
S	Saturation	$-$
S_e	Effective saturation	$-$
S_{max}	Maximum water saturation	$-$
S_r	Residual saturation	$-$
S_r	Residual water saturation	$-$
SA	Reactive surface area	m^2
t	Time	s
T	Temperature	K
T	Absolute temperature	K
$\mathbf{u}$	Displacement vector	m
v	Velocity	$\mathrm{m} \cdot \mathrm{s}^{-1}$
V	Volume	m^3
V_m	Molar volume	$\mathrm{m}^3 \cdot \mathrm{mol}^{-1}$
w	Margules parameter	$\mathrm{J} \cdot \mathrm{mol}^{-1}$
X	Molar fraction	$-$
Z	Ionic integer charge	$-$
Z	Charge	$-$

Indices

$\|$	Co-linear direction
$\perp$	Orthogonal direction
$\parallel$	Parallel to the plane of isotropy
$\perp$	Normal to the plane of isotropy
e	Efficient value
w	Water
s	Solid
0	Reference value

Operators

div, $\nabla \cdot$	Divergence operator
grad, ∇	Nabla, gradient operator
tr	Trace

Index

References

DECOVALEX DEvelopment of COupled models and their VALidation against EXperiments, May 2015. URL `http://www.decovalex.org`.

Abaqus. Abaqus FEA. Technical report, Dassault Systémes, 2007.

P. Ackerer. Preface: Special issue on simulations of reactive transport: Results of the momas benchmarks. *Computational Geosciences*, 14(3):383, 2010. doi: 10.1007/s10596-010-9189-z. URL `http://www.scopus.com/inward/record.url?eid=2-s2.0-77953870681&partnerID=40&md5=bcf4eec2518fdfc90cd2edd12c2846d6`.

A. Aggarwal and J.S. Vitter. The input/output complexity of sorting and related problems. *Commun. ACM*, 31(9):1116–1127, September 1988. ISSN 0001-0782. doi: 10.1145/48529.48535. URL `http://doi.acm.org/10.1145/48529.48535`.

L. Amir and M. Kern. A global method for coupling transport with chemistry in heterogeneous porous media. *Computational Geosciences*, 14(3):465–481, 2010. doi: 10.1007/s10596-009-9162-x. URL `http://www.scopus.com/inward/record.url?eid=2-s2.0-77953873401&partnerID=40&md5=79fe8a8dbc09c27279ceb174f488070b`.

G. Archie. The electrical resistivity log as an aid in determining some reservoir characteristics. *Petroleum Transactions of AIME*, 146:54–62, 1942.

B. Ataie-Ashtiani and M.M. Aghayi. A note on benchmarking of numerical models for density dependent flow in porous media. *Advances in Water Resources*, 29(12):1918–1923, December 2006. ISSN 03091708. doi: 10.1016/j.advwatres.2006.01.009. URL `http://linkinghub.elsevier.com/retrieve/pii/S0309170806000273`.

Autocheck. Autocheck, version 1.0.0. `https://github.com/thejohnfreeman/autocheck`, 2015. Accessed: 7. Nov. 2015.

S. Balay, S. Abhyankar, M.F. Adams, J. Brown, P. Brune, K. Buschelman, L. Dalcin, V. Eijkhout, W.D. Gropp, D. Kaushik, M.G. Knepley, L. Curfman McInnes, K. Rupp, B.F. Smith, S. Zampini, and H. Zhang. PETSc Web page. `http://www.mcs.anl.gov/petsc`, 2015. URL `http://www.mcs.anl.gov/petsc`.

R.A. Beier, M.D. Smith, and J.D. Spitler. Reference data sets for vertical borehole ground heat exchanger models and thermal response test analysis. *Geothermics*, 40(1):79–85, 2011. doi: 10.1016/j.geothermics.2010.12.007.

I. Ben Gharbia and J. Jaffré. Gas phase appearance and disappearance as a problem with complementarity constraints. *Mathematics and Computers in Simulation*, 99:28–36, 2014.

M. A. Biot. General theory of three-dimensional consolidation. *J. Appl. Phys.*, 12:155–164, 1941.

H. Bock. RA experiment: Updated review of the rock mechanics properties of the opalinus clay of the Mont Terri URL based on laboratory and field testing. *Mont Terri Project, Technical Note*, 04, 2008.

J. R. Booker and C. Savvidou. "consolidation around a point heat source". *Int. J. Numerical Analytical Meth. Geomech*, 9:173–185, 1985a.

J.R. Booker and C. Savvidou. Consolidation around a point heat source. *Int J Numer Anal Methods Geomech*, 84:973, 1985b.

Boost. Boost c++ libraries, version 1.59.0. `http://www.boost.org`, 2015. Accessed: 7. Nov. 2015.

A. Bourgeat, M. Jurak, and F. Smaï. Two-phase, partially miscible flow and transport modeling in porous media; application to gas migration in a nuclear waste repository. *Computational Geosciences*, 13(1):29–42, 2009.

A. Bourgeat, M. Jurak, and F. Smaï. On persistent primary variables for numerical modeling of gas migration in a nuclear waste repository. *Computational geosciences*, 17(2):287–305, 2013.

J. Bruno, D. Bosbach, D. Kulik, and A. Navrotsky. Chemical thermodynamics of solid solutions of interest in radioactive waste management: A state-of-the art report. In J.Perrone F.J.Mompean, M.Illemassene, editor, *Chemical Thermodynamics*, volume Series 10. OECD, Paris, 2007.

D. E. Carlson. Linear thermoelasticity. In S. Flügge and C. Truesdell, editors, *Encyclodedia of physics*, volume VIa/2, Mechanics of solids II, pages 297–345. Springer, Berlin, Heidelberg, New York, 1972.

J. Carrayrou. Looking for some reference solutions for the reactive transport benchmark of momas with specy. *Computational Geosciences*, 14(3):393–403, 2010. doi: 10.1007/s10596-009-9161-y. URL `http://www.scopus.com/inward/record.url?eid=2-s2.0-77953872044&partnerID=40&md5=f8211185384fdd6fd4b32a0ac7422b96`.

J. Carrayrou, J. Hoffmann, P. Knabner, S. Kräutle, C. de Dieuleveult, J. Erhel, J. van der Lee, V. Lagneau, K.U. Mayer, and K.T.B. MacQuarrie. Comparison of numerical methods for simulating strongly nonlinear and heterogeneous reactive transport problems-the momas benchmark case. *Computational Geosciences*, 14(3):483–502, 2010a. doi: 10.1007/s10596-010-9178-2. URL `http://www.scopus.com/inward/record.url?eid=2-s2.0-77953872133&partnerID=40&md5=9bb7f059f430b1dd09d53a983232cd97`.

J. Carrayrou, M. Kern, and P. Knabner. Reactive transport benchmark of momas. *Computational Geosciences*, 14(3):385–392, 2010b.

doi: 10.1007/s10596-009-9157-7. URL `http://www.scopus.com/inward/record.url?eid=2-s2.0-77953873862&partnerID=40&md5=46c6dbc910f84566e64684c0f7179133`.

H. S. Carslaw and J. C. Jaeger. *Conduction of heat in solids.* Oxford University Press, London, 2nd edition, 1959.

K. Claessen and J. Hughes. Quickcheck: Automatic testing of haskell programs, version 2.8.1. `https://hackage.haskell.org/package/QuickCheck`, 2015. Accessed: 7. Nov. 2015.

T.P. Clement, W.R. Wise, and F.J. Molz. A physically based, two-dimensional, finite-difference algorithm for modeling variably saturated flow. *Journal of Hydrology*, 161:71–90, 1994.

K.S. Crump. Numerical inversion of Laplace transforms using a Fourier series approximation. *J. Asso. Comp. Mach*, 23(1):89–96, 1976.

C.W. Cryer. A comparison of the three-dimensional consolidation theories of Biot and Terzaghi. *Quart. J. Mech. and Appl. Math.*, 16:401–412, 1963.

C. de Dieuleveult and J. Erhel. A global approach to reactive transport: Application to the momas benchmark. *Computational Geosciences*, 14(3):451–464, 2010. doi: 10.1007/s10596-009-9163-9. URL `http://www.scopus.com/inward/record.url?eid=2-s2.0-77953872559&partnerID=40&md5=954b554283f3e15c82b05a74569f69ef`.

H.-J.G. Diersch, D. Bauer, W. Heidemann, W. Rühaak, and P. Schätzl. Finite element modeling of borehole heat exchanger systems part 2. numerical simulation. *Computers & Geosciences*, 37(1):1136–1147, 2011. doi: 10.1016/j.cageo.2010.08.002.

P. Dove and C. Czank. Crystal chemical controls on the dissolution kinetics of the isostructural sulfates; celestite, anglesite and barite. *Geochemica et Cosmochimica Acta*, 56(4147-4156), 2005.

M.M. Dubinin. Theory of the physical adsorption of gases and vapors and adsorption properties of adsorbents of various natures and porous structures. *Bulletin of the Academy of Sciences of the USSR, Division of Chemical Science*, 9(7):1072–1078, 1960. ISSN 0568-5230. doi: 10.1007/BF01161525. URL `http://dx.doi.org/10.1007/BF01161525`.

I. Fatt, W.A. Klikoff Jr, et al. Effect of fractional wettability on multiphase flow through porous media. *Journal of Petroleum Technology*, 11(10):71–76, 1959.

T. Fischer, L. Bilke, K. Rink, D. Y. Naumov, N. Watanabe, W. Wang, Ogsbot, Carolinh, M. Walther, and Mylese. ogs: 6.0.2 - Intermediate DOI release, August 2015. URL `http://dx.doi.org/10.5281/zenodo.27429`.

M. Frigo, C.E. Leiserson, H. Prokop, and S. Ramachandran. Cache-oblivious algorithms. In *Proceedings of the 40th Annual Symposium on Foundations of Computer Science*, FOCS '99, pages 285–, Washington, DC, USA, 1999. IEEE Computer Society. ISBN 0-7695-0409-4. URL `http://dl.acm.org/citation.cfm?id=795665.796479`.

B. Garitte, A. Gens, J. Vaunat, and G. Armand. Thermal conductivity of argillaceous rocks: determination methodology using in situ heat-

ing tests. *Rock Mechanics and Rock Engineering*, 2012. doi: 10.1007/ s00603-012-0335-x.

C. Geuzaine and J.-F. Remacle. Gmsh: a three-dimensional finite element mesh generator with built-in pre- and post-processing facilities. *International Journal for Numerical Methods in Engineering*, 79(11):1309–1331, 2009.

C. Girardin and C. Nussbaum. CD experiment (cyclic deformations): Installation and procedures of measurement. *Mont Terri Project, Technical Note*, 64, 2006.

Google Test. Google test, google's c++ test framework, version 1.7.0. `https://github.com/google/googletest`, 2015. Accessed: 7. Nov. 2015.

R. R. Goswami and T. P. Clement. Laboratory-scale investigation of saltwater intrusion dynamics. *Water Resources Research*, 43(4):1–11, April 2007. ISSN 0043-1397. doi: 10.1029/2006WR005151.

T. Graf and L. Degener. Grid convergence of variable-density flow simulations in discretely-fractured porous media. *Advances in Water Resources*, 34(6):760–769, June 2011. ISSN 03091708. doi: 10.1016/j.advwatres. 2011.04.002. URL `http://linkinghub.elsevier.com/retrieve/pii/S0309170811000583`.

G. Guennebaud, B. Jacob, et al. Eigen v3. `http://eigen.tuxfamily.org`, 2015. Accessed: 7. Nov. 2015.

M.E. Gurtin. The linear theory of elasticity. In S. Flügge and C. Truesdell, editors, *Encyclodedia of physics*, volume VIa/2, Mechanics of solids II, pages 1–295. Springer, Berlin, Heidelberg, New York, 1972.

Haskell. The glorious glasgow haskell compilation system user's guide, version 7.10.2. `http://www.haskell.org`, 2015. Accessed: 7. Nov. 2015.

A. Hauer. *Beurteilung fester Adsorbentien in offenen Sorptionssystemen für energetische Anwendungen*. PhD thesis, July 2002.

W. He, C. Beyer, J.H. Fleckenstein, E. Jang, O. Kolditz, D. Naumov, and T. Kalbacher. A parallelization scheme to simulate reactive transport in the subsurface environment with ogs#iphreeqc. *Geosci. Model Dev. Discuss.*, 8:2369–2402, 2015a.

W. He, H. Shao, O. Kolditz, W. Wang, and T. Kalbacher. Comments on "a mass-conservative switching algorithm for modeling fluid flow in variably saturated porous media, k. sadegh zadeh, journal of computational physics, 230 (2011)". *Journal of Computational Physics*, 295:815–820, 2015b.

J. Heiss and H. Michael. Saltwater-freshwater mixing dynamics in a sandy beach aquifer over tidal, spring-neap, and seasonal cycles. *Water Resources Research*, 50(8):6747–6766, 2014. doi: 10.1002/2014WR015574.

H.C. Helgeson, D.H. Kirkham, and G.C. Flowers. Theoretical prediction of the thermodynamic behaviour of aqueous electrolytes at high pressures and temperatures: Calculation of activity coefficients, osmotic coefficients, and apparent molal and standard and relative partial molal properties to 600c. *American Journal Science*, 281:1249–1516, 1981.

R. Helmig. *Multiphase flow and transport processes in the subsurface: a contribution to the modeling of hydrosystems*. Springer, Berlin, 1997.

S. Heusermann, K.-H. Lux, and R. Rokahr. *Entwicklung mathematisch-mechanischer Modelle zur Beschreibung des Stoffverhaltens von Salzgestein in Abhängigkeit von der Zeit und der Temperatur auf der Grundlage von Laborversuchen mit begleitenden kontinuumsmechanischen Berechnungen nach der Methode der finiten Elemente*. Fachinformationszentrum Energie, Physik, Mathematik Karlsruhe, 1983.

S. Heusermann, O. Rolfs, and U. Schmidt. Nonlinear finite-element analysis of solution mined storage caverns in rock salt using the {LUBBY2} constitutive model. *Computers & Structures*, 81(8–11):629 – 638, 2003. ISSN 0045-7949. doi: http://dx.doi.org/10.1016/S0045-7949(02)00415-7. URL `http://www.sciencedirect.com/science/article/pii/S0045794902004157`. K.J Bathe 60th Anniversary Issue.

J. Hoffmann, S. Kräutle, and P. Knabner. A parallel global-implicit 2-d solver for reactive transport problems in porous media based on a reduction scheme and its application to the momas benchmark problem. *Computational Geosciences*, 14(3):421–433, 2010. doi: 10.1007/s10596-009-9173-7. URL `http://www.scopus.com/inward/record.url?eid=2-s2.0-77953872308&partnerID=40&md5=18cafaa2874497e3688eb9a0b8a77d79`.

J. Hoffmann, S. Kräutle, and P. Knabner. A general reduction scheme for reactive transport in porous media. *Computational Geosciences*, 16(4):1081–1099, 2012. doi: 10.1007/s10596-012-9304-4. URL `http://www.scopus.com/inward/record.url?eid=2-s2.0-84866437382&partnerID=40&md5=b90664a6ce620e944de08309465d3a07`.

Z. Hou, R. Wolters, R. Rokahr, D. Zapf, K. Salzer, R.-M. Günter, W. Minkley, A. Pudewills, U. Heemann, O. Schulze, F. Zetsche, and A. Hampel. Comparison of advanced constitutive models for the mechanical behaviour of rock salt - results from a joint research project – II. Numerical modeling of two in situ case studies ans comparison. pages 89–98, 2007.

Y. Huang, O. Kolditz, and H. Shao. Extending the persistent primary variable algorithm to simulate non-isothermal two-phase two-component flow with phase change phenomena. *Geothermal Energy*, 3(1), 2015a. doi: 10.1186/s40517-015-0030-8. URL `http://www.scopus.com/inward/record.url?eid=2-s2.0-84942096445&partnerID=40&md5=d68b4854589202695acc57b44e25380e`.

Y. Huang, O. Kolditz, and H. Shao. Extending the persistent primary variable algorithm to simulate non-isothermal two-phase two-component flow with phase change phenomena. *Geothermal Energy*, 3(1):1–23, 2015b.

W. Hummel, U. Berner, E. Curti, F. J. Pearson, and T. Thoenen. Nagra/psi chemical thermodynamic data base. Technical report, Parkland Florida: Universal Publishers, 2002.

ISO. ISO C++ standard. ISO 14882:2011(E), International Organization for Standardization, Geneva, Switzerland, 2011.

J. C. Jaeger and N. G. W. Cook. *Fundamentals of rock mechanics*. Chapman, London, 3rd edition, 1971.

J. C. Jaeger, N. G. W. Cook, and R. W. Zimmerman. *Fundamentals of Rock Mechanics (4th Edition)*. John Wiley & Sons, 2007.

JNC. Second progress report on research and development for the geological disposal of HLW in japan. Supporting Report 2: Repository Design and Engineering Technology TN1410 1000-003, Japan Nuclear Development Institute, April 2000. H12: Project to establish the Scientific and technical Basis for HLW Disposal in Japan.

J.W. Johnson, E.H. Oelkers, and H.C. Helgeson. Supcrt92: A software package for calculating the standard molal thermodynamic properties of minerals, gases, aqueous species, and reactions from 1 to 5000 bar and 0 to 1000^oC. *Computational Geoscience*, 18:899–947, 1992.

A. Kneschke. Elastische Kreisplatten unter einseitiger Temperatureinwirkung. *ZAMM*, 40(1/3):40–46, 1960.

O. Kolditz. *Computational Methods in Environmental Fluid Mechanics*. Springer-Verlag, Berlin - Heidelberg, 2002. ISBN 978-3-662-04761-3.

O. Kolditz, S. Bauer, C. Beyer, N. Böttcher, P. Dietrich, U.-J. Görke, T. Kalbacher, C.-H. Park, U. Sauer, C. Schütze, H. Shao, A. Singh, J. Taron, W. Wang, and N. Watanabe. A systematic benchmarking approach for geologic co2 injection and storage. *Environmental Earth Sciences*, 67(2):613–632, 2012a. URL `http://www.scopus.com/inward/record.url?eid=2-s2.0-84865826006&partnerID=40&md5=b18bfc983d7fa3b985fd09e5dd2ad26b`.

O. Kolditz, S. Bauer, L. Bilke, N. Böttcher, J.O. Delfs, T. Fischer, U.J. Görke, T. Kalbacher, G. Kosakowski, C.I. McDermott, et al. Opengeosys: an open-source initiative for numerical simulation of thermo-hydromechanical/chemical (thm/c) processes in porous media. *Environmental Earth Sciences*, 67(2):589–599, 2012b.

O. Kolditz, U.-J. Görke, H. Shao, and W. Wang. *Thermo-Hydro-Mechanical-Chemical Processes in Fractured Porous Media*. Number 86 in Lecture Notes in Computational Science and Engineering. Springer-Verlag, Berlin Heidelberg, 2012c. doi: 10.1007/978-3-642-27177-9.

O. Kolditz, H. Shao, W. Wang, and S. Bauer. *Thermo-Hydro-Mechanical-Chemical Processes in Fractured Porous Media: Modelling and Benchmarking*. Terrestrial Environmental Sciences. Springer-Verlag, 2015. doi: 10.1007/978-3-319-11894-9.

G. Kosakowski and N. Wanatabe. Opengeosys-gem: A numerical tool for calculating geochemical and porosity changes in saturated and partially saturated media. *Physics and Chemistry of the Earth*, 70-71:138–149, 2014.

D.A. Kulik, Y. Wagner, S.V. Dmytrieva, G. Kosakowski, F.F. Hingerl, and K.V. Chudnenko. Gem-selektor geochemical modeling package: revised algorithm and gems3k numerical kernel for coupled simulation codes. *Computational Geosciences*, 17:1–24, 2013.

H. Kunz. *GINA_OGS*, chapter Appendix C, pages 353–355. In *Lecture Notes in Computational Science and Engineering* Kolditz et al. (2012c), 2012. doi: 10.1007/978-3-642-27177-9.

V. Lagneau and J. van der Lee. Hytec results of the momas reactive transport benchmark. *Computational Geosciences*, 14(3): 435–449, 2010. doi: 10.1007/s10596-009-9159-5. URL `http://www.scopus.com/inward/record.url?eid=2-s2.0-77953869656&partnerID=40&md5=28d4696824c1df167576b5a36aa7e517`.

C.H. Lan, O.A. Ezekoye, J.R. Howell, and K.S. Ball. Stability analysis for three-dimensional Rayleigh–Bénard convection with radiatively participating medium using spectral methods. *International journal of heat and ...*, 46:1371–1383, 2003. URL `http://www.sciencedirect.com/science/article/pii/S0017931002004222`.

E.W. Lemmon, M.O. McLinden, and D.G. Friend. Thermophysical properties of fluid systems. In P.J. Linstrom and W.G. Mallard, editors, *NIST Chemistry WebBook*, volume NIST Standard Reference Database Number 69. National Institute of Standards and Technology, Gaithersburg MD, USA, retrieved Oct, 2014. http://webbook.nist.gov.

LIS. Lis: Library of iterative solvers for linear systems, version 1.5.57. `http://http://www.ssisc.org/lis`, 2015. Accessed: 7. Nov. 2015.

A.I. Lurje. *Räumliche Probleme der Elastizitätstheorie*. Akademie-Verlag, Berlin, 1963.

J. Mandel. Consolidation des sols (étude mathématique). *Géotechnique*, 3: 287–299, 1953.

E. Marchand and P. Knabner. Results of the momas benchmark for gas phase appearance and disappearance using generalized mhfe. *Advances in Water Resources*, 73:74–96, 2014a. doi: 10.1016/j.advwatres.2014.07.005. URL `http://www.scopus.com/inward/record.url?eid=2-s2.0-84907310072&partnerID=40&md5=2c8727cf04d21fd7b368652e2abd9e82`.

E. Marchand and P. Knabner. Results of the momas benchmark for gas phase appearance and disappearance using generalized mhfe. *Advances in Water Resources*, 73:74–96, 2014b.

C.D. Martin and G.W. Lanyon. Measurement of in-situ stress in weak rocks at Mont Terri Rock Laboratory, Switzerland. *International Journal of Rock Mechanics and Mining Sciences*, 40:1077–1088, 2003.

J.M. Matray and A. Möri. CD (Cyclic deformation) experiment, petrophysical measurements on BCD-3 core samples from the Mont Terri rock laboratory. *Mont Terri Project, Technical Note*, 49, 2012.

R.M. Maxwell, M. Putti, S. Meyerhoff, J.-O. Delfs, I.M. Ferguson, V. Ivanov, J. Kim, O. Kolditz, S.J. Kollet, M. Kumar, S. Lopez, J. Niu, C. Paniconi, Y.-J. Park, M.S. Phanikumar, C. Shen, E.A. Sudicky, and M. Sulis. Surface-subsurface model intercomparison: A first set of benchmark results to diagnose integrated hydrology and feedbacks. *Water Resources Research*, 50(2):1531–1549, 2014. URL `http:`

//www.scopus.com/inward/record.url?eid=2-s2.0-84894241336&
partnerID=40&md5=8342baa8643da141ab15294aa308b817.

K.U. Mayer and K.T.B. MacQuarrie. Solution of the momas react-
ive transport benchmark with min3p-model formulation and sim-
ulation results. *Computational Geosciences*, 14(3):405–419, 2010.
doi: 10.1007/s10596-009-9158-6. URL http://www.scopus.com/
inward/record.url?eid=2-s2.0-77953873098&partnerID=40&md5=
c32346ecd599f221488548d9a323d147.

E. Melan and H. Parkus. *Wärmespannungen infolge stationärer Temperat-
urfelder.* Springer, Wien, 1953.

D. Mottaghy and V. Rath. Latent heat effects in subsurface heat transport
modelling and their impact on palaeotemperature reconstructions. *Geo-
physical Journal International*, 164(1):236–245, 2006.

A. Möri, P. Bossart, J.-M. Matray, E. Frank, H. Fatmi, and R. Ababou. Mont
Terri Project, Cyclic deformations in the opalinus clay. In *Clay in Natural
and Engineered Barriers for Radioactive Waste Confinement - Proceedings
of the Meeting „Nantes 2010"*, 2010.

S. Mukhopadhyay, J.T. Birkholzer, J.-P. Nicot, and S.A. Hosseini.
A model comparison initiative for a co 2 injection field test:
An introduction to sim-seq. *Environmental Earth Sciences*, 67
(2):601–611, 2012. doi: 10.1007/s12665-012-1668-1. URL http:
//www.scopus.com/inward/record.url?eid=2-s2.0-84865809070&
partnerID=40&md5=bd0ec2b32ac230d739c7c7fbeeb064ce.

S. Mukhopadhyay, C. Doughty, D. Bacon, J. Li, L. Wei, H. Yamamoto,
S. Gasda, S.A. Hosseini, J.-P. Nicot, and J.T. Birkholzer. The
sim-seq project: Comparison of selected flow models for the s-
3 site. *Transport in Porous Media*, 108(1):207–231, 2015. doi:
10.1007/s11242-014-0361-0. URL http://www.scopus.com/
inward/record.url?eid=2-s2.0-84929061413&partnerID=40&md5=
49515b194504d8ff56de666c1e91892c.

A. E. Mulligan, C. Langevin, and V. E. A. Post. Tidal boundary conditions
in SEAWAT. *Ground Water*, 49(6):866–79, 2011. ISSN 1745-6584. doi:
10.1111/j.1745-6584.2010.00788.x. URL http://www.ncbi.nlm.nih.gov/
pubmed/21275984.

D. Naumov, L. Bilke, and O. Kolditz. Rendering technique of multi-
layered domain boundaries and its application to fluid flow in por-
ous media visualizations. *Environmental Earth Sciences*, 72(10):
3795–3802, 2014. doi: 10.1007/s12665-014-3445-9. URL http:
//www.scopus.com/inward/record.url?eid=2-s2.0-84925528281&
partnerID=40&md5=906d781549da8aeb04a586aafb29ebf2.

F. Neumann. Die partiellen differentialgleichungen. *Physik (5th ed., 1912)*,
2:121, 1860.

R. Neumann, P. Bastian, and O. Ippisch. Modeling and simulation of two-
phase two-component flow with disappearing nonwetting phase. *Compu-
tational Geosciences*, 17(1):139–149, 2013.

T. Núñez. *Charakterisierung und Bewertung von Adsorbentien für Wärmetransformationsanwendungen.* PhD thesis, Universitätsbibliothek Freiburg, February 2002.

C. Oltean, F. Golfier, and M.a. Buès. Experimental and numerical study of the validity of Hele-Shaw cell as analogue model for variable-density flow in homogeneous porous media. *Advances in Water Resources*, 31(1):82–95, January 2008. ISSN 03091708. doi: 10.1016/j.advwatres.2007.06.007. URL `http://linkinghub.elsevier.com/retrieve/pii/S030917080700111X`.

J. Palandri and Y. Kharaka. A compilation of rate parameters of water mineral interaction kinetics for application to geochemical modelling. Usgs report 04-1068, Menlo Park, California: U.S Geological Survey, 2004a.

James L Palandri and Yousif K Kharaka. A compilation of rate parameters of water-mineral interaction kinetics for application to geochemical modeling. Technical report, DTIC Document, 2004b.

David L Parkhurst, CAJ Appelo, et al. User's guide to phreeqc (version 2): A computer program for speciation, batch-reaction, one-dimensional transport, and inverse geochemical calculations. 1999.

D.L. Parkhurst and L. Wissmeier. Phreeqcrm: A reaction module for transport simulators based on the geochemical model phreeqc. *Advances in Water Resources*, 83:176–189, 2015. doi: 10.1016/j.advwatres.2015.06.001. URL `http://www.scopus.com/inward/record.url?eid=2-s2.0-84938521560&partnerID=40&md5=ba9447214561c94f3438474a0963c5ce`.

J. Poonoosamy, G. Kosakowski, L.R. Van Loon, and U. & Mäder. Dissolution-precipitation processes in tank experiments for testing numerical models for reactive transport calculations: Experiment and modelling. *Journal of Contaminant Hydrology*, 177-178:1–17, 2015.

H. Prokop. *Cache-oblivious algorithms.* PhD thesis, Massachusetts Institute of Technology, 1999.

A. Pudewills. Modellierung des mechanischen Verhaltens von Steinsalz: Vergleich aktueller Stoffgesetze und Vorgehensweisen. Technical report, Forschungszentrum Karlsruhe, 2007.

F. Renard, A. Park, P. Ortoleva, and J. P. Gratier. An integrated model for transitional pressure solution in sandstones. *Tectonophysics*, 312(2-4):97–115, November 1999. doi: 10.1016/S0040-1951(99)00202-4.

J.D. Rimstidt. Quartz solubility at low temperatures. *Geochimica et Cosmochimica Acta*, 61(13):2553–2558, July 1997. ISSN 0016-7037.

J.D. Rimstidt and H.L. Barnes. The kinetics of silica-water reactions. *Geochimica et Cosmochimica Acta*, 44(11):1683–1699, 1980. ISSN 0016-7037.

C. Robinson, L. Li, and D.a. Barry. Effect of tidal forcing on a subterranean estuary. *Advances in Water Resources*, 30(4):851–865, April 2007. ISSN 03091708. doi: 10.1016/j.advwatres.2006.07.006. URL `http://linkinghub.elsevier.com/retrieve/pii/S0309170806001217`.

C. Runciman and R. Cheplyaka. smallcheck: A property-based testing library, version 1.1.1. https://hackage.haskell.org/package/smallcheck, 2015. Accessed: 7. Nov. 2015.

J. Rutqvist, L. Börgesson, M. Chijimatsu, A. Kobayashi, L. Jing, T.S. Nguyen, J. Noorishad, and C.-F. Tsang. Thermohydromechanics of partially saturated geological media: governing equations and formulation of four finite element models. *Rock Mechanics and Mining Sciences*, 38:105–127, 2001.

A. Sachse, K. Rink, W. He, and O. Kolditz. *OpenGeoSys-Tutorial: Computational Hydrology I: Groundwater Flow Modeling*. Springer, Heidelberg, 2015.

H. Shao, S. Dmytrieva, O. Kolditz, D. Kulik, D. Pfingsten, and G. Kosakowski. Modeling reactive transport in non-ideal aqueous–solid solution system. *Applied Geochemistry*, 24(7):1287–1300, 2009.

D.T. Snow. Anisotropie permeability of fractured media. *Water Resources Research*, 5(6):1273–1289, 1969. ISSN 0043-1397.

F. Stauffer, P. Bayer, P. Blum, N. Molina-Giraldo, and W. Kinzelbach. *Thermal Use of Shallow Groundwater*. CRC Press. Taylor & Francis Group, LLC, 2014. ISBN 978-1-4665-6019-2.

C.I. Steefel, C.A.J. Appelo, B. Arora, D. Jacques, T. Kalbacher, O. Kolditz, V. Lagneau, P.C. Lichtner, K.U. Mayer, J.C.L. Meeussen, S. Molins, D. Moulton, H. Shao, J. Šimůnek, N. Spycher, S.B. Yabusaki, and G.T. Yeh. Reactive transport codes for subsurface environmental simulation. *Computational Geosciences*, 19 (3):445–478, 2014. doi: 10.1007/s10596-014-9443-x. URL http://www.scopus.com/inward/record.url?eid=2-s2.0-84933181545&partnerID=40&md5=3c43de357e9e4d9405e22f91c961f830.

M. E. Stern. Collective instability of salt fingers. *Journal of Fluid Mechanics*, 35(02):209–218, March 1969. ISSN 0022-1120. doi: 10.1017/S0022112069001066. URL http://www.journals.cambridge.org/abstract_S0022112069001066.

B. Stroustrup and A. Sutton. A concept design for the stl. (N3351=12-0041), 2012.

S. Sugio and C.S. Desai. Residual flow procedure for sea water intrusion in unconfined aquifers. *International Journal for Numerical Methods in Engineering*, 24(8):1439–1450, August 1987. ISSN 1097-0207. doi: 10.1002/nme.1620240803.

Y. Sugita. Property for the simulation of engineered barrier experiment at horonobe url, step 1, 2013.

Y. Sugita. Task b2 - conditions for step 2, 2014.

Y. Sugita and S. Nakama. Decovalex-2015: Description of task b2, 2012.

J. Taron and D. Elsworth. Constraints on compaction rate and equilibrium in the pressure solution creep of quartz aggregates and fractures: Controls of aqueous concentration. *Journal of Geophysical Research: Solid Earth*, 115:B07211, 2010a. ISSN 2156-2202. doi: 10.1029/2009JB007118.

J. Taron and D. Elsworth. Coupled mechanical and chemical processes in engineered geothermal reservoirs with dynamic permeability. *International Journal of Rock Mechanics and Mining Sciences*, 47(8):1339 – 1348, 2010b. ISSN 1365-1609. doi: 10.1016/j.ijrmms.2010.08.021.

K.S. Udell and J.S. Fitch. Heat and mass transfer in capillary porous media considering evaporation, condensation, and non-condensible gas effects. In *23rd ASME/AIChE National Heat Transfer Conference, Denver, CO*, pages 103–110, 1985.

B.M. van Breukelen, D. Hunkeler, and F. Volkering. Quantification of sequential chlorinated ethene degradation by use of a reactive transport model incorporating isotope fractionation. *Environmental Science & Technology*, 39(11):4189–4197, 2005.

M.T. Van Genuchten. A closed-form equation for predicting the hydraulic conductivity of unsaturated soils. *Soil science society of America journal*, 44(5):892–898, 1980.

M. Vauclin, J. Khanji, and G. Vachaud. Experimental and numerical study of a transient, two-dimensional unsaturated-saturated water table recharge problem. *Water Resources Research*, 15(5):1089–1101, 1979.

T. Wagner, D. A. Kulik, F. F. Hingerl, and S. V. Dmytrieva. Gem-selektor geochemical modeling package: Tsolmod library and data interface for multicomponent phase models. *Canadian Mineralogist*, 50:1173–1195, 2012.

J.B. Walsh. Effect of pore pressure and confining pressure on fracture permeability. *International Journal of Rock Mechanics and Mining Sciences & Geomechanics Abstracts*, 18(5):429–435, October 1981. ISSN 0148-9062.

M. Walther, J.-O. Delfs, J. Grundmann, O. Kolditz, and R. Liedl. Saltwater intrusion modeling: Verification and application to an agricultural coastal arid region in Oman. *Journal of Computational and Applied Mathematics*, 236(18):4798–4809, December 2012. ISSN 03770427. doi: 10.1016/j.cam.2012.02.008. URL http://dx.doi.org/10.1016/j.cam.2012.02.008.

M. Walther, L. Bilke, J.-O. Delfs, T. Graf, J. Grundmann, O. Kolditz, and R. Liedl. Assessing the saltwater remediation potential of a three-dimensional, heterogeneous, coastal aquifer system. *Environmental Earth Sciences*, April 2014. ISSN 1866-6280. doi: 10.1007/s12665-014-3253-2. URL http://link.springer.com/10.1007/s12665-014-3253-2.

M. Walther, L. Stoeckl, J.-O. Delfs, and T. Graf. Density-Dependent Flow. In O. Kolditz, H. Shao, W. Wang, and S. Bauer, editors, *Thermo-Hydro-Mechanical-Chemical Processes in Fractured Porous Media: Modelling and Benchmarking SE - 8*, Terrestrial Environmental Sciences, pages 205–212. Springer International Publishing, 2015. ISBN 978-3-319-11893-2. doi: 10.1007/978-3-319-11894-9_8. URL http://dx.doi.org/10.1007/978-3-319-11894-9_8http://link.springer.com/chapter/10.1007/978-3-319-11894-9_8#.

Q. Wang, Y.-J. Cui, A. M. Tang, J.-D. Barnichon, S. Saba, and W.-M. Ye. Hydraulic conductivity and microstructure changes of compacted bentonite/sand mixture during hydration. *Engineering Geology*, 164:67–76, 2013a.

Q. Wang, A. M. Tang, Y.-J. Cui, J.-D. Barnichon, and W.-M. Ye. A comparative study on the hydro-mechanical behavior of compacted bentonite/sand plug based on laboratory and field infiltration tests. *Engineering Geology*, 162:79–87, 2013b.

Q. Wang, A. M. Tang, Y.-J. Cui, P. Delage, J.-D. Barnichon, and W.-M. Ye. The effects of technological voids on the hydro-mechanical behaviour of compacted bentonite–sand mixture. *Soils and foundations*, 53(2):232–245, 2013c.

W. Wang, G. Kosakowski, and O. Kolditz. A parallel finite element scheme for thermo-hydro-mechanical (thm) coupled problems in porous media. *Computers & Geosciences*, 35(8):1631–1641, 2009.

K.M. Wild, L.P. Wymann, S. Zimmer, R. Thoeny, and F. Amann. Water retention characteristics and state-dependent mechanical and petro-physical properties of clay shale. *Rock Mechanics and Rock Engineering*, 2014. doi: 10.1007/s00603-014-0565-1.

M. Xie, U. Mayer, F. Claret, P. Alt-Epping, J. Diederik, C. Steefel, Chiaberge C., and Simunek J. Implementation and evaluation of permeability-porosity and tortuosity-porosity relationships linked to mineral dissolution-precipitation. *Computational Geosciences*, 19(3):655–671, 2014.

H. Yasuhara, A. Polak, Y. Mitani, A.S. Grader, P.M. Halleck, and D. Elsworth. Evolution of fracture permeability through fluid-rock reaction under hydrothermal conditions. *Earth and Planetary Science Letters*, 244(1-2): 186 – 200, 2006. ISSN 0012-821X. doi: 10.1016/j.epsl.2006.01.046.

H. Yasuhara, N. Kinoshita, H. Ohfuji, D.S. Lee, S. Nakashima, and K. Kishida. Temporal alteration of fracture permeability in granite under hydrothermal conditions and its interpretation by coupled chemo-mechanical model. *Applied Geochemistry*, 26(12):2074 – 2088, 2011. ISSN 0883-2927. doi: http://dx.doi.org/10.1016/j.apgeochem.2011.07.005.

C. L. Yaws, J. W. Miller, P. N. Shah, G. R. Schorr, and P. M. Patel. Correlation constants for chemical compounds. *Chem. Eng.*, 83(25):153–162, 1976.

C. Zhu. Coprecipitation in the barite isostructural family: 1. binary mixing properties. *Geochimica et Cosmochimica Acta*, 68:3327–3337, 2004.